

Vulnerability evaluation and strengthening criteria for R.C. bridges

P.E. Pinto, G. Monti (Editors)

TABLE OF CONTENTS

1	INTRODUCTION.....	4
2	BRIDGE SYSTEMS	9
2.1	Analytical seismic assessment of the bridges on a highway system	9
2.2	Screening of the bridges to be examined.....	10
2.2.1	<i>Hazard analysis.....</i>	<i>11</i>
2.2.2	<i>Natural seismic resistance</i>	<i>12</i>
2.2.3	<i>Final selection of bridges.....</i>	<i>14</i>
2.3	Evaluation of the bridges.....	15
2.3.1	<i>Outline of the procedure</i>	<i>15</i>
2.3.2	<i>The data bank SAMOA</i>	<i>16</i>
2.3.3	<i>Simulated design of the piers</i>	<i>17</i>
2.3.4	<i>Evaluation procedure</i>	<i>17</i>
2.3.5	<i>Quantification of risk.....</i>	<i>19</i>
2.3.6	<i>Selected results</i>	<i>21</i>
2.4	Acceptance criterion	23
2.4.1	<i>Calculation of P_f for $A_g = 0.35g$</i>	<i>24</i>
2.5	Results and conclusions.....	26
2.6	References	26
3	IMPORTANT PHENOMENA AFFECTING THE BRIDGE RESPONSE.....	27
3.1	Multi-support excitation.....	27
3.1.1	<i>Soil motion.....</i>	<i>28</i>
3.1.1.1	<i>Spatial model for ground motion.....</i>	<i>28</i>
3.1.2	<i>Conventional bridges.....</i>	<i>36</i>
3.1.2.1	<i>Design of bridges.....</i>	<i>37</i>
3.1.2.2	<i>Elastic response.....</i>	<i>39</i>
3.1.2.3	<i>Non linear response of bridges to multi-support excitation.....</i>	<i>44</i>
3.1.2.4	<i>Bridges with non-synchronous design</i>	<i>44</i>
3.1.2.5	<i>Bridges with synchronous design.....</i>	<i>47</i>
3.1.2.6	<i>Conclusions regarding conventional bridges.....</i>	<i>49</i>
3.1.3	<i>Isolated bridges.....</i>	<i>52</i>
3.1.3.1	<i>Bridge model and equivalent stiffness and damping ratio of the isolator..</i>	<i>52</i>
3.1.3.2	<i>Equations of motion of the bridge.....</i>	<i>53</i>
3.1.3.3	<i>Response of the isolators.....</i>	<i>54</i>
3.1.3.4	<i>Treatment of damping.....</i>	<i>55</i>
3.1.3.5	<i>Iterative procedure.....</i>	<i>56</i>
3.1.3.6	<i>Design of the isolated bridge.....</i>	<i>57</i>
3.1.3.7	<i>Results of the analyses.....</i>	<i>58</i>
3.1.4	<i>References</i>	<i>65</i>

3.2	Soil-structure interaction.....	68
3.2.1	<i>Mechanical model and equation of motion.....</i>	<i>71</i>
3.2.1.1	<i>Superstructure.....</i>	<i>71</i>
3.2.1.2	<i>Foundation and foundation soil.....</i>	<i>72</i>
3.2.1.3	<i>Effective damping of the soil-structure system.....</i>	<i>74</i>
3.2.1.4	<i>Seismic input.....</i>	<i>75</i>
3.2.1.5	<i>Equation of motion.....</i>	<i>75</i>
3.2.2	<i>Cases examined.....</i>	<i>76</i>
3.2.3	<i>Results.....</i>	<i>79</i>
3.2.4	<i>Conclusions.....</i>	<i>86</i>
3.2.5	<i>References.....</i>	<i>86</i>
3.3	Vertical oscillations.....	88
3.3.1	<i>The analyzed structures: geometry and dimensioning.....</i>	<i>89</i>
3.3.2	<i>The numerical models for non-linear time-history analyses.....</i>	<i>93</i>
3.3.3	<i>Results of non-linear analyses.....</i>	<i>95</i>
3.3.4	<i>Simple mechanical model for axial vibrations.....</i>	<i>101</i>
3.3.5	<i>Conclusions.....</i>	<i>105</i>
3.3.6	<i>References.....</i>	<i>106</i>
4	UPGRADING OF BRIDGE PIERS WITH FRP.....	108
4.1	Properties and behavior of FRP-confined concrete.....	108
4.1.1	<i>Basis model for unconfined concrete.....</i>	<i>108</i>
4.1.2	<i>Concrete model with elastic confinement.....</i>	<i>110</i>
4.1.3	<i>Some considerations on modeling concrete confined with steel or FRP.....</i>	<i>112</i>
4.1.4	<i>Comparison with experimental results.....</i>	<i>116</i>
4.1.4.1	<i>Tests by Picher et al. (1996).....</i>	<i>117</i>
4.1.4.2	<i>Tests by Kawashima et al. (1997).....</i>	<i>118</i>
4.1.4.3	<i>Tests by Mirmiran and Shahawy (1997).....</i>	<i>119</i>
4.1.5	<i>Predictive equations of FRP-confined concrete properties.....</i>	<i>121</i>
4.1.6	<i>Agreement with experiments.....</i>	<i>122</i>
4.2	Response of FRP-wrapped sections.....	124
4.2.1	<i>Assessment of the FRP-confined section model.....</i>	<i>128</i>
4.2.2	<i>Parametric study on FRP-confined sections.....</i>	<i>130</i>
4.3	Design criteria for upgrading through FRP wrapping.....	134
4.3.1	<i>Upgrading index of FRP-wrapped pier sections.....</i>	<i>135</i>
4.3.2	<i>Mechanical Model of the Upgrading Index.....</i>	<i>136</i>
4.3.3	<i>Considerations over the error functions E.....</i>	<i>140</i>
4.3.4	<i>Comparison between analytical and numerical indices.....</i>	<i>141</i>
4.3.5	<i>Use of the upgrading index for design of FRP jackets.....</i>	<i>144</i>
4.3.6	<i>Design Example.....</i>	<i>146</i>
4.3.7	<i>Ductility upgrading of piers in seismic regions.....</i>	<i>146</i>
4.4	Conclusions.....	148
4.5	References.....	149

1 INTRODUCTION

The last intense seismic events occurred in 1999 in Turkey, Greece and Taiwan have had the important consequence of confirming, worldwide, the need of developing new and more comprehensive concepts for assessing the state of existing bridges and for designing safer and easy-to-implement strengthening techniques. Nowadays, no other research topic has so direct an influence over practice, as confirmed by the large amount of retrofit work on bridges, taking place with more and more accelerating pace all over the developed seismic countries of the world.

The need for strengthening the existing bridges stems from the consideration that most of the bridges built in the past in seismic zones according to now-obsolete codes are inadequate to meet the more stringent requirements imposed in the new generation of codes, for as regards both strength and ductility. The deficiencies that make existing bridges, even those built until the very last few years, vulnerable to seismic action all have a single common cause: the conventionality of the seismic design approach used in the former codes (and still in some of the present ones).

It is widely known that those codes had the limitations of emphasizing the strength aspects while only making implicit reference to the concept of ductility and, which is more important, gave no provisions to ensure stability of the response in the post-elastic range.

As a consequence, existing bridge piers built according to those codes – as observed either from original project drawings or through in-situ inspections after destructive seismic events – rather frequently, at least in Italy, are equipped with adequate amounts of longitudinal reinforcement (thus complying with the flexural strength requirements), while systematically showing insufficient transverse reinforcements (thus lacking the confinement necessary for ensuring a ductile response).

Another common source of inadequacy of existing bridge piers arises from the nowadays frequent re-classifications of seismic zones (for ex., in Italy, after that of 1981, a new one is under development, based on more accurate hazard studies); in such cases, most bridge piers designed according to a previous seismic zonation do not satisfy the verifications with the new increased seismic actions.

The seismicity of Italy is certainly less than that, for ex., of California or in parts of Japan, but events of Magnitude of the order of 6.5 are rather frequent (the last $M=6.5$ event did occur in Southern Italy in 1981, and the previous $M=6.5$ in Northern Italy in 1976), and events of magnitude larger than 7 have also occurred, at a rate of about twice every century starting from the year 1000. Although the seismicity of Italy is well known to geophysicists, and plenty of hazard studies have been produced and are available, no officially approved hazard map exists, while the zoning of the country for the purposes of seismic design reflects more the information from (recent) past events than the input from geophysical studies. Additionally, the seismic zones have been substantially enlarged after the 70's, *i.e.*, after the completion of the highway system, so that in the end a random relation exists between the location of the bridges, the actual hazard at the sites, the present

definition of the seismic zones, and the way the bridges have been designed (earthquake resistant or not).

Based on the above considerations, it should be clear how the necessity of accurately assessing the state of existing bridges and of retrofitting them has become a deeply felt issue. Luckily enough, the structural types adopted internationally for urban viaducts and highway bridges are mostly similar; this situation has been of help in arriving at a unified view on the appropriate diagnosis methods and on the remedial measures to be adopted, be these necessary for enhancing strength and/or ductility of the piers, for eliminating excessive mobility of the deck, for ensuring safe transmission of the forces through bearings, etc. This amounts to saying that in seismic retrofit of bridges the focus is not so much on theoretical developments, although technological advances are needed, for ex. on materials and techniques for strengthening, as it is on an efficient management of the resources available.

This report tries to cover all of the above aspects, with due consideration to issues concerning bridges, regarded both as single structures and as parts of a whole and more complex system, such as a highway system. The motivation for the studies contained in this report derives from an endeavor promoted by the GNDT, Gruppo Nazionale per la Difesa dai Terremoti (National Group for the Defense Against Earthquakes) that has had many of the Italian Research Centers and Universities involved in a common effort to provide answers and clarify most of those aspects of the seismic behavior of structures, that are still indefinite and not so thoroughly studied. In particular, this report covers the studies conducted at the University of Rome La Sapienza in the last years, where a continuous effort has been devoted to the investigation of different issues regarding the seismic response of bridges, both conventional and isolated. All the work carried out can be grouped under three main topics, and this is actually how this report is articulated:

Chapter 2 – Bridge systems

Chapter 3 – Important phenomena affecting the bridge response

Chapter 4 – Upgrading of bridge piers with FRP

Chapter 2 (**Bridge systems**, page 9, based on the research work by Giannini, R., Nuti, C., and Pinto, P.E.) is essentially of methodological nature, where object of the study is a significant part of the Italian highway network, whose vulnerable elements are supposed to be the bridges. The study, dealt within a probabilistic framework, involves the complete knowledge of the state of all bridges and the verification whether they are adequate for ensuring the network functioning after an earthquake. This is defined as continued linking between any two nodes of the network. The final objective of such study is that of singling out the most critical bridges for the network functioning, as well as quantifying the degree of upgrading required for reaching the target reliability. The study presented in this chapter is developed in four stages: firstly, the present seismic hazard over the Italian highway network has been defined through an accurate hazard study; secondly, a well-

structured database that collects the description of all bridges in the Italian highway network has been analyzed, from which fragility curves for all bridges have been developed in order to obtain a synthetic description of their behavior under seismic condition; thirdly, the current state of all bridges under scenario earthquakes has been determined; the final step has been to rank the bridges in order of importance (value of the bridges and its role in ensuring continued communication), rehabilitation cost, simultaneous necessity of interventions for non seismic maintenance and repair.

Chapter 3 (**Important phenomena affecting the bridge response**, page 27) deals with topics that can be regarded either from the design or the assessment standpoint. These are issues that significantly affect the overall behavior of bridges, modifying the response and affecting the performance, and are seldom included into design considerations without proper account of the subsequent deficiencies that can hamper the design objectives.

The phenomena considered in Chapter 3, which are recognized a certain relevance, are:

- Multi-support excitation
- Soil-structure interaction
- Vertical oscillations

Multi-support seismic excitation (Section 3.1, page 27, based on the research work by Monti, G., Nuti, C., and Pinto, P.E.) denotes the difference in seismic input that is generally observed at the pier supports of long bridges. Recently recorded soil time histories obtained from strong motion arrays installed in seismic areas have clearly demonstrated that the motion of relatively close points on the soil surface is not synchronous, that is, even relatively close points can experience significant relative displacements. This phenomenon is due both to reflection and refraction of seismic waves through underlying soil layers with different mechanical characteristics and to the presence of soils of different nature under different support points. From the point of view of structural analysis, the most important implication of this observed behavior is that the conventionally adopted assumption of equal seismic input under all supports is only acceptable when dealing with bridges of moderate dimensions, while it is far from reality if long-span bridges (isolated or not) are to be studied. In these cases, due consideration should be given to the non-synchronism of the seismic action, since different input motions experienced at adjacent supports can significantly modify the overall structural response thus jeopardizing the design concept. Present guidelines, when they exist, are vague and/or too grossly empirical. Actually, non-synchronous input induces a specific type of excitation in which pseudo-static relative displacements are included, with ensuing possibly significant variations of the displacement field and of the ductility requirements. The above effect is obviously of special relevance for bridges, whose effectiveness is conditioned to an accurate assessment of the relative displacement between deck and pier caps. In section 3.1 this phenomenon is studied through a series of numerical analyses on both conventional and isolated bridges and its effects clarified.

Soil-Structure Interaction (Section 3.2, page 68, based on the research work by Ciampoli, M., and Pinto, P.E.) is the typical effect resulting from the difference between the structural response evaluated assuming an ideal rigid foundation and that obtained with the actual soil foundation. The difference can be attributed to two distinct physical causes: the propagating nature of seismic disturbances in the form of waves, which makes the soil motion at any given instant generally different from point to point within a spatially extended foundation, and the inertia forces transmitted by the structure to the soil during the oscillations, which induce a deformation in the soil that adds up to the one existing in the free-field. In section 3.2 a large parametric study on this second phenomenon concerned with bridge piers of common geometry having spread or strip footing foundations is presented, where, as opposed to all the studies developed thus far, the inelastic response of the superstructure is considered. Quantitative information are given on the extent by which yielding tend to decrease SSI effects, and especially on the effects of SSI on the maximum required ductilities in the critical regions of the superstructure.

Vertical oscillations (Section 3.3, page 88, based on the research work by Petrangeli, M., Pinto, P.E., and Ranzo, G.) is a secondary phenomenon that occurs in bridge piers subjected to horizontal seismic input. Analyses conducted on single column bent systems indicate that flexural cracking produces significant bending-induced axial vibrations. This effect is particularly relevant in squat elements with low axial force where the sway of the cross section neutral axis under alternate bending causes strong hammering impulses at crack closure. Performance and design forces of bearings and other anti-seismic devices should be estimated with more accuracy, based on the expected level of combined vertical and horizontal acceleration response on decks. In section 3.3 this problem is dealt with and a tentative equation for the prediction of this flexural-induced vertical acceleration component is proposed, based on simplified section kinematics and elastic impact analysis.

In Chapter 4 (**Upgrading of bridge piers with FRP**, page 108, based on the research work by Monti, G., Nisticò, N., Santini, S., Spoelstra, M.R.) another topic, which logically follows those treated in the previous Chapters, is treated: that of the rehabilitation of old bridges, with particular reference to the piers. Common retrofitting techniques of bridge piers typically aim at increasing the available ductility by enhancing the confinement action in either the potential plastic hinge region or over the entire pier. Steel jacketing has had an extensive use in practice and has proved to be an effective measure for retrofitting, yet recently advanced composite materials, such as fiber-reinforced polymers (FRP), are increasingly gaining a widely recognized role as structural materials and are now fully recognized to represent an effective alternative retrofit technique for bridge piers. Tests carried out in the USA and in Japan have shown that strengthening with innovative composite jackets improves the strength and the ductility of columns, concluding that wrapping of columns by FRP materials provides an affective and economical alternative for seismic retrofitting of piers.

Following these encouraging results, in the last years, in California, more than 500 bridge piers have been wrapped with advanced composite materials and now similar programs are currently under way in Japan. In Europe, where notable interest exists, the problem is still in an interlocutory phase, mainly because of the lack of established and accepted design rules, which slow down the process of promoting FRP as an 'official' construction material.

The intent of Chapter 4 is to give a contribution towards the development of such design rules to obtain, through FRP jacketing, the desired level of upgrading of insufficiently ductile piers, designed according to obsolete codes. Firstly, a recently developed model of FRP-confined concrete is presented, which has the capability to trace the peculiar response of concrete under the continuously increasing confinement applied by an elastic material such as FRP, as opposed to the traditional models where it is assumed that steel applies a constant confinement after yield. Through such model practical formulae for predicting the ultimate strain and strength of FRP-confined concrete are developed. Subsequently, a study on FRP-confined concrete sections is presented, and practical design equations are developed, which allow to determine the optimal FRP thickness to wrap circular sections with, given a target performance to achieve.

2 BRIDGE SYSTEMS

2.1 Analytical seismic assessment of the bridges on a highway system

In Italy, the largest part (90%) of the existing highway system is owned and operated by a single Company: *Autostrade*. Its network, shown in Figure 2.1, has roughly 5500 km of highways, comprising a total of 2826 bridges. The highways were built essentially in the 60's and in the 70's, with only minor additions going on until presently. Seismic design regulations of the time were almost nominal: horizontal forces equal to 10% of the permanent weights in the zones of highest seismicity (7% in the other seismic zones), with no attention paid to ensure ductile behavior, to check compatibility of displacements between adjacent decks, the strength and admissible displacements of the bearings, etc.; moreover, many areas, which a hazard analysis reveal to be seismic, in those years were not thus classified. In a large percentage of cases, the reinforcement of the piers is not dictated by the seismic forces, but from wind and braking forces, or more simply by minimum percentage requirements. Fortunately, tradition has in Italy that bridge piers should be (and look) rather rigid, as compared to those of similar bridges elsewhere, and this provides in many cases a much appreciated extra strength. Also for the foundations, Italian practice is rather conservative, in order to ensure satisfactory performances under service loads, and this leads in many cases to foundations which are stronger than the superstructure, a desirable property under seismic action.

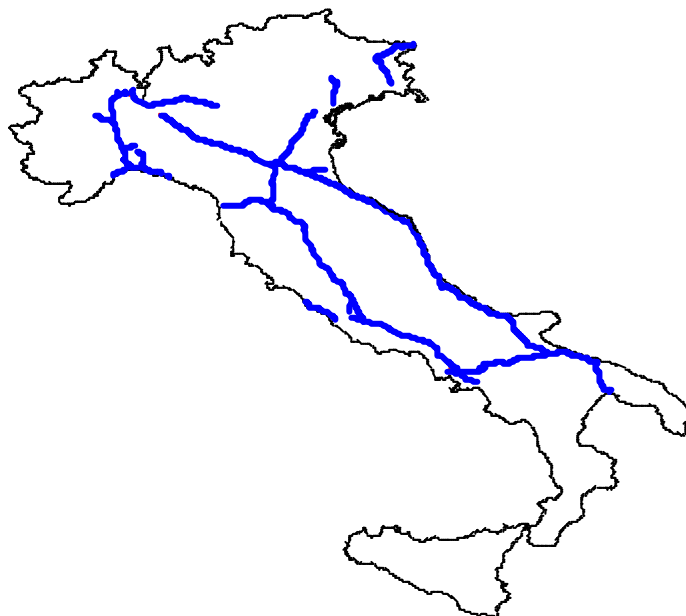


Figure 2.1. The Italian highway network of Autostrade.

The last strong earthquakes in Italy have not produced significant damages to bridge structures (by chance, due to the fact that the highways were far from epicentral areas). In spite of the lack of this, usually potent, incentive to assessment and rehabilitation programs, *Autostrade* has resolved to undertake a systematic scrutiny of its entire bridge stock in terms of seismic performance. Given the unusually large scale of the problem, particular attention has been devoted to the setting up of an appropriate assessment method, with the constraints that it should not be based on qualitative typological vulnerability forms on one hand, nor it should require detailed analyses based on drawings, at the other extreme. A number of alternatives were initially considered; the one receiving more credit at an early stage was to try to categorize the whole stock into a discrete number of types, then to select a representative bridge within each type and to analyze it in detail. All bridges belonging to the same type would have then been assigned the vulnerability found for the representative structure.

A much more accurate and efficient procedure has been finally set up, which relies upon an existing data bank created by *Autostrade* for maintenance purposes, allowing a complete reconstruction of the geometry of all bridges. Details and limitations of the procedure are described in the following.

The outcome of this part of the study is one number for each bridge, expressing the probability of failure of the bridge, given that the peak ground acceleration having a selected (the same for the whole network) annual probability of exceedance occurs at the bridge site. To evaluate this set of numbers, a reference is needed. The criterion adopted has been to consider as acceptable (*i.e.* no intervention on the bridge is required) all values that are equal or below the probability of failure of representative bridges designed in accordance with Eurocode 8/2 (1994), given the occurrence of the design acceleration. Of course no such value can be found in EC8/2. This has required a side study, consisting in designing a number of bridge structures, similar to those of interest, in full accordance with the EC8/2 provisions and, subsequently, in performing on them a probabilistic risk analysis, conditional to the occurrence of the acceleration used in the design. The values obtained had clearly a certain scatter, and a reasonable upper bound was therefore selected.

The end result of the whole study, as reported in the following sections, is a list of bridges, ordered for decreasing values of risk, which do not fulfil the safety requirements for new designs according to a modern code. This is considered to be the point of departure for developing cost-benefit strategies necessary for providing guidance for the amount of strengthening to be provided.

2.2 Screening of the bridges to be examined

About three quarters of the Italian territory is considered as seismically active, and earthquake resistant design is compulsory. Seismicity is not uniform, however, the southern regions having the heaviest record of destructive events. A plot of all the events occurred since the year 1000 with intensity larger than 7 is shown in Figure 2.2.

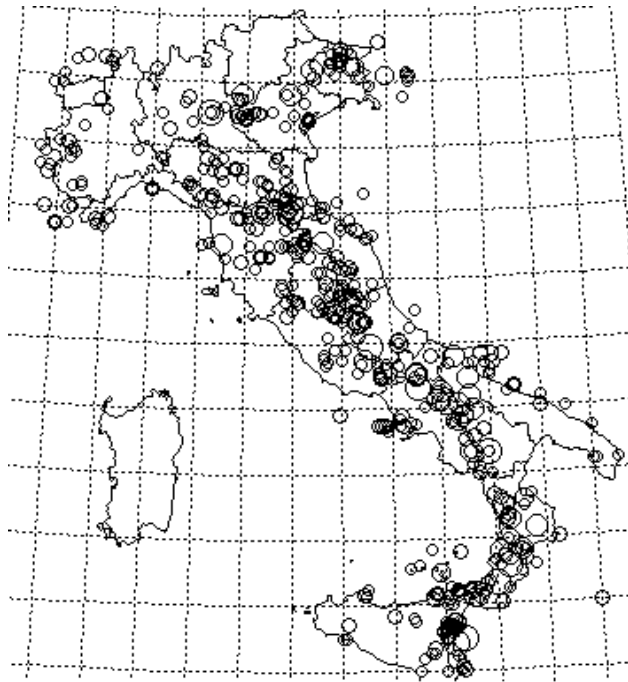


Figure 2.2. Historical events in Italy with $I_{MM} > 7$.

The first necessary step in the study to be undertaken is clearly to determine the seismic hazard along the route of the various highways. This is just one side of the problem, however, the other one being the level of seismic intensity for which a risk evaluation of bridges is warranted.

Whether designed for earthquakes or not, all bridges possess a certain resistance to lateral loads, which comes from requirements of stiffness and from design for wind and other horizontal forces. If this “natural” resistance, expressed in terms of ground acceleration causing failure, is larger than the ground acceleration at the site having an appropriately chosen (large) return period, any seismic verification becomes unnecessary.

The two steps described above have been carried out according to the following criteria.

2.2.1 Hazard analysis

The combined historical-geophysical information available allows to subdivide the Italian territory into 45 homogeneous regions, for each of which the catalogue data are sufficient for determining a separate Gutenberg-Richter law for the intensity, including upper and lower bounds. Using a single attenuation law for the whole range of intensities and for all regions (alternatives are available, but they are not adequately supported), a Cornell type of analysis has been carried out to determine the value of I_{MM} having specified values of the return period, T_R , along the highway route. Values of $T_R = 500$ years and 50 years have been considered, the

former one to be used for ultimate limit states (ULS) verifications. Selected results for two highways, the N-S Milano-Napoli and the W-E Napoli-Canosa are shown in Figure 2.3. The latter highway crosses one of the major seismic regions of the country.

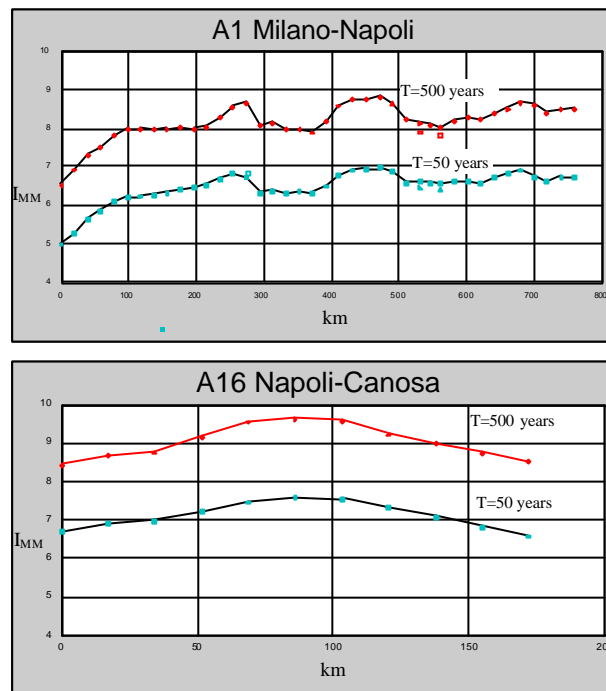


Figure 2.3. Hazard curves for two Italian highways.

2.2.2 Natural seismic resistance

Out of the total of 2826 bridges, more than one third: 1151, are made up of decks which are simply supported on different piers systems. Other 1363 bridges are single span structures directly supported on the abutments, and the remaining 312 bridges are variously distributed among Gerber, arch, continuous deck, cantilever construction and frame-like types.

Leaving out bridges of unique characteristics, like some large arch bridges built in the sixties, as well as other important bridges with large spans (in excess of 100 m), for which specific vulnerability studies are unavoidable, the category of the simply supported bridges has been considered as the one with the largest risk and, inside this category, the piers made up of single bents as the more vulnerable.

Searching in the data base of *Autostrade*, the characteristics of which will be presented later, the whole range of cross-section properties of the piers, the corresponding range of heights for each section geometry, and the span lengths have been examined. Span length is not a strong parameter, since most spans are around 30 m, only the more recent ones reaching 40 m. The key parameter is the ratio

between the cross section dimension and the height of the pier. The choice has finally been made of two cross section shapes, each one associated with a range of heights, as shown in Table 2.1, for a total of 10 cases.

Table 2.1. Representative piers examined.

CROSS SECTION (m)	HEIGHT (m)
Rectangular hollow 6.60 x 3.80	10,15,25,35,45
Circular hollow 3.80	8,12,16,20,24

Although they are representative of the actual population, the cases examined do not correspond to existing bridges: they are believed to be an hypothetical sample lying on the more vulnerable side of the whole set. The virtual bridges have been subsequently designed using the loading and material codes applicable in the period 1960-1970, considering traffic and wind loading, but excluding seismic forces. With the longitudinal and transverse reinforcement known, a numerical model of the bridge can then be constructed.

Flexural behavior is described by means of a bi-linear force-displacement relationship at the top of the pier. The details of this derivation are given later; for the purpose at hand the characteristics that are used are: the yield force F_y , the stiffness $K = F_y / \Delta_y$, where Δ_y is the top displacement at yield, the period $T = 2 / \pi \sqrt{M / K}$, where M is the mass of the deck inclusive of the pier cap and of the part of the pier, and the ultimate ductility $\mu_u = \Delta_u / \Delta_y$, where Δ_u is based on the ultimate curvature of the base section, evaluated by assuming conservative values of the compressive strain of concrete.

If $\bar{S}_a(T)$ denote an appropriate elastic response spectrum normalized to a unit peak ground acceleration, the value of A causing flexural collapse is evaluated as:

$$A_c = \frac{F_y \mu_u}{M \bar{S}_a(T)} \quad (1)$$

provided $V_u \geq F_y$, where V_u is the ultimate shear capacity of the pier. When the above condition is not satisfied, shear failure precedes flexural failure, and the corresponding acceleration is:

$$A_c = \frac{V_u}{M \bar{S}_a(T)} \quad (2)$$

In the analyses, $\bar{S}_a(T)$ has been taken as the normalized elastic spectrum suggested in the Eurocode 8 for intermediate soil conditions, while shear capacity has been evaluated in accordance with Eurocode 2. The values of A_c obtained for the ten cases of piers, in the transverse direction, are reported in Table 2.2.

Shear failure occurs only for the shorter (H=10 m) rectangular pier; in all other piers collapse is governed by exhaustion of ductility. Circular piers have consistently lower values of A_c , due to lower available ductility with respect to the rectangular ones: this in turn is due to the shape of the section and to the higher average vertical stress.

Table 2.2. Values of acceleration causing collapse.

	RECTANGULAR					CIRCULAR				
H (m)	10	15	25	35	45	8	12	16	20	24
A_c (g)	0.25	2.6	1.7	1.4	1.4	0.47	0.37	0.31	0.28	0.34

It is observed however, that all values obtained are rather high, perhaps higher than expected, given the total absence of design provisions for seismic resistance. This is principally a consequence of the relatively large dimensions adopted for the piers, for reasons of minimum stiffness and/or aesthetics.

The same piers have been combined in various ways to form longitudinal bridge configurations: the analyses made assuming equal longitudinal displacements have yielded values of A_c of the same order of magnitude than for single piers in the transverse direction.

In addition to the structural failure mechanisms considered up to now, the possibility of collapse due to loss of support of the deck has also been considered. This type of failure has been frequently observed in recent earthquakes even for bridges of the last generation.

The modeling assumptions for this phenomenon have been rather simple: two identical adjacent piers have been considered to move in the opposite direction, with a maximum relative displacement evaluated as: $\mu_{\max} = \sqrt{2\mu_1^2} = 1.41 \mu_1$, where μ_1 is the maximum displacement at the top of each pier. A seating length of 50 cm has been considered; the most unfavorable situation occurred for the tallest rectangular pier (H=45 m) for which the value of $A_c(50 \text{ cm}) = 0.13g$ was found.

2.2.3 Final selection of bridges

For failures of structural types, the lowest value of A_c within the population considered has been: $A_c = 0.25g$, related to a shear type of failure. According to the relationship adopted between A and I : $A_c = 10^{-2.3356+0.1908I}$, the corresponding value of I is 9.

Considering the variability inherent in the relationship on one hand, and the possible existence in the whole network of bridges more vulnerable than those examined, the threshold below which no seismic evaluation is required has been set to $I_{MM} = 8 \Rightarrow 0.15g$. Analogous considerations of prudence led to adopt a value of

$I=7$ for the threshold below which no intervention preventing decks from failing needs to be considered.

Comparing the values of the two thresholds with the 500 years return period hazard, it has been found that for what concerns structural failure only 6 of the 15 highways, and not all for their entire length, remain: they are shown in Figure 2.4. For the problem of unseating the risk is larger, and 12 out of the 15 highways need to be checked under this respect.

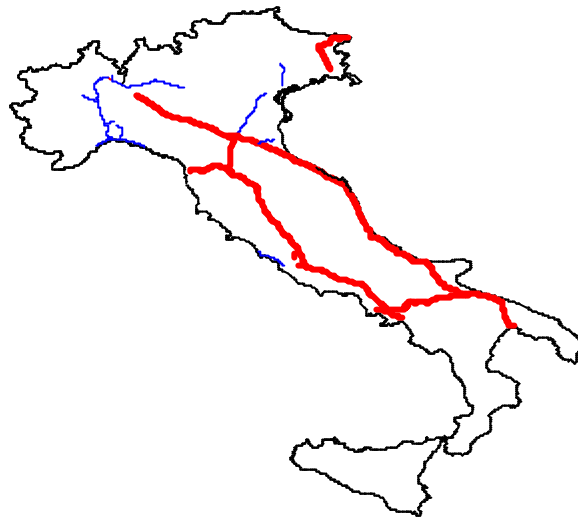


Figure 2.4. Highways for which risk analysis has been performed.

2.3 Evaluation of the bridges

2.3.1 Outline of the procedure

Information on all bridges of the network *Autostrade* is contained in a data-bank, to be described in the following section. The procedure for seismic evaluation reads sequentially, for each of the six highways left from the preliminary screening, the location of each bridge: if the calculated local hazard is less than $I=8$, it passes directly to the next one, until one is found for which $I \geq 8$. The corresponding value of the peak ground acceleration is calculated.

Entering into the data-base, the procedure selects the information required to reconstruct the geometry of the bridge, and all available elements required for the purposes of the evaluation. Given the geometry, and using the loading and material codes in force at the time of the construction, the longitudinal and transverse reinforcement of the piers is determined in turn. The available data allow this simulated design to be carried out for the majority of existing pier types. When data are not sufficient the bridge in question is tagged for a separate ad hoc treatment.

A mechanical model of the pier is then set up. Evaluation consists in determining the probability of collapse of each pier: P_{fi} for a combined mechanism of flexure and shear, given the value of the site peak ground acceleration characterized by an average return period of 500 years. In obtaining P_{fi} , flexural and shear strength, ultimate ductility, elastic spectral ordinates and inelastic force reduction factors are assumed as random variables. The collapse probability for the entire bridge is evaluated with the assumption of independent collapses of all piers:

$$P_f = 1 - \prod (1 - P_{fi}) \quad (3)$$

2.3.2 The data bank SAMOA

SAMOA has been elaborated by *Autostrade* for several purposes, the main ones being the possibility of keeping up-dated the state of each bridge in terms of deterioration phenomena affecting materials (carbonation of concrete, oxidation of steel, etc.) and elements (loss of concrete, cracking, degradation of joints, bearings, movements in the foundations, etc.), as well as for keeping track of all the interventions made, which may range from ordinary maintenance to structural restoration, with or without upgrading.

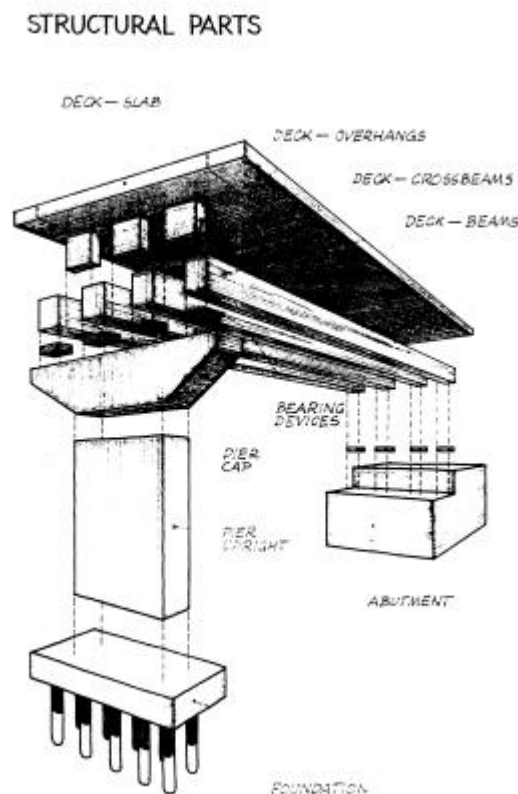


Figure 2.5. Sketch of bridge elements considered in SAMOA.

Bridges in SAMOA are decomposed into the following structural elements: foundations, piers, abutments, arches, decks, bearings, joints. One form is filled for each element. The case of a simply supported bridge is illustrated in Figure 2.5.

For what concerns the piers, that are the elements to be known in more detail for the purpose of evaluation, the following classification is adopted. The structural systems can be: Single bent, Wall, Portal frame and Multi-bay frame, both with or without intermediate transverse beams, plane or spatial. The cross sections of the vertical elements can be: rectangular, circular, polygonal, elliptic and “other”, either solid or hollow, in the latter case simply or multiply connected.

2.3.3 *Simulated design of the piers*

Actions considered in the design include permanent loads, traffic, braking, wind loads and, if at the time of construction the site was classified as seismic, static equivalent seismic forces (to be combined with the permanent loads only).

The action effects are of immediate determination in the case of simple cantilevers. For frames, the assumption has been made of a stiff top transverse beam, so as to allow for the approximation of treating the columns as built in at both ends.

The most unfavorable combination of action effects has been used for the design of the base section of the piers (all piers have uniform dimensions along their height), for bending and for shear. Admissible stress criteria have been adopted, with values consistent with the presumed strength characteristics of concrete and steel. In many cases, the amount of reinforcement (longitudinal as well as transverse) has been found to be governed by minimum requirements. Spot comparisons of the calculated amount of reinforcement with that indicated in the design drawings have shown good agreement between the two.

2.3.4 *Evaluation procedure*

The mechanical model of the pier consists in all cases of a cantilever carrying a mass at the top. If the original structure is a frame, with two or more columns, the force-displacement relationship is evaluated considering the columns as built in at one end and with a height equal to half of the clear height between foundation mat and pier cap. The moment-curvature relationship of the end section is sufficient for obtaining the yield (F_y, μ_y) and the ultimate (F_u, μ_u) points in the $F - \mu$ curve. As shown in Figure 2.6, the variation of the curvature along the height is assumed to be parabolic between yield and decompression sections, and then linear up to the top.

The expressions for the two points are:

$$\mu_y = \frac{h^2}{12} \left[\theta_f \left(1 + \frac{M_d}{M_y} \right)^2 \frac{M_y}{M_d} + \theta_y \left(3 + \frac{M_d}{M_y} \right) \left(1 - \frac{M_d}{M_y} \right) \right] \quad F_y = \frac{M_y - P\mu_y}{h} \quad (4)$$

$$\mu_u = \mu_y \left(1 - \frac{l_p}{h} \right)^2 + \theta_{\mu_p} \left(h - \frac{l_p}{2} \right) \quad F_u = \frac{M_u - P\mu_u}{h} \quad (5)$$

with obvious meaning of the symbols. The length of the plastic hinge has been taken as half of the height of the section. The ultimate compression strain of concrete has been assigned a value of 0.5%.

The $F - \mu$ diagram defines flexural strength and ductility of the pier.

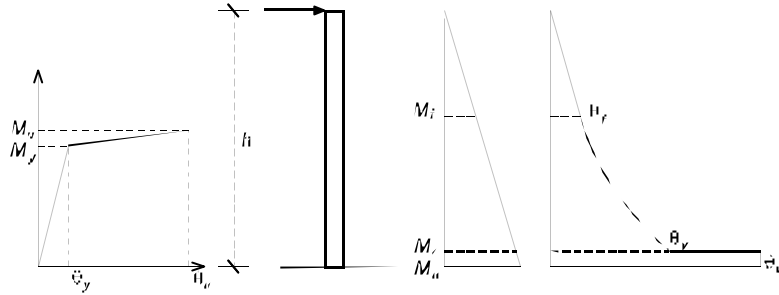


Figure 2.6. Variation of the curvature along the height of the pier.

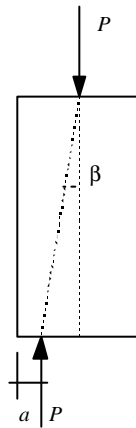


Figure 2.7. Truss model for the shear force equilibrated by vertical load.

For the assessment of shear capacity, use has been made of the expressions proposed by Priestley et al. (1994):

$$V_{\mu} = V_c + V_s + V_p \quad (6)$$

where V_c is the contribution of concrete, V_s is the shear carried by transverse steel and V_p is the horizontal component of the inclined thrust of the vertical load P , which is equilibrated at the base section by the compressive resultant displaced from the axis of the column (see Figure 2.7). The expression of V_c is:

$$V_c = 0.29 k \sqrt{f_c} A \quad (7)$$

with f_c the concrete compressive strength (MPa), $A = 0.8A_g$, where A_g is the gross concrete section and k is a function of the required ductility: is equal to 1 for $\mu \leq 2$, decreases linearly from 1 to 0.3 for $2 < \mu \leq 4$, and remains constant thereafter. V_s is the expression for the truss model and $V_p = P \tan \beta$, where β is given in Figure 2.7.

As indicated previously, the evaluation has been carried out taking into account the uncertain nature of the variables involved, on the action side, on the response side and on the capacity side. On the action side, the starting point has been the elastic response spectrum contained in EC8. The spectral ordinates of EC8 have been assumed as representing the 50% fractile value of the response, and they have been transformed into random variables (r.v.) by multiplying the median $S(T)$ by a r.v.: $\exp(\alpha_S)$, lognormally distributed and with unit median.

Non-linear response behavior has been described through what is commonly called strength reduction factor, representing the ratio between the strength needed in case of elastic response and the minimum strength a structure must have still compatible with its ultimate deformation capacities. The expression adopted for $r(\mu, T)$ is the one proposed by Hidalgo and Arias (1990):

$$r(\mu, T) = 1 + \frac{T}{kT_o + \frac{T}{\mu - 1}} \quad (8)$$

where T is the period of the structure and kT_o is a parameter depending on the expected frequency content of the motion. The previous expression has been assumed to give the median value of $r(\cdot)$, which is then randomized by multiplication for a r.v. $\exp(\alpha_r)$, log-normally distributed and having unit median.

On the side of the capacity, the three quantities: flexural strength F , ultimate ductility μ_u and shear strength V_u , have been treated as r.v.'s in the same way as the previous ones, *i.e.*, by multiplying their median values by the three r.v.'s $\exp(\alpha_F)$, $\exp(\alpha_\mu)$ and $\exp(\alpha_V)$, all having unit median and log-normal distribution.

2.3.5 Quantification of risk

If the response is in the elastic range, the maximum force on the pier is:

$$F_{\max} = M A_g \bar{S}_a(T) \quad (9)$$

where A_g is the local value of the peak ground acceleration, and failure can only occur if F_{\max} exceeds the shear strength V_u . In the inelastic range, the following equation applies:

$$F(\mu) = \frac{M A_g \bar{S}_a(T)}{r(\mu, T)} \quad (10)$$

where the dependence of F on the ductility actually required has been made explicit. Failure in this case can occur due to two different mechanisms: a flexural failure, if to satisfy (10) it must be $\mu \geq \mu_u$; a shear failure if $F(\mu)$ is larger than V_u .

The failure domain can in both cases be expressed as union of two domains:

$$\mathfrak{S} = [\mu \geq \mu_u] \cup [F(\mu) \geq V_u(\mu)] \quad (11)$$

In order to calculate the probability content of \mathfrak{S} it is convenient to separate it into the union of two non-overlapping domains:

$$\mathfrak{S} = \{[\mu \geq \mu_u] \cap [F(\mu) < V_u(\mu)]\} \cup \{F(\mu) \geq V_u(\mu)\} \quad (12)$$

in which the first domain represents a flexural failure excluding shear failure and the second one a pure shear failure. The probability contents of the two domains are directly summable, while the total probability of failure includes a third contribution, i.e., the probability of a shear failure for $\mu < 1$. Introducing the notations:

$$m(\mu) = \log\left(\frac{\mu}{\mu_u}\right) \quad v(\mu) = \log\left(\frac{V_u(\mu)}{F(\mu)}\right) \quad (13)$$

$$X = \alpha_F + \alpha_r - \alpha_S \quad Y = \alpha_F - \alpha_V \quad (14)$$

$$g(\mu) = \log\left(\frac{M A_g \bar{S}_a(T)}{F(\mu)r(\mu,T)}\right) \quad (15)$$

it can be shown that the probability for flexural failure conditioned to survival in shear is given by the expression:

$$P_{f1} = \frac{1}{\sqrt{2\pi\sigma_X}} \int_1^{\infty} \Phi\left(\frac{m(\bar{\mu})}{\sigma_\mu}\right) \Phi\left(\frac{v(\bar{\mu})/\sigma_Y + \rho g(\bar{\mu})/\sigma_X}{\sqrt{1-\rho^2}}\right) \exp\left(-g(\bar{\mu})^2/2\sigma_X^2\right) \left|\frac{dg(\bar{\mu})}{d\bar{\mu}}\right| d\bar{\mu} \quad (16)$$

while that for shear failure in the inelastic range is:

$$P_{f2} = \frac{1}{\sqrt{2\pi\sigma_X}} \int_1^{\infty} \Phi\left(\frac{-v(\bar{\mu})/\sigma_Y + \rho g(\bar{\mu})/\sigma_X}{\sqrt{1-\rho^2}}\right) \exp\left(-g(\bar{\mu})^2/2\sigma_X^2\right) \left|\frac{dg(\bar{\mu})}{d\bar{\mu}}\right| d\bar{\mu} \quad (17)$$

and that for elastic shear failure:

$$P_{f3} = \frac{1}{\sqrt{2\pi}} \int_1^{\infty} \frac{v_o - g_o}{\sigma_X} \Phi\left(\frac{(\sigma_Y \rho' - \sigma_{X'})u_1 - g_o}{\sigma_Y \sqrt{1-\rho^2}}\right) \exp\left(\frac{-u_1^2}{2}\right) du_1 \quad (18)$$

where in (18) the new symbols stand for:

$$v_o = \log\left(\frac{V_u(1)}{F(1)}\right) \quad g_o = \log\left(\frac{M A_g \bar{S}_a(T)}{F(1)}\right) \quad X' = \alpha_S - \alpha_V \quad (19)$$

In the previous equations, $\Phi(\cdot)$ is the Gauss normal distribution function and ρ is the coefficient of correlation between the r.v.'s X and Y :

$$\rho = \frac{\sigma_F^2}{\sqrt{\sigma_F^2 + \sigma_S^2 + \sigma_r^2} \sqrt{\sigma_F^2 + \sigma_V^2}} \quad (20)$$

similarly, ρ' is the coefficient of correlation between X' and Y .

The three integrals above are rapidly performed numerically.

2.3.6 Selected results

The procedure computes P_f in sequence for all bridges belonging to each of 6 highways for which seismic evaluation is warranted, according to the screening procedure illustrated previously. A sample of the results is presented graphically in Figure 2.8 and Figure 2.9, which refer to the longest highway (A1: Milano-Napoli), and to the most hazardous one (A16: Napoli-Canosa), respectively.

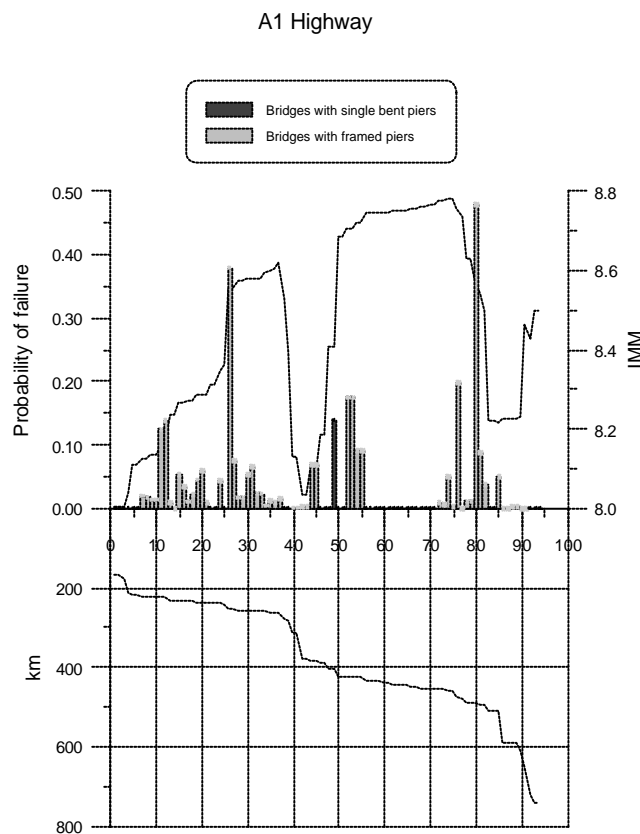


Figure 2.8. Risk of bridges in the A1 highway.

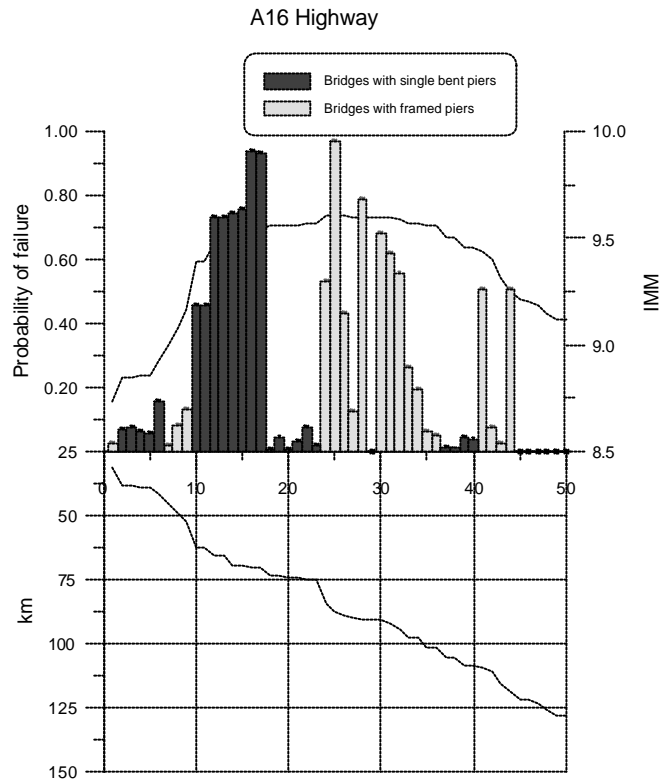


Figure 2.9. Risk of bridges in the A16 highway.

In the horizontal axis the bridges examined are numbered in progression, their distance from the origin appearing in the lower part of the figure. The vertical axis at left gives the values of P_f corresponding to the spikes in the figure, while in the background the variation of the hazard is also given, with the values to be read in the right vertical scale. A distinction is made between single bent and frame-like type of piers.

One can immediately note that while in the A1 only a few isolated bridges have values of P_f larger than, say, 0.10, in the A16 the risk is much more diffused, with a good number of bridges having a P_f close to 1, given the occurrence of the 500 years event.

Results for the six highways are summarized in Figure 2.10, which gives for the total population of bridges examined the distribution of the probabilities of failure. A systematic difference appears between the bridges of the two categories, with framed piers clearly more vulnerable than those with a single bent. For example, about 75% of the latter have a $P_f \leq 10^{-2}$, against 30% of the former. The difference becomes smaller, however, with increasing value of risk, and for $P_f > 0.5$ the situation is inverted.

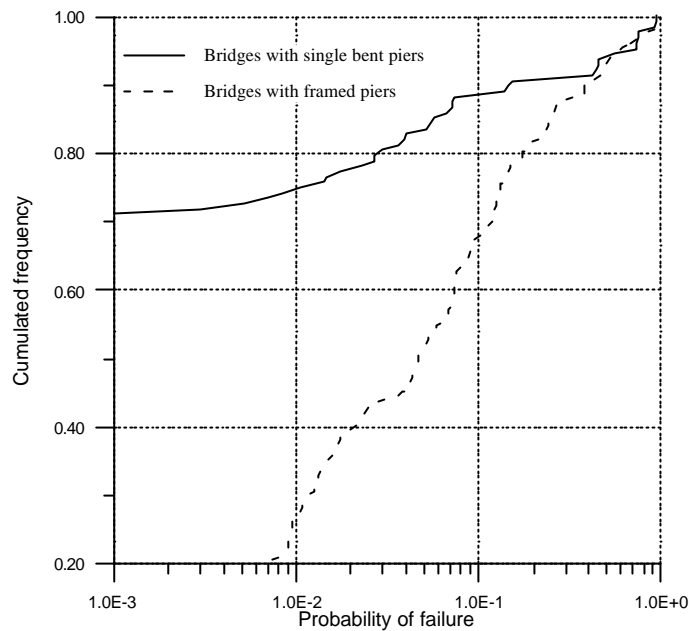


Figure 2.10. Cumulated frequency of probability of collapse of examined bridges. Continuous line: bridges with single bent piers; dashed line: bridges with framed piers.

2.4 Acceptance criterion

The values of P_f obtained with the procedure described in the previous paragraph represent a measure of the risk of the bridges: to judge whether they are acceptable or not an homogeneous reference measure is necessary. Among various alternative possibilities the choice has been made to use as acceptance threshold the safety provided by the modern codes for new structures. This choice might in principle be considered as overly conservative and uneconomical, as it is widely accepted that for existing structures the amount of retrofit can be somewhat less than “complete”, *i.e.*, a lower safety level than for new ones can be accepted.

But for the type of bridges under consideration, in which the vulnerable elements are essentially the piers, the economical arguments play differently than, for ex., in the case of substandard reinforced concrete or masonry buildings. In the case of bridges, the total cost of the intervention is made up principally by fixed costs, which do not depend on the amount of strengthening to be provided, while the extra cost due to extra strength is an insignificant fraction of the total cost. Thus, the attainment of a safety level equal to that for new structures is a logical target.

Modern codes, however, are not explicit on the level of protection they provide: it should be inferred from the logic inherent in these documents. Eurocode

8, for example, after stating its objective as that of ensuring, “with an adequate level of reliability”, that communications should not be disrupted as a consequence of seismic events, implements the concept in practice in the following way.

The first step consists in selecting, according to the importance of the bridge, the return period (T_R) of the design seismic event for the ULS. Given T_R (say, 500 years) the corresponding seismic intensity is found and the design made accordingly.

The design rules (analysis, dimensioning and detailing) are deemed to be such as to guarantee, with an adequate level of reliability, that, given the occurrence of the design event, bridges maintain their integrity and a limited capacity for traffic load, though they may need substantial repair work. The idea is therefore clearly expressed of the existence of a probability that a bridge, designed following the code and for an action of given return period, may collapse at the occurrence of this action.

How high is this conditional probability is not to be found in the code, however, for reasons that are obvious. If, as in the present case, the order of magnitude of the probability inherent for ex. in EC8 is desired, it must be estimated by means of ad hoc analyses on representative designs. This is what has been actually done, by first selecting a number of possible candidate structures and finally by identifying one specific pier type and a single geometry. In detail, the pier is a single bent, with circular hollow cross section having an external diameter $D=2.60$ m and thickness of 0.30 m. The height is $H=10$ m and the mass at the top is 1,000 t, corresponding to a deck length of 40 m.

The criterion adopted for the choice has been that pier dimensions should be related to actual strength requirements and not, as it is often the case, to extraneous reasons as uniformity, aesthetic, etc. Regarding the height, it can be shown that an increase of it within reasonable limits would reduce the response and the necessary amount of reinforcement.

The material properties have been chosen as follows. For concrete: average strength: $f_c = 30$ MPa (design: $f_{cd} = 20$ MPa), average tensile strength: $f_{ct} = 0.3 f_c^{2/3} = 2.9$ MPa, average ultimate compressive strain: $\epsilon_{cu} = 0.012$. For steel: average strength: $f_y = 500$ MPa (design: $f_{yd} = 380$ MPa).

The design peak acceleration has been set at $A_g = 0.35g$, and the value of behavior factor given in EC8: $q = 3.5$ has been adopted. The design spectrum is that of EC8 for intermediate soil sites.

2.4.1 Calculation of P_f for $A_g = 0.35g$

The rules in EC8 are such as to make shear failure practically a zero probability event. Hence failure can only occur due to exceedance of the available ductility. The mechanical model of the pier is the same used for the seismic assessment of existing piers, and is represented by a bilinear force-displacement relationship. Using mean values of the mechanical properties of the materials, the displacement ductility results to be: $\mu_u = 9.08$.

The failure condition writes as usual:

$$F(\mu) = \frac{M A_g \bar{S}_a(T)}{r(\mu, T)} \quad (21)$$

with the known meaning of the symbols.

The quantities assumed as random are: F , μ_u , $\bar{S}_a(T)$ and $r(\mu, T)$. Each random variable is obtained multiplying the median values by a random variable $\exp(\alpha_i)$, lognormally distributed with unit median. For the parameters of the distributions of the normal variables α_i , the following values have been adopted:

Strength	$\sigma_{\alpha_F} \cong CoV(F) = 0.15$
Ductility	$\sigma_{\alpha_\mu} \cong CoV(\mu_u) = 0.20$
Spectrum	$\sigma_{\alpha_S} \cong CoV(S_a) = 0.20$
Reduction factor	$\sigma_{\alpha_r} \cong CoV(r) = 0.25$

With:

$$g(\mu) = \log\left(\frac{M A_g \bar{S}_a(T)}{F(\mu)r(\mu, T)}\right) \quad \sigma_{\alpha_g}^2 = \sigma_{\alpha_F}^2 + \sigma_{\alpha_S}^2 + \sigma_{\alpha_r}^2 \quad (22)$$

the probability of failure can be expressed in closed form as:

$$P_f = \int_1^\infty \Phi\left(\frac{\log(\mu/\mu_u)}{\sigma_{\alpha_\mu}}\right) \frac{1}{\sigma_{\alpha_g}} \Phi\left(\frac{g(\mu)}{\sigma_{\alpha_g}}\right) \frac{dg(\mu)}{d\mu} d\mu \quad (23)$$

and the integral evaluated numerically.

The value of P_f obtained for the pier under consideration is:

$$P_f \cong 2 \cdot 10^{-2} \quad (24)$$

This value is in general agreement with the results of other studies on the subject. It should not be considered as a "rigid" reference: with different geometry and dimensions, different estimates of the parameters defining the randomness, possible inclusion of other parameters, refinements in the mechanical models, etc., the range of values could expand of one order of magnitude in both senses.

If not in absolute terms, however, the result obtained is significant as a relative measure. The same mechanical models have in fact been used in the assessment of the existing and of the new bridges: the possible bias and deficiencies of the models should disappear in the comparison. The values of the parameters defining the randomness are either the same, or are reasonably differentiated for taking into account of the differences between the two situations. The arguments above support the conclusion that the values of P_f attached to each bridge provide a correct ordering criterion in terms of risk, and that the threshold separating the categories of acceptable and non acceptable risk is placed in a defensible position.

2.5 Results and conclusions

Starting from 1151 bridges with simply supported decks belonging to the *Autostrade* network, the screening procedure based on the comparison between the 500 years return period hazard and their “natural” seismic resistance has reduced the number of those to be evaluated to 425; 307 of these bridges (*i.e.*, those for which the data bank SAMOA allowed a reconstruction of their geometry to be made) have been evaluated quantitatively following the criterion of designing them according to the code of the time and then performing on them a reliability analysis.

The measure of the risk adopted has been the probability of collapse conditioned to the local 500 years return period hazard. The values of P_f obtained for the 307 bridges have then been compared with a reference value: $P_f = 10^{-2}$, considered to be representative of the safety provided by a modern code (EC8/2) to bridges of new construction. The result is that 155 bridges have a risk larger than or equal to the acceptable one. Only for about half of them, however, the difference with the target is really significant, while the rest has a risk within a narrow range around the target (values of P_f down to $5 \cdot 10^{-3}$ are included in the count of 155). While for the former half an intervention of seismic retrofit is warranted *per se*, for the second half the decision of intervening should be based on a combination of factors, rather than just on seismic risk.

As far as the procedure in itself is concerned, a few aspects are worth to be mentioned in concluding. The idea of utilizing the geometric data from a data bank to reconstruct the characteristics of the bridges by means of a simulated design has proven to be both accurate and very fast.

The limits of the procedure are equally obvious as its advantages. First of all it presupposes the existence of a data bank of the type described in the paper, where the necessary data can be easily extracted from, which is other than to have the full design of the bridges informatically stored. Secondly, the procedure works reliably for bridge of simple structural types. Hyperstatic bridges, or even hyperstatic piers of simply supported bridges, cannot be designed automatically on the basis of the geometry alone, due to the multiplicity of the design options. These bridges, however, represent a small portion of the existing stock, so small that their seismic evaluation can be realistically carried out on an individual basis.

2.6 References

- Eurocode 8 (1994). Design Provisions for Earthquake Resistance of Structures ENV 1998-2 - Bridges. Brussels, October, CEN.
- Hidalgo, P.A., and Arias, A. (1990). New Chilean code for earthquake resistant design of buildings. 4th Nat. Conf. of Earthquake Engrs., Vol 2, 927-936, Palm Springs, California.
- Priestley, M.J.N., Verna, R., and Xiao, Y. (1994). Seismic shear strength of reinforced concrete columns. *Journal of Structural Engineering ASCE*, 120.
- Priestley, M.J.N., Seible, F., and Chai, Y.H. (1992). Design guidelines for assessment, retrofit and repair of bridges for seismic performance. Report SSRP 92/01, Dept. of Applied Mechanics and Engineering Sciences, Univ. of California, San Diego, August.

3 IMPORTANT PHENOMENA AFFECTING THE BRIDGE RESPONSE

3.1 Multi-support excitation

From the point of view of structural analysis, the most important implication of multi-support excitation is that the conventionally adopted assumption of equal seismic input under all the supports of a structure is a pure abstraction, acceptable only when dealing with buildings of moderate dimensions, and it is even farther from reality if extended-in-plan structures are to be studied. In some cases, such as long-span isolated bridges like those examined in this report, due consideration should be given to the non-synchronism of the seismic action, since different input motions experienced at adjacent supports can significantly modify the overall structural response thus jeopardizing the design concept. It is in fact common to observe, in every major seismic event, spectacular failures of bridges due to unseating of the decks, which leave little doubt that considerable relative displacements can exist in the free-field, even between points a few tenths of meters apart.

Studies on the response of extended-in-plan structures subjected to different motions at the supports have started some thirty years ago and continue until today (for ex., Bodganoff et al. 1965, Perotti 1990, Moerland et al. 1993), the recent ones making use of the stochastic models just mentioned. Many of these studies focus on the algorithm to obtain the response and are often illustrated with reference to simple examples having a scant connection with real design cases. Others, (for ex., Der Kiureghian and Neuenhofer 1992, Heredia-Zavoni and Vanmarcke 1994), are more design-oriented, in that they provide more or less simplified methods to account for the effects of the correlation between the support motions.

No study is known which considers the inelastic behavior of the structure, excluding those by the authors (Moerland et al. 1993, Monti et al. 1995, 1996, Monti and Pinto 1998). This is surprising, because if it is true that present design practice is based on linear analysis, and that non-linear behavior effects are accounted for by means of a simple factor, there is *a priori* no reason to believe that this approach may extend its validity to non-synchronous situations, at least not with the same factors.

This manifest lack of knowledge on the subject is reflected in modern seismic codes for bridge design, where the non-synchronous nature of seismic input is accounted for only by means of semi-empirical provisions for extra seating lengths, adequate joint gaps, minimum relative displacements between adjacent foundations.

While seismic design codes cater pragmatically for this phenomenon by means of increasingly severe provisions, research is looking since many years now for more rational and substantiated answers. For these answers to come, two aspects need to be covered in sequence: a) acquiring a sufficient knowledge of the mechanisms underlying the spatial variability of the motion, dealt with in section 3.1.1, and b) assessing through numerical studies its relevance on the response, possibly in terms articulated enough to be of direct use for design, as reported in sections 3.1.1.1 and 3.1.3 for conventional and isolated bridges, respectively.

3.1.1 Soil motion

As regards the representation of the soil motion including the phenomena producing multi-support excitation, a breakthrough has occurred with the installation of strong motion arrays. The approach consists in gathering data, and processing them on the basis of an assumed stochastic model. The information is sufficient to implement but the simplest of the models, *i.e.*, second moment fields fully characterized by the power spectral densities at each station and by a coherence spectrum, assumed to depend only on the relative distance between stations. The simplicity of this model needs not to be emphasized, as well as its dubious applicability to cases of pronounced soil inhomogeneity, not to speak of irregular soil profiles. Its merits, however, are great enough to justify its use for shedding light upon what really matters: the sensitivity of the structural response to the gross features of the phenomenon.

3.1.1.1 Spatial model for ground motion

From a physical point of view, the spatial variation of seismic ground motion may be schematically thought of as the result of the combination of three different phenomena: a) the *incoherence* effect, resulting from reflections and refractions of waves through the soil during their propagation (this effect is also referred to as *geometric incoherence*), b) the so-called *wave-passage* effect, that is the difference in the arrival times of seismic waves at different stations, and c) the *site response* effect, due to differences in local soil conditions under the various stations.

Within the stochastic model assumed here, spatial variability is described by means of the cross-PSD matrix of the ground acceleration as follows

$$\mathbf{S}_{\ddot{U}\ddot{U}}(d, \omega) = \mathbf{G}(d, \omega) \times \mathbf{S}_{AA}(\omega) \quad (1)$$

where the symbol \times denotes the Hadamard product by which each element of $\mathbf{G}(d, \omega)$ is multiplied by the corresponding element of $\mathbf{S}_{AA}(\omega)$, ω = circular frequency, and $\mathbf{S}_{AA}(\omega)$ is the (full) matrix of the ground acceleration cross-PSD functions at the N locations, given as

$$\mathbf{S}_{AA}(\omega) = S_{A_j A_l}(\omega) = \sqrt{S_{A_j A_j}(\omega) S_{A_l A_l}(\omega)} \quad j, l = 1 \dots N \quad (2)$$

and $\mathbf{G}(d, \omega)$ is the (full) matrix of the complex coherency functions accounting for the three effects of incoherence, wave passage (Luco and Wong 1986) and site response (Der Kiureghian and Neuenhofer 1996)

$$\begin{aligned} \mathbf{G}(d, \omega) &= \gamma_{jl}(d, \omega) = \gamma_{jl}(d, \omega)^{\text{incoherence}} \cdot \gamma_{jl}(d^L, \omega)^{\text{wave passage}} \cdot \gamma_{jl}(\omega)^{\text{site response}} \\ &= \exp \left[- \left(\frac{\alpha \omega d_{jl}}{v_s} \right)^2 \right] \cdot \exp \left(-i \frac{\omega d_{jl}^L}{v_{app}} \right) \cdot \exp [i\theta_{jl}(\omega)] \quad j, l = 1 \dots N \end{aligned} \quad (3)$$

The *incoherence* term decays exponentially with the circular frequency ω , with the horizontal separation distance d_{jl} between two stations j and l and, through the shear waves velocity v_s , with the inverse of the mechanical characteristics of the soil. The second term depends on the projected horizontal distance d_{jl}^L along the wave propagation direction and on the wave circular frequency ω , and is a measure of the *wave-passage* delay due to the surface apparent velocity of waves v_{app} . The *site response* term is represented through a phase shift independent of the distance

$$\theta_{jl}(\omega) = \tan^{-1} \frac{\text{Im}[H_j(\omega)H_l(-\omega)]}{\text{Re}[H_j(\omega)H_l(-\omega)]} \quad (4)$$

and dependent on the frequency-response functions of the soil columns at the different stations

$$H_j(\omega) = \frac{\omega_j^2 + 2i\zeta_j\omega_j\omega}{\omega_j^2 - \omega^2 + 2i\zeta_j\omega_j\omega} \quad j, l = 1 \dots N \quad (5)$$

which represent the amplitude of a harmonic motion at the surface of the ground caused by a harmonic motion of the form $\exp(i\omega t)$ at the bedrock level. It is important to note that the phase shift is completely defined in terms of the two frequency-response functions, which only depend on the properties of the two soil columns. In particular, it does not depend on the distance between the two stations, or the power spectral densities of the bedrock motion. It should be emphasized that the site-response component of the coherency function does not account for the effect of incoherence resulting from scattering of waves within the two soil columns. This contribution is rather included in the incoherence term.

Apart from the site response effect, which depends on the locally selected PSD functions, in this study the coherency function is considered basically as a two-parameter function, having lumped the mechanical characteristic of the soil and the factor α into a single parameter expressed as the ratio v_s/α , and the second one being v_{app} . When $v_s/\alpha \rightarrow \infty$, the first term tends to 1 and the incoherence effect results from wave travelling and site effect only; if $v_{app} \rightarrow \infty$, the second term tends to 1 and the incoherence is due to the incoherence and the site effect only. Note that in this formulation the geometric incoherence effect is given a higher weight (square power) with respect to the wave-passage effect.

In the soil frequency-response functions $H_j(\omega)$ in (5) the parameters depend on the soil type (F=firm, M=medium, S=soft) as follows (Der Kiureghian and Neuenhofer 1996):

$$\begin{aligned}
\omega_j(\text{F}) &= 6\pi \text{ rad/sec}, & \zeta_j(\text{F}) &= 0.6 \\
\omega_j(\text{M}) &= 3\pi \text{ rad/sec}, & \zeta_j(\text{M}) &= 0.4 \\
\omega_j(\text{S}) &= \pi \text{ rad/sec}, & \zeta_j(\text{S}) &= 0.2
\end{aligned} \tag{6}$$

The PSD function adopted in this work is the well-known modified Kanai-Tajimi spectrum of ground accelerations (Clough and Penzien 1975), expressed as

$$S_{A_j A_j}(\omega) = S_{0_j} S_{CP_j}(\omega) = S_{0_j} \frac{\omega_{f_j}^4 + 4\zeta_{f_j}^2 \omega_{f_j}^2 \omega^2}{\left(\omega_{f_j}^2 - \omega^2\right)^2 + 4\zeta_{f_j}^2 \omega_{f_j}^2 \omega^2} \frac{\omega^4}{\left(\omega_{g_j}^2 - \omega^2\right)^2 + 4\zeta_{g_j}^2 \omega_{g_j}^2 \omega^2} \tag{7}$$

where S_{0_j} = scale factor, $S_{CP_j}(\omega)$ = normalized (two-sided) Clough-Penzien spectrum, ω_f and ζ_f may be thought of as characteristic ground frequency and damping, and ω_g and ζ_g are the parameters of an additional filter, introduced to assure finite power for the PSD. All these parameters depend on the location j .

Note that the PSD of the ground displacement process is:

$$S_{D_j D_j}(\omega) = S_{0_j} \frac{S_{CP_j}(\omega)}{\omega^4} = S_{0_j} \frac{\omega_{f_j}^4 + 4\zeta_{f_j}^2 \omega_{f_j}^2 \omega^2}{\left(\omega_{f_j}^2 - \omega^2\right)^2 + 4\zeta_{f_j}^2 \omega_{f_j}^2 \omega^2} \frac{1}{\left(\omega_{g_j}^2 - \omega^2\right)^2 + 4\zeta_{g_j}^2 \omega_{g_j}^2 \omega^2} \tag{8}$$

The scale factors S_{0_j} at all location can be found based on either the peak ground acceleration or the peak ground displacement (PGA and PGD, respectively, selected in this work as equal for all locations) according to the following relation:

$$S_{0_j} = \frac{\text{PGA}^2}{p_{A_j,0.5}^2 \cdot \text{Var}_{A_j}^*} = \frac{\text{PGD}^2}{p_{D_j,0.5}^2 \cdot \text{Var}_{D_j}^*} \tag{9}$$

where $p_{A_j,0.5}$, $p_{D_j,0.5}$ = peak factors corresponding to a 50% probability of exceedance of the peak level (either PGA for the ground acceleration process or PGD for the ground displacement process) at location j .

For a generic process Y , the peak factor can be calculated according to (Vanmarcke 1977):

$$p_{Y,0.5} = \sqrt{2 \cdot \ln \frac{2.8 \cdot \Omega_Y \cdot t_s}{2\pi}} \tag{10}$$

where t_s = duration of the (stationary part of the) process and

$$\Omega_Y = \sqrt{\frac{\text{E}[\dot{Y}^2]}{\text{Var}[Y]}} \tag{11}$$

where $\text{E}[\dot{Y}^2]$ = mean square of the derivative of the process and $\text{Var}[Y]$ = variance (total power) of the process having PSD $S_{YY}(\omega)$:

$$E[\dot{Y}^2] = \int_{-\infty}^{\infty} \omega^2 S_{YY}(\omega) d\omega \quad (12)$$

$$\text{Var}[Y] = \int_{-\infty}^{\infty} S_{YY}(\omega) d\omega \quad (13)$$

Note that Ω_Y only depends on the shape of the PSD and not on the scale factor; thus, it can be written for the ground acceleration and the ground displacement processes, respectively, as:

$$\Omega_{A_j} = \sqrt{\frac{E^*[\dot{A}_j^2]}{\text{Var}^*[A_j]}} \quad \text{and} \quad \Omega_{D_j} = \sqrt{\frac{E^*[\dot{D}_j^2]}{\text{Var}^*[D_j]}} \quad (14)$$

where

$$E^*[\dot{A}_j^2] = \int_{-\infty}^{\infty} \omega^2 S_{CP_j}(\omega) d\omega \quad \text{and} \quad E^*[\dot{D}_j^2] = \int_{-\infty}^{\infty} \omega^{-2} S_{CP_j}(\omega) d\omega \quad (15)$$

$$\text{Var}^*[A_j] = \int_{-\infty}^{\infty} S_{CP_j}(\omega) d\omega \quad \text{and} \quad \text{Var}^*[D_j] = \int_{-\infty}^{\infty} \omega^{-4} S_{CP_j}(\omega) d\omega \quad (16)$$

The characteristic ground frequency ω_f of the Cbugh-Penzien spectrum depends on the soil type (F=firm, M=medium, S=soft) as follows (Der Kiureghian and Neuenhofer 1992):

$$\begin{aligned} \omega_f(F) &= 15 \text{ rad/sec} \\ \omega_f(M) &= 10 \text{ rad/sec} \\ \omega_f(S) &= 5 \text{ rad/sec} \end{aligned} \quad (17)$$

while the other parameters can be determined as follows:

$$\zeta_f = \frac{\omega_f}{25} \quad \omega_g = \frac{\omega_f}{10} \quad \zeta_g = 0.6 \quad (18)$$

The PSD functions of the three soil types are presented in Figure 3.1 along with the acceleration and displacement response spectrum.

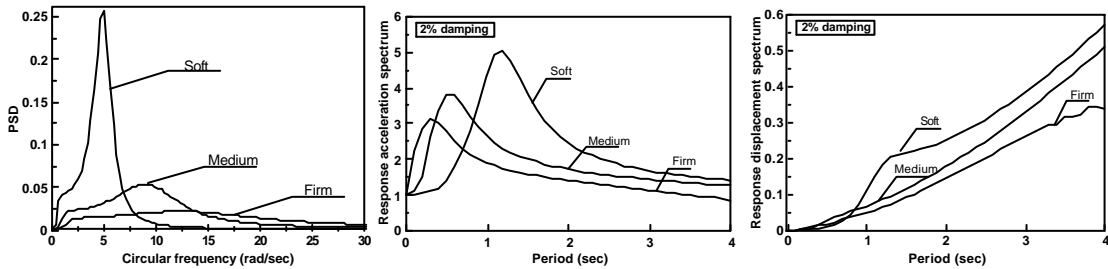


Figure 3.1. PSD and response spectra for soil types F, M and S.

The values of Var^* and Ω for the three soil types are:

$$\text{Var}_{A_j}^*(F) = 92.055 \quad \text{Var}_{A_j}^*(M) = 62.764 \quad \text{Var}_{A_j}^*(S) = 45.082 \quad (19)$$

$$\Omega_{A_j}(F) = 46.276 \text{ rad/sec} \quad \Omega_{A_j}(M) = 21.963 \text{ rad/sec} \quad \Omega_{A_j}(S) = 6.4977 \text{ rad/sec} \quad (20)$$

$$\text{Var}_{D_j}^*(F) = 0.78974 \quad \text{Var}_{D_j}^*(M) = 2.6690 \quad \text{Var}_{D_j}^*(S) = 21.403 \quad (21)$$

$$\Omega_{D_j}(F) = 15521 \text{ rad/sec} \quad \Omega_{D_j}(M) = 1.0578 \text{ rad/sec} \quad \Omega_{D_j}(S) = 0.5622 \text{ rad/sec} \quad (22)$$

Thus, the peak factor of the three soil types can be directly expressed as follows:

$$\begin{aligned} p_{A_j,0.5}(F) &= \sqrt{2 \ln t_s + 6.053} & p_{D_j,0.5}(F) &= \sqrt{2 \ln t_s - 0.737} \\ p_{A_j,0.5}(M) &= \sqrt{2 \ln t_s + 4.562} & \text{and} & & p_{D_j,0.5}(M) &= \sqrt{2 \ln t_s - 1.504} \\ p_{A_j,0.5}(S) &= \sqrt{2 \ln t_s + 2.126} & & & p_{D_j,0.5}(S) &= \sqrt{2 \ln t_s - 2.768} \end{aligned} \quad (23)$$

Note that from (9) it is observed that:

$$\Psi_{soil}(t_s) = \frac{\text{PGD}}{\text{PGA}} = \frac{p_{D_j,0.5} \sigma_{D_j}^*}{p_{A_j,0.5} \sigma_{A_j}^*} \quad (24)$$

where $\sigma_Y^* = \sqrt{\text{Var}_Y^*}$ and Ψ_{soil} is a function of the soil type and of t_s through the peak factors.

For example, for a stationary duration $t_s = 20$ sec, it is:

$$\Psi_F(20) = 0.0612 \text{ sec}^2 \quad \Psi_M(20) = 0.1345 \text{ sec}^2 \quad \Psi_S(20) = 0.4342 \text{ sec}^2 \quad (25)$$

The above approach, where the soil motion is characterized by its PSD function, is sufficient to allow a random vibration approach, which will be adopted for the analyses of isolated bridges (section 3.1.3).

On the other hand, if full nonlinear analyses under generated time histories are to be performed, a stochastic field needs to be generated. This is the procedure followed in the case of conventional bridges in section 3.1.2.

A possible procedure to generate a stochastic field can make use of the so-called *spectral representation method* (Shinozouka 1972). The space-time random field with zero mean, space-time covariance function $R(d, t)$, d being the separation distance, and frequency-wavenumber (F-K) spectrum $S(\kappa, \omega)$, where $\kappa =$ wavenumber, is here simulated through

$$f(x,t) = \sqrt{2} \sum_{\eta=\pm 1} \sum_{j=0}^{J-1} \sum_{n=0}^{N-1} [S(\kappa_j, \omega_n) \Delta \kappa \Delta \omega]^{1/2} \cos \left(\eta \kappa_j x + \omega_n \left(t - \frac{x}{v_{app}} \right) + \phi_{jn}^{(\eta)} \right) \quad (26)$$

in which $\phi_{jn}^{(\eta)}$ are two sets of independent random phase angles uniformly distributed in $(0, 2\pi]$.

In order to use the above equation, a discretization of the frequency-wavenumber spectrum is to be performed. The F-K spectrum is obtained as follows:

$$S(\kappa, \omega) = S(\omega) \cdot \Gamma(\kappa, \omega) \quad (27)$$

where

$$\Gamma(\kappa, \omega) = \frac{1}{2\pi} \int_{-\infty}^{\infty} |\gamma(d, \omega)| e^{-i\kappa d} dd = \frac{1}{2\sqrt{\pi}} \exp \left[- \left(\frac{v_s \kappa}{2\alpha\omega} \right)^2 \right] \frac{v_s}{\alpha|\omega|} \quad (28)$$

is the transform of the coherency function. Note that

$$\int_{-\infty}^{\infty} \Gamma(\kappa, \omega) d\kappa = 1 \quad (29)$$

which implies

$$\int_{-\infty}^{\infty} S(\kappa, \omega) d\kappa = S(\omega) \quad (30)$$

that is, the power pertaining to a frequency is distributed among all the wavenumbers.

In the definition of Γ only the module of the coherency function is employed

$$|\gamma(d, \omega)| = \exp \left[- \left(\frac{\alpha\omega d}{v_s} \right)^2 \right] \quad (31)$$

that is, only the geometric incoherence term is included in the F-K spectrum. An advantage of adopting Eq. (31) is that the resulting F-K spectrum is quadrant-symmetric:

$$S(\kappa, \omega) = S(-\kappa, \omega) = S(\kappa, -\omega) = S(-\kappa, -\omega) \quad (32)$$

and this permits to simplify the discretization of the spectrum. The concept of quadrant-symmetry was first introduced by Vanmarcke (1983). Note that coherency functions yielding quadrant-symmetric F-K spectra can depict only the incoherence (change in shape) of the seismic motions (Zerva 1992), and therefore the apparent propagation (wave-passage effect) of the seismic motions should be explicitly included in the equation of the simulated field, by means of the time-shift x/v_{app} .

The discretization is performed within the limits of an upper cut-off wavenumber κ_u and an upper cut-off frequency ω_u , beyond which the contribution

to the total power can be considered as negligible for practical purposes. On the basis of regressions on the F, M and S spectra, these can be determined as follows:

$$\begin{aligned}\omega_u &= 20 \cdot \omega_f \\ \kappa_u &= 6.65 \cdot \frac{\alpha}{v_s} \cdot \omega_f^{0.84} e^{0.047 \omega_f}\end{aligned}\quad (33)$$

The upper cut-off frequency was determined by satisfying the following condition

$$\frac{\int_0^{\omega_u} S(\kappa, \omega) d\omega}{\int_0^{\omega_u + 2\pi} S(\kappa, \omega) d\omega} - 1 = 10^{-5}\quad (34)$$

whereas the upper cut-off wavenumber was determined by satisfying the following conditions

$$\begin{aligned}S(\kappa_u, \omega) &= S_{\max} \cdot 10^{-3} \\ \frac{\partial}{\partial \omega} S(\kappa_u, \omega) &= 0\end{aligned}\quad (35)$$

where $S_{\max} \approx 2.218 \frac{v_s}{\alpha \omega_f}$ = peak value of the spectrum, which occurs at the point with coordinates $(\kappa = 0, \omega \approx 0.123 \omega_f)$.

A way to check whether the upper cut-off frequency is correct for practical purposes is to make use of Eq. (30) as follows

$$\sum_{\kappa=-\kappa_u}^{\kappa_u} S(\kappa, \omega_n) \Delta \kappa \approx S(\omega_n) \quad \omega_n = 0, \dots, \omega_u\quad (36)$$

Once the cut-offs are determined, the discrete wavenumber and frequency are given by

$$\begin{aligned}\kappa_j &= j \Delta \kappa \quad j = 0, \dots, M-1 \quad \text{with } M \geq 2J \\ \omega_n &= n \Delta \omega \quad n = 0, \dots, L-1 \quad \text{with } L \geq 2N\end{aligned}\quad (37)$$

where M and L are powers of 2, and J and N are also powers of 2, such that J is greater or equal than the number of points for the discretization in space of the field (number of sites where the field is needed) and N is greater or equal than the number of points for the discretization in time of the field (number of points in the time histories). Note that $J \Delta \kappa = \kappa_u$ and $N \Delta \omega = \omega_u$.

Eq. (26) can be rewritten so to allow the utilization of the FFT method, as

$$f\left(x_r, t_s - \frac{x_r}{v_{app}}\right) = \sqrt{2} \text{Re} \left[e^{-i\omega x_r / v_{app}} \left\{ \sum_{\eta=\pm 1} \sum_{j=0}^{J-1} \sum_{n=0}^{N-1} \left[S(\kappa_j, \omega_n) \Delta \kappa \Delta \omega \right]^{1/2} e^{i\phi_{jn}^{(\eta)}} \right\} e^{i\eta 2\pi r j / M} e^{i 2\pi s n / L} \right] \quad (38)$$

in which:

$$\begin{aligned} x_r &= r \Delta x = r \frac{2\pi}{M \Delta \kappa} & r &= 0, \dots, M-1 \\ t_s &= s \Delta t = s \frac{2\pi}{L \Delta \omega} & s &= 0, \dots, L-1 \end{aligned} \quad (39)$$

The two-dimensional FFT is to be applied to the term in the braces in Eq. (38). Due to the presence of $\eta = \pm 1$, a forward-forward FFT and a backward-forward FFT are to be performed.

A different discretization scheme can be used (for ex., Zerva 1992) with: $\kappa_j = (j + \frac{1}{2})\Delta\kappa$ and $\omega_n = (n + \frac{1}{2})\Delta\omega$ in order to obtain ergodicity in the mean. However, in this case the simulations obtained by means of Eq. (38) are already ergodic in the mean, because the value of the F-K spectrum at the origin ($\kappa = 0, \omega = 0$) is zero (Shinozouka 1972), therefore the discretization in Eq. (39) can be used.

As a last remark, note that the period of the simulations is

$$T_0 = \frac{2\pi}{\Delta\omega} = L \Delta t \geq N_p \Delta t = t_{\max} \quad (40)$$

that is, it is always longer or equal to the duration of the generated motion.

In order to account for the nonstationary nature of ground accelerations, the stationary time histories generated by means of Eq. (38) are modulated by means of an envelope function. The function chosen in this study is:

$$\begin{aligned} \zeta(t) &= \left(\frac{t}{t_1} \right)^2 & \text{for } 0 \leq t \leq t_1 \\ \zeta(t) &= 1 & \text{for } t_1 \leq t \leq t_2 \\ \zeta(t) &= \exp \left\{ \frac{t-t_2}{t_{\max} - t_2} \cdot \ln \beta \right\} & \text{for } t_2 \leq t \leq t_{\max} \end{aligned} \quad (41)$$

where t_1, t_2 = ramp duration and decay starting time, respectively, t_{\max} = time history duration and β = ratio of the amplitude envelope at t_{\max} to that during the stationary phase ($t_1 \leq t \leq t_2$). In this work: $t_1 = 2$ sec, $t_2 = 14$ sec, $t_{\max} = 20$ sec and $\beta = 0.25$.

Velocity and displacement histories, which are needed in a multi-support analysis, are obtained by integration of the acceleration histories according to a method known as *baseline correction* (Jennings et al. 1969), which minimizes the errors introduced in the numerical integration when passing from accelerations to velocities and displacements.

Figure 3.2 compares the auto-spectrum (left) and the autocorrelation function (right) of the simulations of Eq. (38) with the target spectrum in Eq. (7) and the target autocorrelation function for soil types F and M. The number of simulations

performed was 70. It is seen that both the generated PSD and the generated autocorrelation practically coincide with the target PSD and autocorrelation.

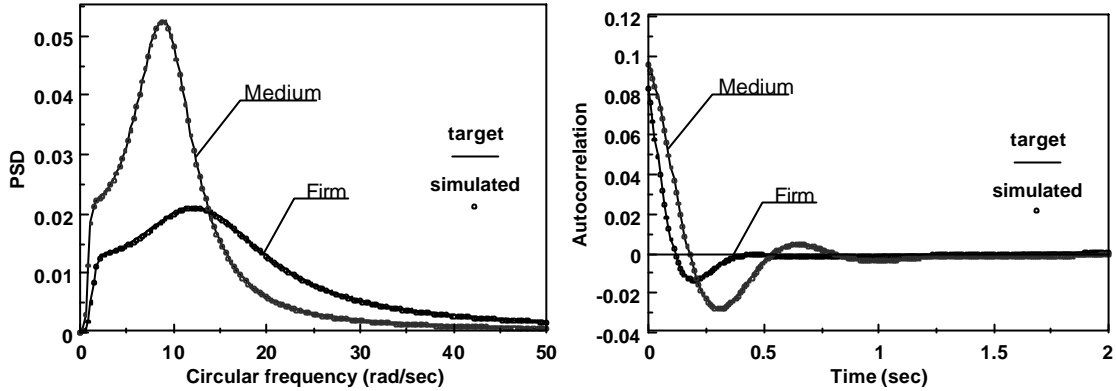


Figure 3.2. Target and simulated PSD (left) and autocorrelation (right) for soil types F and M.

Figure 3.3 compares the coherency functions of the simulations with the target coherency functions at different stations having separation distance $d=50, 100, 150, 200, 250$ and 300 m (note that in the figures ξ stands for d) and for two values of the parameter $v_s/\alpha = 300$ and 600 m/s. Also in this case 70 simulations were performed. It should be observed that for both values of the parameter v_s/α the agreement is satisfactory.

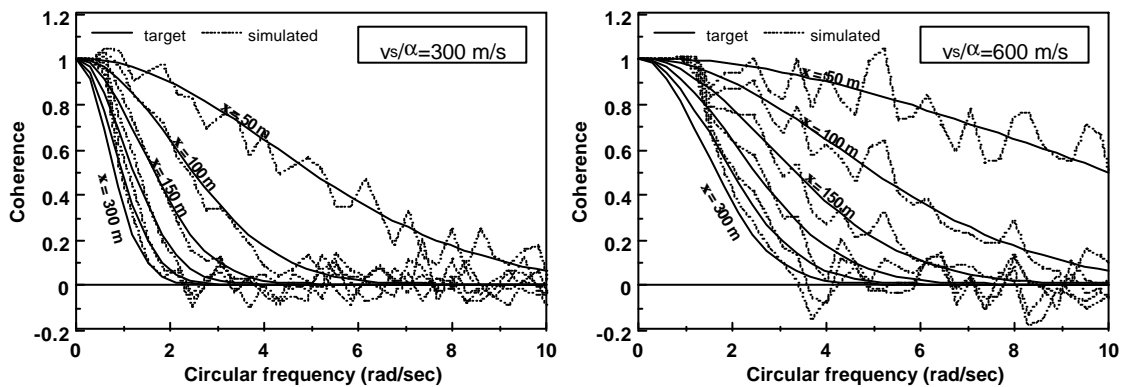


Figure 3.3. Target and simulated coherency functions at different stations at distance ξ for $v_s/\alpha = 300$ (left) and 600 m/s (right).

3.1.2 Conventional bridges

The purpose of the study presented in this section is to gain insight precisely into this question: the relevance of non-rigid input motion on the peak inelastic response of bridge structures, and the extent of validity of the “ q -factor” approach.

It consists of a parametric analysis having a sufficient, although far from exhaustive, width of scope, whose essential elements are outlined here and described in full detail subsequently. Three bridge types are considered: they all have 6 spans, of 50 m length each; the superstructure is the same in all cases, while the (uniform) heights of the piers take the values of 7.5, 10 and 15 m.

The soil motion is characterized by two different power spectral densities (the same at all stations in each case, therefore no site response is included), while the parameters controlling the loss of coherence have been made to vary between their respective extremes. Finally, the design of the piers has been made for three different values of the behavior factor and according to two strategies, *i.e.*, either accounting for the non-synchronism of the input or neglecting it.

3.1.2.1 Design of bridges

The bridge under consideration is represented in Figure 3.4. It is a 6-span continuous deck with 5 piers of the same height H and of 2.5 m diameter. The span length is 50.0 m. The deck, transversely hinged to the piers and the abutments, has a dead load of 200 kN/m. The piers (acting as cantilevers) are considered as fixed on the soil.

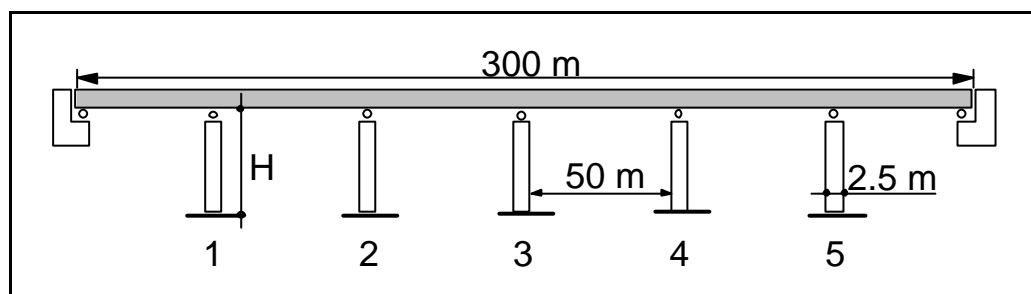


Figure 3.4. Schematic view of the bridge.

All the analyses of the bridge have been performed in transverse direction. The design peak ground acceleration (PGA) has been taken as: $0.42 g/q$, where q = behavior factor.

Table 3.1. Values considered in the parametric study.

Parameter	Values			
	Firm (F)		Medium (M)	
Soil type				
Pier height H (m)	7.50	10.00	15.00	
Behavior factor q	2	4	6	
v_s/α (m/s)	300	600	∞	
v_{app} (m/s)	300	600	1200	∞

The parameters considered in the study are: a) the soil type, b) the structure stiffness, represented by the piers height H , c) the design level, given by the behavior factor: q , and d) the coherency parameters: v_s/α and v_{app} . The numerical values assigned to the above parameters are indicated in Table 3.1.

The choice regarding the soil type affects the values of the parameters in the PSD function in Eq. 7. The values adopted are obtained from Eqs. (17) and (18) and are listed in Table 3.2 for each type of soil.

Table 3.2. PSD filter parameters for the soil types considered.

Soil type	ω_f (rad/sec)	ζ_f	ω_g (rad/sec)	ζ_g
Firm (F)	15.0	0.6	1.5	0.6
Medium (M)	10.0	0.4	1.0	0.6

The three different pier heights are intended to produce three different degrees of bridge stiffness and have been chosen so as to get bridges with fundamental periods varying within rather large limits. The first three periods of vibration are listed in Table 3.3.

Table 3.3. Periods of vibration of the bridges.

Period	$H = 7.50$ m	$H = 10.00$ m	$H = 15.00$ m
T_1 (sec)	0.43	0.60	1.20
T_2 (sec)	0.40	0.57	0.84
T_3 (sec)	0.33	0.41	0.48

The bridges have been designed elastically for non-synchronous as well as synchronous ground motion using accelerograms generated according to Eq. (38). The design has been made for the average of the maximum values of the response (bending moments and shear at the pier base) obtained using ten sets of accelerograms scaled according to Eq. (9) to a PGA of 0.42 g, divided by the behavior factor q . In these analyses, the piers cracked stiffness has been used, obtained from the uncracked stiffness (gross section) divided by a factor 2.5. No minimum reinforcement ratio was considered. The following material strengths have been used: for concrete $f_c = 35,000$ kPa, for steel $f_y = 440,000$ kPa, with ultimate strains equal to $\epsilon_{cu} = 0.008$ and $\epsilon_{su} = 0.10$, respectively. Material design factors were: 1.5 for concrete and 1.15 for steel.

By combining all the values of the parameters in Table 3.1 above, 216 cases resulted. Among those are the 18 bridges designed under synchronous soil motion ($v_s/\alpha = \infty$ and $v_{app} = \infty$), corresponding to the usual design assumption adopted in engineering practice.

Both linear analyses (for design) and nonlinear analyses (for verifications) have been carried out through step-by-step integration by means of the program ASPIDEA (Giannini et al. 1992), where each pier is modeled with two elements in series: a Takeda-type plastic hinge zone at the lower support, having fixed length equal to one-tenth of the pier height, and the remaining elastic part of the pier, whose flexibility is doubled to account for cracking.

3.1.2.2 Elastic response

It is known, (see for ex., Clough and Penzien 1975), that the response of an elastic structure subjected to non-synchronous input can be obtained from the superposition of two contributions: a *dynamic* component induced by the inertia forces and a so-called *pseudo-static* component, due to the differences in the support displacements. These latter can induce significant distortions in the structure thus modifying the internal forces with respect to the case of synchronous input. The two components can be synthetically represented at each time step by means of two values: the mean ground displacement under the supports, which corresponds to a rigid body motion of the structure and can be partly identified with the dynamic component, and the ground displacements standard deviation, which can be considered as representative of the pseudo-static distortion imposed to the structure.

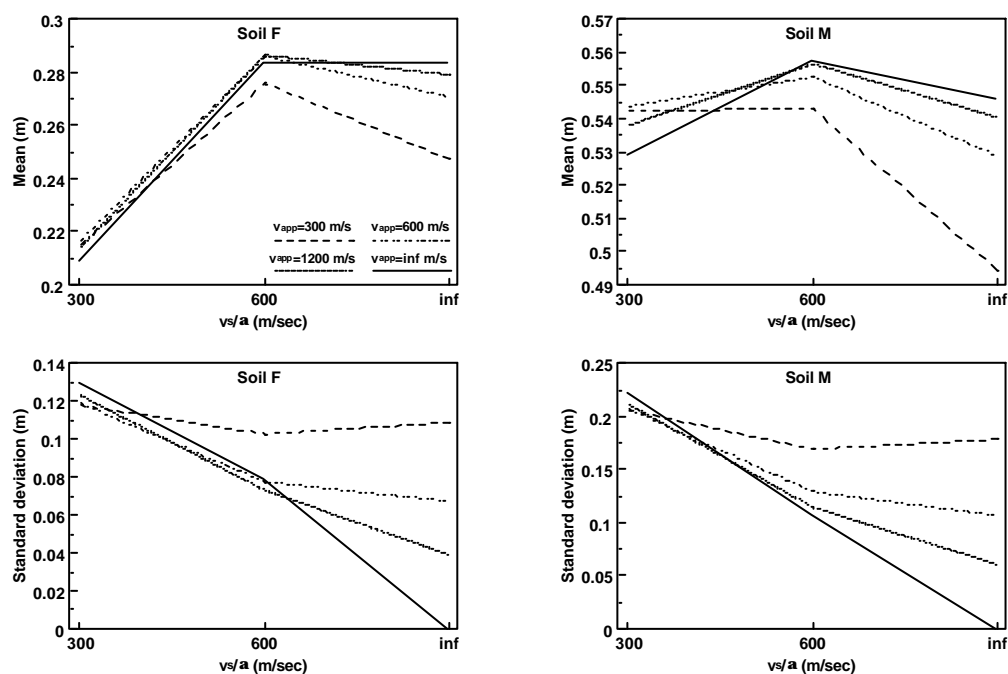


Figure 3.5. Mean and standard deviation of ground displacements on soil F (left) and M (right).

In Figure 3.5 the maxima of the two values attained during the ground displacement history are presented for soil types F and M and with values $v_s/\alpha = 300, 600$ and ∞ m/s for the geometric incoherence term. In each diagram four distributions corresponding to different values of the apparent velocity of waves $v_{app} = 300, 600, 1200$ and ∞ m/s (wave-passage effect) are represented. It should be kept in mind while observing Figure 3.5 and the following ones that *geometric incoherence* (i.e. that ruled by the first term in Eq. 3) decreases as v_s/α increases from 300 m/s to ∞ m/s. In each diagram the *wave-passage* delay (i.e. that ruled by the second term in Eq. 3) decreases as v_{app} increases from 300 to ∞ m/s.

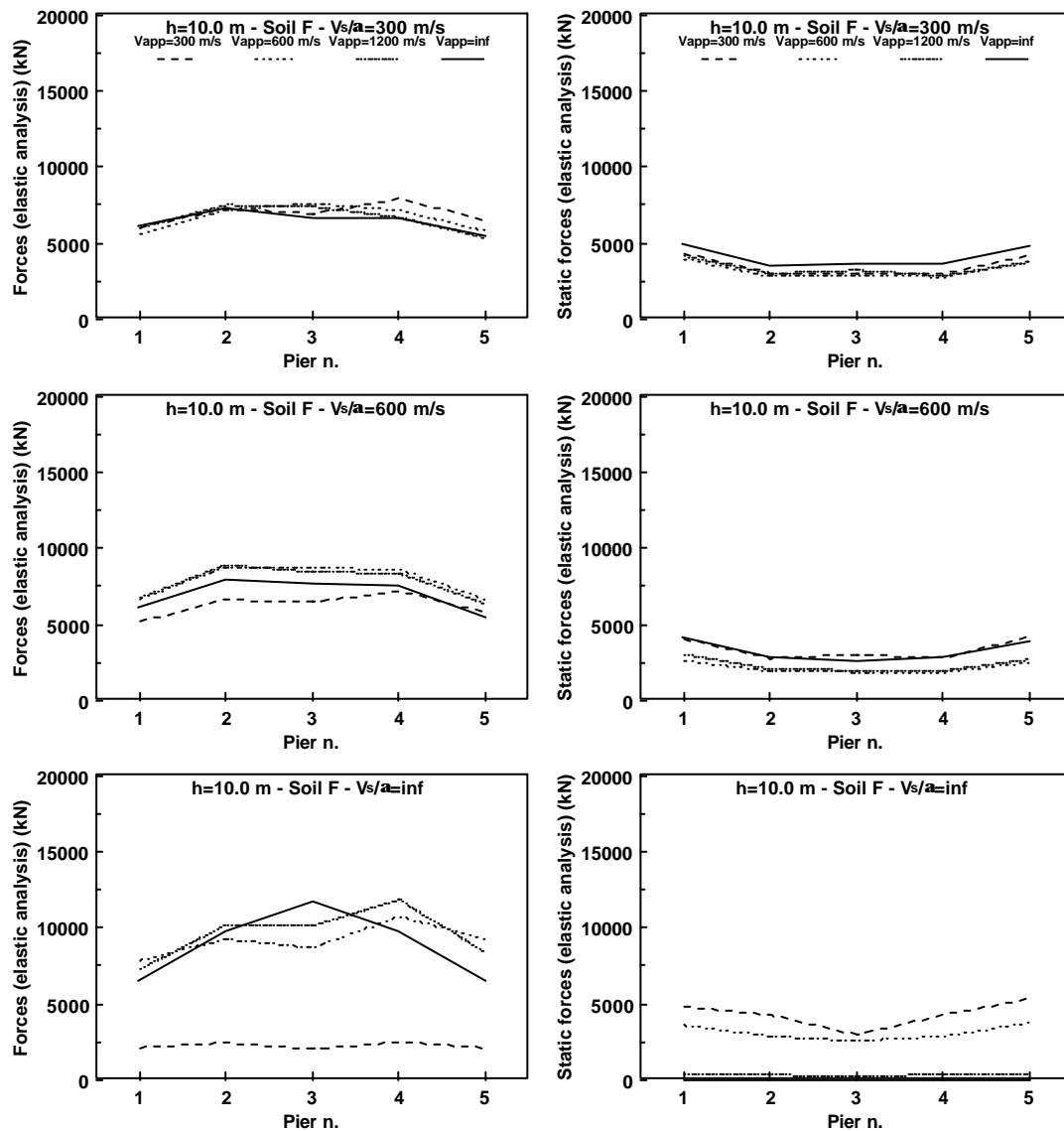


Figure 3.6. Bridge $H=10.0$ m on soil F. Total and static forces for $v_s/\alpha = 300$ m/s (top), $v_s/\alpha = 600$ m/s (middle), and $v_s/\alpha = \infty$ m/s (bottom).

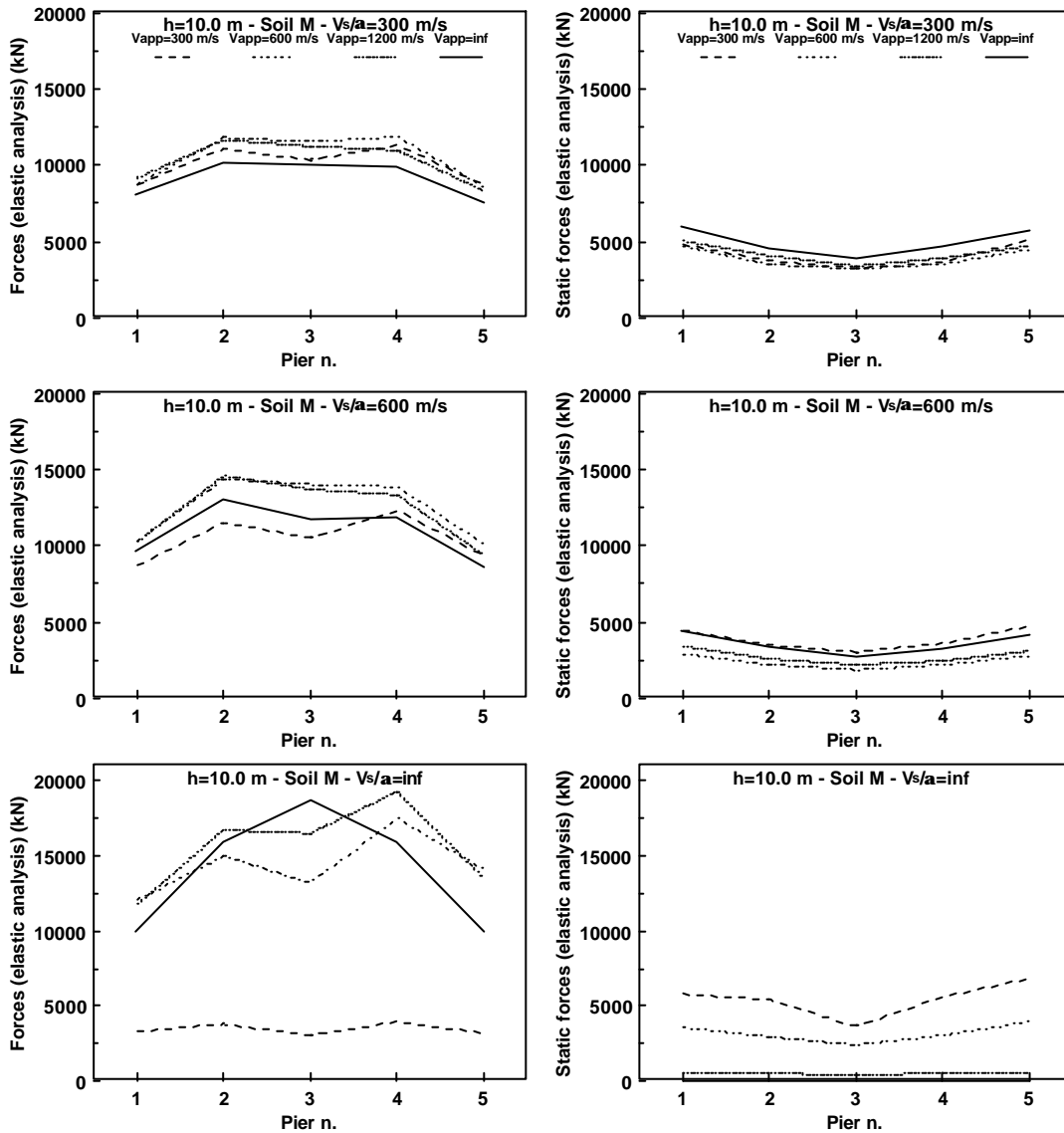


Figure 3.7. Bridge $H=10.0$ m on soil M. Total and static forces for $v_s/\alpha = 300$ m/s (top), $v_s/\alpha = 600$ m/s (middle), and $v_s/\alpha = \infty$ m/s (bottom).

For soil F an evident phenomenon is the sensible reduction of the mean displacement for increasing geometric incoherence, therefore we expect a reduction of the dynamic component as v_s/α decreases from ∞ m/s to 300 m/s. For soil M this is less evident and we rather expect an increase of the dynamic component when $v_{app} = 300$ m/s. For both soils a remarkable increase of standard deviation is observed as v_s/α decreases but this phenomenon is less evident as v_{app} decreases from ∞ to 300 m/s. Therefore, high pseudo-static distortions are expected either for low values of v_s/α or, if $v_s/\alpha = \infty$, for low values of v_{app} . Note that in all cases the variation of

v_{app} has a notable effect only for $v_s/\alpha = \infty$, while in the presence of a certain degree of geometric incoherence its effect is sensibly reduced.

In Figure 3.6 and Figure 3.7, at left, are the envelopes of the maximum total shear forces acting on each pier derived from non-synchronous linear dynamic analyses, while at right are the envelopes of the maximum pseudo-static component of the shear forces, derived from linear static analyses by applying the displacement histories at the pier supports. The results are presented for the bridge with $H = 10.00$ m only, but the comments made in the following apply also to the bridges with $H = 7.50$ and 15.00 m which show similar force distributions.

We comment first the total force distributions (left-side diagrams) to evaluate the effects of geometric and wave-passage incoherence on the bridge response. The extreme cases are those with maximum incoherence $v_s/\alpha = 300$ m/s and $v_{app} = 300$ m/s (dashed lines in Figure 3.6 and Figure 3.7, top) and those with perfect coherence corresponding to the synchronous support motion cases (solid lines in Figure 3.6 and Figure 3.7, bottom).

For these latter cases it should be observed that the total shear force distribution follows essentially the shape of the first mode of vibration of the bridge. In the other cases it is seen that for increasing incoherence (decreasing values of v_s/α and v_{app}) the responses show a flattened shape, thus suggesting that higher modes are excited by multi-support input.

A first important effect that can be noted by comparing the cases of fully synchronous input (solid lines in Figure 3.6 and Figure 3.7, bottom) with all other cases in which some degree of uncorrelation of geometric nature is present (all lines in Figure 3.6 and Figure 3.7, top and middle) is that the synchronous forces are systematically larger, although to different degrees. If confirmed by non-linear analyses, this fact would be comforting, since it would mean that bridges designed disregarding the multi-support excitation (as in the usual practice) would be automatically covered against non-synchronous effects.

For the case of incoherence due to wave-travelling alone (Figure 3.6 and Figure 3.7, bottom), a reduction of the forces in the central pier is observed, whereas the forces acting on the lateral piers are increased with respect to the synchronous case (solid lines). Only when the wave-passage delay becomes large ($v_{app} = 300$ m/s) there is a substantial reduction in the forces for all the piers. In the presence of incoherence due to wave-passage alone, a clear directionality in the response is observed. This phenomenon is already triggered for $v_{app} = 1200$ m/s, that is for trains of waves arriving at two consecutive supports with a time delay of only $4/100$ seconds, and it is due to the fact that the second term in Eq. 3 depends on the sign of the separation distance ξ . Since the first term describing the geometric incoherence effect is independent of the sign of ξ , when it increases the response distribution tends to be more symmetric.

The possibility of coincident resonance, *i.e.* a phase-matching between the excitation wave and the natural wave in the structure (Lin et al. 1990), was not

investigated, because this phenomenon occurs only for the case of wave-travelling incoherence, and it is beyond doubt that in many situations geometric incoherence is a more credible source of uncorrelation than that due to deterministic wave-travelling.

A confirmation of this and of what already observed in Figure 3.5, is that the response to multi-support excitation is not significantly influenced by the wave-passage effect when high geometric incoherence (low values of v_s/α) is present: the left-side diagrams in Figure 3.6 and Figure 3.7, top and middle, show essentially the same force distributions for different values of v_{app} . As already remarked in the comments to Eq. 3, this is mainly due to the fact that the term containing v_s/α in the coherence function is squared.

In comparing the left-side diagrams (total shear forces) with the right-side ones (pseudo-static shear forces) a first obvious observation is that in the cases of synchronous or nearly synchronous seismic motion the contribution of the pseudo-static component (right side diagrams in Figure 3.6 and Figure 3.7, bottom) is zero or negligible, since synchronous seismic input by definition does not introduce distortions in the piers.

It is seen that the contribution of the pseudo-static component to the total shear force becomes more and more significant as the geometric incoherence increases. For the lowest value considered of $v_s/\alpha = 300$ m/s (Figure 3.6 and Figure 3.7, top) the pseudo-static forces are about 50-80% of the total forces for the mid pier and about 80-100% for the lateral piers. In these cases, *i.e.* when the geometric incoherence is high, the effect of the other component is almost negligible. On the other hand, when the wave-passage delay only is present (Figure 3.6 and Figure 3.7, bottom), its effect remains very low for $v_{app} = 1200$ m/s (less than 1% for the mid pier) and low up to $v_{app} = 600$ m/s (25-50% for the mid pier).

An unexpected behavior occurs for $v_{app} = 300$ m/s, where the pseudo-static component is greater than the total shear force (about 200% for the lateral piers). In these latter cases the contribution of the dynamic forces reduces the effect of the distortions introduced in the structure by the non-synchronous soil displacements. This fact is physically explainable, since the maxima of the two components do not necessarily occur in phase.

As a final remark, for low values of the geometric incoherence (*e.g.* for $v_s/\alpha = \infty$ m/s, Figure 3.6 and Figure 3.7, bottom) the wave-passage delay tends to decrease the total shear forces on the piers, while it tends to increase the pseudo-static components. The opposite occurs for high values of the geometric incoherence (*e.g.* for $v_s/\alpha = 300$ m/s, Figure 3.6 and Figure 3.7, top).

3.1.2.3 Non linear response of bridges to multi-support excitation

Non linear analyses of bridges designed either accounting for multi-support excitation or neglecting it have been carried out under the same ground motion histories used for non-synchronous design, with $PGA = 0.42g$. The results are presented in the following.

3.1.2.4 Bridges with non-synchronous design

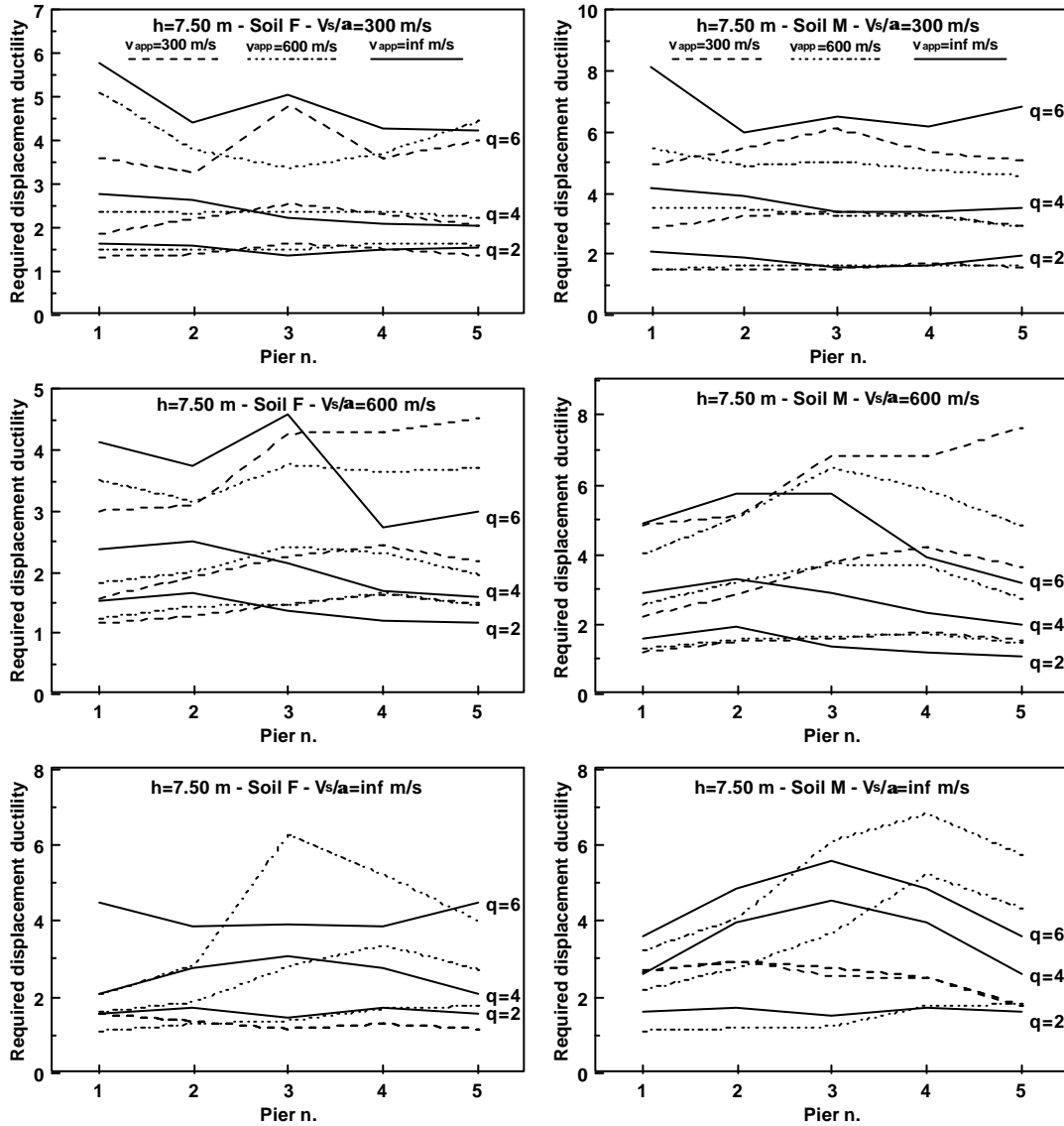


Figure 3.8. Bridge $H=7.5$ m on soil F and M. Required ductility for $v_s/\alpha = 300$ m/s (top), $v_s/\alpha = 600$ m/s (middle) and $v_s/\alpha = \infty$ m/s (bottom).

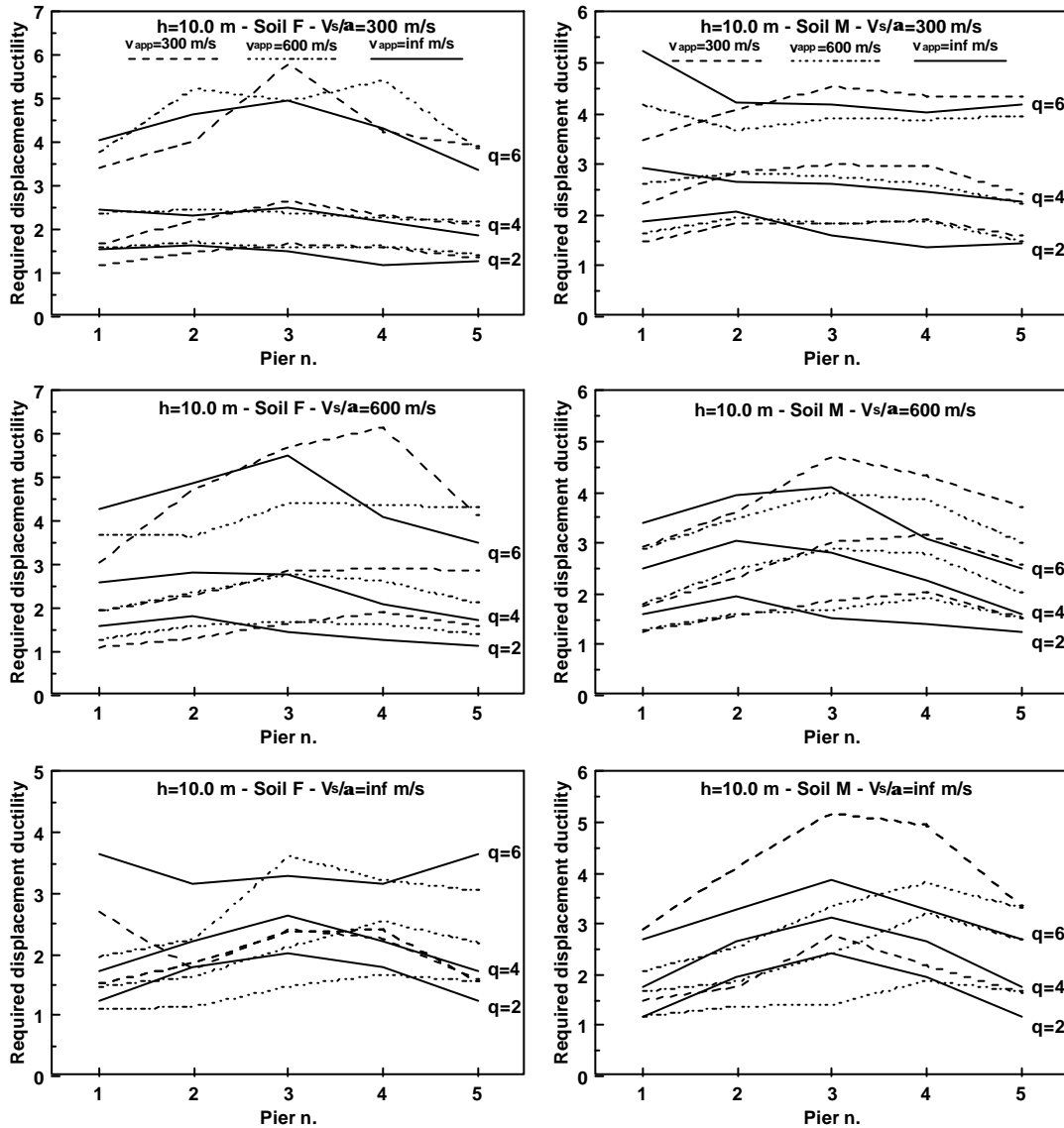


Figure 3.9. Bridge $H=10.0$ m on soil F and M. Required ductility for $v_s/\alpha = 300$ m/s (top), $v_s/\alpha = 600$ m/s (middle) and $v_s/\alpha = \infty$ m/s (bottom).

In Figure 3.8 and Figure 3.9 the results are presented in terms of required displacement ductility for the bridges with $H = 7.5$ and 10.0 m only, on soil types F and M with values $v_s/\alpha = 300, 600$ and ∞ m/s for the geometric incoherence term. In each diagram, for each value of the structure behavior factor $q = 2, 4$ and 6 adopted in the design, three curves obtained for $v_{app} = 300, 600$ and ∞ m/s (the wave-passage effect) are represented. For the sake of clarity, the curves relative to $v_{app} = 1200$ m/s are not represented.

As a general comment, one has to observe that the correlation between q -factors and requested ductility is reasonably good, at least for the central piers.

A first important point to note is that bridges designed for multi-support excitation show relatively uniform displacement ductility demands to the different piers, at least for the lower two values of q . This is not exactly what inelastic analyses usually reveal for bridges designed with a rigid base motion, and this can be checked for in Figure 3.8 and Figure 3.9, bottom, where the solid lines represent the bridges designed for synchronous input.

A second point of systematic nature that goes together with the one previously mentioned is a noticeable trend to increase the ductility demand in the lateral piers with increasing uncorrelation of the motions, especially when this is of the geometric type and for higher values of the q -factor. To check this, compare for example the top Figures with the bottom ones in Figure 3.8 and Figure 3.9. On the other hand, when the geometric uncorrelation is high, in most cases the contribution to the ductility demand of the other source is almost negligible, a fact which was already noted in terms of forces in the linear case.

This result can be explained by looking at the diagrams obtained from the linear analyses shown in the preceding paragraph, where the pseudo-static component of the shear force is compared to the total shear force acting on the piers. In case of high geometric incoherence, the shear forces on the piers are primarily due to the motions at the supports, which are imposed pseudo-statically, while the dynamic response component is very low. Thus, the design forces result to a large extent from the pseudo-static forces, deriving from a ground motion affected by the q -factor. When analyzing the bridge in the non-linear field, the pseudo-static displacements imposed at the supports are q times those adopted in the design and therefore they produce a request of ductility in the piers which is very close to q . The remaining part of the displacement of the piers derives from the dynamic response of the bridge. For low that this latter can be, the required ductility can only further increase. For example, in the bridge with $H = 75$ m on soil M and $v_s/\alpha = 300$ m/s the required displacement ductility in the piers designed with $q=2, 4, \text{ and } 6$ is about 2, 4 and 7, respectively.

When the pseudo-static component is only a small part of the total force (cases with $v_s/\alpha = \infty$, Figure 3.8 and Figure 3.9, bottom), the request of ductility depends on the dynamic response of the bridge which is obviously conditioned by its geometrical and mechanical characteristics. For the cases considered in this study, the effect of v_{app} becomes significant as soon as it takes on lower values ($v_{app} = 1200$ (not shown) and 600 m/s), in which cases it is also accompanied by the already noted directionality effect. This effect tends systematically to extract a larger amount of ductility from the last encountered piers.

In concluding this section, it appears that the q -factor approach can be extended to non-synchronous design, with a degree of accuracy which is often better than for synchronous design. More explicitly, it has been found that bridges designed elastically for a non-synchronous input of *given* stochastic properties and affected by

a q -factor, if analyzed inelastically for the *same* non-synchronous motion with $q = 1$, exhibit displacement ductility demands which are in good accordance with the selected value of q . It has been shown that this depends on the notable reduction of the dynamic response component with respect to the pseudostatic one.

3.1.2.5 Bridges with synchronous design

This section tries to provide an answer to the following question: what happens to bridges designed for a rigid input motion in case they are subjected to motions having the same frequency content but varying types and amounts of correlation between the support points?

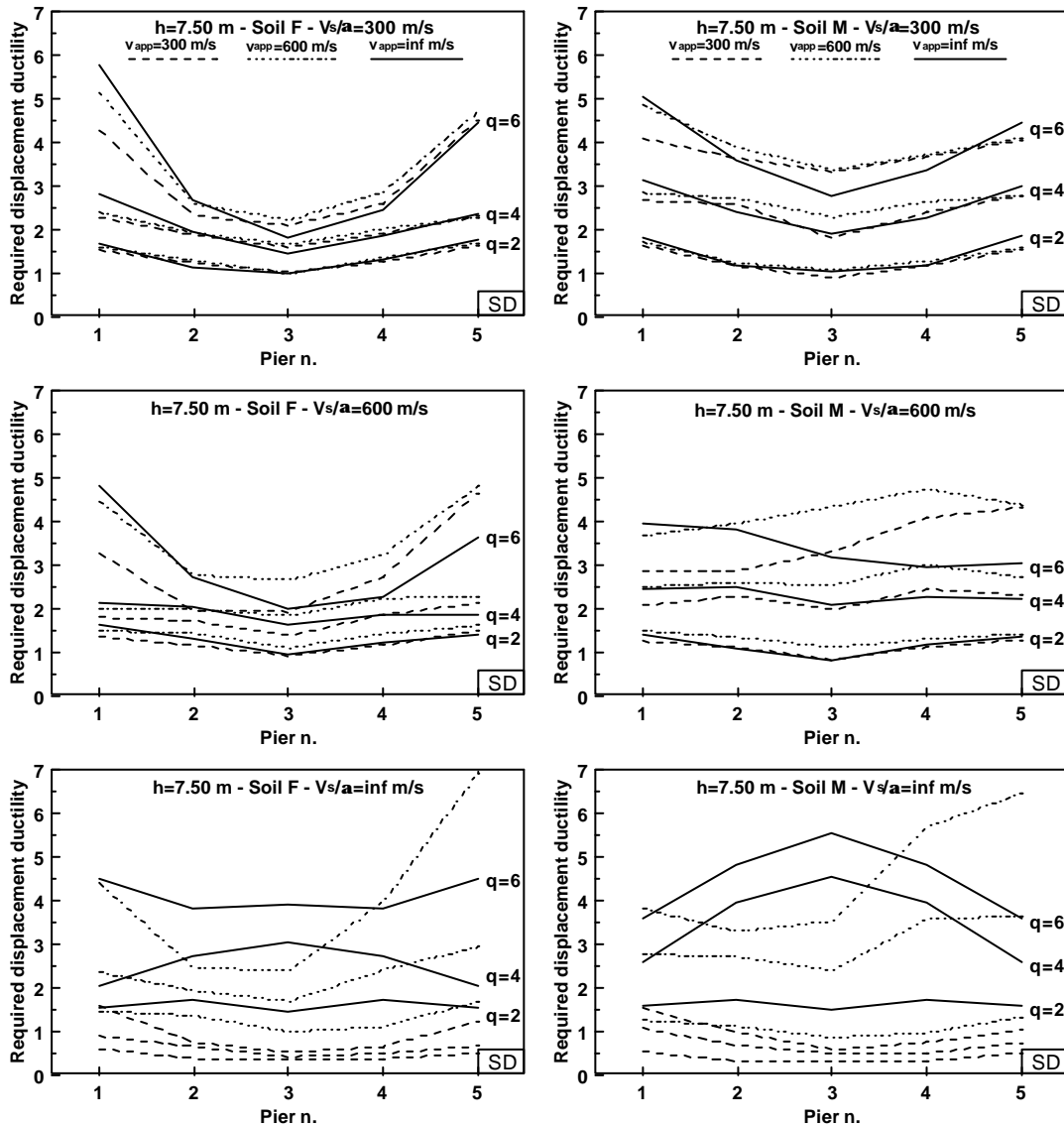


Figure 3.10. Bridge $H=7.5$ m on soil F and M. Synchronous Design (SD). Required ductility for $v_s/\alpha = 300$ m/s (top), $v_s/\alpha = 600$ m/s (middle), and $v_s/\alpha = \infty$ m/s (bottom).

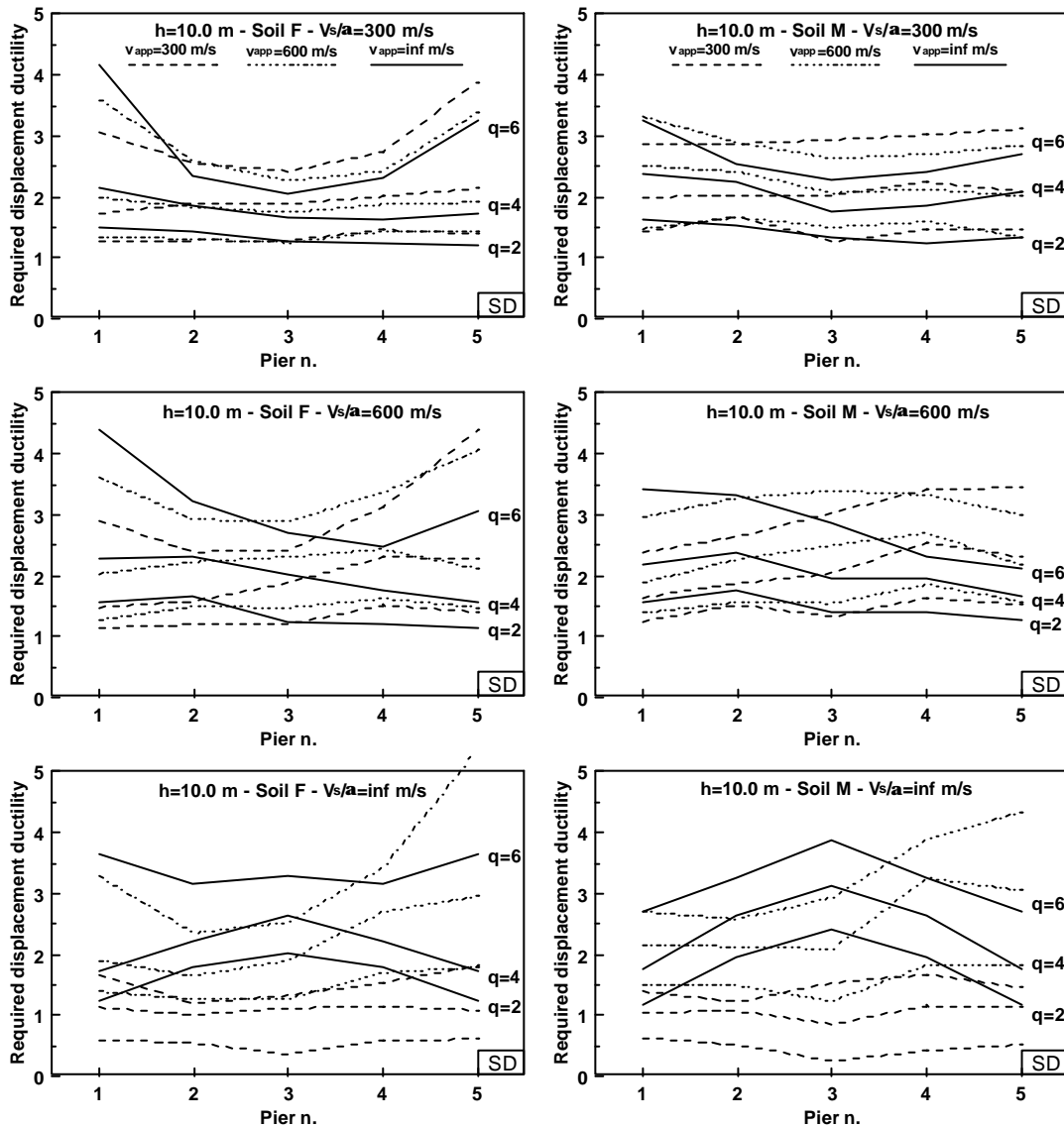


Figure 3.11. Bridge $H=10.0$ m on soil F and M. Synchronous Design (SD). Required ductility for $v_s/\alpha = 300$ m/s (top), $v_s/\alpha = 600$ m/s (middle), and $v_s/\alpha = \infty$ m/s (bottom).

As in the previous section, the results are presented in terms of required displacement ductility. The results of bridges with $H=7.5$ and 10.0 m only are presented, on soil types F and M with values $v_s/\alpha = 300, 600$ and ∞ m/s for the geometric incoherence term. In each diagram, for each value of the behavior factor $q = 2, 4$ and 6 adopted in the design, three curves obtained for $v_{app} = 300, 600$ and ∞ m/s (the wave-passage effect) are represented. Also in this case, for the sake of clarity, the curves relative to $v_{app} = 1200$ m/s are not represented.

We first comment on the top Figure 3.10 and Figure 3.11, *i.e.*, the ones containing the cases of largest geometric uncorrelation. We know from the previous section that the response is due mainly, when not exclusively, to the imposed pseudo-static differential displacements at the piers bases. Wave propagation effects are irrelevant in this case. The results in Figure 3.10 and Figure 3.11, top, come to no surprise: in the rigid base design the lateral piers are subjected to lower forces than the central ones, and are consequently weaker. Since the soil displacements are such as to impose almost equal distortions to all piers, the weakest ones are called to greater ductility demands. This leads to the situation illustrated in the Figure 3.10 and Figure 3.11, top, where the central piers have ductilities of about half of q , while for the lateral ones the values are close to q .

The second extreme situation is when geometric incoherence is absent and the lack of correlation is only due to wave propagation (see Figure 3.10 and Figure 3.11, bottom). In this case we observe, as in the previous section, a significant sensitivity of the results to the parameter v_{app} , for a given value of q .

Overall, however, in almost all cases the presence of a certain amount of incoherence acts towards reducing the ductility demand in the central piers and increasing that in the lateral ones, with respect to the limit case of synchronous motion. This fact is significantly corroborated for the higher values of q . In any case, the values of the requested ductilities are still quite close to the selected values of q .

In concluding this section it appears that designing for a rigid motion provides the bridge with a higher global strength than for a non-synchronous motion. The request of ductility is not as uniform among the various piers as observed for the bridges designed for multi-support excitation, but the values are well below the selected q -factors, with the only exception of a few sporadic cases. This amount of strength is enough to cope with the possibility of receiving a non-synchronous motion. The only exception has been observed for the lateral piers in the bridge with $H=7.5$ m, for which the rigid base assumption adopted in the design leads to a request of ductility close to the q -factor.

3.1.2.6 Conclusions regarding conventional bridges

The essential facts emerging from the study are easier to express than it might be supposed from the multiplicity of different cases that have been examined in the previous sections. It all descends from the model that has been assumed for describing spatial variability. In this model, the power density correlation function is the product of two terms. The first one, which rests on qualitative physical bases, uncorrelates the motions at different points exponentially with the product: $\omega d_{ij} / \sqrt{G/\rho}$, where G and ρ are the shear modulus and the density of the soil, respectively. The second one represents the correlation between two generic points simply due to a time lag d_{ij}/v_{app} in the arrival of the waves.

Once v_{app} fixed, samples taken from the stochastic field represented by the second term only would be trains of waves travelling with the same speed and

differing from one to another by random phase angles only. Roughly speaking, the second term has somewhat the nature of a deterministic model, whose effects on a given bridge structure can, at least qualitatively, be anticipated. Incidentally, it is the only term usually considered in the design of pipelines. The first one, on the contrary, is of purely stochastic nature: when $\omega d_{ij} / \sqrt{G/\rho}$ takes on large values the motions at two points become statistically uncorrelated (and, given the implicit assumption of gaussianity, also independent), so that at a given instant in time the two motions might hypothetically be the same but opposite in sign.

Adhering to the recommendations contained in several modern bridge codes, to consider spatial variability of ground motions in the case of long bridges, three representative bridge models have been selected and designed for spatial variability, assuming a variety of combinations for the absolute and relative importance of the two terms of the coherence function, for a total of 216 cases. The designs have been made elastically, for different values of the q -factor.

The first question a bridge designer would probably like to ask is whether accounting for spatial variability leads to larger amounts of reinforcement, for a given value of q , than what one would obtain by ignoring it. The analyses made allow to answer to this question both in global terms as well as with more articulate distinctions. In global terms, it has been found that incoherent motions lead to a decrease of the design forces, hence to lower amounts of reinforcements, with respect to the synchronous ones. This result admits no exceptions, for the cases considered.

Obviously, the amount of the decrease is very variable, depending on the particular combination of the parameters and, given these latter, it varies from pier to pier, with a systematic trend to be larger for the central piers and practically nihil for the lateral ones.

In more detailed terms, it is of interest to discern the role played by each of the two components of the coherence function. When the motions (accelerations) input to the supports are (almost) independent (*i.e.* the first term is dominant), the net dynamic excitation tends to zero. In this case the response becomes of purely static nature, and it is due to the differential displacements of the ground at the supports. Since the motions are already uncorrelated, the effects of the second term are negligible, whatever its value may be. The amplitude of the differential displacements and, hence, of the forces induced in a given structure, is directly related to the assumed shape of the power density spectrum of the ground motion.

When the first source of incoherence is absent, on the other hand, the degree of uncorrelation produced by wave travelling is rather limited, for the range of apparent velocities one would consider more frequently (say, in excess of 500 m/s), and the effect on the response consists essentially in a reduction of the dynamic part due to the incomplete synchronism of the excitation. It requires to have very low values of v_{app} in order to start seeing significant effects of relative displacements between the supports, but in this case we assist also to a significant reduction of the dynamic contribution to the response.

After having looked into the nature of the effects of spatial variability, and having designed a number of bridges for these effects, it is all too natural to check whether the inelastic response is consistent with the expectation that ductility demands are of the same order of the q -values used for the design.

Here again there could be an answer in global terms, that would be outright positive, even more favorable than what one is accustomed to accept in the case of rigid motion design, and one with finer distinctions. To limit these latter to the essential, one might say that the ductility demand gets closer to q when the uncorrelation of the motions due to the first term increases. There is a simple physical explanation for that, not worth to be repeated here, especially since beyond this due verification of the validity of the q -factor approach for non-synchronous excitation there is still a major issue ahead to be discussed.

At the design stage, the quantification of the spatial variability cannot be but affected by a large degree of uncertainty. It is true that uncertainty is also large in the prediction of the local frequency content of the motion, but this aspect is covered in most cases by the codes, which in turn rely on large amounts of statistical information, so that the spectral shapes can be reasonably accepted as conservative estimates of “uniform risk” functionals. On the other hand, no “envelope” concepts can be applied to the quantification of the degree of correlation: at most one might consider upper and lower estimates. But the chances that the future earthquakes will be characterized by the amount and type of correlation assumed in design are really slight. In the light of this basic uncertainty, what is the appropriate procedure for ensuring an adequate degree of reliability to the design?

Excluding any attempt to sophisticated approaches, whose reaches in this specific case appear as limited, the problem has been posed in the following terms. Since it would not be sensible to design for spatial variability and then to check the design for the case of a synchronous earthquake, which is clearly an abstraction, the reverse has been made, *i.e.*, to design for the abstraction, which means following consolidated practice, and then see if and how large inadequacies of under- or over-design this practice involves.

The results of this last part of the study have been illustrated and commented in the appropriate section. They are summarized again since they might be assumed as the conclusion of the whole study: designing for a rigid motion provides a global upper bound of the response and therefore a globally conservative design. There is difference, however, between the rigid and non-rigid design in how the strengths are distributed among the different elements. In the rigid case, the distribution follows essentially the shape of the dominant mode, while in the other one, the strength requirements tend to be uniform.

It is difficult at this point to resist the temptation of offering some practical suggestion, even if this is beyond the intentions and especially the reach of the study performed. The fact could be noted, however, that the higher the selected q -factor, the larger the difference between the requested ductility in the lateral and the central piers, when uncorrelation of motion is present. In those cases, in order to obtain a uniform request of ductility in all the piers, it would be beneficial to halve the design

forces in the central piers, which always show a ductility request of about $0.5q$ under multi-support excitation.

It is understood that the results obtained in this study are strictly dependent on the extremely regular bridge configuration examined and on the model describing the spatial variability of the seismic motion. Additional investigations are needed to study the response of irregular bridges with piers of different heights under non-synchronous seismic action modeled with different coherence functions.

3.1.3 Isolated bridges

For the case of isolated bridges, present design practice is based on a linear analysis, where the protection offered by the non-linear behavior of the isolators is globally accounted for by means of a simple factor. In principle, there is no evidence that this approach may extend its validity to non-synchronous situations, or at least not with the same protection factors. Thus, the purpose of this section is to make a further step into this question: the relevance of non-rigid input motion on the inelastic response of isolated bridge structures, and the extent of validity of the “protection factor” approach.

A parametric analysis has been conducted of a bridge with 6 spans, of 50 m length each and piers 10 m tall, same as that analyzed in section 3.1.2 and represented in Figure 3.4, but in this case it is equipped with isolators that are designed according to common design practice. The bridge is subsequently analyzed under different multi-support excitation conditions. The method employed is that of a stationary random vibration analysis where the non-linear isolators are linearized with Kelvin elements, having effective stiffness and equivalent damping determined through an equivalence equation. To this purpose, the accuracy of three different equations is evaluated.

The soil motion is represented through a second moment random field fully characterized by (equal or different) power spectral densities at each station and by a coherence spectrum, assumed to depend on three different sources of incoherence. All the parameters controlling the loss of coherence have been made to vary between their respective extremes, as done in section 3.1.2 and reported in Table 3.1.

3.1.3.1 Bridge model and equivalent stiffness and damping ratio of the isolator

The bridge is modeled as an elastic system, where both the piers and the isolators are considered as elastic. As regards the piers, this assumption is valid if the adopted procedure for the design of the isolators is such to maintain them in the elastic range, whereas the isolators, which of course enter well into the inelastic range, are represented through equivalent linear elements whose hysteretic damping is condensed into a viscous damping ratio. Both these quantities can be expressed as function of the required ductility.

The equivalent stiffness $k_{eq,j}$ and the damping ratio $\xi_{eq,j}$ of the $j = 1 \dots N$ isolators, equivalent to their hysteretic dissipation can be evaluated according to

different criteria. Three are selected in this work, based on k_E = isolator elastic stiffness and α = isolator hardening ratio:

a) the first one is that adopted in AASHTO (Guide specification 1991)

$$k_{eq,j} = k_E \frac{1 + \alpha(\mu_j - 1)}{\mu_j} \quad \xi_{eq,j} = \frac{2(1 - \alpha)(\mu_j - 1)}{\pi \mu_j [1 + \alpha(\mu_j - 1)]} \quad (42)$$

b) the second one is that presented in (Hwang et al. 1995)

$$k_{eq,j} = k_E \frac{1 + \alpha(\mu_j - 1)}{\mu_j} \left(1 - 0.737 \frac{\mu_j - 1}{\mu_j^2} \right)^{-2} \quad \xi_{eq,j} = \frac{2(1 - \alpha)(\mu_j - 1)}{\pi \mu_j [1 + \alpha(\mu_j - 1)]} \frac{\mu_j^{0.58}}{6 - 10\alpha} \quad (43)$$

c) the third one is that presented in (Hwang et al. 1994)

$$k_{eq,j} = k_E \left\{ 1 + \ln \left[1 + 0.13(\mu_j - 1)^{1.137} \right] \right\}^{-2} \quad \xi_{eq,j} = 0.0587(\mu_j - 1)^{0.371} \quad (44)$$

On passing, it should be observed that the first of the above equations is obtained through simple geometrical considerations, while the other two have been calibrated on the response of sdof oscillators: in particular, the second one is just a correction of the first one in order to maximize the accuracy in predicting the inelastic maximum response of bi-linear elastic bearings, while the third one is based on the optimal prediction of the period shift of a base-isolated regular bridge.

Note that the purpose of the equivalence is to substitute the hysteretic isolators with equivalent Kelvin elements. A Kelvin element, a linear spring in parallel with a pure viscous damper, satisfies the following equation:

$$f_j = k_{eq,j} y + c_{0j} \dot{y} \quad (45)$$

which can be transformed in the frequency domain as follows:

$$f_j(i\omega) = (k_{eq,j} + ic_{0j}\omega) y(i\omega) \quad (46)$$

Its transfer function from deformation y to force f is therefore:

$$H_j(i\omega) = k_{eq,j} + ic_{0j}\omega = k_{eq,j} + i2\xi_{eq,j}k_{eq,j} \quad (47)$$

where the real and the imaginary parts are the non-negative real-valued storage and loss moduli, respectively. This representation will be used in the following developments.

3.1.3.2 Equations of motion of the bridge

The equation of motions for the deck (subscript D) masses and the pier (subscript P) masses with the interposed isolators (subscript I) are, respectively:

$$\begin{aligned} \mathbf{M}_D(\ddot{\mathbf{X}}_P + \ddot{\mathbf{X}}_I + \ddot{\mathbf{U}}) + \mathbf{C}_D(\dot{\mathbf{X}}_P + \dot{\mathbf{X}}_I + \dot{\mathbf{U}}) + \mathbf{K}_D(\mathbf{X}_P + \mathbf{X}_I + \mathbf{U}) + \mathbf{C}_I(\dot{\mathbf{X}}_I) + \mathbf{K}_I(\mathbf{X}_I) &= \mathbf{0} \\ \mathbf{M}_P(\ddot{\mathbf{X}}_P + \ddot{\mathbf{U}}) + \mathbf{C}_P(\dot{\mathbf{X}}_P) + \mathbf{K}_P(\mathbf{X}_P) - \mathbf{C}_I(\dot{\mathbf{X}}_I) - \mathbf{K}_I(\mathbf{X}_I) &= \mathbf{0} \end{aligned} \quad (48)$$

where $\mathbf{K}_I = \text{diag}_j(k_{eq,j})$. Eq. (48) can be written in matrix form as:

$$\begin{bmatrix} \mathbf{M}_D & \mathbf{M}_D \\ \mathbf{0} & \mathbf{M}_P \end{bmatrix} \cdot \begin{Bmatrix} \ddot{\mathbf{X}}_I \\ \ddot{\mathbf{X}}_P \end{Bmatrix} + \begin{bmatrix} \mathbf{C}_D + \mathbf{C}_I & \mathbf{C}_D \\ -\mathbf{C}_I & \mathbf{C}_P \end{bmatrix} \cdot \begin{Bmatrix} \dot{\mathbf{X}}_I \\ \dot{\mathbf{X}}_P \end{Bmatrix} + \begin{bmatrix} \mathbf{K}_D + \mathbf{K}_I & \mathbf{K}_D \\ -\mathbf{K}_I & \mathbf{K}_P \end{bmatrix} \cdot \begin{Bmatrix} \mathbf{X}_I \\ \mathbf{X}_P \end{Bmatrix} = \begin{bmatrix} \mathbf{M}_D & \mathbf{C}_D & \mathbf{K}_D \\ \mathbf{M}_P & \mathbf{0} & \mathbf{0} \end{bmatrix} \cdot \begin{Bmatrix} \ddot{\mathbf{U}} \\ \dot{\mathbf{U}} \\ \mathbf{U} \end{Bmatrix} \quad (49)$$

If it is assumed that: a) the contribution to the overall damping given by $\mathbf{C}_D \cdot \dot{\mathbf{X}}_I$, $\mathbf{C}_D \cdot \dot{\mathbf{X}}_P$ and $\mathbf{C}_P \cdot \dot{\mathbf{X}}_P$ is negligible with respect to that of the isolators $\mathbf{C}_I \cdot \dot{\mathbf{X}}_I$; b) $\mathbf{C}_D \cdot \dot{\mathbf{U}}$ can be neglected with respect to the other quantities on the left-hand side of the equation. Thus, the resulting equations are:

$$\begin{bmatrix} \mathbf{M}_D & \mathbf{M}_D \\ \mathbf{0} & \mathbf{M}_P \end{bmatrix} \cdot \begin{Bmatrix} \ddot{\mathbf{X}}_I \\ \ddot{\mathbf{X}}_P \end{Bmatrix} + \begin{bmatrix} \mathbf{C}_I & \mathbf{0} \\ -\mathbf{C}_I & \mathbf{0} \end{bmatrix} \cdot \begin{Bmatrix} \dot{\mathbf{X}}_I \\ \dot{\mathbf{X}}_P \end{Bmatrix} + \begin{bmatrix} \mathbf{K}_D + \mathbf{K}_I & \mathbf{K}_D \\ -\mathbf{K}_I & \mathbf{K}_P \end{bmatrix} \cdot \begin{Bmatrix} \mathbf{X}_I \\ \mathbf{X}_P \end{Bmatrix} = \begin{bmatrix} \mathbf{M}_D & \mathbf{K}_D \\ \mathbf{M}_P & \mathbf{0} \end{bmatrix} \cdot \begin{Bmatrix} \ddot{\mathbf{U}} \\ \mathbf{U} \end{Bmatrix} = [\boldsymbol{\mu} \quad \mathbf{k}] \cdot \begin{Bmatrix} \ddot{\mathbf{U}} \\ \mathbf{U} \end{Bmatrix} \quad (50)$$

The advantage of casting the equation in this form, rather than the more classical version in (Clough and Penzien 1975) where a dynamic and a pseudo-static part are separately solved and subsequently added up, stems from the fact that this is computationally of great convenience, since it allows to directly obtain the expression of the PSD matrix of the isolators response, instead of deriving it as PSD of a sum process, where also the cross PSDs between the dynamic and the pseudo-static process must be evaluated.

The whole problem can then be stated as:

$$\mathbf{M} \ddot{\mathbf{X}} + \mathbf{C} \dot{\mathbf{X}} + \mathbf{K} \mathbf{X} = \boldsymbol{\mu} \ddot{\mathbf{U}} + \mathbf{k} \mathbf{U} = \mathbf{F} \quad (51)$$

3.1.3.3 Response of the isolators

Using elementary notions of stationary random vibration theory, the matrix of the response PSD is obtained by filtering the cross-PSD matrix $\mathbf{S}_{FF}(\omega)$ of the action \mathbf{F} with the frequency response matrix $\mathbf{H}_X(i\omega)$ of the system

$$\mathbf{S}_{XX}(\omega) = \mathbf{H}_X(i\omega) \mathbf{S}_{FF}(\omega) \mathbf{H}_X^T(-i\omega) \quad (52)$$

where the first N values on the diagonal are the auto-PSD of the isolators.

The cross-PSD matrix $\mathbf{S}_{FF}(\omega)$ in (52) is obtained from the cross-correlation matrix of the action \mathbf{F} :

$$\mathbf{R}_{FF}(\tau) = \boldsymbol{\mu} \mathbf{R}_{\ddot{U}\ddot{U}} \boldsymbol{\mu}^T + \mathbf{k} \mathbf{R}_{UU} \mathbf{k}^T + \boldsymbol{\mu} \mathbf{R}_{\ddot{U}U} \mathbf{k}^T + \mathbf{k} \mathbf{R}_{U\ddot{U}} \boldsymbol{\mu}^T \quad (53)$$

which is then Fourier-transformed into the cross-PSD matrix

$$\begin{aligned}\mathbf{S}_{FF}(\omega) &= \boldsymbol{\mu} \mathbf{S}_{\ddot{U}\ddot{U}} \boldsymbol{\mu}^T + \mathbf{k} \mathbf{S}_{UU} \mathbf{k}^T + \boldsymbol{\mu} \mathbf{S}_{\ddot{U}U} \mathbf{k}^T + \mathbf{k} \mathbf{S}_{U\ddot{U}} \boldsymbol{\mu}^T \\ &= \boldsymbol{\mu} \mathbf{S}_{\ddot{U}\ddot{U}} \boldsymbol{\mu}^T + \frac{1}{\omega^4} \mathbf{k} \mathbf{S}_{\ddot{U}\ddot{U}} \mathbf{k}^T + \frac{1}{\omega^2} (\boldsymbol{\mu} \mathbf{S}_{\ddot{U}\ddot{U}} \mathbf{k}^T + \mathbf{k} \mathbf{S}_{U\ddot{U}} \boldsymbol{\mu}^T)\end{aligned}\quad (54)$$

(where in the above equation the relation $S_{U\circ} = S_{\ddot{U}\circ}/\omega^2$ has been used).

The frequency response matrix $\mathbf{H}_X(i\omega)$ in (52) can be obtained from the modal frequency response (diagonal) matrix

$$\mathbf{H}_Z(i\omega) = \text{diag}_k \left[\left(\hat{\omega}_k^2 - \omega^2 + 2i\xi_k \hat{\omega}_k \omega \right)^{-1} \right] \quad (55)$$

where $\hat{\omega}_k$ is the circular frequency of the k -th mode and ξ_k the associated modal damping. The frequency response matrix $\mathbf{H}_Z(i\omega)$ is transformed into the frequency response matrix $\mathbf{H}_X(i\omega)$ through the eigenmatrices of the system (51), which implies that an eigenproblem has to be solved.

Before solving the eigenproblem, it should be noticed that the matrices \mathbf{M} and \mathbf{K} in (51) are non-symmetrical. In this case, it is convenient to cast the equation in the following form:

$$\ddot{\mathbf{X}} + \mathbf{M}^{-1} \mathbf{C} \dot{\mathbf{X}} + \mathbf{M}^{-1} \mathbf{K} \mathbf{X} = \mathbf{M}^{-1} \mathbf{F} \quad (56)$$

Thus, modal decomposition can be performed of the (assumed classically damped) eigenproblem

$$\mathbf{M}^{-1} \mathbf{K} \mathbf{F} = \mathbf{F} \mathbf{L} \quad (57)$$

whose solution is the eigenvalues matrix $\mathbf{L} = \text{diag}_k(\hat{\omega}_k^2)$ and the couple of eigenmatrices: the right-hand eigenmatrix \mathbf{F} , and the left-hand eigenmatrix \mathbf{F}_L , for which the following relation holds: $\mathbf{F}_L^T = \mathbf{F}^{-1}$.

3.1.3.4 Treatment of damping

The equations of motion can be uncoupled by writing $\mathbf{X} = \mathbf{F} \mathbf{Z}$

$$\ddot{\mathbf{Z}} + \mathbf{F}^{-1} \mathbf{M}^{-1} \mathbf{C} \mathbf{F} \dot{\mathbf{Z}} + \mathbf{F}^{-1} \mathbf{M}^{-1} \mathbf{K} \mathbf{F} \mathbf{Z} = \mathbf{F}^{-1} \mathbf{M}^{-1} (\boldsymbol{\mu} \ddot{\mathbf{U}} + \mathbf{k} \mathbf{U}) = \mathbf{Y} \quad (58)$$

where it is noted that the modal damping matrix $\hat{\mathbf{C}} = \mathbf{F}^{-1} \mathbf{M}^{-1} \mathbf{C} \mathbf{F} = \overline{\mathbf{F}}_L^T \mathbf{C} \mathbf{F}$ (where $\overline{\mathbf{F}}_L^T = \mathbf{F}^{-1} \mathbf{M}^{-1} = \mathbf{F}_L^T \mathbf{M}^{-1}$ is the mass-normalized left-hand eigenmatrix) is not diagonal, therefore the equations are not completely uncoupled. An analysis of the error resulting from neglecting the off-diagonal terms can be found in (Veletsos and Ventura 1986) where it is shown that for modal damping ratios lower than 30% the error is acceptable, if not negligible.

Under this consideration, the modal damping ratios are obtained as

$$\xi_k = \frac{1}{2\hat{\omega}_k} \text{diag}_k \left[\mathbf{F}^{-1} \mathbf{M}^{-1} \mathbf{C}(\hat{\omega}_k) \mathbf{F} \right] = \frac{1}{2\hat{\omega}_k} \text{diag}_k \left[\bar{\mathbf{F}}_L^T \mathbf{C}(\hat{\omega}_k) \mathbf{F} \right] \quad (59)$$

where the damping matrix $\mathbf{C}(\hat{\omega}_k)$ is built for each eigenvalue as follows (Zambrano *et al.* 1996):

$$\mathbf{C}(\hat{\omega}_k) = \text{diag}_j \left(\frac{\text{Im}(H_j)}{\hat{\omega}_k} \right) = \text{diag}_j \left(\frac{2\xi_{eq,j} k_{eq,j}}{\hat{\omega}_k} \right) \quad (60)$$

where the numerator is the imaginary part of the transfer function (47) of the j -th isolator.

With the values of the modal damping ratios in (59) the modal frequency response matrix $\mathbf{H}_Z(i\omega)$ in (55) can be built and then transformed into the frequency response matrix $\mathbf{H}_X(i\omega)$

$$\mathbf{H}_X(i\omega) = \mathbf{F} \mathbf{H}_Z(i\omega) \bar{\mathbf{F}}_L^T \quad (61)$$

This expression, along with that of the cross-PSD of the action in (54), can be inserted into (52) to get the PSD matrix of the response.

3.1.3.5 Iterative procedure

The response of the bridge depends on the isolator stiffness and damping. Since this is evaluated with either (42) or (43) or (44) as function of the ductility required to the isolators, which in turn depends on the isolators characteristics, an iterative procedure must be followed. This can be summarized as follows:

- 1) Guess value for the required ductility μ_j in all $j=1 \dots N$ isolators along the bridge (usually, $\mu_j=1$)
- 2) Calculate the vector of the variances of the response of each isolator through (52) (that is, only the first N values on the diagonal need to be evaluated, since they are the auto-PSD of the isolators)

$$\sigma_{iso,k}^2 = \text{Var}[X_{iso,k}] = \int_{-\infty}^{\infty} S_{X_k X_k}(\omega) d\omega \quad k = 1 \dots N \quad (62)$$

- 3) Update the vector of the required ductility in each isolator

$$\mu_k = \frac{p \cdot \sigma_{iso,k}}{X_{y,k}} \quad k = 1 \dots N \quad (63)$$

where p is a peak factor taken as 2.5.

- 4) Compare the ductilities with the current value: if convergence is attained then exit, else repeat procedure with the new estimate of ductilities.

3.1.3.6 Design of the isolated bridge

The bridge under consideration is represented in Figure 3.4 (in this case the hinges on top of the piers are replaced by isolators), purposely selected equal to that extensively studied in section 3.1.2. The piers height has been taken $H = 10$ m. The deck, transversely supported by isolators to the piers and the abutments, has a dead load of 200 kN/m. The piers (acting as cantilevers) are considered as fixed on the soil. All analyses of the bridge have been performed in the transverse direction.

The isolated bridge has been designed elastically for the transverse direction only, under synchronous ground motion ($v_s/\alpha = \infty$ and $v_{app} = \infty$) which corresponds to the usual design assumption adopted in engineering practice.

In the elastic analyses performed to design the bridges, the cracked stiffness of the piers has been used, obtained from the uncracked stiffness (gross section) divided by a factor 2.5. The following material strengths have been used: for concrete $f_c = 35,000$ kPa, for steel $f_y = 440,000$ kPa, with ultimate strains equal to $\varepsilon_{cu} = 0.008$ and $\varepsilon_{su} = 0.10$, respectively. Material design factors were: 1.5 for concrete and 1.15 for steel.

The design has been made for the average of the maximum values of the response (force at the pier top) obtained using ten sets of accelerograms scaled to a PGA of 0.42 g. A protection level equal to $\mu = 4.2$, which correspond to the design PGA = 0.10 g, was considered. For the design phase, the deck was considered as rigid, hinged on the piers and supported by rollers on the abutments.

The design criterion aimed at equally sharing the total shear force among all the elements (piers and abutments), which basically imply that the same isolators are used on all the piers and abutments and that all the piers have the same strength.

The design of the isolators is performed according to:

$$F_{Y,iso} = \frac{F_{D,max}}{\mu} \quad (64)$$

where $F_{Y,iso}$ is the isolator yield strength, $F_{D,max}$ is the maximum force (average on 10 analyses) transmitted from the deck to the pier below, and μ is the reduction factor of this force. The isolator stiffness is obtained as: $K_I = 150 \cdot F_Y$, which basically assures that the isolator yield displacement is always equal to 6 mm. The isolator hardening ratio b was selected as $b = \bar{b}$ such that the hardening ratio of the pier-isolator system be equal to $b_{tot} = 0.10$. The value of \bar{b} is easily obtained from

$$\bar{b} = b_{tot} \left(\frac{1}{K_p} + \frac{1}{K_I} \right)^{-1} \cdot \frac{1}{K_I} \quad (65)$$

where K_p is the stiffness of the pier considered as a cantilever. In the bridge examined, the isolators hardening ratio turned out to be: $\bar{b} \approx 0.03$.

The piers, of height H , are designed to satisfy the following inequality

$$M_u \geq H \cdot (F_{Y,iso} + F_{P,max} + c \cdot N_D + N_T \cdot \Delta_{max}) \cdot \gamma_o \quad (66)$$

where M_u is the resisting moment of the section at the pier base, $F_{P,max}$ is the base shear due to the mass of the pier itself and of the pier top (which are under the isolator), c is a friction coefficient, taken equal to 0.03 (teflon bearings assumed), N_D is the load applied on the isolator by the supported deck, N_T is the total load (deck+pier) considered lumped at the pier top, Δ_{max} is the maximum displacement (average on 10 analyses) at the pier top and $\gamma_o = 1.2$ is an overstrength factor recovering the uncertainties in the evaluation of $F_{Y,iso}$, c and Δ_{max} . The reinforcement ratio in all piers resulted equal to 2.07%. Such conservative design procedure ensures that all the piers remain in the elastic range.

3.1.3.7 Results of the analyses

The bridge in Figure 3.4, whose isolators were designed with the above described procedure, was analyzed through stationary random vibration analysis to assess the effect of fully incoherent ground motion on the isolators response. In the linear bridge model, all isolators are substituted with equivalent Kelvin elements, with stiffness and damping proportional to the required ductility.

It is known, (see for ex., Clough and Penzien 1975), that the response of an elastic structure subjected to non-synchronous input can be obtained from the superposition of two contributions: a *dynamic* component induced by the inertia forces and a so-called *pseudo-static* component, due to the differences in the support displacements. These latter can induce significant distortions in the structure thus modifying the internal forces with respect to the case of synchronous input. The two components can be represented at each time step by means of two values: the mean ground displacement under the supports, which corresponds to a rigid body motion of the structure and can be partly identified with the dynamic component, and the ground displacements standard deviation, which can be considered as representative of the pseudo-static distortion imposed to the structure. The ground displacements for the three types of soils can be evaluated through (24) and considering that all the analyses are performed under a PGA=0.42g: this corresponds to a PGD of 0.20 m, 0.50 m and 1.70 m for the soil types F, M and S, respectively. Since the latter value appears unrealistically high, it has been decided not to include the soil type S in the analyses.

It should be kept in mind while observing the following figures that *geometric incoherence* (i.e. that ruled by the first term in Eq. 3) decreases as v_s/α increases from 300 m/s to ∞ m/s. In each diagram the *wave-passage delay* (i.e. that ruled by the second term in Eq. 3) decreases as the apparent velocity v_{app} increases from 300 to ∞ m/s.

As reported in section 3.1.2, for soil F an evident phenomenon is the significant reduction of the mean displacement for increasing geometric incoherence, therefore we expect a reduction of the dynamic component as v_s/α decreases from

∞ m/s to 300 m/s. For soil M this is less evident and we rather expect an increase of the dynamic component when $v_{app} = 300$ m/s. For both soils a remarkable increase of standard deviation is observed as v_s/α decreases but this phenomenon is less evident as v_{app} decreases from ∞ to 300 m/s. Therefore, high pseudo-static distortions are expected either for low values of v_s/α or, if $v_s/\alpha = \infty$, for low values of v_{app} . Note that in all cases the variation of v_{app} has a notable effect only for $v_s/\alpha = \infty$, while in the presence of a certain degree of geometric incoherence its effect is sensibly reduced.

A first task pursued was to assess the relevance on the simulated response of the selected equivalence equation, either (42) or (43) or (44), referred to as: AASHTO, Hwang and CALTRANS, respectively. In Figure 3.12 the adopted equations are compared for two different hardening ratios: 0% and 3% (the CALTRANS equation is insensitive to the hardening ratio). It can be observed that major differences exist in the estimation of the equivalent damping ratio, with relative differences of the order of 300%, whereas for the effective stiffness ratio the differences are less evident with the only exception of the CALTRANS equations, which yields a lower stiffness reduction with increasing ductility.

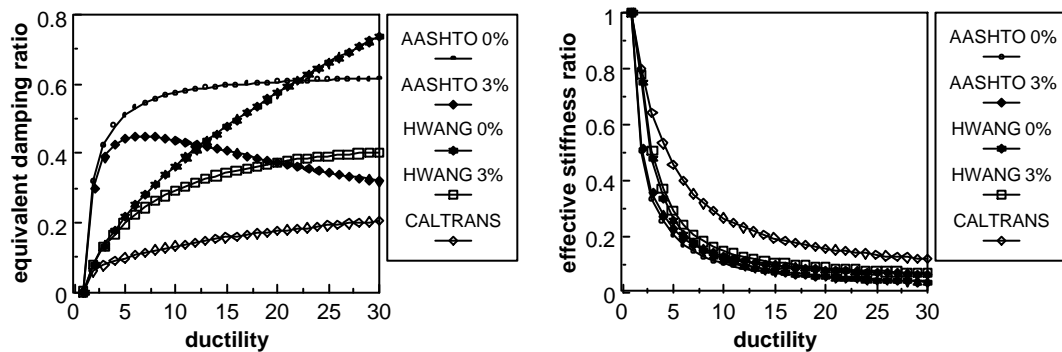


Figure 3.12. Isolator equivalent damping and stiffness ratios as function of the required ductility according to Eqs. 42 (AASHTO), 43 (Hwang) and 44 (CALTRANS), with hardening ratio 0% and 3%.

In Figure 3.13, the response of the isolators, in terms of peak displacement (where the peak factor is exactly computed), is represented for each of the above equivalence equations, compared with Montecarlo simulations on 300 nonlinear analyses. The benchmark cases considered are those on Firm and Medium soil, with either fully coherent or low coherence ground motion, corresponding to v_s/α and v_{app} equal to infinity and 300 m/s, respectively. All the comparisons above are conducted without accounting for the site response effect on the incoherence of the ground motion, but it is deemed that the conclusions reached above can be extended to the case of site response effect.

It is seen that in all cases the best approximation to the Montecarlo response is obtained with the CALTRANS equations but it is recognized that the accuracy decreases with increasing incoherence. The weakness of the AASHTO equivalence equations can be attributed to the fact that those are obtained through simple geometrical considerations, whereas the other two equations are derived by minimizing the RMS error of the inelastic maximum responses of sdof bi-linear hysteretic isolators. The two equations have a satisfactory performance when the bridge deforms according to the first modal shape, whereas they have a lower accuracy for high incoherence. In the following analyses the equations (44) are adopted to linearize the isolators.

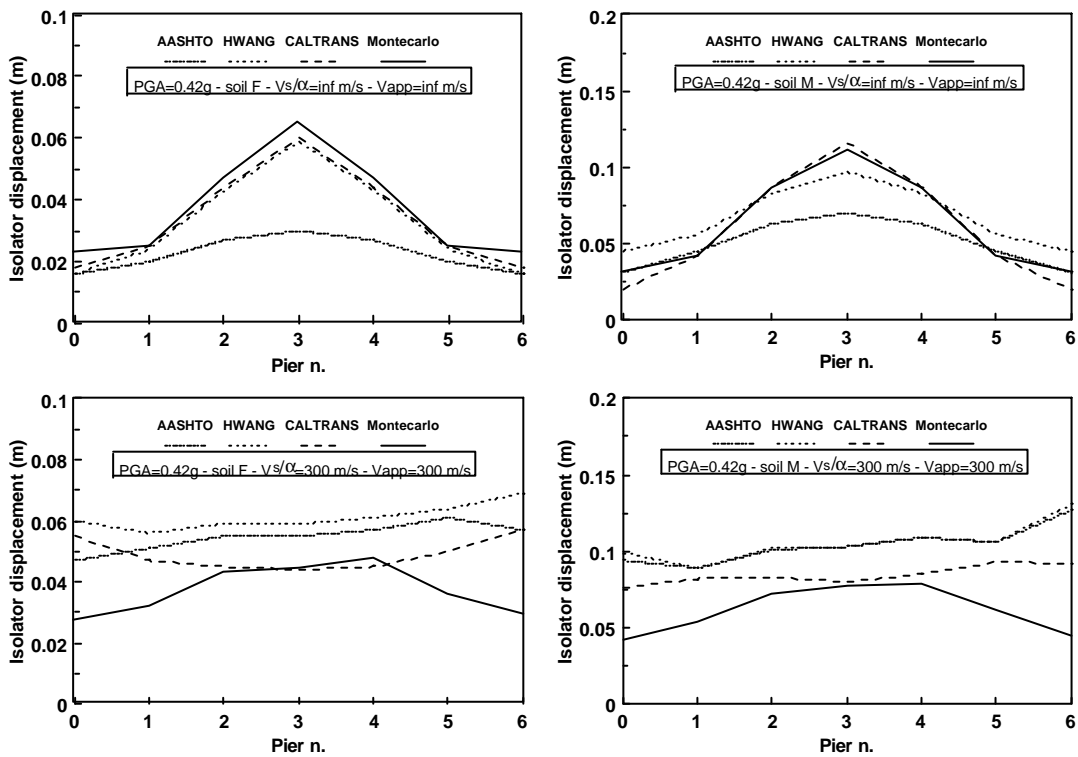


Figure 3.13. Validation of equivalence equations 42 (AASHTO), 43 (Hwang) and 44 (CALTRANS) for Firm (left) and Medium (right) soil and with high (top) and low (bottom) coherence.

For the cases examined above, in Table 3.4 the equivalent damping ratios and effective stiffnesses of the isolators are reported along with, in Table 3.5, the modal damping ratio ξ_k , computed with (59), of the first four modal shapes, for the bridges in full synchronism on soil types F and M (reference is therefore made to Figure 3.13, top). It is noted that the AASHTO and Hwang equations yield approximately the same fundamental period, as expected because of the slight differences in the estimation of the effective stiffness, whereas the periods computed with the

CALTRANS equation are systematically lower. On the other hand, it is noted that both the damping ratios of the single isolators and the modal ones are significantly higher in the two former equations, while the latter gives rise to low damping ratios. Thus, it can be said that the two former equations rely on the dissipation to predict the peak response of the isolators, whereas the latter, with lower damping ratios, relies on the stiffness.

Table 3.4. Equivalent damping ratios with three different equivalence equations (A=AASHTO, H=Hwang, C=CALTRANS) for full synchronism.

		Equivalent damping (%) and effective stiffness		
Eq.	Soil	1	2	3
A	F	36.4 (.40)	41.2 (.30)	42.4 (.28)
H	F	13.4 (.48)	21.5 (.25)	25.7 (.18)
C	F	7.8 (.62)	10.4 (.41)	11.9 (.32)
A	M	44.8 (.19)	44.4 (.14)	44.0 (.13)
H	M	25.1 (.19)	30.8 (.13)	32.8 (.11)
C	M	10.2 (.43)	14.1 (.24)	15.8 (.19)

Table 3.5. Modal damping ratios with three different equivalence equations (A=AASHTO, H=Hwang, C=CALTRANS) for full synchronism.

		Modal damping (%) and period (sec)			
Eq.	Soil	$\xi_1(T_1)$	$\xi_2(T_2)$	$\xi_3(T_3)$	$\xi_4(T_4)$
A	F	41.6 (0.75)	32.0 (0.63)	24.1 (0.47)	26.6 (0.38)
H	F	22.3 (0.81)	14.6 (0.62)	9.0 (0.45)	7.9 (0.33)
C	F	12.2 (0.68)	9.2 (0.57)	6.7 (0.43)	6.7 (0.33)
A	M	44.4 (1.01)	35.1 (0.79)	35.4 (0.59)	34.9 (0.48)
H	M	30.8 (1.05)	21.9 (0.80)	20.6 (0.61)	18.9 (0.50)
C	M	15.3 (0.82)	10.8 (0.64)	7.2 (0.46)	7.0 (0.34)

After having chosen the model to linearize the isolators, it is now possible to consider the isolators response under different incoherence conditions. For the sake of clarity, we recall that the overall phenomenon of multi-support excitation can be split into two parts: one is the so-called non-synchronism effect, which are the two effects of *geometric incoherence* and *wave passage*, the other is the *site response* effect. In Figure 3.14 the isolators response with no site response effect is represented, therefore only the case FFFFF and M MMMM are considered, that is,

soil type F and M under all supports: on the left, the response under perfectly synchronous conditions is graphed, while on the right the effect of non-synchronism is represented.

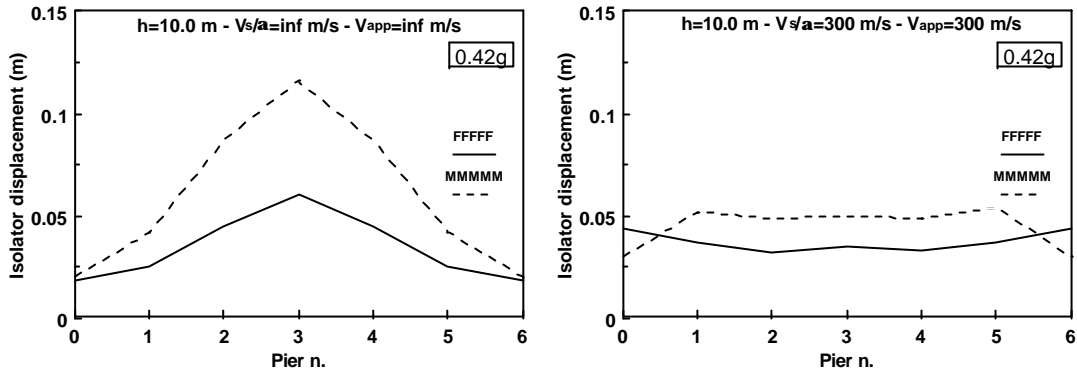


Figure 3.14. Isolators response without site response effect: synchronous (left) and non-synchronous (right).

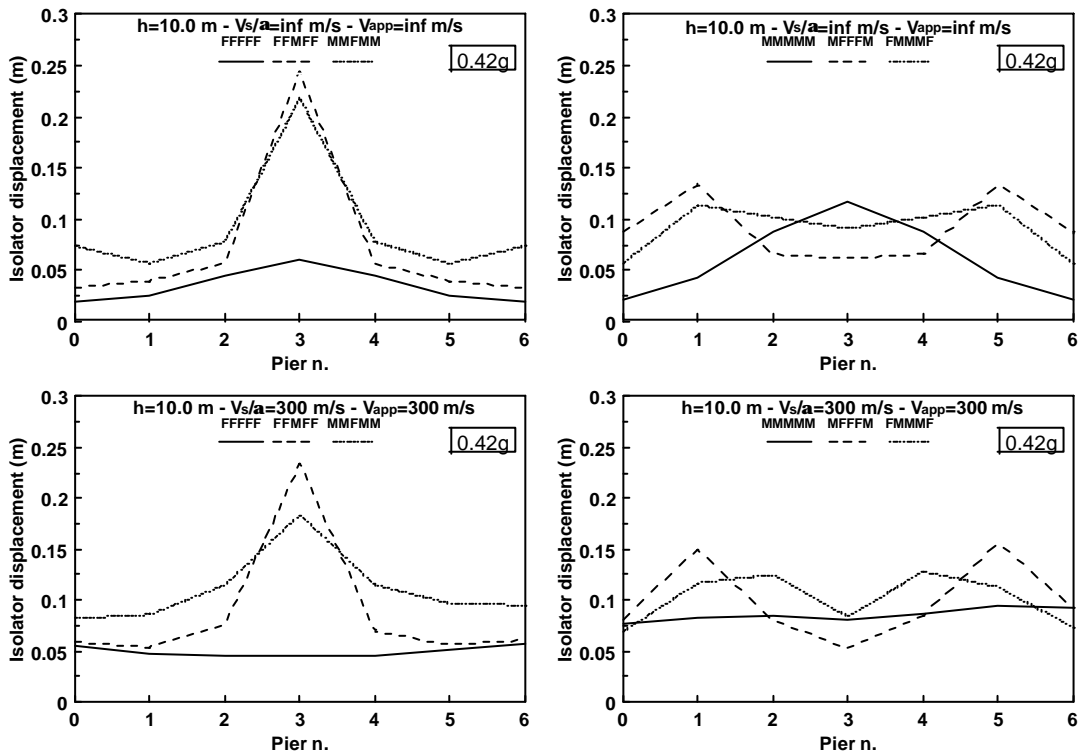


Figure 3.15. Isolators responses with varying site response effect: one-step combinations (left) and three-step combinations (right) of Firm and Medium soil, synchronous (top) and non-synchronous (bottom).

The non-synchronous action has a twofold effect: one is to reduce the peak response (which is more than halved for the case of soil F), the other is to break the modal response, which in the first case is driven by the first modal shape, while in the second becomes practically flat. It is therefore confirmed that non-synchronism has a favorable effect on the response of isolated bridges, as already reported in (Monti et al. 1995, 1996).

The consequences of the site response effect are depicted in Figure 3.15 where the effect of one-step and three-step variations are considered, for the case of synchronism and non-synchronism. Four different combinations between soil type F (Firm) and M (Medium) are considered, denoted with the sequence of soil types under the five piers of the bridge under consideration. One-step and three-step combinations are considered, defined as a change in the soil type in the mid pier and the three mid piers, respectively. It should be noted that for each combination, the reciprocal is considered as well, that is, both FFMFF and MMFMM are studied.

From the diagrams, the following observations can be made:

- when site effect is present, the response is only slightly affected by non-synchronism; this essentially confirms the deterministic nature of the site response effect which implies the application of differential displacements at the supports, as opposed to the non-synchronous part of the action, which implies instead both a dynamic and a pseudo-static part,
- the effect on the response of the one-step combinations is more significant than that of the three-step combinations,
- reciprocal combinations produce similar response shapes.

Site effect can be interpreted as a problem of differential displacements imposed at the pier supports. It has been noticed above that soil type F and M have a PGD of 0.20 m and 0.50 m, respectively, which can be appreciated in the case depicted in Figure 3.15 (top, left) where a differential displacement of about 0.20 m affects the isolators 2, 3 and 4.

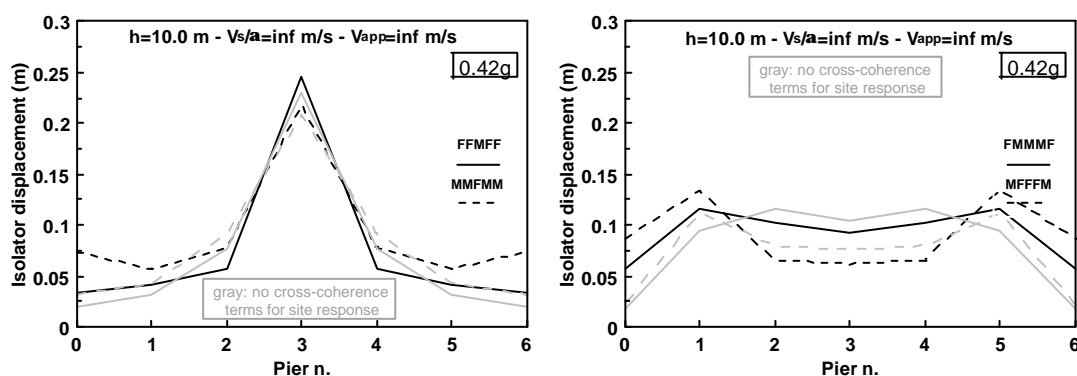


Figure 3.16. Isolators response considering the complete ground motion model (black lines) and the simplified model with no cross-coherence terms for the site response (gray lines), for one-step combinations (left) and three-step combinations (right) of Firm and Medium soil.

From the above, it can be concluded that, in case one wants to consider the presence of varying soil profiles under different support, the effect of non-synchronism can be disregarded.

Since we have now reduced the case of multiple-support excitation to a case where only the site effect is considered, one could wonder what is the difference in the global response if one models the site response effect considering only different soils in the diagonal terms of the PSD functions matrix (2), as opposed to the above described model where, in addition to this, all the off-diagonal terms in the coherency functions matrix (3) are calculated as function of distance-independent phase shifts in (4) and representing the cross-coherence among the different ground motions. In order to assess such difference, analyses have been carried out where the results obtained with the complete model of the ground motion are compared with results obtained by taking the site response coherence functions in (3) equal to 1. These comparisons are shown in Figure 3.16 for the same different soil combinations as above, but only for the case of full synchronism.

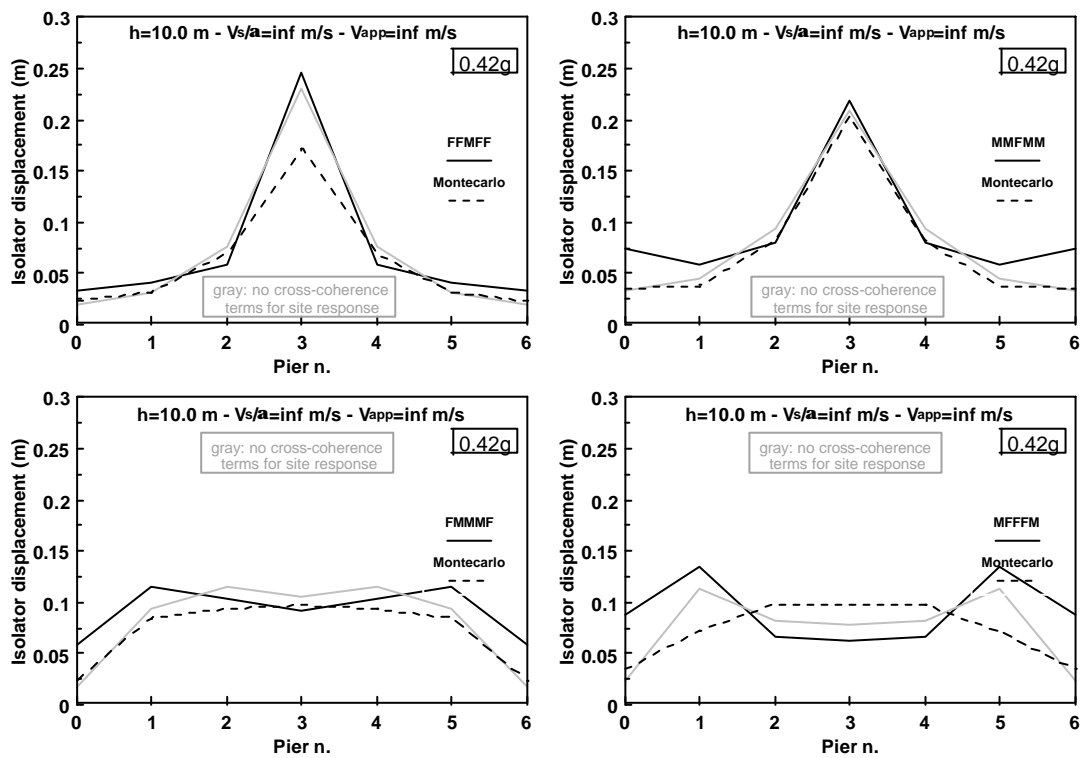


Figure 3.17. Isolators displacements obtained with Monte Carlo analyses (dashed lines), compared to random vibration analyses with the complete ground motion model (black lines) and to the simplified model with no cross-coherence terms for the site response (gray lines): one-step (top) and three-step (bottom) combinations.

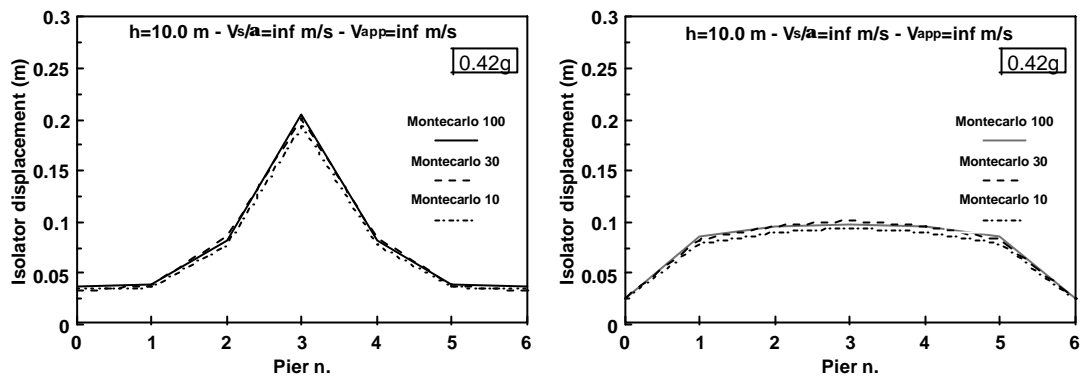


Figure 3.18. Isolators response with different number of Montecarlo analyses: cases MMFMM (left) and FMMMF (right).

By observing the results it can be concluded that a model that does not account for the cross-coherence terms, yields quite different results, even though it should be recognized that the differences are in most cases acceptable. This amounts to saying, for instance, that time history analyses could be performed by applying, at different supports, accelerograms generated from different power density spectra, without introducing any significant error on the estimation of the peak response of the isolators.

This is exactly what has been done in Figure 3.17 where the results of the random vibration analyses are compared with results obtained from Montecarlo analyses (dashed lines) on 100 samples, with accelerograms applied as mentioned above. It can be seen that for those cases with prevailing M soil (top-right and bottom-left) there are minor differences with respect to the case of the random vibration analysis with the complete model (black line), while for the cases with prevailing F soil (top-left and bottom-right) the differences are more significant but still acceptable.

Thus, a conclusion is reached, of course relative to the cases at hand but of sufficient generality, that in case the site response effect is to be included into the analysis of an isolated bridge, an acceptable estimate of the isolators peak displacement can be obtained through Montecarlo nonlinear analysis. An optimal number of 10 analyses (Figure 3.18) can be selected to approximate with sufficient accuracy the exact result, thus confirming the deterministic nature of the site response effect.

3.1.4 References

- AASHTO (1991). 'Guide Specifications for Seismic Isolation Design'. American Association of State Highway and Transportation Officials, Washington, D.C.
- Bodganoff, J.L., Goldberg, J.E. and Schiff, A.J. (1965). *Bull. of Seismological Society of America*, 55, 627-640.

- Clough, R.W. and Penzien, J. (1975). *Dynamics of Structures*. McGraw-Hill, New York, N.Y.
- Der Kiureghian, A. (1996). 'A coherency model for spatially varying ground motions'. *Int. J. of Earthquake Engineering and Structural Dynamics*, Vol. 25, 99-111.
- Der Kiureghian, A. and Neuenhofer, A. (1992). 'Response spectrum method for multiple support seismic excitations'. *Int. J. of Earthquake Engineering and Structural Dynamics*, Vol. 21, 713-740.
- Franchin, P., Monti, G. and Pinto, P.E. (1999). On the accuracy of simplified methods for the analysis of isolated bridges. *Journal of Earthquake Engineering and Structural Dynamics*, New York (under review)
- Giannini, R., Monti, G., Nuti, C. and Pagnoni, T. (1992). 'ASPIDEA. A program for nonlinear analysis of isolated bridges under nonsynchronous seismic action'. *Report n. 5/92, Dip. di Ingegneria delle Strutture delle Acque e del Terreno*, Università dell'Aquila, L'Aquila, Italy.
- Heredia-Zavoni, E. and Vanmarcke, E.H. (1994). 'Seismic random-vibration analysis of multisupport-structural systems'. *J. of Engineering Mechanics ASCE*, Vol. 120, No. 5, May, 1107-1128.
- Hwang, J.S., Change, L.H. and Gates, J.H. (1994). 'Practical analysis of base-isolated bridges with bi-linear hysteresis characteristics', *Earthquake Spectra*, Vol. 10, No. 4, 705-727.
- Hwang, J.S., Chiou, L.H. and Change, L.H. (1995). 'Establishment of an equivalent linear model of seismically isolated bridges using a system identification method', *Proc. 4th U.S. Conference on Lifeline Earthquake Engineering*, ACE, San Francisco, 416-423.
- Jennings, P.C., Housner, G.W. and Tsai, N.C. (1969). 'Simulated earthquake ground motions for design purposes'. *Proc. 4th WCEE*, Santiago, Chile, 145-160.
- Lin, Y.K., Zhang, R. and Yong, Y. (1990). 'Multiply supported pipeline under seismic wave excitations'. *J. of Engineering Mechanics ASCE*, Vol. 116, No. 5, May, 1094-1108.
- Luco, J.E. and Wong, H.L. (1986). 'Response of rigid foundation to a spatially random ground motion'. *Int. J. of Earthquake Engineering and Structural Dynamics*, Vol. 14, 891-908.
- Moerland, P., Nuti, C. and Pinto, P.E. (1993). 'Risposta dei ponti ad azioni nonsincrone'. *Proc. 6th Conference "L'Ingegneria Sismica in Italia"*, 13-15 October, Perugia, Italy, 1201-1212 (in Italian).
- Monti, G. and Pinto, P.E. (1998). Effects of multi-support excitation on isolated bridges. *Proc. U.S.-Italy Workshop on Seismic Protective Systems for Bridges*, New York, April 27-28.
- Monti, G., Nuti C. and Pinto P.E. (1995). 'Response of conventional and isolated bridges under non-synchronous seismic motion'. *Proc. SECED Conference European Seismic Design Practice*, Chester, UK.
- Monti, G., Nuti, C. and Pinto, P.E. (1996). Nonlinear response of bridges under multi-support excitation. *Journal of Structural Engineering ASCE*, Vol. 122, n. 10.
- Oliveira, C.S., Hao, H. and Penzien, J. (1991). 'Ground modelling for multiple input structural analysis'. *Structural Safety*, Special Issue, Vol. 10, Nos. 1-3, May, 79-93.

- Perotti, F. (1990). 'Structural response to non-stationary multiple-support random excitation'. *Int. J. of Earthquake Engineering and Structural Dynamics*, Vol. 19, 513-527.
- Shinozouka, M. (1972). 'Monte Carlo solution of structural dynamics'. *Comput. struct.* 2, 855-874.
- Somerville, P., McLaren, J.P, Mrinal, K.S. and Helmberger, D.V. (1991). 'The influence of site conditions on the spatial incoherence of ground motions.' *Structural Safety*, 10, 1-13.
- Vanmarcke, E.H. (1977). 'Structural response to earthquakes'. *Seismic Risk and Engineering Decision*. Lomnitz Ed., McGraw-Hill, New York, N.Y., 287-337.
- Vanmarcke, E.H. (1983). *Random fields: Analysis and synthesis*. The MIT Press, Boston, Mass.
- Veletsos, A.S. and Ventura, C.E. (1986). 'Modal analysis of non-classically damped linear systems'. *Int. J. of Earthquake Engineering and Structural Dynamics*, Vol. 14, 217-243.
- Zambrano A., Inaudi, J.A. and Kelly, J.M. (1996). 'Modal coupling and accuracy of modal strain energy method'. *Journal of Engineering Mechanics*, ASCE, Vol. 122, No. 7, July, 603-612.
- Zerva, A. (1992). 'Seismic ground motion simulations from a class of spatial variability models'. *Int. J. of Earthquake Engineering and Structural Dynamics*, Vol. 21, 351-361.

3.2 Soil-structure interaction

Soil-Structure Interaction (SSI) effects consist, by definition, in the difference in the structural response evaluated assuming an ideal rigid and the actual soil foundation, respectively.

In general, the difference stems from two distinct physical causes. The first cause for a difference is due to the propagating nature of seismic disturbances in the form of waves, that makes the soil motion at any given instant generally different from point to point. The ensuing interaction effect with a spatially extended foundation is called *kinematic* interaction: a necessary condition for this effect to be of importance is that the foundation dimensions are of the same order of magnitude of the main wavelengths contained in the motion. The second cause for a difference is due to the inertia forces transmitted by the structure to the soil during the oscillations: these forces induce a deformation in the soil that adds up to the one existing in the free-field, leading to a modified translational component of the motion and to the presence of a rocking component, whose effect may become significant for tall and slender structures.

Especially this second phenomenon, referred to as *inertial* interaction, has been the subject of intensive research over a period of thirty years and more; one could therefore expect by now the main parameters having influence on it to be adequately understood, and practical procedures available for taking it into account in design.

A cursory glance at the evolution occurred in this field may serve to better appreciate the scope and limitations of the present state of knowledge.

The reference structural model on which the phenomenon has been studied has not changed over the years: an elastic, damped oscillator having a rigid mat foundation resting on, or partially embedded into, a homogeneous or stratified (visco-)elastic (hysteretic-)half space. While early studies (see for ex. Parmalee 1968, Tajimi 1969, Castellani 1970) provided fundamental insight into the problem, their generality was restricted by the then necessarily simple assumptions on soil profile and by the approximate solutions available for the dynamic impedances of the footings.

Regarding this latter mixed boundary-value problem, accurate solutions for rigid footings started to appear by the end of the sixties and their production has continued until approximately the mid seventies (among the more recent contributions, see for ex. Veletsos and Verbic 1973, Luco 1974, Gazetas 1976): therefore, solutions are now available for rigid circular, rectangular and strip foundations on various combinations of soil profiles (Gazetas 1983).

Currently, efforts are concentrated in providing discretized impedance matrices for general, excavated, spatial soil profiles (Wolf 1984, Apsel and Luco 1987, Gaitanaros and Karabalis 1988), thus enabling full SSI analyses (kinematic + inertial) to be performed on extended, embedded structures of general shape.

Concurrently with the developments in the description of soil responses, several studies have been made on the simple structural model described above in order

to identify the parameters having the major influence on SSI, and to set up approximate procedures for accounting of its effects in the design. The most extensive efforts in these two directions have been made by Veletsos and his co-workers (see for ex. Veletsos and Meek 1974, Veletsos 1977), who succeeded in providing a simple procedure by which the actual building is reduced to a so-called *replacement oscillator*, a single d.o.f. structure having period of vibration T' and damping ξ' properly adjusted for SSI. This procedure was later incorporated in the ATC 3.06 Provisions (1983).

Through the mentioned studies, two parameters were found to essentially regulate the importance of the phenomenon:

- the wave parameter:

$$\sigma = \frac{V_s \cdot T}{H} \quad (1)$$

expressing the relative stiffness of the foundation medium and the structure. V_s denotes the shear wave velocity in the soil, T the fixed-base period of the structure, H its height.

- the ratio: H/r , where r is the (equivalent) radius of the foundation.

Intuitively, SSI effects are expected to be more significant with σ decreasing and H/r increasing, respectively.

These two parameters can be combined into a third one:

$$\phi = \frac{1}{\sigma} \left(\frac{H}{r} \right)^{1/4} \quad (2)$$

which is best suited to measure the limit condition below which SSI effects are not worth consideration in the design. The indicated threshold value for ϕ is: $\phi \leq 0.125$ (Veletsos 1977).

It is appropriate to note that all the methods that have been briefly reviewed thus far are based on the assumption that the superstructure behaves elastically, a significant limitation for structures that are intended to resist severe earthquakes, for which inelastic action is intentionally accepted. Under strong shaking, one should of course also consider possible soil non linearity: at present, this can only be dealt with practically by using appropriate *effective* values for the modulus of elasticity and the (frequency-independent) damping factor.

Investigations on the effect of SSI in presence of yielding of the superstructure (as compared with the elastic case) are scarce, if at all. In qualitative terms, yielding may be viewed globally as a decrease of stiffness of the structure, hence it could be inferred that it would tend to decrease SSI effects (see parameter ϕ). No quantitative information, however, has been up to now derived on this aspect, and especially on the effects of SSI on the maximum required ductilities in the critical regions of the superstructure.

Yet the question is not of negligible consequences, as it can be easily demonstrated through the following case, taken from (Priestley and Park 1987).

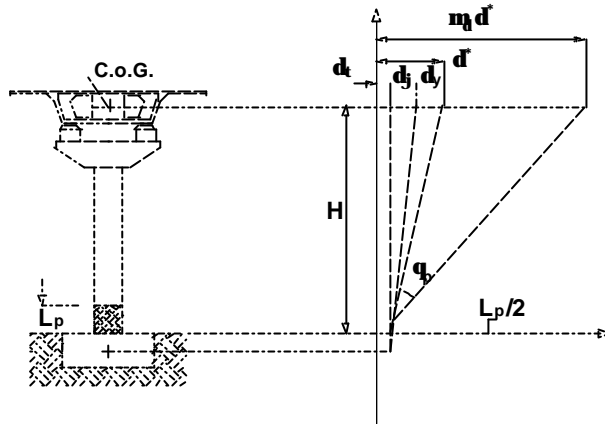


Figure 3.19. Components of the total displacement for compliant foundation (after Priestley and Park 1987)

For the isolated bridge pier shown in Figure 3.19, the maximum allowable horizontal displacement at the center of gravity (C.o.G.) of the upper deck is in general made up of four contributions:

$$\delta_{\max} = \delta_{\tau} + \delta_{\phi} + \delta_y + \delta_p \quad (3)$$

where δ_{τ} and δ_{ϕ} are the rigid-body contributions corresponding to the translation and the rotation of the foundation, δ_y is the contribution due to the deformation of the pier when yielding is first reached at the base, and δ_p is due to the maximum admissible rotation of the plastic hinge located in the lower portion of the pier:

$$\delta_p = (\phi_p \cdot L_p) \left(H - \frac{L_p}{2} \right) = \theta_p \cdot \left(H - \frac{L_p}{2} \right) \quad (4)$$

L_p being the equivalent plastic hinge length.

If the available ductility of the pier, expressed in terms of the displacement at the deck C.o.G., is defined as:

$$\mu_{\delta} = \frac{\delta_{\tau} + \delta_{\phi} + \delta_y + \delta_p}{\delta_{\tau} + \delta_{\phi} + \delta_y} \quad (5)$$

writing: $d_{\tau} + d_{\phi} = c$, it follows that:

$$\mu_{\delta} = \frac{(1+c)\delta_y + \delta_p}{(1+c)\delta_y} \quad (6)$$

For the case under examination, Eq. (6) is often directly used as the force-reduction factor R (i.e., the behavior factor) in the design of the structure.

A value frequently adopted for R is: $R = 4$. Therefore, let's put 4 at the left-hand side of Eq. (6), and examine the two cases in which $c = 0$ and $c = 1$, respectively. One gets: for $c = 0$, $\delta_p = 3\delta_y$; for $c = 1$, $\delta_p = 6\delta_y$; that is, even a relatively

modest deformability of the base requires a large increase in the required plastic deformation of the hinge, if the displacement ductility has to remain unchanged.

This fact leads back to the initial question: how does the incorporation of SSI affects the response in terms of maximum required ductility?

The investigation reported in this study attempts to answer this question with reference to a simple structural configuration: a vertical cantilever carrying a mass at the top, whose mechanical model is, apart from the inelasticity of the superstructure, identical with the “historical” one described earlier.

Since the present study is concerned with bridge piers of common geometry having spread or strip footing foundations, the assumption of a uniform motion underneath is sufficiently realistic, and therefore the kinematic effect will not be considered. Moreover, since the context of this study is the calibration of the values of the R factors to be used in the design of bridges, it has been considered more appropriate to use data corresponding to realistic geometries (as concerns foundations, cross-sections, heights, etc.), weights of the deck, steel ratios, range of soil data, etc., rather than to conduct parametric analyses using the non-dimensional quantities mentioned previously. Once the results are obtained, however, their presentation has also been arranged in terms of the parameters μ , and T'/T , and H/r , to facilitate their appreciation in terms of classical quantities.

3.2.1 Mechanical model and equation of motion

3.2.1.1 Superstructure

The piers are modeled as single d.o.f. oscillators characterized by mass, damping and restoring force. The mass M equals the weight of the supported deck plus a fraction of the distributed self weight of the pier ($\cong 25\%$ of the total weight): the fraction adopted is such as to lead to the same natural period for the actual distributed mass cantilever and a massless cantilever with a single mass on top. The damping is assumed to be of the viscous type, and characterized by a given value of the damping ratio with respect to the critical. The pier stem is assumed to respond elastically all through its height, except for the plastic hinge zone at the base, extending for a length L_p (Figure 3.20a). The plastic hinge has a moment-curvature relationship of the Takeda type (Figure 3.20b), *i.e.*, elasto-plastic with strain-hardening and stiffness degradation with increasing cyclic deformation amplitude. The yielding moment of the Takeda model corresponds to yielding of the furthestmost layer of reinforcing bars, considering the normal force actually present at the pier base. To account for cracking of concrete, the elastic portion of the pier has been attributed a stiffness EI equal to that of the gross, unreinforced cross section divided by the factor 2.50.

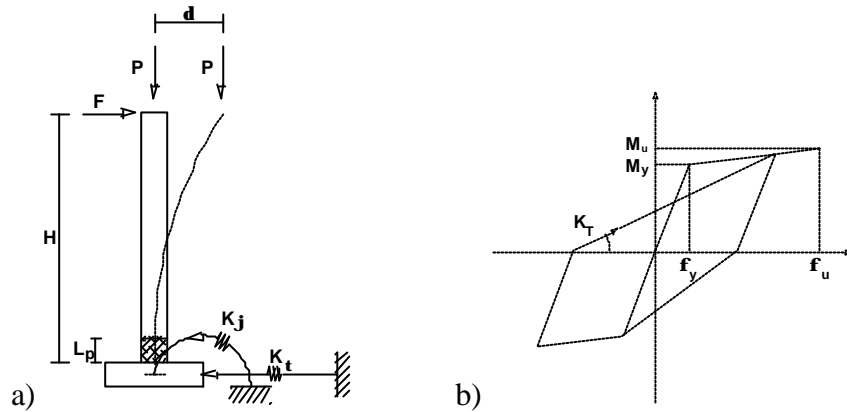


Figure 3.20. a) Mechanical model of the pier with soil springs;
b) Moment-curvature relationship of the plastic-hinge zone

3.2.1.2 Foundation and foundation soil

Having considered piers of rectangular cross sections, the foundation mats have also been taken as rectangular in plan. They are considered in the analysis as rigid and perfectly bonded to the soil; moreover, the effect of their mass and of their moment of inertia about the horizontal axis has been disregarded.

For evaluating the dynamic impedances, use has been made of the solutions for rigid circular footings on an elastic half-space obtained by (Veletsos and Wei 1971), as reported in (Gazetas 1983). To enter these solutions, equivalent radii have been evaluated using the relationships:

$$r = \left(\frac{2B \cdot 2L}{\pi} \right)^{1/2}, \quad r = \left(\frac{16LB^3}{3\pi} \right)^{1/4} \quad (7)$$

for the lateral and rocking stiffnesses, respectively ($2B$ and $2L$ denote the lengths of the two sides of the block, the former being the side orthogonal to the axis of rocking).

The dynamic impedances of the soil, relative to the i th degree of freedom, are usually cast in the form:

$$K_i = K_{st,i} (k_i + i a_0 c_i) \quad (8)$$

i.e., they are expressed as the product of a *static* term $K_{st,i}$, which is actually equal to the static stiffness of the soil system, times a *dynamic* term, this latter being a complex, frequency-dependent quantity. In particular, the stiffness coefficient k_i reflects the dynamic part of the stiffness, as well as the inertia of the soil, while the dimensionless damping coefficient c_i in the imaginary component accounts for the frequency-dependent loss of energy due to the radiation of the waves away from the foundation; a_0 is a dimensionless frequency factor that is a function of the vibrational frequency and is given by the expression:

$$a_0 = \frac{\omega \cdot r}{V_s} \quad (9)$$

From a computational point of view, it is convenient to treat the dissipative component as it was viscous in nature, and characterized by an (approximately) constant viscous factor C_i . The value of C_i is easily obtained from the equality:

$$i\omega C_i = iK_{st,i} a_0 c_i \quad (10)$$

which gives:

$$C_i = \frac{K_{st,i} \cdot c_i \cdot r}{V_s} \quad (11)$$

where for c_i one may take its average value over the range of frequencies of interest.

The parameters needed to quantify the dynamic impedances are illustrated in Figure 3.21 for the horizontal (index τ) and rocking (index ϕ) components, respectively (Gazetas 1983). It can be observed that c_i (and hence C_i) is nearly constant over the whole range of frequencies for the translational motion, while for rocking it tends to stabilize for values of a_0 in excess of 2-3. The values of interest for a_0 in the present application, however, are much lower than unity (the values vary in the range $0.08 < a_0 < 0.56$), so that damping due to rocking can be anticipated to be of negligible importance.

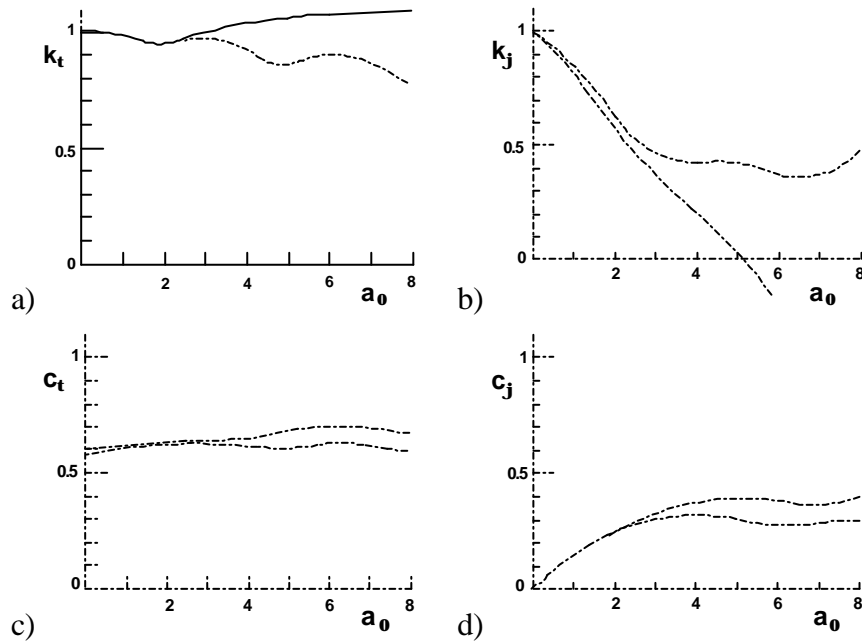


Figure 3.21. Impedance functions of rigid circular footings on homogenous half space (Gazetas 1983)
 (——— $n = 0.5$; - - - - $n = 0.33$): a) horizontal stiffness coefficient k_{τ} ; b) horizontal damping coefficient k_{ϕ} ; c) rocking stiffness coefficient k_{ϕ} ; d) rocking damping coefficient c_{ϕ}

In addition to the damping due to radiation, the always present dissipation of energy due to internal damping of the soil is usually introduced in the form of frequency-independent hysteretic damping. The equivalence between this latter and that of viscous type is then found by equating the normalized amounts of energy dissipated in one cycle of amplitude A at the frequency ω in the two forms:

$$\text{viscous:} \quad \frac{E_d}{E_e} = \frac{\pi C \omega A^2}{\frac{1}{2} K A^2} = 2\pi C \frac{\omega}{K} = 4\pi\beta \frac{\omega}{\Omega} \quad (12)$$

$$\text{hysteretic:} \quad \frac{E_d}{E_e} = \frac{2\pi K A^2 \xi}{\frac{1}{2} K A^2} = 4\pi\xi \quad (13)$$

where $\beta = C / (2 \cdot \sqrt{Km})$ is the ratio of the damping to its critical value, and $\Omega = \sqrt{K/m}$ is the eigenfrequency of the 1 d.o.f. mass-spring-dashpot system (that is characterized by an effective damping C and an effective stiffness K) equivalent to the massless footing-soil system.

For lightly damped systems it is known that the damping affects the magnitude of response in the frequency region close to resonance, allowing to put: $\omega/\Omega \approx 1$ in Eq. (12) and getting:

$$\beta = \xi \quad (14)$$

that is: the hysteretic energy loss ratio can be treated in the same way as the critical viscous ratio, and therefore simply added to the equivalent viscous damping related to radiation.

3.2.1.3 Effective damping of the soil-structure system

As shown in the following, the 3 d.o.f.s system illustrated in Figure 3.20a can be reduced to a 1 d.o.f. system in which the only variable is the displacement of the mass on top.

In parallel, one also needs to evaluate a single *effective* damping force acting on the mass, encompassing the combined effect of the reinforced concrete portion and of the soil. This can be done by having recourse to a well known approximate criterion (described in Roesset et al. 1973), often denominated as of *weighted damping*. In the case at hand the criterion simply consists of assuming that:

a) the system in Figure 3.20a oscillates according to a fixed shape, given by its undamped elastic first mode;

b) the effective damping of the system is given by the weighted sum of the damping of its parts, the weight being the normalized elastic energy stored into each of them for a deformed shape corresponding to the first mode.

This leads to the expression:

$$\beta_{eq} = \frac{1}{4\pi} \frac{E_{ds} + 4\pi(\beta_s E_{es} + \beta_p E_{ep})}{E_{ds} + E_{es} + E_{ep}} \quad (15)$$

where: $E_{ds} = \pi \Omega \sum C_i x_i^2$ is the energy dissipated within the soil by radiation, and x_i being the first mode frequency and the modal coordinates of the soil d.o.f.'s respectively, and C_i is the damping constant relative to the i -th degree-of-freedom characterizing the soil-structure interaction (*i.e.* horizontal translation or flexural rotation); E_{es} is the modal elastic energy stored in the soil springs; E_{ep} is the modal elastic energy in the piers; β_s and β_p are the effective damping of the soil and of the pier.

3.2.1.4 Seismic input

All the analyses made in the present study have been performed using a seismic input characterized by a value of the peak ground acceleration equal to 0.35 g and by a frequency content corresponding to the amplification spectrum given in the Euro-code No. 8 (1988) for soils of the intermediate type.

Seven simulated time-histories have been generated from the target spectrum, having a total duration of 27 s, with a stationary portion of 20 s and two linearly modulating functions at both ends. Figure 3.22 shows one of the samples and Figure 3.23 the comparison between the given and the average spectrum from the seven accelerograms. The response quantities from the non linear analyses presented in the following (peak displacements, ductilities, etc.) correspond to the averages out of the seven values obtained from each analysis.

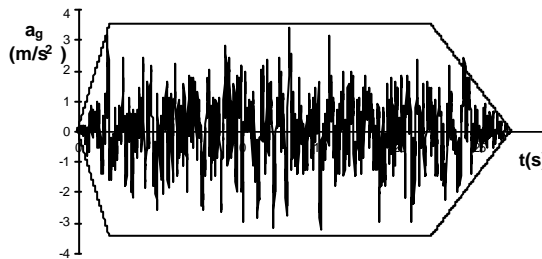


Figure 3.22. One of the adopted sample-accelerograms

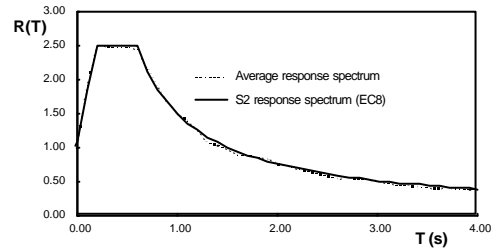


Figure 3.23. Comparison between target and average spectrum from seven accelerograms

3.2.1.5 Equation of motion

The mechanical model of the piers previously described and shown in Figure 3.20a has 3 d.o.f.s: a translational and a rotational component at the base: u , φ , and the total displacement of the mass at the top.

Since, however, u and φ are not associated with mass and moment of inertia, they can be eliminated through static condensation and a single equation can be written, related to the dynamic equilibrium of the upper mass.

The only quantity that has yet to be derived is the instantaneous tangent stiffness, relating the increment of displacement: Δ to the incremental force F . This derivation follows. With the symbols indicated in Figure 3.20a and Figure 3.20b, given an increment F , the corresponding increment can be expressed as:

$$\Delta\delta = \Delta\delta_\tau + \Delta\delta_\varphi + \Delta\delta_e + \Delta\delta_p \quad (16)$$

where:

$$\Delta\delta_\tau = \frac{\Delta F}{K_\tau}, \quad \Delta\delta_\varphi = \frac{\Delta M \cdot H}{K_\varphi}, \quad \Delta\delta_e \cong \frac{H^2 \Delta M}{3 EJ}, \quad \Delta\delta_p = \left(H - \frac{L_p}{2} \right) L_p \Delta M \left(\frac{1}{K_T} - \frac{1}{EJ} \right) \quad (17)$$

and: K and K are the stiffnesses of the translational and rotational springs modeling the pier connection to the soil; K_T is the tangent stiffness of the hysteretic hinge; $\Delta M = \Delta F \cdot H + (\delta - \delta_e) \cdot P$.

Upon substitution and separation of the terms containing F and Δ one gets:

$$K(\delta) = \frac{\Delta F}{\Delta\delta} = \frac{1 - P \left[\frac{H}{K_\varphi} + \frac{H^2}{3EJ} + \left(H - \frac{L_p}{2} \right) L_p \left(\frac{1}{K_T} - \frac{1}{EJ} \right) \right]}{\frac{1}{K_\tau} + H C_p \left[\frac{H}{K_\varphi} + \frac{H^2}{3EJ} + \left(H - \frac{L_p}{2} \right) L_p \left(\frac{1}{K_T} - \frac{1}{EJ} \right) \right]} \quad (18)$$

$$(C_p = 1 - P / (K_\tau \cdot H))$$

The equation of motion is finally:

$$M \ddot{\delta} + 2\omega_{eq} \dot{\delta} + K(\delta)\delta = M \cdot a(t) \quad (19)$$

to be integrated numerically, iterating at each step until $K(\delta)$ becomes consistent with the current value of δ .

3.2.2 Cases examined

As mentioned in the introduction, the primary purpose of this study is to assess the relevance (in absolute terms) of the SSI effects on dynamic response of bridge piers responding in the inelastic range. In case these effects were found to be important, either favorably or unfavorably, then a second purpose would have been that of identifying the range of parameters leading to the two situations, and finally of devising appropriate procedures for dealing with both.

In order to achieve the primary purpose with results of sufficient generality, a quite large number of design parameters have been considered with their likely variations, the total number of cases analyzed being 240.

The selected parameters are:

- the piers cross sections, with two types, *A* and *B*, both hollow rectangular;
- the height of the piers, with five values ranging from 10 m to 50 m;
- the spans of the decks, which have been taken as 30 m (deck a) and 50 m (deck b). This variation has influence on the mass that is present at the top of the piers (inertial effects) as well as on the amount of normal force acting at the pier base. The unit weight of the deck is taken equal to 200 kN/m;
- the dimensions of the foundation mats, which have been given two different values for each of the cross sections *A* and *B*;
- the percentage of steel ρ in the piers cross sections (the ratio between steel and gross concrete areas) which has been attributed two values, equal to 0.25% and 1%, respectively. The background for the selection of these values, and in particular of the lowest one, is illustrated in the report of a previous study by the authors (Calvi et al. 1990).
- the shear modulus of the soil, for which two values have been selected: $G = 100$ MPa and 300 MPa, the first one representing a likely lower bound for a direct foundation. The case of fixed foundation, which has been obviously also considered, can be treated as a third limiting case of $G = \infty$.

Table 3.6. Summary of the variables considered in the parametric analysis

Soil characteristics	$G = 100 / 300 / \infty$ MPa
Pier sections	type "A" (4 m x 2 m x 0.30 m) type "B" (6 m x 2.20 m x 0.40 m)
Superstructure span length L	30 m (deck "a") / 50 m (deck "b")
Equivalent radius of foundation r	4 m / 6 m for piers type "A" 6 m / 9 m for piers type "B"
H (m)	10 / 20 / 30 / 40 / 50
r (%)	0.25 / 1.00

With the parameters varying as indicated in the above, the periods of oscillation of the piers in the elastic, uncracked state were comprised in the range 0.22 to 2.60 seconds, thus covering a large percentage of actual cases.

The values assigned to the parameters are summarized in Table 3.6, while Table 3.7 and Table 3.8 give the values of the soil stiffness and viscous constants for the various cases, derived through the relationship:

$$C_{\tau,\varphi} = c_{\tau,\varphi} \frac{r}{V_s} K_{\tau,\varphi} \quad (20)$$

In Figure 3.24 the values of β_{eq} are shown for the various cases as function of the parameter σ . It is seen from Figure 3.24 that the global damping goes rapidly down with increasing σ close to the value of the structure alone, which has been set at 2%. Therefore radiation and hysteretic damping contributes significantly to the overall damping only for the extreme combination of stiff structures on weak soil.

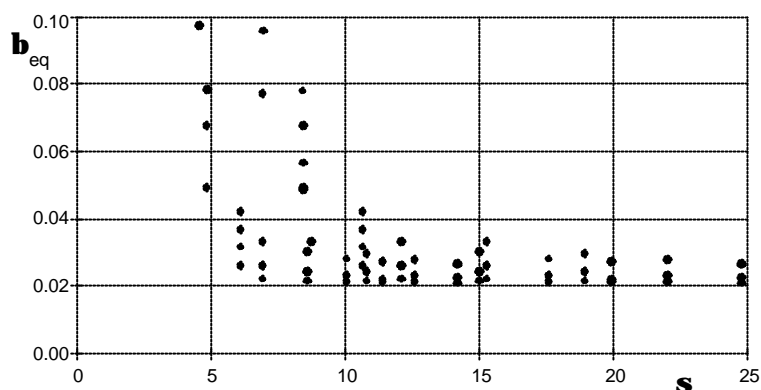


Figure 3.24. Resulting b_{eq} as a function of s

Table 3.7. Stiffnesses and damping of the soil model: pier type "A"

G (MPa)	n	r (m)	K_t (GN/m)	K_j (GNm/rad)	C_t (MN s/m)	C_j (MNms/rad)
100	0.33	4	1.92	16.00	20.90	46.30
100	0.33	6	2.88	54.00	47.10	235.00
300	0.33	4	5.76	48.00	36.02	79.80
300	0.33	6	8.64	162.00	81.05	404.00

Table 3.8. Stiffnesses and damping of the soil model: pier type "B"

G (MPa)	n	r (m)	K_t (GN/m)	K_j (GNm/rad)	C_t (MN s/m)	C_j (MNms/rad)
100	0.33	6	2.88	54.00	47.03	235.00
100	0.33	9	4.32	182.25	105.82	1187.00
300	0.33	6	8.64	162.00	81.05	404.00
300	0.33	9	12.96	546.75	182.4	2045.00

3.2.3 Results

The response quantities will be presented and discussed as functions of three dimensionless variables:

- $\sigma = \frac{V_s \cdot T}{H}$

This quantity contains in the numerator the square root of the ratio G/K where K is the elastic stiffness of the pier: therefore SSI effects are expected to be more significant for low values of σ . For a given value of the product $V_s \cdot T$, the higher is the value of H the lower is σ , a fact that intuitively reinforces the idea that one should expect greater SSI effects for low values of σ .

- $\frac{T'}{T}$

The ratio between the fundamental periods of the elastically supported and the fixed base pier can be expressed, in the elastic range, as:

$$\frac{T'}{T} = \left[1 + \frac{K}{K_\tau} \cdot \left(1 + \frac{K_\tau \cdot H^2}{K_\phi} \right) \right]^{1/2}$$

and tends to unity for $K_\tau \gg K$ and $K_\phi \rightarrow \infty$. Even more evidently than σ , this ratio reflects the importance of the interaction in modifying a fundamental dynamic characteristic of the system. Generally, with the exception of very short piers, an increase of T'/T tends to reduce the response in terms of acceleration and to increase it (in all case) in terms of displacements. What it does produce in terms of ductility is the main object of the present investigation.

- $\frac{H}{r}$

This parameter is clearly incomplete in describing both the characteristics of the pier (stiffness and mass properties are absent) and those of the soil, that are completely missing. It is, however, a geometric parameter of immediate engineering significance, which justifies the attempt of using it as a variable for showing the effects of SSI.

The response quantities examined are the maxima of the top displacements, of the curvature ductility demand μ_ϕ at the pier bases, and of the displacement ductility demand μ_δ at the pier tops. Each maximum value in the plots represents the average from seven independent spectrum-compatible accelerograms. The associated coefficients of variation, not indicated in the diagrams, are approximately uniform and with a magnitude comprised in the range 0.20 - 0.30.

The parameter η in Figure 3.25 is the ratio of the maximum top displacements with and without SSI effects (fixed base). For the sake of completeness, the fixed base values of the maximum top displacements are reported in Table 3.9. There is nothing unexpected to be noted in Figure 3.25: adding flexibility to the foundations leads to increased maximum displacements. The results can be demonstrated in

terms of σ , as in Figure 3.25a, where the increase of η is seen to be higher for lower values of σ (that is, for higher SSI effects), or in terms of T'/T , as in Figure 3.25b, where is the lengthening of the period to produce higher values of η .

Considering the width of the examined range, however, the effect does not appear as really significant: in more than 90% of the cases η is less than 1.25, and it is below 1.50 for almost all cases. In a not negligible percentage of cases, a (generally) slight reduction ($\eta < 1$) also shows up.

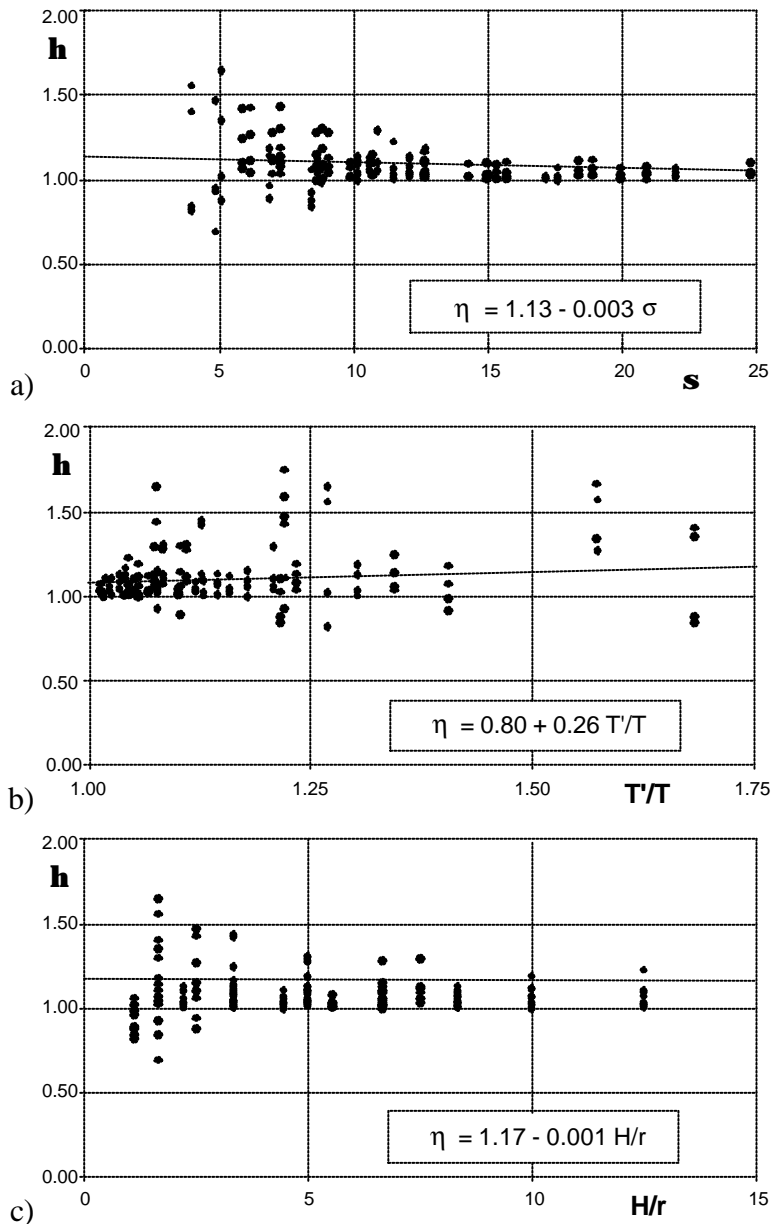


Figure 3.25. Ratio of the maximum top displacements with and without SSI effects: a) as a function of σ ; b) as a function of T'/T ; c) as a function of H/r

Table 3.9. Maximum top displacements (in m) for the fixed-base case

H	Pier A deck a $\rho = 0.25$	Pier A deck a $\rho = 1.00$	Pier A deck b $\rho = 0.25$	Pier A deck b $\rho = 1.00$	Pier B deck a $\rho = 0.25$	Pier B deck a $\rho = 1.00$	Pier B deck b $\rho = 0.25$	Pier B deck b $\rho = 1.00$
10	0.028	0.033	0.046	0.033	0.011	0.010	0.018	0.014
20	0.129	0.113	0.150	0.158	0.061	0.061	0.081	0.075
30	0.270	0.257	0.293	0.306	0.109	0.125	0.149	0.150
40	0.443	0.412	0.501	0.525	0.202	0.211	0.257	0.277
50	0.556	0.586	0.703	0.642	0.292	0.340	0.368	0.414

This result is due to a combination of two factors: the higher damping contributed by the soil (especially for squat piers), and the amount of inelastic response. While in fact $\eta < 1$ could not occur for equal damping and in the elastic range, the behavior of a yielding and degrading oscillator does not rule out a reduction. As a final comment on the displacement, the nearly horizontal trend of the regression lines in the Figure 3.25 demonstrates that η is only weakly sensitive to all of three variables.

The remarks made thus far have only an introductory character with respect to the actual issue of the study, which relates to the influence of SSI on the inelastic response. This influence appears directly in Figure 3.26, where the ordinate χ represent the ratio between peak curvature ductility demands μ_ϕ (averages from seven accelerograms), with and without SSI effects, as functions of the three variables: σ , T'/T , H/r . The ordinates scale has been magnified on purpose for an immediate appreciation of the results, which can be simply summarized as follows: the majority of the points lie on or below the line $\chi = 1$; the total scatter does not exceed $\pm 25\%$; the regression lines really should be taken as horizontal for all practical purposes.

Table 3.10. Peak curvature ductility demand (fixed-base case)

H	Pier A deck a $\rho = 0.25$	Pier A deck a $\rho = 1.00$	Pier A deck. b $\rho = 0.25$	Pier A deck b $\rho = 1.00$	Pier B deck a $\rho = 0.25$	Pier B deck a $\rho = 1.00$	Pier B deck b $\rho = 0.25$	Pier B deck b $\rho = 1.00$
10	6.48	3.33	6.84	4.74	3.13	2.20	4.30	3.13
20	4.00	2.61	4.71	3.38	2.91	1.92	3.72	2.52
30	3.56	2.44	3.77	2.65	2.13	1.57	2.74	1.92
40	3.09	2.02	3.43	2.45	2.00	1.35	2.53	1.76
50	2.18	1.67	1.99	2.00	1.74	1.32	2.15	1.62

Looking at the results in more detail, one could observe a systematic reduction of χ for the lower value of the reinforcement ratio ($\rho = 0.25\%$). In other words, the curvature ductility demand μ_ϕ decreases when SSI combines with low yielding structures. The range of values of the μ_ϕ 's for all the fixed-base cases, and in particular for $\rho = 0.25\%$, can be seen in Table 3.10.

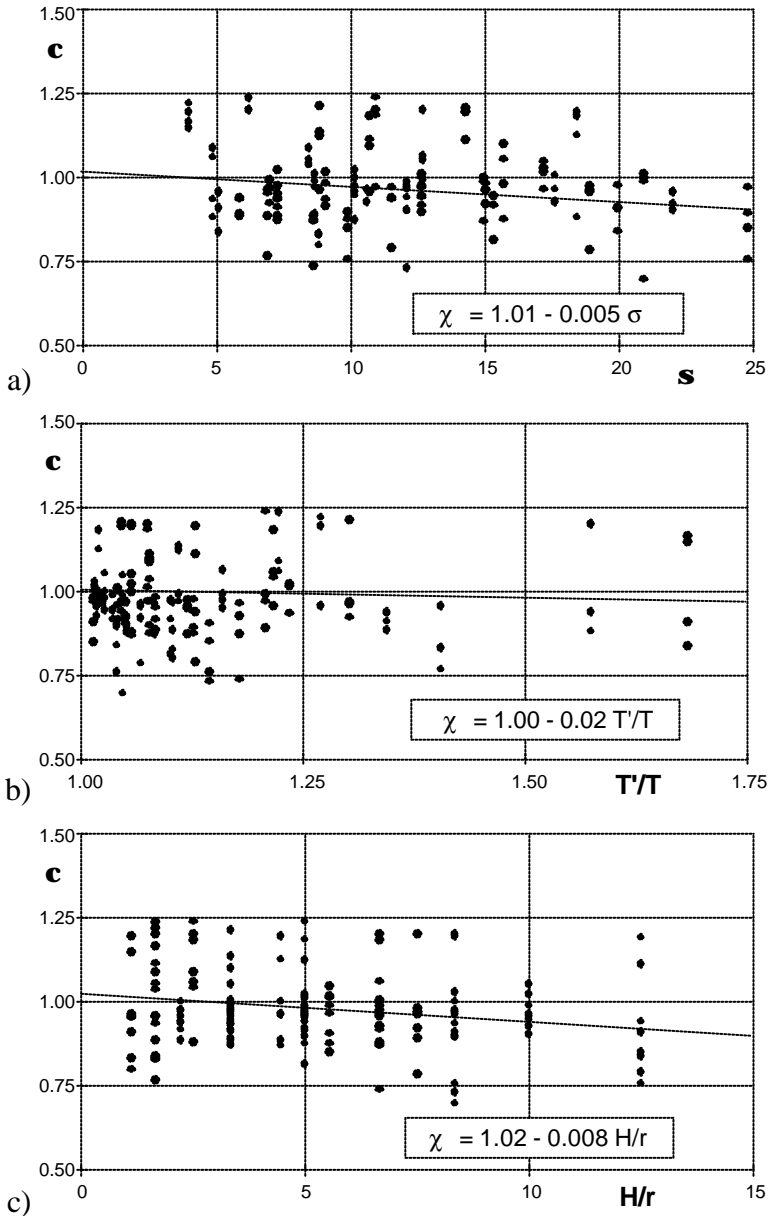


Figure 3.26. Ratio of the maximum curvature ductility demands with and without SSI effects: a) as a function of S ; b) as a function of T'/T ; c) as a function of H/r

The result depicted in Figure 3.26, *i.e.*, the fact that μ_ϕ is substantially insensitive to SSI, was not obvious beforehand and has a direct bearing on the argument raised in the introduction. In fact, if μ_ϕ remains approximately constant independently on SSI, and the factor c in Eq. (6) is anything greater than zero, then the displacement ductility demand μ_δ as defined in Eq. (6) can only decrease.

This fact is confirmed by Figure 3.27, where the ratio of the μ_δ with ($\mu_{\delta,SSI}$) and without ($\mu_{\delta,fix}$) SSI is plotted as function of σ . The observed reduction is systematic and the average is about 0.85. In the cases examined the factor c was comprised in the range 0.1 - 1.85.

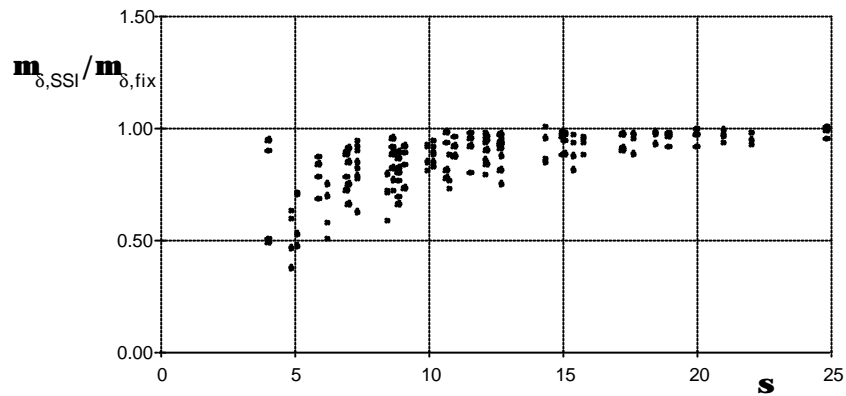


Figure 3.27. Ratio of max displacement ductility demands w/ and w/out SSI as function of σ

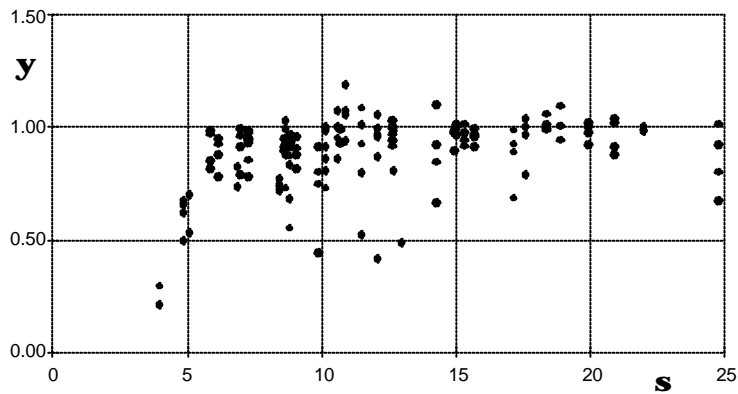


Figure 3.28. Ratio of plastic components of top displacements w/ and w/out SSI as function of σ

One may therefore conclude that the increase of the peak top displacement generally produced by the SSI is due to the rigid body motion components originating from the soil deformation at the foundation level, and not to greater inelastic demands at the base section. The inelastic demand does not show systematic dependencies from the parameters that regulate the SSI phenomenon, but is statistically lower (though to a small degree) in the case of a flexible foundation.

To further force this point, in Figure 3.28 the ratio ψ of the plastic components of the top displacements, with and without SSI effects, is plotted as function of σ . Practically all points lie below the line indicating unity, with an average of 0.90 and a c.o.v. of 0.18.

As a final remark, one might argue that the definition of the displacement ductility for the case of a compliant soil as given in Eq. (6) may not be totally appropriate, since it introduces displacement components not related to the state of strain of the structural part. If these components were eliminated from the definition, *i.e.*, if the results were plotted using the standard definition of displacement ductility (which accounts to putting $c = 0$ in Eq. (6)), the plot in Figure 3.29 is obtained. The ordinates have the same meaning as in Figure 3.27, that is the ratio μ^* of μ_δ for the SSI and the rigid-base cases (whose values are reported in Table 3.11). The points have a relatively low dispersion and the average value is 0.98.

The essence of what has been discussed thus far is that soil compliance does not appear to have a significant bearing on inelastic demand, at least for the simple structural types that have been considered.

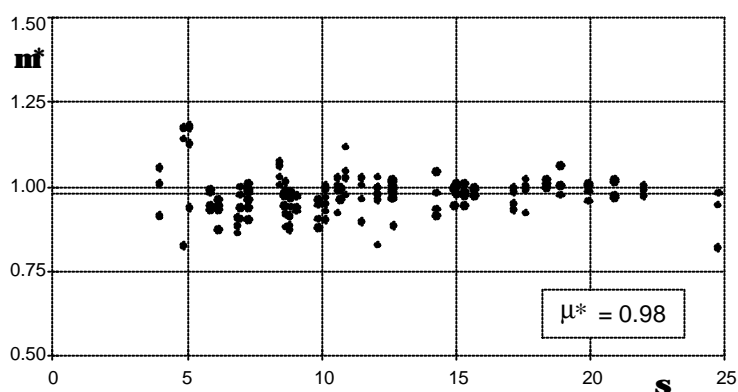


Figure 3.29. Ratio of max displacement ductility demands w/ and w/out SSI, evaluated neglecting the rigid-body components of the pier top displacement, as function of s

Table 3.11. Peak displacement ductility demand (fixed-base case)

H	Pier A deck a $\rho = 0.25$	Pier A deck a $\rho = 1.00$	Pier A deck. b $\rho = 0.25$	Pier A deck b $\rho = 1.00$	Pier B deck a $\rho = 0.25$	Pier B deck a $\rho = 1.00$	Pier B deck b $\rho = 0.25$	Pier B deck b $\rho = 1.00$
10	5.68	2.24	4.88	2.59	2.39	1.72	3.45	1.91
20	3.64	1.87	3.40	2.06	2.21	1.64	3.40	1.80
30	3.19	1.84	2.81	1.75	2.18	1.43	2.60	1.58
40	2.77	1.60	2.56	1.64	2.15	1.30	2.36	1.54
50	2.09	1.41	1.75	1.45	1.91	1.29	2.04	1.43

Since this fact is not commonly recognized, controversial opinions actually exist among specialists: it is then of importance to know whether the validity of the obtained results is restricted to the ranges of variation attributed to the parameters or, on the contrary, the results are expression of a trend having a character of stability.

To this end, additional “bounding” cases have been analyzed, in which the stiffness of the soil is decreased down to $G = 30$ MPa, and the intensity of the input is doubled to 0.7 g. In this way, the effects of soil compliance are magnified, and the structural response is moved deeper in the inelastic range.

The limit to 30 MPa ($V_S = 120$ m/s) has been set in consideration that it corresponds to about half of the value of V_S which in some recent seismic codes marks the separation between intermediate and soft soil conditions. Below this value, it is likely that site-specific soil amplification studies would be required, ruling out the recourse to standard response spectrum shapes. For these latter cases, which are outside the scope of the present work, indications of general validity do not seem possible.

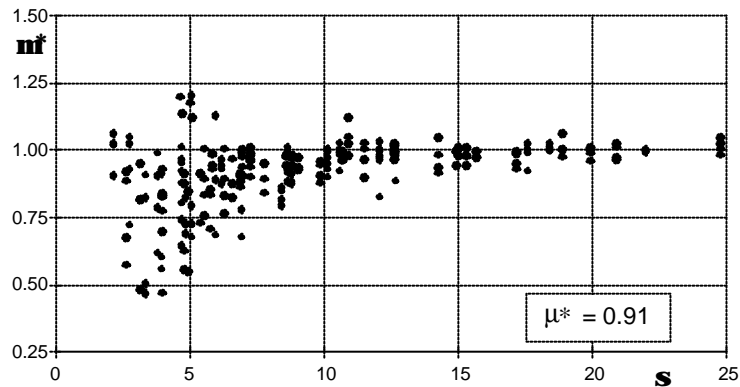


Figure 3.30. Ratio of max displacement ductility demands w/ and w/out SSI, evaluated as in Figure 3.29, as function of s : also the case $G = 30$ MPa is considered

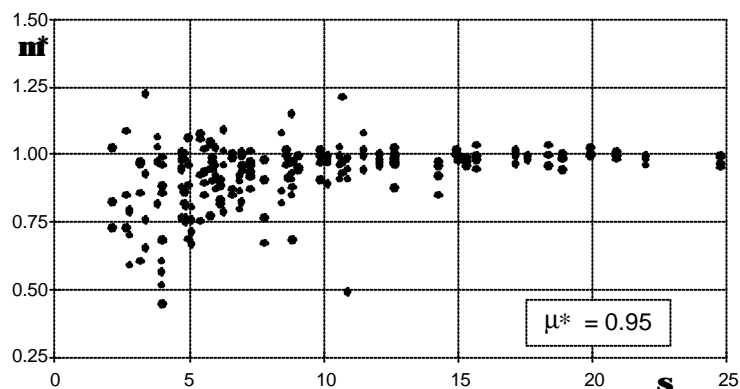


Figure 3.31. Ratio of max displacement ductility demands w/ and w/out SSI, evaluated as in Figure 3.29, as function of s : all cases are considered ($G = 30 - 100 - 300$ MPa), with peak ground acceleration set equal to 0.7 g

The results from the additional analyses are summarized in the two Figure 3.30 and Figure 3.31, which should be compared directly with Figure 3.29. In particular, Figure 3.30 includes all the old as well as the new cases ($G = 30$ MPa) with the peak ground acceleration (PGA) fixed at 0.35 g, while Figure 3.31 repeats the total number of cases for a PGA = 0.7 g. In both figures the results for $G = 30$ MPa are represented by the points corresponding to smaller values of σ , and they indicate a significant systematic decrease of the inelastic effects with the increased compliance of the soil.

The average values of all the ordinates (Figure 3.30) is 0.91 instead of 0.98, but for the new cases only it would be of the order of 0.8. Finally, comparison between the Figs. 12 and 13 indicates that the ratio of the ductility demands with and without consideration of SSI is virtually independent of the intensity of the shaking, that is to say, of the amount of ductility actually exploited.

3.2.4 Conclusions

A large parametric study has been undertaken with the purpose of determining the effects of SSI on the inelastic response of realistic cases of pier heights and shapes. Wide-band frequency content and adequate intensity of the seismic motion have led the response of the piers well in the inelastic range, with maximum curvature ductility demand in the order of 7.

The results indicate that while in most cases SSI produces an increase of the maximum displacements, this effect is not very significant and, furthermore, is only due to the rigid body components arising from the soil deformation at the base.

The inelastic demand in terms of curvature remains essentially unaffected by SSI, showing however a tendency to decrease. If the rigid body components are subtracted from the total displacements, then the displacement ductility demands on the piers are consistently also decreased by the SSI effects.

These conclusions have been proven to remain valid also in cases where soil compliance takes on values which are the lowest still compatible with the use of standard shapes of the response spectra, as well as for peak ground acceleration (0.7 g) close to the upper bound presently considered in areas of very high seismicity.

3.2.5 References

- Apsel, R. J., and Luco, J. E. (1987). "Impedance Functions for Foundations Embedded in a Layered Medium: an Integral Equation Approach", *International Journal of Earthquake Engineering and Structural Dynamics*, 15(1), 213-231.
- Applied Technology Council. ATC 3.06 (1983). "Tentative Provisions for the Development of Seismic regulations for Buildings", Palo Alto, California, August.
- Calvi, G. M., Ciampoli, M., and Pinto, P. E. (1990). "Guidelines for the Seismic Design of Bridges. Background Studies: Part 1", *European Earthquake Engineering* (2), 3-16.
- Castellani, A. (1970). "Foundation Compliance Effects on Earthquake Response Spectra", *Journal of Soil Mechanics and Foundation Division*, ASCE, 96(4), 1335-1355.

- EUROCODE No. 8: Structures in Seismic Regions - Design. Part 1: General and Buildings". (1988). Commission of the European Communities, Report EUR12266EN, May, Directorate General Telecommunications, Information Industries and Innovation, L-2920, Luxembourg.
- Gaitanaros, A. P., and Karabalis, D. L. (1988). "Dynamic Analysis of 3-D Flexible Embedded Foundations by a Frequency Domain BEM-FEM". *International Journal of Earthquake Engineering and Structural Dynamics*, 16(5), 653-674.
- Gazetas, G. (1975). "Dynamic Stiffness Functions of Strip and Rectangular Footings on layered Soil", S.M. Thesis, Massachusetts Institute of Technology.
- Gazetas, G. (1983). "Analysis of Machine Foundation Vibrations: State of the Art", *Soil Dynamics and Earthquake Engineering*, 2(1), 2-42.
- Luco, J.E. (1974). "Impedance Functions for a Rigid Foundation on a Layered Medium", *Nuclear Engineering and Design*, 31, 204-217.
- Parmalee, R. A., Perelman, D. S., Lee, S. L., and Keer, L. M. (1968). "Seismic Response of Structure Foundation Systems", *Journal of Engineering Mechanics*, ASCE, 94(6), 1295-1315.
- Priestley, M. J. N., and Park, R. (1987) "Strength and Ductility of Concrete Bridge Columns under Seismic Loading", *ACI Structural Journal*, 84(1), 61-76.
- Roesset, J. M., Whitman, R. V., and Dobry, R. (1973). "Modal Analysis for Structures with Foundation Interaction", *Journal of Structural Division*, ASCE, 99(3), 399-416.
- Tajimi, H. (1969). "Dynamic Analysis of a Structure Embedded in an Elastic Stratum", *Fourth World Conference on Earthquake Engrg.*, Editorial Universitaria, Santiago of Chile, 3, 53-70.
- Veletsos, A. S., and Wei, Y. T. (1971). "Lateral and Rocking Vibrations of Footings", *Journal of Soil Mechanics and Foundation*, ASCE, 97(9), 1227-1248.
- Veletsos, A. S., and Verbic, B. (1973). "Vibrations of Viscoelastic Foundations", *International Journal of Earthquake Engineering and Structural Dynamics*, 2(2), 87-102.
- Veletsos, A. S., and Meek, J. W. (1974). "Dynamic Behaviour of Building-Foundation Systems", *International Journal of Earthquake Engineering and Structural Dynamics*, 3(2), 121-138.
- Veletsos, A. S. (1977). "Dynamics of Structure-Foundation Systems", *Structural and Geotechnical Mechanics - A Volume honoring N.M. Newmark*, Ed. W.J. Hall, Prentice Hall, New Jersey, 333-361.
- Wolf, J. P., Darbre, G. R. (1984). "Dynamic Stiffness Matrix of Soil by the Boundary Element Method: Embedded Foundation", *International Journal of Earthquake Engineering and Structural Dynamics*, 12(3), 385-416.

3.3 Vertical oscillations

In view of the field evidence (Ono *et al.* 1996) of the damaging effects due to axial vibrations in vertical members of RC structures during past earthquakes, various authors have investigated this problem in the past few years. In particular, the effects of vertical ground motion components on buildings and bridges (Papazoglou and Elnashai 1996, Elnashai and Papazoglou 1997) have been studied. The ground motion vertical component tends, in general, to be ignored or underestimated in current seismic analysis of structures. On the contrary, some studies have shown that it has a considerable relevance, particularly in the field of soil-structure interaction (Mohammadioun 1997). A remarkable field evidence of this fact was found in the near past, during the Hyogo-ken Nanbu earthquake of 1995, where (JSCE 1995) ground vertical acceleration components experienced little attenuation from bedrock to ground surface (as opposed to horizontal ones), even in potentially liquefiable soils. As a consequence, high vertical seismic inputs on structures were observed and unusual failures of vertical members occurred.

While a number of studies has been presented on the effects of vertical ground motion on structures in general (Papalentiou and Roesset 1993), little or no attention has been dedicated to vertical accelerations induced in RC members by flexural cracking. Independently of the vertical ground motion input, this source of vertical impulses can cause particularly severe effects in some types of structures. For a realistic estimate of the global response of RC structures, the two components outlined above should be added together.

Most seismic codes do not give, in fact, specific recommendations on this issue. Nonetheless, structural members may experience sudden failures associated with instantaneous decay of shear or flexural strength due to high axial force fluctuations. As reported in (Elnashai *et al.* 1995), axial force fluctuations due to combined effects of vertical ground motion and bending-induced vertical accelerations may easily exceed $\pm 60\%$ of the static axial load. In these circumstances, the piers become obviously very vulnerable. Moreover, maximum bending-induced vertical accelerations should occur approximately at maximum horizontal response, therefore determining a case of extreme severity. The issue is particularly relevant when considering the performance of joints and bearings.

Scope of the present work is to quantify the component of vertical oscillations due to concrete cracking and rocking mechanism in bridge piers, with particular reference to systems in which the deck is made of multiple girders supported by large cap beams. In this kind of structures, very frequent in European and Japanese highway networks, bending-induced axial vibrations may have a significant effect on the general structural performance, including that of bearings. The frequency content and magnitude of the vertical motion associated with this effect is analyzed for different structures, with different natural periods. Typical existing viaducts, as well as similar structures, designed using Eurocode8 seismic code provisions (Eurocode 8 1994) are analyzed. A simplified model, based on the cracked section kinematics, is developed to predict the magnitude of bending-induced axial accelerations.

3.3.1 The analyzed structures: geometry and dimensioning

Three different structures, meant to be representative of typical prestressed concrete viaducts in seismic regions, have been analyzed. The three structures have the same 30 m span superstructure and different pier heights: 6, 12 and 18 m respectively. Each analyzed structure is supposed to be part of a viaduct made of a sequence of equal spans, simply supported on piers of similar heights. The analysis of the seismic response of these structures in the transverse direction is then carried out on a 2D schematization, taking into consideration one pier only with two half spans each side.

The superstructure, with a total platform width of 15.7 m, is made of a 0.25 m reinforced concrete slab connecting four prestressed concrete girders as shown in Figure 3.32. This deck configuration requires a 11.5 m wide cap beam, in order to seat four bearings with a center to center distance of 3.5 m. The weight of one span has been assumed equal to 6000 kN, therefore a vertical load of 1500 kN acts on each bearing support. An additional weight of 600 kN has been considered to account for the cap beam.

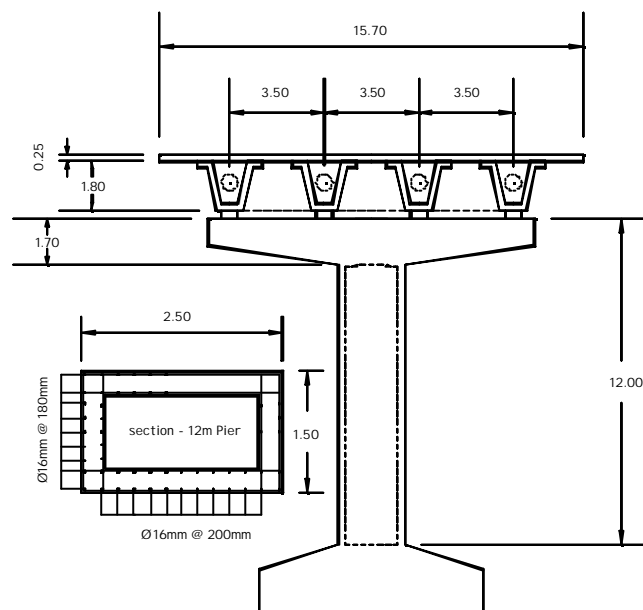


Figure 3.32. Pier type considered with superstructure.

Dimensioning of the pier cross section has been carried out so as to obtain a normalized axial load $P/(f'_c A_g) = 0.1$ under self weight alone, as typical for this kind of structures (f'_c is the unconfined concrete compression strength and A_g is the area of the gross section). The flexural capacity of the pier cross section, reflecting the actual situation of most existing viaducts, has been dimensioned according to allowable stress criteria. For each structure, the design moment is computed based on a constant response spectrum of 0.1g. The required flexural capacities are therefore

proportional to the pier height since the total mass is roughly the same for the three cases; the base bending moments are computed on a cantilever scheme, neglecting the influence of deck torsional inertia and cap beam flexibility.

The same hollow cross-section has been adopted in the three cases with different amount of longitudinal reinforcing steel ρ_l . Table 3.12 summarizes the main design characteristics.

Table 3.12. Pier geometry and mechanical properties

Pier Height [m]	Section dimensions [m]	Wall Thick. [m]	r_l [%]	M_y [kNm]	M_n [kNm]
6	2.5 x 1.5	0.3	0.35	9667	10166
12	2.5 x 1.5	0.3	0.70	12204	13939
18	2.5 x 1.5	0.3	1.00	14090	16929

Note that the longitudinal reinforcement ratios have been expressed as a function of the concrete section net area (excluding the hollow portion). The first yield moment M_y (bending moment at first yield of longitudinal rebars) and the nominal moment M_n (defined here as the bending moment at 5 times yield curvature) are indicated to conventionally define the mechanical properties.

The choice of this kind of structures, with extremely low longitudinal reinforcement, reflects the intention of approaching the problem from the assessment of existing bridge piers. The use of current design codes based on ultimate limit state analysis and period-dependent response spectra would lead in fact to different flexural capacities. For comparison, the design moments obtained using the EC8 Design Code (Eurocode 8 1994) for a peak ground acceleration of $0.35g$, are reported in Table 3.13.

Table 3.13. EC8 Dimensioning

Pier height [m]	M_d [kNm] - EC8	Behavior Factor q
6	13300	2.5
12	10941	3.5
18	10002	3.5

Following the EC8 design procedure, design moments M_d have been computed using modal analysis of the structure including cap beam flexibility and lumped masses with horizontal as well as vertical components. A reduced ductility level (behavior factor q) has been used for the 6m pier as suggested by the EC8 in case of squat members.

Shear dimensioning of the three structures is omitted since the investigations are focused on axial-flexural coupling, however it is assumed that adequate shear reinforcement is provided to ensure a flexural dominant response when large inelastic displacements occur.

Before analyzing the nonlinear behavior of these structures under a selected earthquake, it is interesting to see the results of the modal analysis to gain an insight on their dynamic properties. When these structures are modeled with realistic flexibility for the cap beam and both vertical and rotational masses are included to account for the vertical loads of the superstructure acting on the bearing supports, higher modes significantly influence the global behavior. Especially in the case of the short pier, a significant percentage of horizontal modal mass is found in the second mode, which is of the double bending type. In the following, the important consequences of these aspects on the phenomenon of bending-induced axial vibrations will be discussed.

Two different configurations have been analyzed for the structural systems under consideration: the first assumes an infinitely rigid superstructure (rigid deck model), the second assumes a realistic flexibility for the superstructure (flexible deck model). The corresponding mass and stiffness distributions are represented in Figure 3.33 and Figure 3.34, respectively. The main difference between the two models is that vertical masses are rigidly connected to the pier cap beam in one case, and via elastic supports (simulating the deck flexibility in the vertical plane) in the other case.

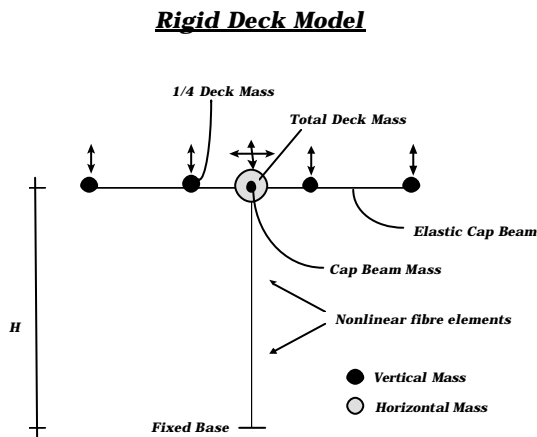


Figure 3.33. Rigid deck model.

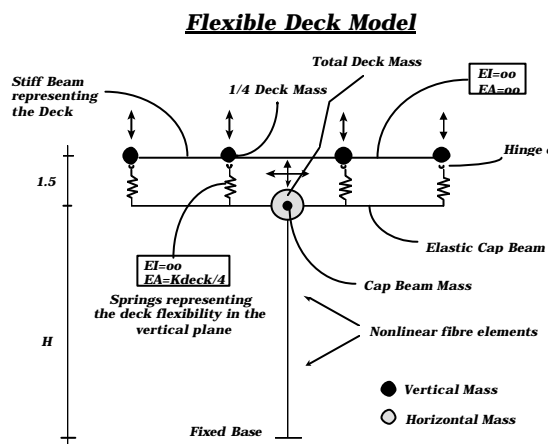


Figure 3.34. Flexible deck model.

Natural frequencies and participating masses in x and y direction are indicated in Table 3.14 for the two models. The mode shapes of the 6 m pier structure are depicted in Figure 3.35 in the case of rigid deck assumption and in Figure 3.36 in the case of flexible deck assumption.

Table 3.14. Results of modal analyses

Pier height [m]	Mode number	Participating Mass % - X dir.	Participating Mass % - Y dir.	T [sec.]
<i>Rigid Deck</i>				
6	1	51.0	-	0.583
	2	48.0	-	0.123
	3	-	76.0	0.070
12	1	79.9	-	1.190
	2	20.1	-	0.232
	3	-	90	0.090
18	1	89.9	-	1.960
	2	10.1	-	0.303
	3	-	95	0.104
<i>Flexible Deck</i>				
6	1	36.0	-	0.637
	2	-	87.0	0.322
	3	59.0	-	0.243
12	1	76.2	-	1.220
	2	23.1	-	0.363
	3	-	84.0	0.326
18	1	88.7	-	1.970
	2	11.1	-	0.427
	3	-	82.0	0.330

As anticipated before, it can be noted that the horizontal mass has a relatively low contribution to the first mode in the 6 m pier (especially in the flexible deck assumption). Rotation of the pier top is very limited in this case, thus enforcing a reverse bending behavior. Concrete cracking will therefore take place in the top and bottom sections, possibly increasing the hammering effect at bending reversal. In the 12 m and 18 m piers instead, the deck rotational inertia is not significant when compared to the pier flexibility. The pier deforms mainly in simple bending with concrete cracking located at pier base only.

In all linear elastic modal analyses, cracked stiffnesses have been assumed for the pier section using the expression proposed in (Kowalsky *et al.* 1995).

Particular attention has been given to the modeling and to the distribution of lumped masses, since axial vibrations on the pier might excite vertical vibration modes. For this reason it has been decided to also investigate the influence of deck flexibility.

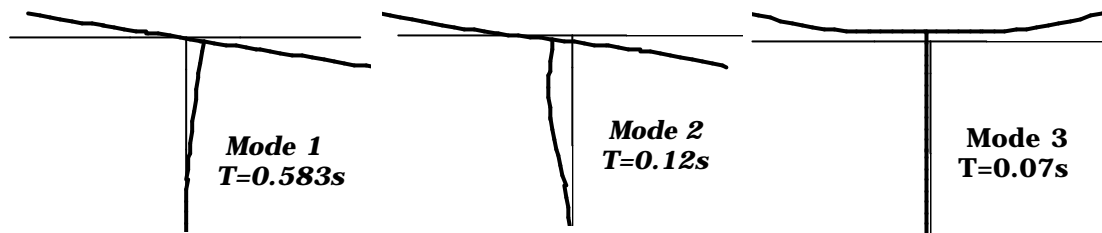


Figure 3.35. Rigid Deck Model – Modal Shapes.

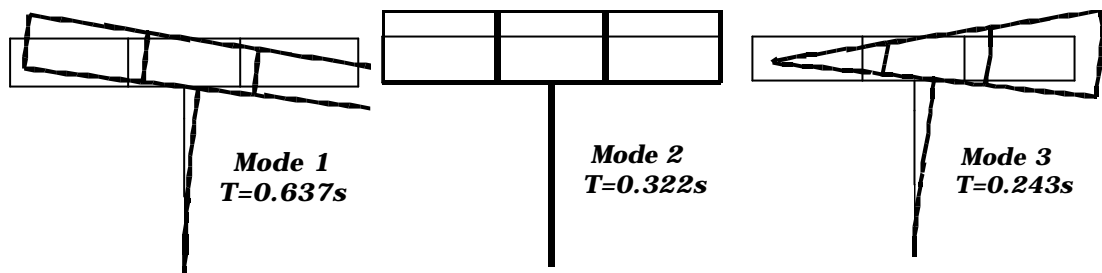


Figure 3.36. Flexible Deck Model – Modal Shapes

3.3.2 The numerical models for non-linear time-history analyses

The three structures have been modeled using a flexibility-based fiber beam element developed by the authors (Petrangeli 1996, Petrangeli and Pinto 1998). The peculiarity of this element being that equilibrium, compatibility and constitutive equations are satisfied along the element, at each load increment, using an equilibrium based iterative solution (Petrangeli and Ciampi 1997). This feature is particularly relevant to the problem under consideration since, using the traditional stiffness approach, the axial force impulse associated to the non-linear flexural behavior would result in an internal element unbalance which would not be correctly integrated along the element length.

Each pier has been modeled using two fiber beam elements with three, four and five integration Gauss points (monitoring sections) for the 6, 12 and 18 m piers respectively. The number of integration points has been selected in order to attain the same numerical precision in integrating the longitudinal strain field in the three structures, while maintaining the same tributary length to each integration point. The integration of the element strain field would require in fact a larger number of integration points for the shorter piers which have a predominant double bending type of deformation compared to the single bending type of the taller ones. The opposite would be required to keep a constant tributary length for each monitoring

section. In fact, in the short pier shear cracking will take place over at least 2/3 of column height, indicating the presence of a larger plastic hinge region. On the other side, the extremely low longitudinal reinforcement ratio will localize plastic hinging at the base. As a consequence, it is believed that, in this specific case, the suggested integration scheme applies successfully to all three piers.

The pier cap has been modeled using linear elastic elements with equivalent mechanical properties. Rigid offsets have been introduced to account for the pier cross section width and the pier cap height.

Constitutive models for concrete and reinforcing steel use state-of-the-art uniaxial stress-strain relationships based on the work of Mander *et al.* (1988) and Menegotto and Pinto (1977), respectively. In the concrete model, a crack-bridging branch has been introduced, providing a smooth transition between the tensile and the compression branches. This feature was required in order to avoid an overestimation of the impulsive component of vertical acceleration at crack closure which the original concrete model could have caused as a result of the abrupt transition between the zero stiffness, zero stress cracked state and the reloading branches to compression.

Mechanical properties of the steel have been assumed as follows: yield strength = 400 MPa, ultimate strength = 570 MPa, Young's modulus = 200000 MPa, ultimate strain = 0.10. Mechanical properties of the concrete are: unconfined strength = 35 MPa, confined strength = 42 MPa, strain at ultimate stress = 0.0035, Young's modulus = 30000 MPa, tensile strength = 2.5 MPa, fracture energy = 0.1 kN/m.

The deck horizontal mass (600 t) has been placed in one node only (at pier top, as indicated in Figure 3.33 and Figure 3.34) to avoid axial (horizontal) vibrations in the pier cap beam; vertical masses have been placed instead at each beam support (150 t each) and at pier top (60 t). In the rigid deck model, the mass of the superstructure is rigidly connected to the cap beam (Figure 3.33). In the flexible deck model instead, deck vertical masses are connected to the cap beam via elastic supports (Figure 3.34). The stiffness of these elastic supports has been assumed such that the vertical oscillation of the rigid horizontal beam representing the superstructure (upper beam in Figure 3.34), has the same period of the first vertical mode of a typical prestressed concrete deck of 30 m span; this period is estimated at 0.3 sec.

The first mode natural frequencies computed with modal analysis have been used to quantify the viscous component of the structural damping. A viscous damping, in addition to the hysteretic one, has been considered in fact by means of a mass proportional damping factor C , where, for elastic systems, $C = 2\xi\omega m$ with m the mass, ξ the percentage of critical damping and ω the circular frequency. A value of 3% of critical damping has been assumed in our case to be representative of all viscous damping components acting within the elastic structural response. This value does add up to the significant energy dissipation provided by the hysteretic behavior of concrete in tension (fracture and bond energy). It mainly accounts for the damping effects caused by deformation in the bearings, in the cap beam and in the deck.

3.3.3 Results of non-linear analyses

A set of non-linear time-history analyses using the general purpose F.E. code FIBER (Petrangeli 1996) has been performed using an accelerogram compatible with the EC8 response spectrum with $PGA=0.35g$ as horizontal ground motion input. The vertical component has been purposely ignored in a first stage, while it has been included in a second set of analyses to evaluate the coupling effect on the pier axial response. A generated accelerogram, rather than a natural one, has been considered for the reason of simplicity. Several different ground motion inputs should be considered in fact for a more complete analysis.

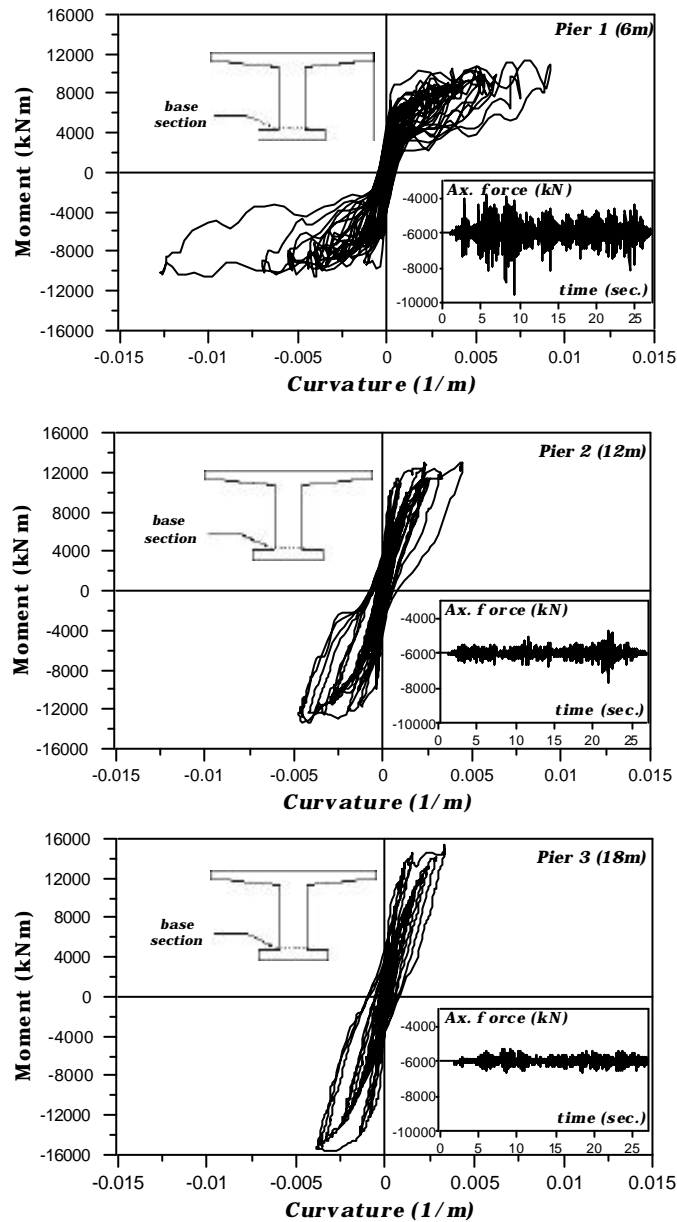


Figure 3.37. Moment curvature cycles.

Under the imposed horizontal ground motion, large inelastic deformations occur in the three structures. In all cases a plastic hinge forms at pier base, where longitudinal reinforcing bars reach (for the 6 m pier) a maximum strain of approximately 2.0%. Maximum base shears are 2500 kN, 1250 kN and 980 kN for the 6 m, 12 m and 18 m pier respectively.

Moment curvature cycles at pier base are plotted in Figure 3.37 for the rigid deck models. In the same graphs the corresponding axial force time history is also reported. The largest ductilities are found for the 6 m pier with a curvature ductility $\mu_\phi = 8\div 9$. For this pier, the inflection point is located at 0.54H (with H full height of the pier), while for the 12 m and 18 m is 0.66H and 0.69H respectively. Note that the maximum axial force fluctuations are found for the 6 m pier (+58% in compression and -35% in tension). None of the piers experienced steel yielding in the top section below the pier cap beam.

In the 6 m pier a global displacement ductility of about 5.0 is reached, compared to 2.5 and 2.0 in the 12 m and 18 m pier respectively. This remarkable difference in global damage is due to the inappropriate strength provided by the allowable stress design criterion and to the flat design spectrum adopted (0.1g). However, this result reflects the actual situation on existing viaducts where squat piers tend to have very light longitudinal reinforcement ratios.

Maximum displacements drifts are in a range of 0.75% to 1% of pier height. Maximum vertical displacements at external bearing locations are insensitive to the pier height and are always around 0.05 m.

The maximum response of the three structures is summarized in Figure 3.38 and Figure 3.39 for the rigid deck and flexible deck model respectively. Maximum accelerations at bearing locations are indicated for each structure as a function of their fundamental elastic flexural period. It can be seen that in the proposed examples, the deck horizontal maximum acceleration does not vary significantly with pier height while the vertical acceleration does, due to varying axial/flexural period ratio as well as cap beam width/pier height ratio.

As anticipated before, vertical acceleration response is particularly high for the squat pier, where a peak value of 0.9g is found at external bearing location. Generally, bending-induced vertical accelerations decrease with increasing pier height as also confirmed by other analyses. Vertical acceleration of the outer bearings includes in fact both an amplification of the pier vertical acceleration due to the pier cap beam flexibility and a “geometric” component due to the rotational acceleration of the pier cap beam itself. This component obviously decreases with decreasing cap beam width/pier height ratio. The distribution of the vertical acceleration along the cap beam from pier top to external bearing location can be easily be derived from the graphs of Figure 3.38. In Figure 3.38 and Figure 3.39 the elastic response spectrum (with 5% damping) corresponding to the generated accelerogram used in the analyses as ground motion input, is also reported.

Minor differences between the rigid and flexible deck models in terms of maximum accelerations are detected, although for the 18 m pier, the vertical acceleration on the outer bearing is higher due to dynamic amplification.

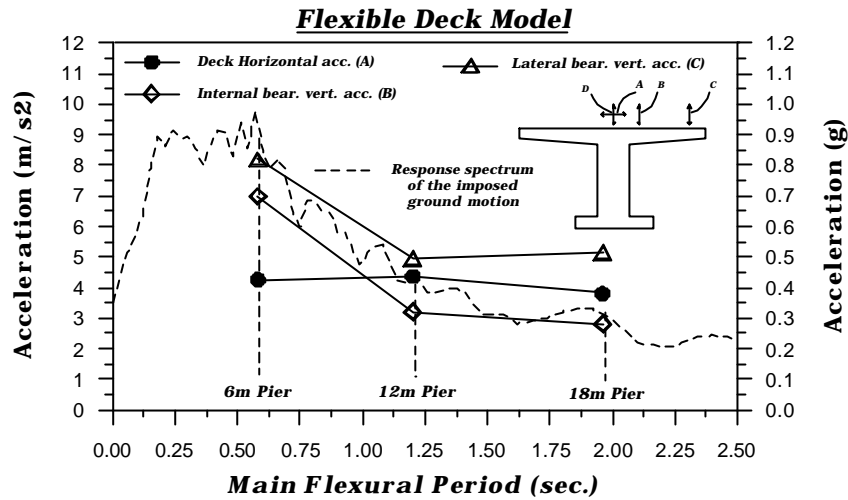


Figure 3.38. Maximum response for rigid deck model.

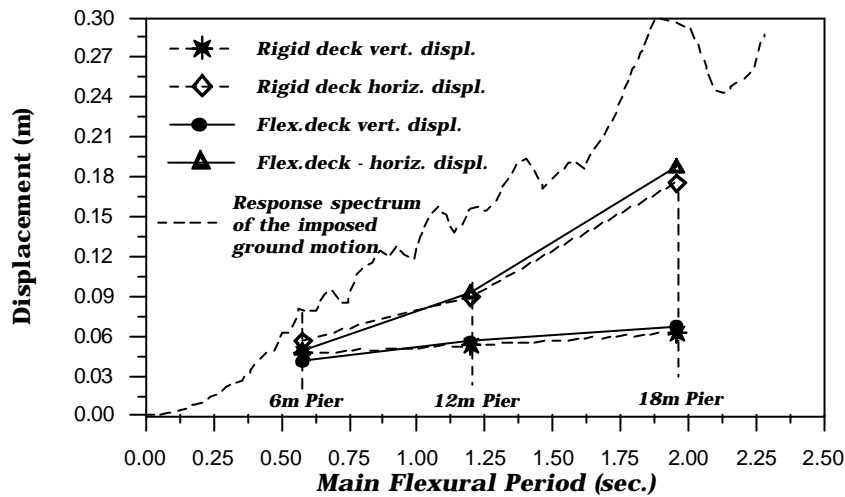


Figure 3.39. Maximum response for flexible deck model.

Maximum vertical response at pier top for the flexible deck model (Figure 3.38) has been omitted since no significant mass is lumped in that location. Results seem to indicate that, in this kind of structures, the deck flexibility does not influence the structural response in the vertical plane. However, it has to be noted that other ground motions might induce a different response, leading to different conclusions.

Maximum displacement envelopes are shown in Figure 3.39 for rigid and flexible deck models. It should be noted that both the maximum horizontal and vertical displacements mainly depend on pier flexural response, which is driven by the horizontal mass inertia and does not significantly vary with deck flexibility. The same result is found for the three structures, indicating that deck flexibility has little influence on displacements in a wide range of pier flexural periods.

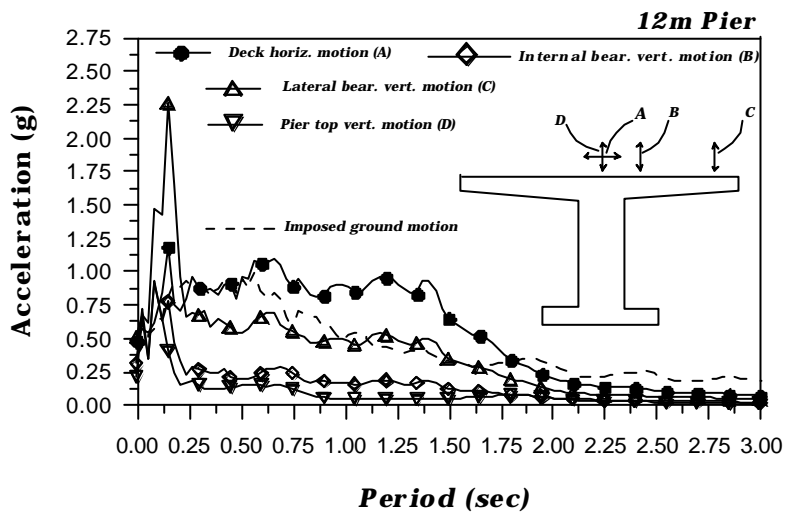
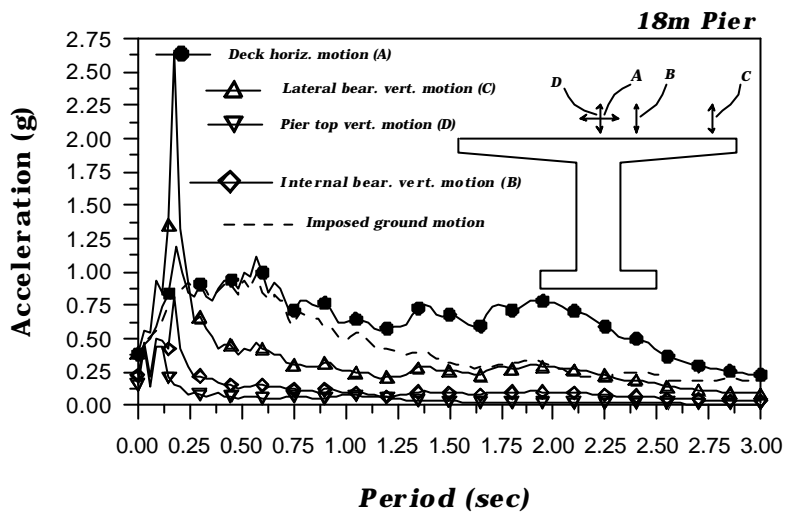
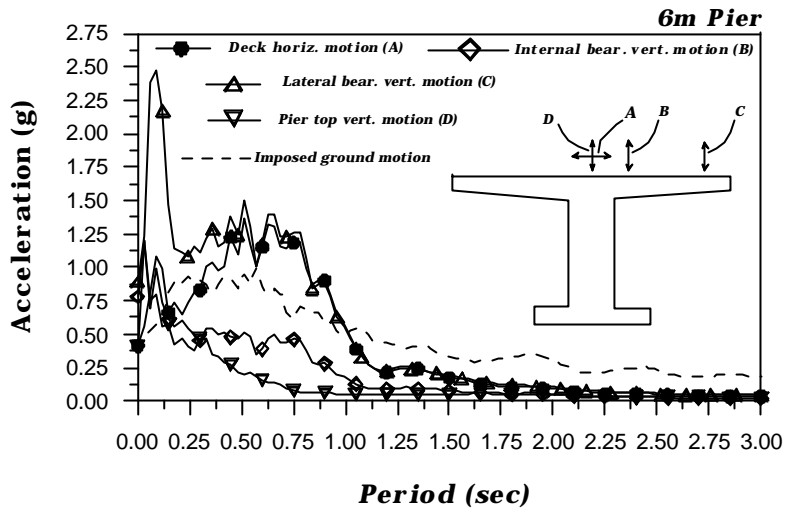


Figure 3.40. Acceleration response spectra (5% damping) of the horizontal and vertical deck motion at each bearing location and at pier top.

In the following, the analysis of the frequency content of vertical motion will be carried out for the rigid deck model only, since minor differences are found for the flexible deck case. The plots of Figure 3.40 show the acceleration response spectra (with 5% damping) of the horizontal and vertical deck motion recorded at each bearing location and at pier top. The ground motion spectrum is plotted for comparison. These spectra provide an idea of the frequency content and magnitude of the structural response. Their values for $T=0$ correspond to the maximum accelerations plotted in Figure 3.38 and Figure 3.39 which are the ones to be used to evaluate the maximum vertical and horizontal force transmitted between deck and piers. In Figure 3.40, the peak below 0.2 sec. At the outer bearing location is clearly due to the selective amplification of the first vertical vibration mode of the pier (see mode 3 in Figure 3.35). It can be seen that the response spectra of vertical accelerations tend to be more concentrated in a narrow band of frequencies as the pier flexural period increases, while those of horizontal accelerations tend instead to have a constant level of response (*i.e.*, frequency independent) around 0.75g

It can be noted from the results discussed above that on external bearings vertical acceleration response is equal or greater (up to a factor of 2 for the 6 m pier) than the horizontal one. With the ratio between vertical and horizontal force on bearings (R_v/H) falling to such low values, unseating phenomena are likely to occur. The most significant examples of these low values occurred during the analysis are reported in Table 3.15 for both internal and external bearing in the 6 m pier. The situation at maximum response ($t=24.54$ sec) is also reported. Note that the vertical reaction under self weight alone is equal to 1500 kN.

Table 3.15. Forces on bearings during earthquake response

Time (sec.)	External Bearing		Internal Bearing	
	Shear (kN)	Load (kN)	Shear (kN)	Load (kN)
5.23	-469	305	-469	1119
8.22	43	2639	43	1932
8.26	-572	556	-572	1500
24.54	291	1172	291	1388

Response at 8.22 sec shows a case, opposite to the ones discussed above, in which the maximum vertical reaction of the bearings is nearly twice the static one. The full time history of the vertical reaction has been plotted as a function of the corresponding shear force in Figure 3.41. During the analysis the external bearing experiences a minimum ratio between vertical reaction R_v and shear force H equal to 0.65, while the internal bearing has a minimum value of 2.26.

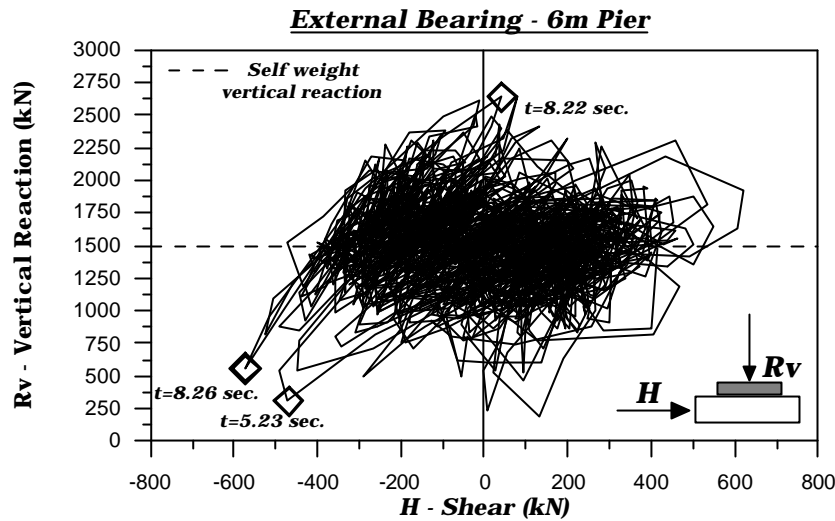


Figure 3.41. Vertical reaction as function of the corresponding shear force.

This result confirms that bending-induced axial vibrations can produce severe effects when amplified by the presence of wide cap beams. Moreover, when the pier has a low aspect ratio, the level of axial accelerations induced by flexural cracks is particularly high.

If the time-history analyses of the three structures are repeated using the longitudinal reinforcing ratios found dimensioning according to EC8 (see Table 3.13), lower accelerations are found. Displacement ductilities at maximum response are 2.5, 3.5 and 4.0 for the 6, 12 and 18 m pier respectively, showing a remarkable accuracy of the EC8 methodology. Vertical accelerations at pier top are 20-25% lower with respect to the piers previously analyzed, showing that no direct proportionality can be established between axial impulse and pier ductility. This is confirmed by the fact that a 50% reduction in ductility for the EC8-6 m pier (with respect to the pier of previous analyses) is associated to a 20% reduction of the vertical accelerations while in the EC8-18 m the same reduction in vertical acceleration is associated with a doubling of displacement ductility. It is thus confirmed that the pier aspect ratio and the maximum horizontal acceleration response, rather than the global ductility level, have influence on the axial vibrations.

The effect of the vertical ground motion component can now be introduced to attempt a quantification of the relative importance of the two different sources of axial vibrations.

The analyses carried out above are repeated again for the first set of structures (*i.e.*, allowable stress designed) with inclusion of a vertical motion with peak ground acceleration equal to 2/3 of horizontal peak acceleration. This ground motion component is still compatible with the EC8 response spectrum and has the same duration and starting time step of that of horizontal motion. In these analyses the two sources of axial vibrations are therefore taken into account and their effects appear combined. Maximum acceleration results are reported in Figure 3.42. The values are

in all cases larger than the corresponding ones in Figure 3.38, where the ground vertical acceleration is absent, but it is perhaps surprising to note that the order of magnitude has not changed. In other words, from the ‘spot’ cases examined it would seem that the predominant contribution to the vertical response accelerations comes from the rocking mechanism, not from the vertical acceleration input. This is probably a hasty conclusion, not supported by adequate evidence and generality of the cases under consideration, but it is at least an indication that if vertical acceleration are of some consequence for the resistance of bridge piers and deck supports, the rocking mechanism effect should not be neglected.

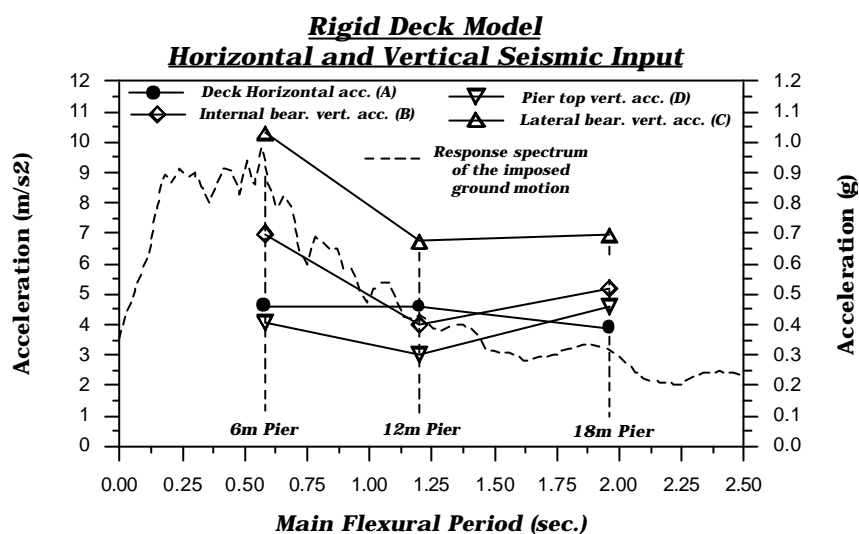


Figure 3.42. Maximum acceleration results.

3.3.4 Simple mechanical model for axial vibrations

An attempt to establish a closed form approximate relationship between these axial vibrations and the pier flexural response will be presented herein. The main assumption is that cracked sections can be treated as rigid bodies during their motion induced by flexural response. In this idealization the sections rotate about a point that coincides with the position of the neutral axis. The impact of the sections during bending reversal will be assumed elastic with initial conditions (*i.e.*, values of velocity and acceleration) found from the rigid body motion assumption.

Assuming that plane sections remain plane the following relation holds between the curvature χ and axial elongation ϵ_p for a RC section:

$$\epsilon_p = |\chi| \left(k - \frac{1}{2} \right) d \quad (1)$$

where k is a scalar parameter ($0 \leq k \leq 1$) defining the neutral axis depth $(1-k)d$.

Let us now assume the flexural response of a generic section be described by a simple sinusoidal function as follows:

$$\chi(t) = \chi^{\max} \sin\left(\frac{2\pi t}{T_f}\right) \quad (2)$$

with T_f being the predominant flexural period of the pier. The section axial deformation, according to (1), can therefore be written:

$$\varepsilon_p(t) = \chi^{\max} \left| \sin\left(\frac{2\pi t}{T_f}\right) \left(k - \frac{1}{2}\right) d \right| \quad (3)$$

where the absolute value of the sinusoidal function is taken since the axial elongation is always positive.

In order to obtain simple expressions for the velocity and the acceleration of the axial strain \mathfrak{S} we assume that the position of neutral axis is fixed (*i.e.*, k is constant), even though with increasing curvature the neutral axis tends to shift outwards (*i.e.*, k increases). Axial displacement, axial velocity and axial acceleration as a function of time have been qualitatively plotted in Figure 3.43.

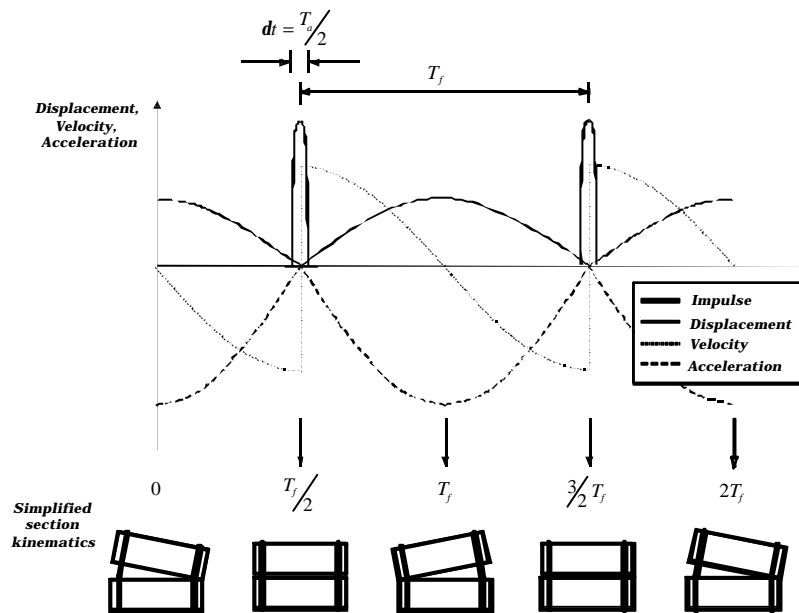


Figure 3.43. Axial displacement, axial velocity and axial acceleration as function of time.

The velocity is discontinuous for $t = nT_f/2$ (with $n=1,2,\dots$). In these characteristic points, the section is subjected to a vertical impulse which reverses the displacement direction, changing sign to the axial velocity. These points correspond to the crack closure and the sudden shift of the neutral axis from one side of the section to the other (as depicted in Figure 3.43 in the section kinematics). These

impulses are the main cause of the vertical oscillations observed in the analyses. Outside these points, the section is still subjected to a vertical acceleration as the result of the flexural response. This component of the acceleration, smaller than the impulsive one at bending reversal, is found as the second derivative of β). Its maximum value is :

$$\left[a^{\max} \right]_{\left(t \neq n \frac{T_f}{2} \right)} = \left[\left(\frac{d^2 \epsilon_p}{dt^2} \right)^{\max} \right]_{\left(t \neq n \frac{T_f}{2} \right)} = \chi^{\max} \frac{4\pi^2}{T_f^2} \left(k - \frac{1}{2} \right) d \quad (4)$$

In the following it will be shown that this component of the vertical acceleration is negligible when compared to that due to the impulse at bending reversal (see Eq.(7)).

In order to obtain an estimate for the magnitude of this impulse, the assumption of rigid body motion must be relaxed and the impact at crack closure treated as an elastic rebound. We assume therefore that this elastic impact takes place in a finite time interval Δt . With these hypotheses, the impulse amplitude can be computed as follows :

$$m\Delta v = \int_{\Delta t} f dt = \int_{\Delta t} m a dt \quad (5)$$

where m is the mass and f the inertia force. The velocity variation Δv that takes place during the time interval Δt can be set according to Fig.14 by computing the right and left limit of the first derivative of (3) for $t \approx nT_f/2$. The time interval Δt is tentatively set equal to one half the fundamental axial period of the pier-deck system ($\Delta t = T_a/2$), so that Δt corresponds to the compressive semi-cycle of the pier elastic rebound. Therefore, the velocity variation within the specified time interval is :

$$\Delta v = 2 \left[\frac{d\epsilon_p}{dt} \right]_{\left(t \rightarrow n \frac{T_f}{2} \right)} = 2\chi^{\max} \frac{2\pi}{T_f} \left(k - \frac{1}{2} \right) d \quad (6)$$

If we assume that the impulse has a sinusoidal shape, we obtain from (5):

$$\left[a^{\max} \right]_{\left(t = n \frac{T_f}{2} \right)} = \frac{\pi}{2} \frac{\Delta v}{\Delta t} = \frac{\pi}{2} \frac{2}{T_a} \chi^{\max} \frac{4\pi}{T_f} \left(k - \frac{1}{2} \right) d \quad (7)$$

where the $\pi/2$ factor is found by integrating the sinusoidal impulse over the time interval Δt in (5).

A simple relation between the pier maximum horizontal acceleration response and the curvature maximum acceleration can be easily obtained by assuming the flexural deformations taking place in a localised plastic hinge at the column base. In this case we obtain that the maximum acceleration at pier top is :

$$a_h = \beta(T_f) = l_{cp} H \left(\frac{d^2 \chi}{dt^2} \right)^{\max} = l_{cp} H \chi^{\max} \frac{4\pi^2}{T_f^2} \quad (8)$$

where l_{cp} is the plastic hinge length, H the pier height and $\beta(T_f)$ is the ordinate of the acceleration response spectrum for the pier predominant flexural period. The simplification associated with this kinematic mechanism is valid for single column bents in general, also for members that tend to oscillate in double bending, because maximum curvature at column base is, in most cases, one order of magnitude greater than that at column top, where yielding of steel seldom occurs.

Similarly, if the largest axial deformations take place within the plastic hinge region, as it is for the plastic rotations, the maximum value of the impulsive ($a_{v,i}$) component of the pier vertical acceleration can be written as:

$$a_{v,i} = l_{cp} \left[\left(\frac{d^2 \varepsilon_p}{dt^2} \right)^{\max} \right]_{\left(t = n \frac{T_f}{2} \right)} = \left(\frac{T_f}{T_a} \right) \beta(T_f) \left(k - \frac{1}{2} \right) \frac{d}{H} \quad (9)$$

The following remarks need to be made:

- Eq. (9) has been derived by using the velocity reversal found with a rigid section kinematics hypothesis and therefore it should provide an upper bound estimate of the axial impulses
- Eq. (9) should not be taken as an estimate of the structural response in the vertical direction but rather as an estimate of the axial input associated to the flexural response. However, large amplifications of this vertical input are unlikely since these vertical impulses have the same frequency of the pier flexural response, which is generally smaller than both pier and superstructure vertical frequencies.

The numerical analyses presented above seem to show that, in spite of the crude approximation used in deriving Eq. (9), it still encompasses the governing variables of the problem. A comparison between the values found with Eq. (9) and the results of the non-linear analyses for the rigid deck model are presented in the following Table 3.16. Horizontal and vertical accelerations found from time-history analyses are indicated with β_h and β_v respectively. The flexural period of the piers T_f has been calculated by using the secant flexural stiffness at maximum response (average stiffness). The axial period T_a instead has been computed using the cracked elastic stiffness and the neutral axis depth at maximum response. In this case study, both secant stiffness and neutral axis depth, were available from the results of the non-linear analyses; for design purpose instead, they should be calculated by using the assumed structural ductility or the maximum expected displacement, if a displacement-based design approach is being used.

Table 3.16. Numerical analysis versus prediction with Eq. (9)

Pier Height [m]	β_h [m/sec ²]	β_v [m/sec ²]	T_a [sec]	T_f [sec]	(k -1/2)	$a_{v,i}$ [m/sec ²]	$\beta_v / a_{v,i}$
6	4.12	3.96	0.10	0.69	0.27	3.19	1.24
12	4.72	2.00	0.13	1.21	0.22	2.0	1.00
18	3.83	1.43	0.15	1.92	0.18	1.22	1.17

The results from Table 3.16 seem to indicate the soundness of the assumptions used to derive Eq. (9) and the capability of it to provide a correct estimate of the magnitude of these axial vibrations. This is demonstrated by the stability of the computed values, which show a constant ratio with the results of the non-linear analyses, although referred to piers of different period and different response in both horizontal and vertical direction.

From the cases presented above it seems that little or no amplification of the axial motion is found between pier base and pier top. However, it is important to note that the axial input found with (9) might have been overestimated due to the assumption of section rigid body motion.

Results obtained with Eq. (9) are strongly affected by the value assumed for $\beta(T_f)$. In our case this value was given by the results of non linear time history analyses (β_h), whereas in design it must be found from a design spectrum based on the maximum expected ductility (*i.e.*, behavior factor). Accuracy on $a_{v,i}$ is therefore strongly influenced by the accuracy of the design methodology in estimating the maximum horizontal response.

3.3.5 Conclusions

Although experimental results are needed to confirm the predictions of the numerical study presented herein, there is no doubt that a significant contribution to the vertical acceleration in RC piers subjected to seismic excitation is due to the rocking mechanism. This contribution is neglected in ordinary design, based on linear modal analysis and response spectra. The intensity of this vertical acceleration may instead be greater than the structural response to the vertical component of the seismic input motion. In fact, the vertical acceleration associated with the rocking mechanism is generated by the horizontal acceleration response of the pier which is always greater than the horizontal ground motion input.

The effect of this additional motion in the vertical direction can be particularly severe on deck bearings, which may experience the maximum horizontal shear forces associated with very low vertical reactions. This mechanism may provide an additional explanation for the widespread phenomenon of bearing failure and deck unseating observed during past earthquakes.

When proposing a simple predictive equation for the quantification of this phenomenon, to be used together with the commonly accepted procedure of seismic design based on modal analysis and response spectra, one should take into account the following features of this mechanism:

Direct proportionality seems to exist between bending-induced vertical oscillations and the horizontal acceleration of the pier, while the same cannot be said for flexural damage (*i.e.*, maximum displacement ductility).

The structural response to this axial input may have a larger impact than the response to the vertical component of the seismic ground motion since it has the same frequency as the flexural response.

Based on the preliminary investigations presented herein, it seems that eq. (9) provides a reasonable estimate of the vertical accelerations in bridge piers of current use subjected to horizontal seismic input motion only. This equation could be used as a starting point towards the definition of a design formula for the quantification of this additional vertical component to be used in the dimensioning of bridges in seismic areas. The effect of maximum ductility and pier cross section configuration should be further investigated and possibly included in the equation. Results of the present model would greatly benefit from comparisons with experiments performed on shaking tables.

3.3.6 References

- Elnashai, A.S., Bommer, J.J., Baron, C.I., Lee, D., Salama, A.I., (1995), "Selected Engineering Seismology and Structural Engineering Studies of the Hyogo-ken Nambu (Great Hanshin) Earthquake of 17 January 1995", *Research Report ESEE-92/2*, Imperial College, Sept. 1995.
- Elnashai, A.S., Papazoglou, A.J. (1997), "Procedure and Spectra for Analysis of RC Structures Subjected to Strong Vertical Earthquake Loads", *Journal of Earthquake Engineering*, Vol.1, n.1, pp. 121-155, Imperial College Press.
- EUROCODE 8 "Design Provisions for Earthquake Resistance of Structures" ENV 1998-2: Bridges. CEN, Brussels, October 1994.
- JSCE (Japan Society of Civil Engineers), "The Great Hanshin Earthquake, January 17, 1995", Preliminary Report, 1995.
- Kowalsky, M.J., Priestley, M.J.N., Macrae, G.A. (1995) "Displacement Based Design of RC Bridge Columns in Seismic Regions", *Earthquake Engineering and Structural Dynamics*, Vol.24, pp. 1623-1643.
- Mander, J.B., Priestley, M.J.N., and Park, R. (1988). "Theoretical Stress-Strain Model for Confined Concrete." *Journal Struct. Engrg.*, ASCE, 114(8), 1804-1826.
- Menegotto, M. and Pinto, P.E. (1977). "Slender RC Compressed Members in Biaxial Bending." *J. Struct. Engrg.*, ASCE, 103(3), 587-605.
- Mohammadioun, B. (1997), "Nonlinear Response of Soils to Horizontal and Vertical Bedrock Earthquake Motion", *Journal of Earthquake Engineering*, Vol.1, n.1, pp. 93-119, Imperial College Press.

- Ono, K., Kasai, H., Sasagawa, M. (1996), "Up-down Vibration Effects on Bridge Piers", *Special issue of Soils and Foundations*, Japanese Geotechnical Society, pp. 211-218.
- Papalentiou, C., Roesset, J.M. (1993), "Effect of Vertical Accelerations on the Seismic Response of Frames", *Structural Dynamics – Eurodyn '93*, Balkema, Rotterdam.
- Papazoglou, A.J., Elnashai, A.S., (1996), "Analytical and Field Evidence of the Damaging Effect of Vertical Earthquake Ground Motion", *Earthquake Engineering and Structural Dynamics*, Vol.25., pp. 1109-1137.
- Petrangeli, M. (1996). "Modelli Numerici per Strutture Monodimensionali in Cemento Armato" *Dissertation*, University of Rome "La Sapienza", Rome, Italy. (in Italian).
- Petrangeli, M. and Ciampi, V. (1997). "Equilibrium based numerical solutions for the nonlinear beam problem", *Int. Journal for Num. Meth. in Engrg.*, 40(3), 423-438.
- Petrangeli, M. and Pinto, P.E. (1998). "A Fiber Beam Element for cyclic bending and shear." *Proc. of "EURO-C 1998"*, BadGastein, Austria.

4 UPGRADING OF BRIDGE PIERS WITH FRP

4.1 Properties and behavior of FRP-confined concrete

A first step towards the comprehension of the response of bridge piers wrapped with FRP should aim at defining the behavior of concrete confined with FRP sheets. Although several experimental studies on this subject have been carried out (Fardis and Khalili 1981, Saadatmanesh *et al.* 1994, Howie and Karbhari 1995, Nanni and Bradford 1995, Seible *et al.* 1995, Picher *et al.* 1996), studies aiming at obtaining reliable and accurate numerical models are still in a development phase. An FRP jacket, as opposed to a steel one that applies a constant confining pressure after yield, has an elastic behavior up to failure and therefore exerts a continuously increasing confining action. The amount of this action depends on the lateral dilation of concrete, which in turn is affected by the confining pressure. A major obstacle to the development of a reliable concrete model is the lack of a simple analytical expression describing the interaction between the laterally expanding concrete and the confining device.

4.1.1 Basis model for unconfined concrete

A general but simple constitutive model for unconfined concrete under uniaxial compressive loading (Pantazopoulou and Mills 1995) is used as a basis for the following developments. In this model, the uniaxial stress response f'_c of plain concrete under compressive axial strain ϵ_c is described by

$$f'_c = E_{\text{sec}} \epsilon_c \quad E_{\text{sec}} = E_c \frac{1}{1 + \beta \epsilon_A} = E_c \frac{1}{1 + 2\beta \epsilon_l} \quad (1a,b)$$

The innovative aspect is that the area strain ϵ_A is taken as a measure of the internal damage from cracking, which reduces the current secant modulus E_{sec} , starting from the initial tangent modulus E_c . The constant β (here, the reciprocal of that given in the original paper is considered) is a property of concrete and will be discussed below. Note that in (1b) the assumption of radial symmetry ($\epsilon_A = 2\epsilon_l$) is adopted, which allows to point out the dependence on the lateral strain ϵ_l . Sign convention is: compressive ϵ_c and f'_c are negative and dilating ϵ_A and ϵ_l are positive.

The variation of the unrestrained lateral strain ϵ_l under the imposed axial strain ϵ_c is evaluated with an experimentally derived formula (Figure 4.1), which, under the assumption of radial symmetry, is expressed as

$$\epsilon_l = -\nu \epsilon_c - \frac{1}{2}(1 - 2\nu)\alpha \epsilon_{co} \frac{\langle \epsilon_{\text{lim}} - \epsilon_c \rangle^2}{(\epsilon_{\text{lim}} - \alpha \epsilon_{co})^2} \quad (2)$$

where ν = Poisson's ratio, $\epsilon_{\text{lim}} \approx -0.001$ = limit axial strain beyond which microcracking starts, and $\alpha \epsilon_{co}$ = axial strain at volume strain $\epsilon_V = \epsilon_A + \epsilon_c = 0$,

being $\alpha = 0.9 \div 1.0$ for unconfined concrete and $\epsilon_{co} \approx -0.002$ = strain at unconfined peak-stress f'_{co} . The McAuley brackets $\langle x \rangle = 0.5(x + |x|)$, indicate that the squared term is only considered when $\epsilon_c < \epsilon_{lim}$.

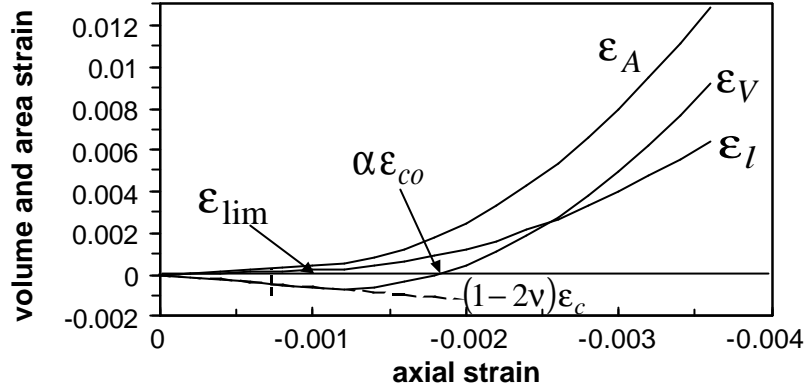


Figure 4.1. Volume, area and lateral strain vs. axial strain for unconfined concrete.

Pantazopoulou and Mills (1995) proposed to evaluate the constant β from the volume fraction of paste and the water-cement ratio. However, it seems more convenient to express β in terms of readily available mechanical properties of the unconfined concrete, such as f'_{co} , ϵ_{co} and E_c . Here, a formula is suggested that is valid for a wide range of different concrete types. To this aim, it is noted that, since β is a constant, *i.e.*, independent of ϵ_c , it can be calculated from (1b) in correspondence to a convenient value of ϵ_c . Selecting $\epsilon_c = \epsilon_{co}$, one has

$$\beta = \frac{E_c/E_{sec0} - 1}{2\epsilon_{lo}} \quad (3)$$

where

$$E_{sec0} = \frac{f'_{co}}{\epsilon_{co}} \quad \text{and} \quad \epsilon_{lo} = -\nu\epsilon_{co} - \left(\frac{1}{2} - \nu\right)\alpha\epsilon_{co} \frac{\langle \epsilon_{lim} - \epsilon_{co} \rangle^2}{(\epsilon_{lim} - \alpha\epsilon_{co})^2} \quad (4a,b)$$

so that β is only dependent on the unconfined concrete properties f'_{co} , ϵ_{co} , E_c , ν and α . Alternatively, an explicit formula can be derived by letting $\alpha = 1.0$, for which one has $\epsilon_{lo} = -\frac{1}{2}\epsilon_{co}$, and the constant β becomes:

$$\beta = \frac{1}{\epsilon_{co}} - \frac{E_c}{f'_{co}} = \frac{E_c}{|f'_{co}|} - \frac{1}{|\epsilon_{co}|} \quad (5)$$

Note that β can be expressed as a function of only the unconfined concrete strength f'_{co} , by assuming $\epsilon_{co} = -0.002$ and $E_c = 5700\sqrt{|f'_{co}|}$ (MPa):

$$\beta = \frac{5700}{\sqrt{|f'_{co}|}} - 500 \quad (f'_{co} \text{ in MPa}) \quad (6)$$

even though it should be remarked that this formula is correct if the estimated value of E_c is close to the actual elastic modulus.

4.1.2 Concrete model with elastic confinement

Eq. (2) models the lateral expansion as function of the monotonic axial compressive strain, only for the case of laterally unrestrained (unconfined) concrete. In the case of confined concrete, this relation should be modified to account for the confinement pressure exerted by the confining device, either constant, as applied by yielding devices (steel), or increasing, as applied by elastic devices (FRP). It is clear that, due to the experimental nature of the formula, any modification should be substantiated by quite a large amount of experimental data for different levels and types of confinements. An alternative and more general procedure is here proposed, by which the lateral dilation of concrete is implicitly derived through equilibrium of the dilating concrete and the confining device.

The starting point is a well-known stress-strain model for confined concrete (Mander *et al.* 1988a,b), which has been extensively tested against experimental data. The model, also of the $f'_c - \epsilon_c$ type, is based on the formula (Popovics 1973)

$$f'_c = \frac{f'_{cc} \cdot x \cdot r}{r - 1 + x^r} \quad (7)$$

$$x = \frac{\epsilon_c}{\epsilon_{cc}} \quad \epsilon_{cc} = \epsilon_{co} \left[1 + 5 \left(\frac{f'_{cc}}{f'_{co}} - 1 \right) \right] \quad r = \frac{E_c}{E_c - E_{sec}} \quad E_{sec} = \frac{f'_{cc}}{\epsilon_{cc}} \quad (8)$$

where ϵ_{cc} = compressive strain at confined peak strength f'_{cc} . The confined peak strength f'_{cc} is expressed in terms of a *constant* effective confining pressure f_l as:

$$\frac{f'_{cc}}{f'_{co}} = 2.254 \sqrt{1 + 7.94 \frac{f_l}{f'_{co}}} - 2 \frac{f_l}{f'_{co}} - 1.254 \quad (9)$$

The effective confining pressure is calculated as function of the transverse steel volumetric ratio ρ_s and its yield stress f_s , as follows:

$$f_l = \frac{1}{2} k_e \rho_s f_s \quad \text{with} \quad \rho_s = \frac{4 A_s}{s d_s} \quad (10)$$

where k_e = arching-effect coefficient, s = spacing (pitch) of hoops (spiral), and d_s = diameter of hoops (spiral).

In recent years, researchers have attempted to extend Mander's model to predict the behavior of concrete accounting for the effect of confinement provided by elastic FRP jackets. A major obstacle is that this model is based on a *constant* value of the confining pressure throughout the loading history. In reality, passive

confinement increases as concrete expands laterally, its amount depending on the stress-strain law of the confining device. For the case of steel transverse reinforcement, the constant confining pressure assumption is realistic when the steel is in the yield phase: therefore, Mander's model correctly represents the behavior of steel-confined concrete, except for the initial phase when steel is still elastic. Conversely, FRP behaves elastically until failure, and the inward pressure increases continuously, so that this assumption is not appropriate. Therefore, the following approach is taken.

Eqs. (1a,b) are rewritten as

$$E_{\text{sec}}(\epsilon_c, f_l) = \frac{f'_c(\epsilon_c, f_l)}{\epsilon_c} \quad \epsilon_l(\epsilon_c, f_l) = \frac{E_c - E_{\text{sec}}(\epsilon_c, f_l)}{2\beta E_{\text{sec}}(\epsilon_c, f_l)} \quad (11a,b)$$

and merged into a single equation

$$\epsilon_l(\epsilon_c, f_l) = \frac{E_c \epsilon_c - f'_c(\epsilon_c, f_l)}{2\beta f'_c(\epsilon_c, f_l)} \quad (12)$$

where the dependence of the quantities f'_c and ϵ_l on the current strain ϵ_c and the confining pressure f_l is rendered explicit. The constant β is evaluated as proposed in the previous section.

Once ϵ_l is calculated from (12), the strain ϵ_j in the confining jacket can be found (e.g., for the case of axially loaded concrete cylinders it is simply: $\epsilon_j = \epsilon_l$), along with its current stress $f_j = E_j \epsilon_j$, with E_j = the modulus of the composite material of the jacket. The corresponding confining pressure f_l can be evaluated analogously to (10) as

$$f_l = \frac{1}{2} \rho_j f_j = \frac{1}{2} \rho_j E_j \epsilon_{j=l} \quad \text{with} \quad \rho_j = \frac{4t_j}{d_j} \quad (13)$$

where it should be noted that $k_e = 1$ for jackets.

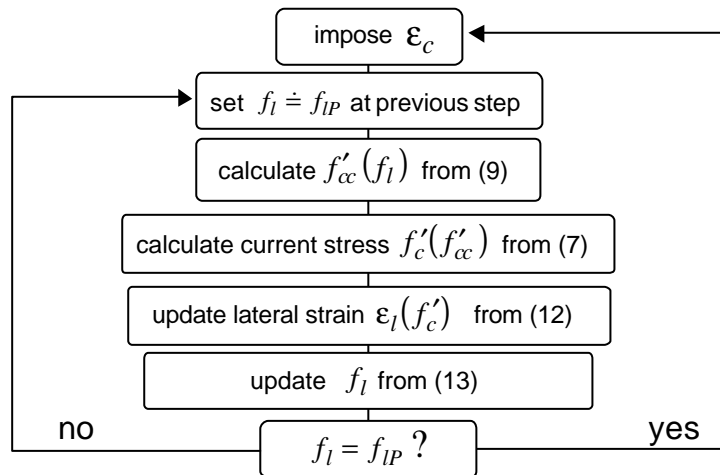


Figure 4.2. Iterative procedure.

This updated value of f_l can be used for a new estimate of ε_l through (12), giving rise to an iterative procedure (Figure 4.2) until f_l converges to a stable value. The whole procedure is repeated for each ε_c , over the complete stress-strain curve. This latter can be regarded as a curve crossing a family of Mander's curves, each one pertaining to the level of confining pressure corresponding to the current lateral strain. The stress-strain characteristics of the confining mechanism are explicitly accounted for, while the lateral strain of concrete is implicitly obtained through the iterative procedure. All numerical tests have shown that convergence is very fast.

4.1.3 Some considerations on modeling concrete confined with steel or FRP

The proposed model is here used to simulate the monotonic behavior of concrete confined with three different jacket types: steel, carbonfiber (CFRP) and fiberglass (GFRP). The purpose of these comparisons is to identify, mainly from a qualitative standpoint, the main aspects of the confinement action mechanisms in the three cases and compare the relative effectiveness of the three materials, before proceeding to model the experimental results.

The unconfined concrete properties of this example are: $f'_{co} = 35$ MPa, $\varepsilon_{co} = 0.002$, $E_c = 29,580$ MPa, $\nu = 0.20$, and $\alpha = 0.90$, therefore $\beta = 303$ through (3) and (4a,b). The FRP jackets consist of plies with 0° winding angle, whose mechanical properties are listed in Table 4.1 along with those of steel. It is remarked that the same confinement volumetric ratio ρ_j is considered in the three cases. In this example and the following tests, all quantities related to the FRP material (E_j , f_{ju} and ε_{ju}) are computed through the Classical Lamination Theory (see, e.g., Kim 1995) from the characteristics of each ply.

For steel-confined concrete, the ultimate compressive axial strain is computed through an experimentally derived formula (Seible *et al.* 1995a):

$$\varepsilon_{cu} = 0.004 + 1.4 \frac{\rho_j f_{ju} \varepsilon_{ju}}{f'_{cc}} \quad (14)$$

where f_{ju}, ε_{ju} = steel yield strength and ultimate strain, respectively, and f'_{cc} = confined concrete strength, computed with (9) and (13) with $\varepsilon_j = \varepsilon_{ju}$.

For FRP-confined concrete, the ultimate compressive axial strain of concrete is considered to be attained when:

$$\varepsilon_l = \varepsilon_{ju} \quad (15)$$

that is, when the lateral strain of concrete reaches the ultimate or allowable strain of the FRP material (under multiaxial state) and the jacket fails (no progressive ply failure is considered). This definition of failure exploits the characteristic of the proposed model, in which the lateral strain is tracked stepwise. It will be used in the parametric study presented in the next section to arrive at an explicit predictive equation of the ultimate strain of concrete.

Table 4.1. Properties of confining devices (E_j = elastic modulus, f_{ju} = yield or ultimate strength, ϵ_{ju} = ultimate strain, ρ_j = confinement volumetric ratio).

Jacket material	Fiber/resin	E_j (MPa)	f_{ju} (MPa)	ϵ_{ju} (%)	ρ_j (%)
steel	--	204,000	440	12.0	1.60
Carbonfiber (CFRP)	AS / Epoxy	138,000	1447	1.05	1.60
Fiberglass (GFRP)	E-glass / Epoxy	38,600	1062	2.75	1.60

In all the next graphs, differences in behavior are evidenced for the three jacket types considered. All the stress and strain quantities are normalized with respect to f'_{co} and ϵ_{co} , respectively. In Figure 4.3 (top, left), the stress-strain relation is shown. Here, a fundamental difference can be observed: the FRP-confined concrete shows a continuously increasing branch, as opposed to the steel-confined one, which, after reaching the peak strength, decays on a softening branch. As suggested by (1b), concrete degradation is proportional to the lateral strain: the increasing confinement action of the elastic FRP limits the lateral strain thus delaying the degradation; on the other hand, when steel yields, which occurs at 2.5 normalized axial strain, degradation of concrete takes place, because steel offers a zero stiffness to the lateral dilation of concrete.

The idea emerges from these graphs, which will be confirmed in the next sections, that CFRP should be used to provide concrete with higher strength increase and moderate ductility, whereas GFRP should be used to provide higher ductility and moderate strength increase. As regards the ultimate strain, and therefore the ductility attained through the confinement action, it should be noted that, notwithstanding the low values of ϵ_{ju} of the FRP-jackets, in these cases the ultimate strain is comparable or even greater than that obtained through the use of a ductile confining device, *i.e.* steel. This supports the consideration (Mirmiran *et al.* 1996) that the energy-balance approach (Mander *et al.* 1988a), which reckons the concrete ductility proportional to the energy stored in the confining device, cannot be extended to the case of FRP. In fact, the energy stored in the steel, the CFRP, and the GFRP jackets is, respectively: 51.8 MPa, 7.6 MPa, 14.6 MPa, and the latter two would give rise to ultimate concrete strains significantly lower than those actually observed and obtained through (15).

In order to account for this different behavior, it has been proposed (Seible *et al.* 1995b) to adopt the same predictive equation as (14) with a coefficient 2.5-2.8 instead of 1.4. However, in the following sections it will be shown that, when FRP jackets are used, the ultimate axial strain of concrete is only weakly governed by the ultimate confinement pressure (proportional to $\rho_j f_{ju}$), whereas it is mostly dependent on the ultimate deformation. This is proven by the fact that the fiberglass-confined specimen shows an almost twice as large deformability than the carbonfiber-confined one, although the ultimate confinement pressure of the latter is roughly 50% larger. Following these considerations, in the next sections, a different predictive equation will be derived, consistently with the actual mechanics of the confining device.

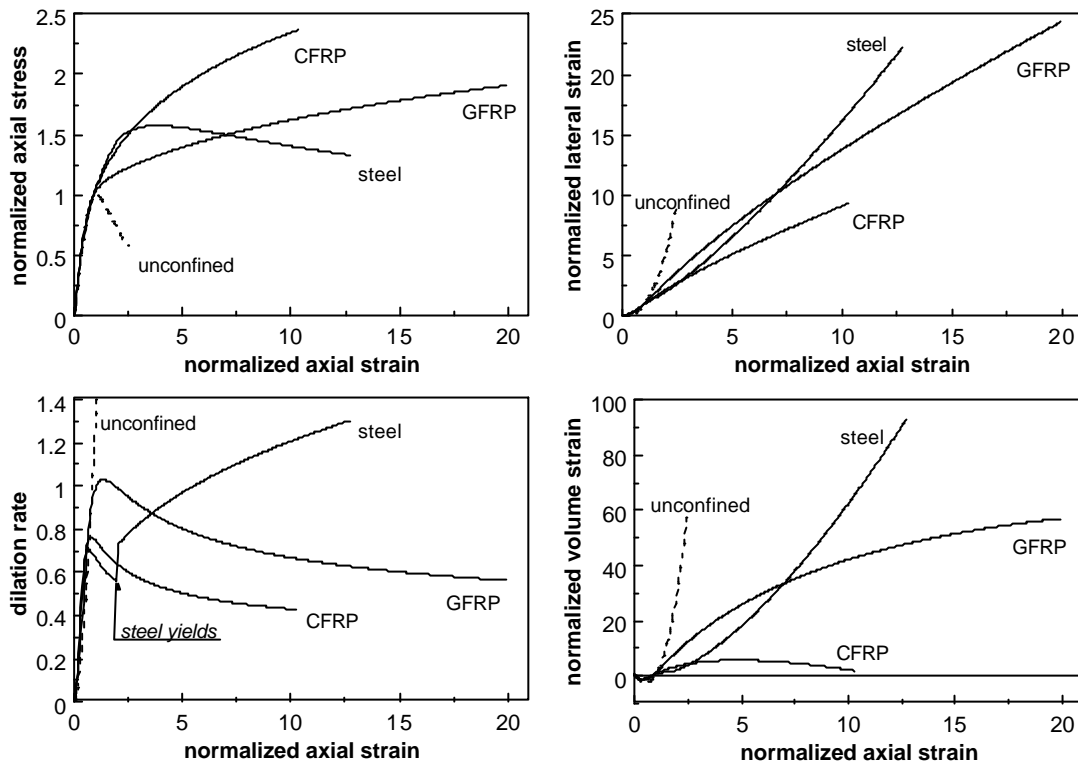


Figure 4.3. Modeling of behavior of concrete confined with steel, CFRP and GFRP: axial stress vs. axial strain (top, left), lateral strain vs. axial strain (top, right), volume strain vs. axial strain (bottom, left), dilation rate vs. axial strain (bottom, right).

In Figure 4.3 (top, right), the lateral-axial strains relation is shown. It can be observed that the branches slope depends on the stiffness of the confining device (also observed in the previous diagram): steel and CFRP start with almost the same slope, but after steel yields at 2.5 normalized axial strain, it departs towards higher lateral strains. GFRP shows a more stable behavior, in the sense that it starts with a higher slope (meaning that concrete has a higher initial lateral dilation), which however remains constant until the jacket fails. CFRP reduces the initial lateral strain, but its effectiveness has a shorter duration, due to its lower ultimate strain ϵ_{ju} .

This can be better appreciated in Figure 4.3 (bottom, left), where the dilation rate $\mu = \Delta\epsilon_l / \Delta\epsilon_c$ (lateral strain increment $\Delta\epsilon_l$ per axial strain increment $\Delta\epsilon_c$) is given as function of the axial strain. It is seen that when steel yields a discontinuity occurs, due to the abrupt change in modulus; after this, the dilation rate increases indefinitely. Conversely, for FRP, it constantly decreases towards an asymptotic value. Note that the position of the point where the confinement action starts becoming effective (*i.e.*, when the branches depart from the unconfined one) depends on the stiffness of the confining device: the GFRP-confined concrete departs later than the other two. This is the point where a sufficient lateral pressure develops that prevents the lateral dilation of concrete from increasing unrestrained.

In Figure 4.3 (bottom, right), it is interesting to observe from the volume strain vs. axial strain curve that for the CFRP jacket the volumetric strain first decreases, as expected, then reverts to zero and beyond a certain level of axial strain the ever increasing confinement pressure curtails the volumetric expansion and inverts its direction.

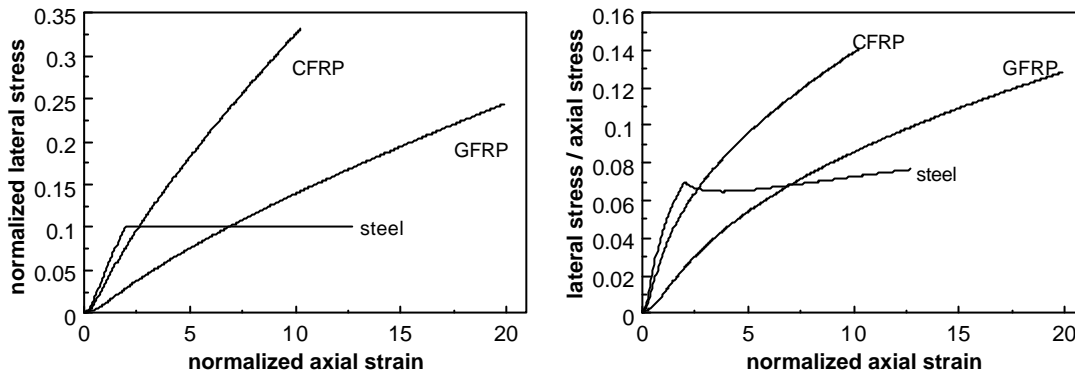


Figure 4.4. Comparison of confinement effectiveness.

In Figure 4.4, left, the confinement effectiveness (lateral stress vs. axial strain) for all three types of jackets is compared. It is explicitly shown what expected, that is, before yielding the steel jacket exerts a higher confining action, which however remains constant after yield, whereas the FRP jackets show a monotonically increasing confinement, thus arriving at applying a confinement action twice (GFRP) or thrice (CFRP) that of steel, with the same volumetric ratio ρ_j . In Figure 4.4, right, it is interesting to compare the jacket effectiveness expressed in terms of ratio of the lateral stress to the *current* axial stress. It is seen that the increase in the steel jacket effectiveness after yield is only due to the softening behavior of concrete, whereas in the other two cases it is the elastic behavior of the FRP jackets that increases the ratio. Here it should be evident how the two FRP materials reach almost the same level of effectiveness, but at different axial strain levels, which again renders more attractive the use of GFRP jackets that also exploit ductility while maintaining the same effectiveness of CFRP jackets.

From these results some very preliminary conclusions can be drawn, which however do not lack a certain generality, also considering that the values selected for the FRP materials are deemed to be representative of a large class of composite materials that are used for wrapping interventions. The effectiveness of an FRP confinement is mainly to ascribe to the modulus and the ultimate strain rather than to its strength. Thus, it can be affirmed that GFRP wrapping provides concrete with a more “effective” confinement than CFRP (even more, if cost considerations are taken into account) in terms of strength increase and ductility enhancement. These considerations will be confirmed in the next sections where comparisons with test results are carried out and predictive equations are developed.

4.1.4 Comparison with experimental results

Generally, in experimental tests performed on axially loaded cylindrical concrete specimens wrapped with FRP sheets, the measured quantities are: axial stress, axial strain and radial strain (equal to the transverse strain in the jacket). According to (15), failure of the wrapped specimen is expected when the radial strain ϵ_r equals the jacket ultimate strain ϵ_{ju} . However, experimental evidence shows that failure mostly occurs at lower radial strains. This reduction is due to the fact that FRP jackets undergo a triaxial stress state.

This is shown in Figure 4.5, where the concept of *composite action* is introduced, which denotes the ability of the jacket of providing transverse confinement and, at the same time, longitudinal load-carrying capacity. This latter depends on the bond interface characteristics, which in turn depend on a large number of factors, such as stiffness of the glue layer between jacket and concrete specimen, roughness of jacket and concrete surface, and bond transfer length.

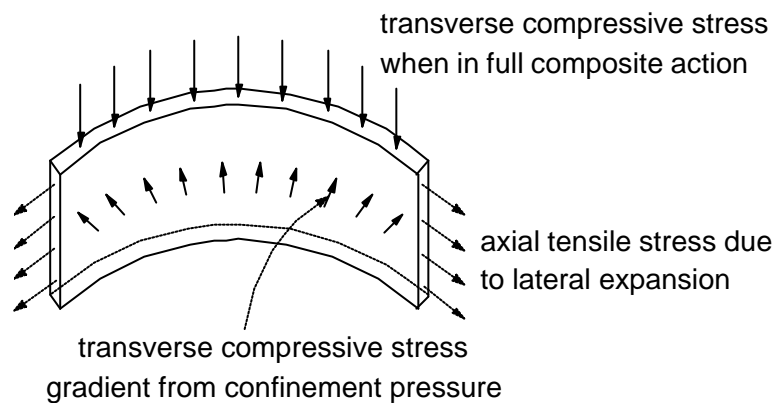


Figure 4.5. Triaxial state of stress in FRP jackets.

In case of no composite action, the jacket only undergoes transverse strains and therefore can only fail in extension mode, due to either fiber collapse or delamination between plies. Moreover, if one wants to consider the transverse compressive stress gradient in the jacket due to the confinement pressure (Figure 4.5), failure occurs when the concrete radial strain ϵ_r reaches a value even slightly lower than ϵ_{ju} . In case of full composite action, the jacket undergoes both transverse and longitudinal strains. The extensional ultimate stress and strain are then reduced, with potential microbuckling and delamination to develop. Thus, failure of the specimen occurs at even lower radial strains than in case of no composite action.

The above considerations will help the interpretation of the following correlation studies, where three sets of tests on FRP-confined concrete specimens are used as benchmarks for the proposed model.

4.1.4.1 Tests by Picher et al. (1996)

Tests were carried out on five concrete cylinders (152 mm in diameter and 304 mm in length): one unconfined and four confined with different configurations of carbon-fiber sheets. The sheets consisted of three layers, wrapped around the concrete specimens with winding angles: $[0^\circ_3]$, $[0^\circ, \pm 6^\circ]$, $[0^\circ, \pm 12^\circ]$ and $[0^\circ, \pm 18^\circ]$. The unconfined concrete properties were: $f'_{co} = 39.7$ MPa, $\epsilon_{co} = 0.002$, $E_c = 31,500$ MPa, $\nu = 0.20$ and $\alpha = 1.0$. Through (5) it was computed: $\beta = 294$.

Table 4.2. Results of experiments and of analyses with the proposed model.

Cylinder	E_j (GPa)	experiment			analysis		
		f_{cu}/f'_{co}	ϵ_{cu} (%)	ϵ_{lu} (%)	f_{cu}/f'_{co}	ϵ_{cu} (%)	ϵ_{lu} (%)
unconf.	0.0	1.00	0.20	0.65	1.00	0.20	0.65
C18	70.2	1.16	0.66	0.50	1.19	0.58	0.50
C12	77.4	1.24	1.03	0.64	1.26	0.75	0.64
C6	81.9	1.32	0.88	0.72	1.31	0.86	0.72
C0	83.0	1.41	1.07	0.84	1.35	1.01	0.84

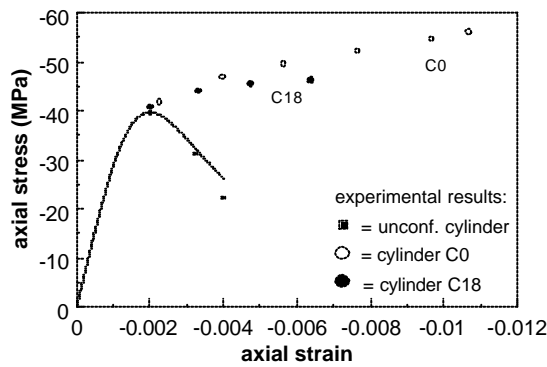


Figure 4.6. Axial stress vs. Axial strain.

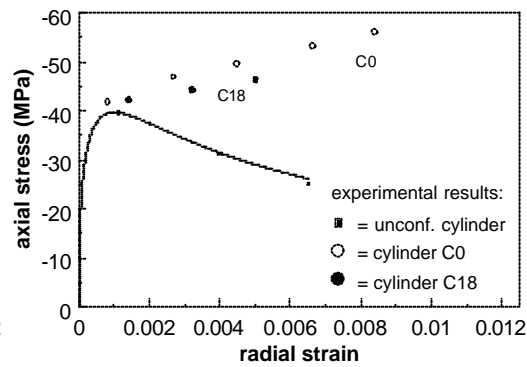


Figure 4.7. Axial stress vs. Radial strain.

The experimental ultimate strain of the CFRP-sheet with 0° winding angle was 1.5%, which coincided with the value given by the manufacturer. However, the concrete cylinders failed at lower radial strain values (0.84%), because the sheets were in full composite action with the concrete (a thin layer of concrete glued to the innermost composite layer was always observed on the failed specimen). The observed failure modes under composite action clearly show a load-carrying action of the sheets in the axial direction, which reduces the ultimate stress and strain in the radial direction. Therefore, in these correlation studies, the ultimate strains of the sheets were taken equal to the values of the ultimate lateral strain measured in the experiments (fifth column in Table 4.2), and not equal to those given by the

manufacturer. Therefore, the purpose of these comparisons regards essentially the ultimate characteristics (*i.e.*, strength and strain) of concrete.

As it can be seen in Table 4.2 and Figure 4.6 and Figure 4.7, the agreement between analytical (solid lines) and experimental results (markers) is very satisfactory.

4.1.4.2 Tests by Kawashima et al. (1997)

Kawashima *et al.* (1997) performed a set of experiments on cylindrical reinforced concrete specimens, confined with carbon fiber sheet jackets with different elastic moduli and volumetric jacket ratios ρ_j ranging from 0.5% to 1.3%. The specimens were 200 mm in diameter and 600 mm in height, and were provided with a longitudinal steel reinforcement ratio of 1%, with yield stress $f_{yh} = 295$ MPa, whose contribution is here subtracted from all the experimentally measured stresses. Tests were conducted on three series of four concrete specimens: a) unconfined, b) wrapped with normal modulus (250 GPa) carbon-fiber sheets, and c) wrapped with high modulus (439 GPa) carbon-fiber sheets, two of which, specimens H3 and H4, are examined here.

The average unconfined peak strength was $f'_{co} = 39$ MPa, while the concrete elastic modulus was inferred from the tests as $E_c = 20000$ MPa. With $\epsilon_{co} = 0.0034$, the simplified expression (5) yields $\beta = 207$ for both specimens.

Table 4.3. Results of experiments and of analyses with the proposed model.

Spec.	E_j (GPa)	ρ_j (%)	f_{ju} (MPa)	ϵ_{lu} (%)	experiment		analysis	
					f_{cu} (MPa)	ϵ_{cu} (%)	f_{cu} (MPa)	ϵ_{cu} (%)
H3	439	0.676	2810	0.63	70.1	1.15	77.2	1.39
H4	439	1.352	2327	0.53	89.8	1.52	90.8	1.45

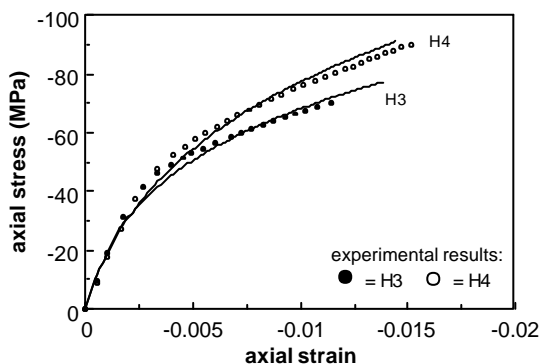


Figure 4.8. Axial stress vs. axial strain.

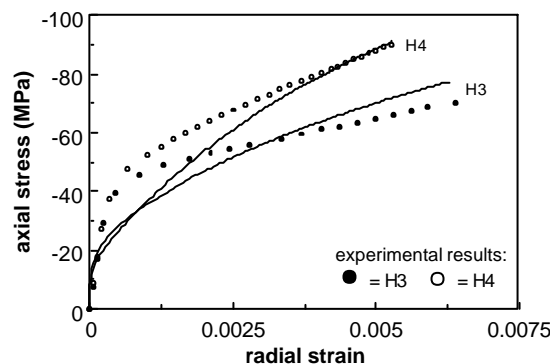


Figure 4.9. Axial stress vs. radial strain.

In Table 4.3 the mechanical properties of the two specimens are listed, along with the experimental results and those obtained from the analyses.

In Figure 4.8 and Figure 4.9, the curves for the axial stress vs. axial strain, and axial stress vs. radial strain, respectively, are shown.

From Table 4.3 and Figure 4.8 and Figure 4.9, it can be seen that the agreement between the proposed model and the experimental data is extremely satisfactory for the axial stress vs. axial strain. In the axial stress vs. radial strain graphs, there is a significant discrepancy in the earliest range of deformation, which however does not affect the axial modeling; however, with increasing deformation the differences become smaller. The ultimate point on the axial stress vs. axial strain graph is rather overestimated for the specimen H3, while it is determined with excellent accuracy for the specimen H4.

4.1.4.3 Tests by Mirmiran and Shahawy (1997)

A total of 24 concrete-filled FRP tubes and 6 plain concrete specimens were tested. All 30 specimens were cylindrical (152.5 mm in diameter and 305 mm in height), and divided in three batches with different strengths and water-to-cement ratios. Here the results of the proposed model are compared to the third batch, with the following properties: $f'_{co} = 32$ MPa, $\epsilon_{co} = 0.002$ and $E_c = 30,000$ MPa. It was estimated that $\nu = 0.16$ and $\alpha = 0.90$, therefore, by using (4b) it results: $\epsilon_{lo} = 0.00128$, and with (3) $\beta = 343$.

The FRP tubes consisted of a filament-wound angle-ply laminate of polyester resin with unidirectional E-glass fibers at winding angle $\theta = \pm 15^\circ$. Direct interaction between jacket and concrete in the axial direction was prevented. Three different tube thicknesses were tested, with properties as listed in Table 4.4.

Table 4.4. Properties of FRP encasing

Specimen	E_j (MPa)	ρ_j (%)	f_{ju} (MPa)	ϵ_{ju} (%)
6-layer tube	37233	3.41	696	1.87
10-layer tube	40336	5.51	565	1.40
14-layer tube	40749	7.87	550	1.35

Close to the ultimate load, local buckling and waving in the tubes were observed, but shear failure was noted as the primary mode of failure. The observed failure process clearly shows a composite action, with a partial ply failure mechanism: the resin fails in transverse or shear stresses, but the tube still has a load-carrying capacity left, until the fibers fail.

In Table 4.5 and Figure 4.10 through Figure 4.13, the experimental data are compared to the results of the proposed model.

Table 4.5. Results of experiments and of analyses with the proposed model.

Specimen	experiment				analysis			
	f_{cu} (MPa)	ϵ_{cu} (%)	μ_{max}	μ_u	f_{cu} (MPa)	ϵ_{cu} (%)	μ_{max}	μ_u
unconf.	32.0	0.20	---	---	32.0	0.20	---	---
6-layer	59.95	3.45	1.364	0.435	64.69	3.42	1.047	0.429
10-layer	76.46	3.71	0.879	0.304	81.08	3.77	1.0	0.292
14-layer	84.40	4.24	0.774	0.233	91.85	4.13	1.0	0.262

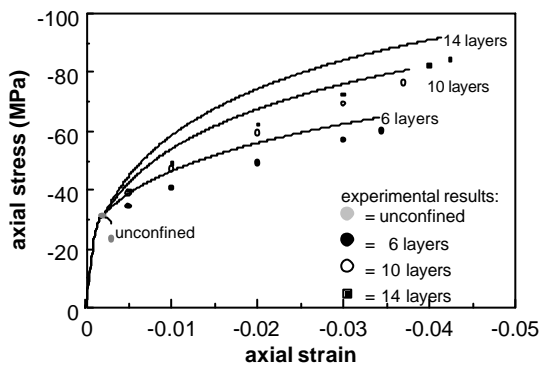


Figure 4.10. Axial stress vs. axial strain.

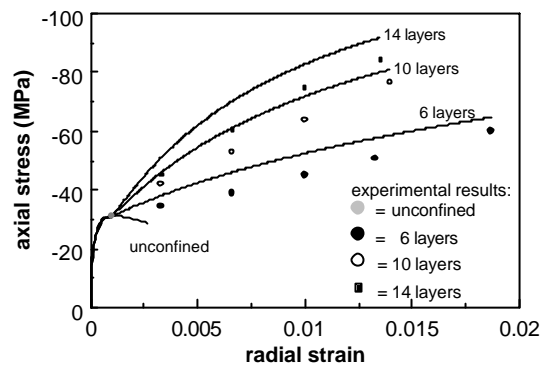


Figure 4.11. Axial stress vs. radial strain.

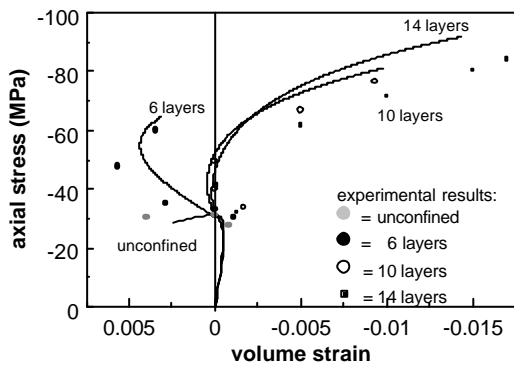


Figure 4.12. Axial stress vs. volume strain.

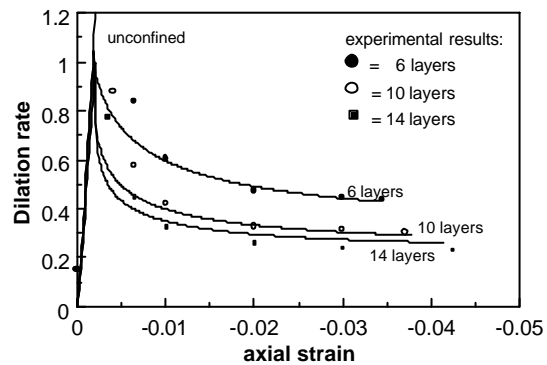


Figure 4.13. Dilation rate vs. axial strain.

From Figure 4.10 it is seen that the ultimate strengths calculated with the proposed model are higher (less than 10%) than the experimental values. On the other hand, the stiffness of all three specimens at larger deformations is equal to the experimental results and the ultimate axial strains show close agreement. In the earliest range of axial deformation (from 0% to 1%) the stresses are overestimated, while beyond this range the values get closer to the experimental ones, as also

observed in Figure 4.11. In Figure 4.12 the significantly different volumetric change can be observed: after reaching the peak strength, the specimen with 6 layers shows a volume expansion, while the two others both have a volume contraction. In all three cases the trend is correctly modeled. It should be noticed that, though the strain values are not exactly determined, this has low influence on the axial stress vs. axial strain behavior.

The observed differences may be explained by the way the specimens were manufactured: the FRP encasing was made first, and then filled with concrete after curing. It is suspected that the concrete shrinkage could have caused a gap between encasing and concrete surface, thus delaying the deformation of the FRP encasing upon loading of the specimens. In other words, in the early range of loading the concrete laterally deformed at a high rate in an unconfined state, before reaching the encasing and activating the confining mechanism. This can be inferred from Figure 4.13: the dilation rate in the range of axial strain of 0% to 1% as calculated by the proposed model is lower (around 35%) than observed in the experiments, but beyond the axial strain of 1% the values show very close agreement.

4.1.5 Predictive equations of FRP-confined concrete properties

In the previous section, the specimens collapse was identified with the condition (15), at which the ultimate strength and strain of concrete were evaluated. In all cases, the simulations were conducted by imposing, as ultimate strain of the jacket, the value measured in the test and then the resulting ultimate strength f'_{cu} and strain ϵ_{cu} of concrete were compared with the experimental ones. In many cases, it is useful to know in advance the value of the ultimate strength and strain, by means of expressions that directly give the values of interest without carrying out the entire test. The objective of this section is to develop practical formulae to evaluate the ultimate compressive strength and strain for concrete confined with FRP, which should be useful for design practice.

For the case of steel-confined concrete, ϵ_{cu} is predicted through an energy-balance method (Mander *et al.* 1988a), in which it is assumed that the increase in strain energy capacity of compressed concrete due to confinement be provided by the confining device strain energy capacity. The ultimate strain energy capacity of the confining device is given by the area under the stress-strain curve times the volumetric ratio. When this is attained, the confining device collapses and the corresponding concrete strain is taken as the ultimate strain. However, it has been commented (Mirmiran *et al.* 1996, and also above) that the energy-balance method cannot be extended to the case of FRP confinement.

Two approximate formulae are developed for the ultimate concrete compressive strain and strength, based on regression analyses of results obtained through the model presented above. The observed behavior in experimental tests suggests that the ultimate strength and strain have a direct dependence on: the ultimate strain of the confining member ϵ_{ju} , the maximum confinement pressure

f_{lu} , and the concrete modulus E_c , while they have an inverse dependence on the unconfined concrete strength f'_{co} .

Thus, three independent parameters were identified:

$$\bar{f}_{lu} = \frac{f_{lu}}{f'_{co}} \quad \varepsilon_{ju} \quad \bar{E}_c = \frac{E_c}{f'_{co}} \quad (16)$$

and were made to vary within their respective extremes, identified as: $\bar{f}_{lu} = 0 \div 2$, $\varepsilon_{ju} = 0 \div 0.03$, $\bar{E}_c = 700 \div 1200$. The upper bound of \bar{f}_{lu} , though unusually high, can occur for example in a 30 MPa concrete cylinder of 100 mm diameter, wrapped with a 2 mm thick jacket, having an ultimate strength of 1500 MPa. The range of ε_{ju} was selected considering a considerable amount of experimental data on composite materials, while the range of \bar{E}_c was selected considering a 20% variation of the concrete's effective elastic modulus with respect to the conventional average value of $5700\sqrt{f'_{co}}$ (MPa), for a range $f'_{co} = 30 \div 50$ MPa. Two minor assumptions were made: $\varepsilon_{co} = 0.002$, and $\alpha = 1$ (the latter allows use of (5) for the determination of β), which are however valid for most concretes.

From the resulting 600 cases, the two following predictive equations were obtained:

$$f'_{cu} = f'_{co} \left(0.2 + 3\sqrt{\bar{f}_{lu}} \right) \quad (17)$$

$$\varepsilon_{cu} = \varepsilon_{co} \left(2 + 1.25 \bar{E}_c \varepsilon_{ju} \sqrt{\bar{f}_{lu}} \right) \quad (18)$$

Note that for no confinement ($\bar{f}_{lu} = 0$) the resulting parameters are those of an unconfined concrete with $\varepsilon_{cu} = 0.004$ and ultimate strength equal to 20% of the peak strength, which is the value usually adopted for it. It is again emphasized that, for the considerations given above, the value of ε_{ju} to input in (18) should be computed from f_{ju}/E_j , and not taken from the manufacturer.

4.1.6 Agreement with experiments

The values of the ultimate strength and strain obtained with the predictive equations (17) and (18) were compared with several experimental data (Picher *et al.* 1996, Harmon *et al.* 1995, Kawashima *et al.* 1997, Mirmiran and Shahawy 1997, Karbhari and Gao 1997). The results are shown in Figure 4.14 and Figure 4.15.

From Figure 4.14 it can be seen that the predictive equation for the ultimate strength shows a satisfactory correlation with the experiments, with the only exception of two tests conducted by Harmon, which were carried out on high strength concrete, outside the range considered in the parametric study. Excluding these two cases, the maximum error in the predictions was 9%, while the average error was 6%.

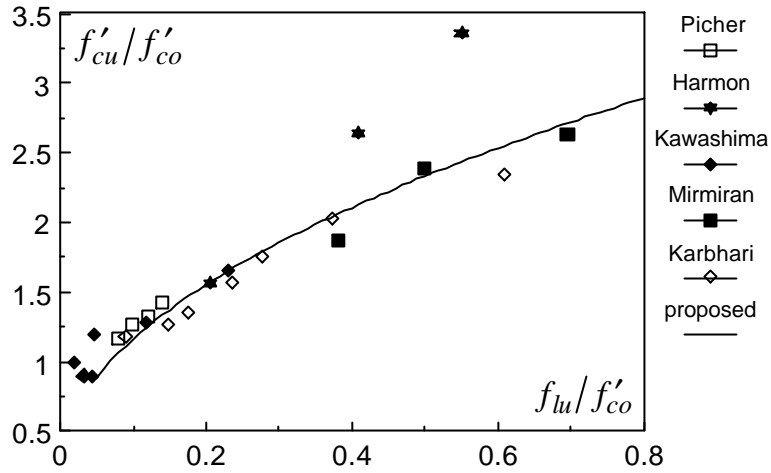


Figure 4.14. Comparison of (17) with experimental data of ultimate strength.

In Figure 4.15 the ultimate strains predicted with (18) are compared with the considered tests. In this case the error is higher (about 14% in average) but still acceptable.

From the above results it is concluded that both (17) and (18) can be used with a reasonable accuracy to predict the ultimate strain and strength of normal strength concrete confined with FRP.

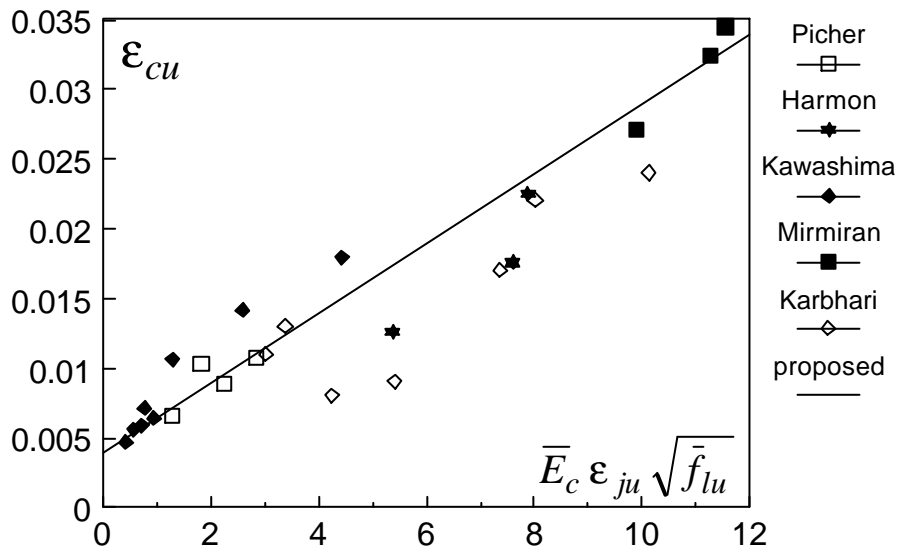


Figure 4.15. Comparison of (18) with experimental data of ultimate strain.

4.2 Response of FRP-wrapped sections

The next step towards the development of a design equation for determining the optimal thickness of FRP wrappings to enhance the ductility of existing r.c. bridge piers is the insertion of the above-developed FRP-confined concrete model into a fiber section model.

The fiber section model allows to trace the behavior until collapse of r.c. sections under constant axial load (as is the case for bridge piers under earthquake loading, if the vertical component of the seismic action is neglected) and imposed curvature (Monti et al. 1996). Sections are discretized into fibers of unconfined concrete (cover), confined concrete (core), steel rebars and FRP jacket.

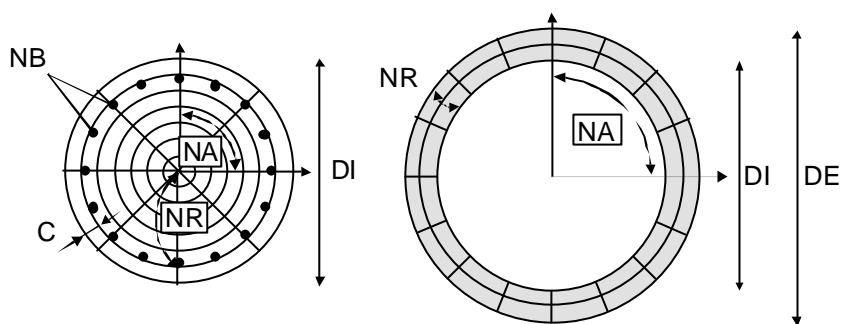


Figure 4.16. Model of fiber section. Section without wrapping (right), and FRP wrapping (left).

The symbols are: DI = Diameter, C = Concrete cover thickness, NB = Number of bars, NR = Number of radial subdivisions, NA = Number of angular subdivisions, DE = External diameter.

As shown in Figure 4.16, left, in the initial state, before upgrading, the section is made of fibers representing the concrete cover, the concrete core and the steel bars. In the upgraded state, right, an FRP jacket is added around the initial section, under the assumption of perfect bond on the concrete surface. It is well known that FRP jackets apply a deeply different confinement effect with respect to steel confining devices: these latter apply a constant confinement pressure after yielding, while FRP exerts a continuously increasing confinement pressure. In the presence of FRP confinement, the existing confinement models are inadequate to represent the continuous interaction between the expanding concrete and the elastic FRP jacket, and therefore the above-presented FRP-confined concrete constitutive model (Spoelstra and Monti 1999), which correctly accounts for such a peculiar behavior, has been implemented in the fiber section model.

A problem regards the distribution of the confining pressure over the cross section. Let us consider a circular section with a linearly distributed axial strain field imposed on it. It is assumed that, at a given distance from the section's centroid, the lateral strain can be calculated, by means of the proposed model, from the corresponding axial strain. On the circumference, this allows to calculate the transverse strain in the jacket from the corresponding radial strain, and therefore the stress in the jacket and the induced confining pressure. This amounts to assuming

that the confining pressure only depends on the distance from the neutral axis (Figure 4.17).

This assumption has been verified in numerical analyses conducted in the linear range (Monti and Spoelstra 1997) giving results that corroborate the chosen simplified approach. More refined analysis are being carried out with advanced nonlinear FE codes to account for the nonlinear behavior of concrete under triaxial stress states.

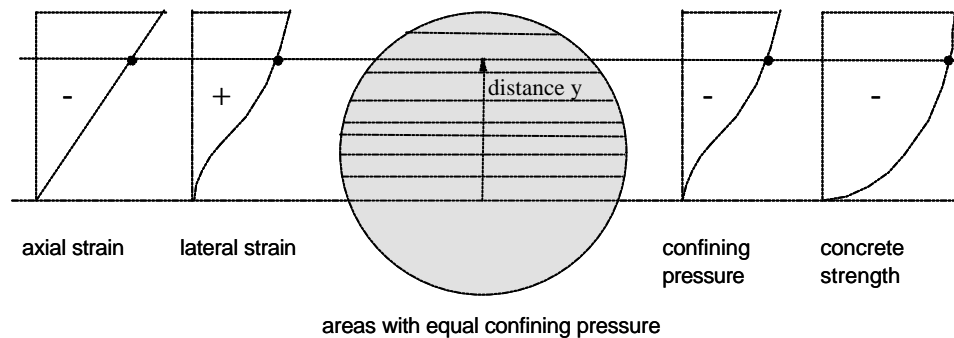


Figure 4.17. Calculation method for confining pressure f_1 and concrete strength σ_1 .

In most cases, retrofitting of existing bridge piers only concerns enhancement of ductility, while normally flexural strength is adequate. It is believed that composite action between jacket and pier should be avoided as much as possible, since it generally enhances flexural strength to a larger extent than ductility. Also, a study by Orito *et al.* (1987) reported that unbonded concrete-filled steel tubes would perform better than bonded tubes, because in the former case the jacket does not undergo longitudinal stresses. Therefore, the jacket will not buckle, and will continue confining the pier up to its maximum strength.

These considerations imply that a fiber winding-angle of 0° is the most effective, when no composite action is foreseen, even though, in reality, a certain degree of composite action between pier and FRP jacket cannot be excluded *a priori*, so that, in general, it is to be expected that, with 0° winding-angle, the jacket will fail under longitudinal tensile strains, due to separation of parallel fibers. A jacket made of several plies with different winding-angles would be a more practical option.

Special care should be devoted to the shear capacity of a retrofitted pier. Because there will always be some degree of composite action, the flexural strength will increase. Since the shear capacity should always exceed the flexural capacity, in order to avoid brittle shear collapse, it should be checked that the shear capacity is still adequate after retrofitting.

As an example of retrofitting a pier with an FRP jacket, a moment-curvature analysis has been carried out with the programs CYRUS (Monti *et al.* 1996).

The cross-section of the selected pier, taken from another parametric study (Mirmiran *et al.* 1996), is shown in Figure 4.18.

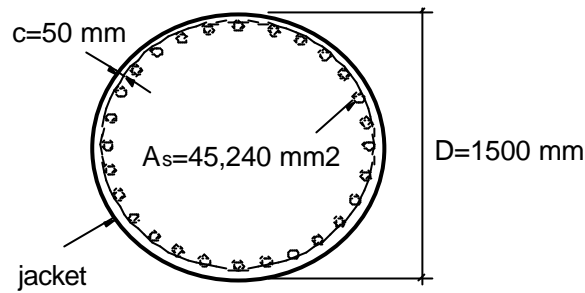


Figure 4.18. Typical reinforced concrete pier section.

The pier is 1500 mm in diameter and has 36 ϕ 40 mm rebars (total area: 45,240 mm², with $\rho_s = 2.94\%$) having yield strength 440 MPa and ultimate strain 12%. The unconfined concrete properties are: $f'_{co} = 35$ MPa and $E_0 = 29,580$ MPa. The transverse reinforcement consists of ϕ 16mm ties at a spacing of 80 mm ($\rho_t = 0.72\%$).

Table 4.6. Equivalent mechanical properties of CFRP/GFRP jacket, with corresponding ultimate axial strain of concrete.

θ (degree)	E_x (MPa)	σ_x^+ (Mpa)	ε_x^+ (%)	E_y (MPa)	σ_y^+ (MPa)	ε_y^+ (%)	ε_{cu} (t=9 mm) (%)
[75, 15]	61760	953	1.54	21971	570	2.59	3.10

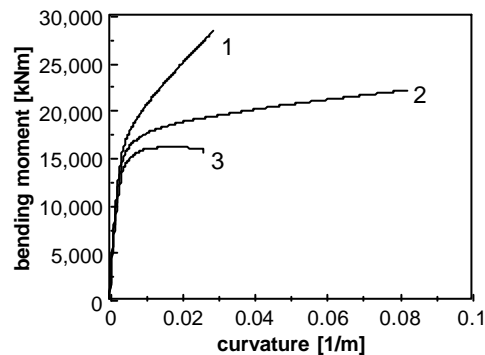


Figure 4.19. Numerical monotonic analyses:
1- full composite action, 2- no composite action, 3- as built.

The pier is confined with layers of carbon fiber/epoxy composite material, with fiber winding-angle of $\pm 15^\circ$, and with layers of fiberglass/epoxy, with fiber winding-angle of $\pm 75^\circ$. For the sake of example, a jacket thickness of 9 mm has been chosen: this value is much larger than those usually adopted in practice, but it allows to amplify the differences between the different behaviors, before and after

upgrading. Thus, with a total thickness of the jacket of 9 mm and using the CLT relations, the mechanical properties of the jacket result as in Table 4.6, where the indices x and y denote the directions orthogonal and parallel to the pier longitudinal axis, respectively; the corresponding ultimate strain for concrete, as evaluated with the proposed model, is also shown.

The results of the monotonic analyses are shown in Figure 4.19, where the effects of having full composite action or no composite action can be observed. In Table 4.7 the quantities of interest for upgrading (moment and curvature) are listed along with the resulting ductility factors.

Table 4.7. Curvature ductility factors for the retrofitted pier.

Pier	M_y [kNm]	ϕ_y [1/m]	M_u [kNm]	ϕ_u [1/m]	μ_ϕ
As-built	12848	0.0031	17418	0.0320	10.3
Full comp.	14589	0.0030	28254	0.0283	9.4
No comp.	13753	0.0030	22072	0.0820	27.3

Table 4.8. Properties of the different confining mechanisms.

Column	ρ_t (%)	E_j (MPa)	f_y or f_u (MPa)	$\varepsilon_{j,u} = \varepsilon_{lat,u}$ (%)	ε_{cu} (%)
As-built	0.72	200000	400	12.0	1.58
Steel jacket	2.67	200000	400	12.0	3.60
CFRP jacket	2.13	87600	955	1.10	2.75
GFRP jacket	1.60	38700	832	2.10	3.90

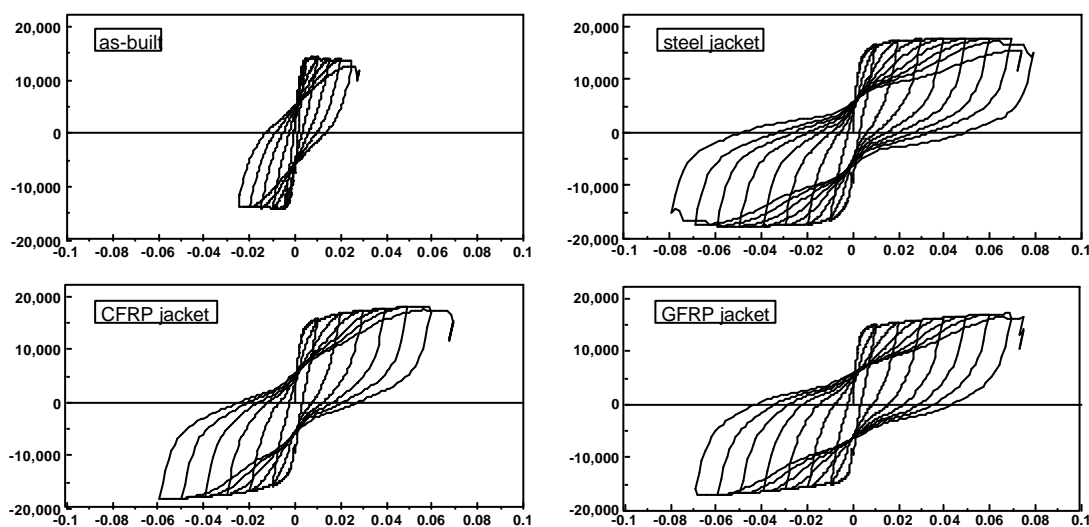


Figure 4.20. Cyclic moment (kNm)-curvature (1/m) responses for different jacket types.

In Figure 4.20, the cyclic behavior of the as-built pier and of the retrofitted pier without composite action is shown. The ultimate concrete compressive strains ϵ_{cu} are computed by a single-iteration with the procedure described before. It can be seen that the retrofitted pier shows very stable hysteresis loops, until failure occurs at a curvature ductility factor of about 27. The CFRP layout results in a higher strength but less ductility than the GFRP layout, as expected.

4.2.1 Assessment of the FRP-confined section model

The section model shortly presented in the previous paragraph has been extensively verified against experimental tests on r.c. circular bridge piers, wrapped with FRP jackets. Here, two of those tests are presented: one by Seible *et al.* (1995c), the other by Saadatmanesh *et al.* (1996). Each test was performed on two specimens: one “as-built”, and the other “upgraded” with GFRP jackets. The geometrical and mechanical properties of the “as-built” specimens and of the composite materials used for upgrading are listed in Table 4.9. The pier height h denotes the distance of the pier cap centroid (where the load was applied) from the top of the footing.

Table 4.9. Geometrical and mechanical parameters of the “as-built” and “upgraded” specimens considered in the assessment of the FRP-confined section model.

Geometrical and mechanical properties	Seible <i>et al.</i> 1995c	Saadatmanesh <i>et al.</i> 1997
“As built” specimens		
Pier height h (m)	2.90	1.892
Section diameter D (m)	0.608	0.305
Reduced axial load n	0.046	0.176
Unconfined concrete strength f'_{co} (MPa)	44.3	34.5
Steel yield strength f_{sy} (MPa)	293 (bars), 403 (ties)	358 (bars), 301 (ties)
Longitudinal reinforcement ratio ρ_{sl}	0.025	0.0248
Transverse reinforcement ratio ρ_{st}	0.003	0.0017
Confinement pressure of hoops f_l (MPa)	0.484	0.256
Composite materials of “upgraded” specimens		
Ultimate strength f_{ju} (MPa)	793	298 *
Ultimate strain ϵ_{ju}	0.023	0.016 *
Young's Modulus E_j (GPa)	33.78	18.6
Jacket thickness t_j (mm)	3.81	4.8
Volumetric ratio of jacket ρ_j	0.0247	0.063
Confinement pressure f_l (MPa)	9.8	9.4 *

* This test was interrupted before the jacket failure. The values reported in the table refer to that stage. Ultimate values, not attained, were: $f_{ju} = 532$ MPa, $\epsilon_{ju} = 0.029$, and $f_l = 16.7$.

In the above experimental studies, the response is given as lateral load vs. lateral displacement, while the fiber-section model yields the moment-curvature response at the pier base section. In order to compare the results in terms of displacement, the following relation is used to pass from curvature ductility δ_χ to displacement ductility δ_d :

$$\delta_d = 1 + 3(\delta_\chi - 1) \frac{l_p}{L} \left(1 - 0.5 \frac{l_p}{L} \right) \quad (19)$$

where L represents the shear span to the plastic hinge. The plastic hinge length, l_p , was directly measured in the tests by Saadatmanesh *et al.* (1997), while in the tests by Seible *et al.* (1995c), l_p was taken as (Priestley *et al.* 1996):

$$l_p = 0.08L + 0.022f_{sy} \cdot d_b \quad (20)$$

where f_{sy} and d_b are the yield strength and bar diameter of the main column reinforcement, respectively.

Based on the above considerations, numerical tests were carried out and compared to the experimental results (Figure 4.21). All piers were tested under increasing cyclic quasi-static lateral loads, while here only the envelopes are compared. In Table 4.10 the experimental and numerical values of the ultimate load F_u and of the maximum displacement ductility δ_d are listed, along with the error committed by the model.

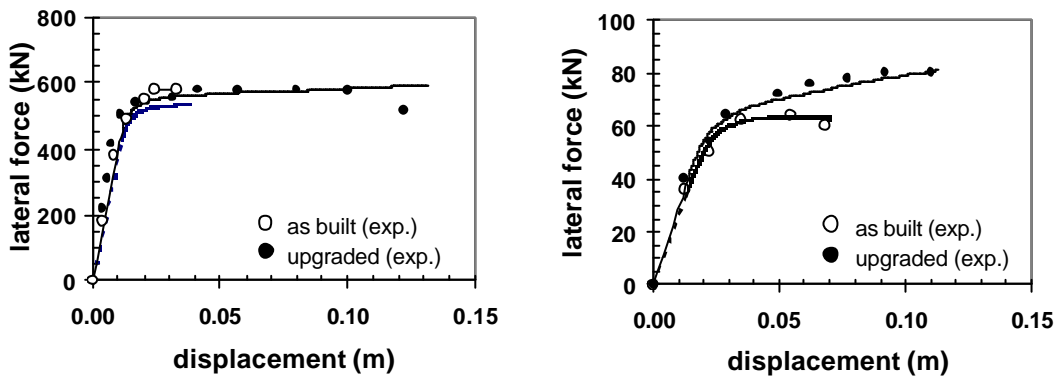


Figure 4.21. Comparison of experimental (dots) and numerical (solid lines) results for the “as-built” and “upgraded” piers by Seible *et al.* (1995c) (left) and by Saadatmanesh *et al.* (1997) (right).

Table 4.10. Comparison between experimental and numerical results of the “as-built” and the “upgraded” piers. Errors in the prediction of ultimate load F_u and ductility δ_d .

Ultimate load F_u and ductility δ_d		Seible <i>et al.</i> 1995c			Saadatmanesh <i>et al.</i> 1997		
		Experiment	Numerical	Error %	Experiment	Numerical	Error %
As- built	F_u (kN)	532.50	532.69	0.0	64.00	63.14	-1.3
	δ_d^{ava}	3.10	3.88	25.2	4.00	3.93	-1.7
Upgrad ed	F_u (kN)	566.40	593.66	4.8	84.00	80.82	-3.8
	δ_d^{tar}	12.14	12.79	5.3	6.50	6.76	4.0

From these results, it can be concluded that the fiber section model with FRP confinement gives a satisfactory interpretation of the behavior of circular bridge piers confined with FRP jackets.

4.2.2 Parametric study on FRP-confined sections

A parametric study has been carried out with the program CYRUS (Monti *et al.* 1996), on the same section considered above, to examine the influence of different configurations of the FRP external reinforcement on relevant response quantities, such as: flexural strength, ductility and failure mechanism.

The proposed confinement model was used to determine the response of the concrete fibers. The Classical Lamination Theory (CLT) was used to evaluate the equivalent stiffness and ultimate strain and strength of the jackets for both the longitudinal and the transverse directions.

Two limit situations were studied, among other factors depending on the stiffness of the glue layer between jacket and pier:

- full composite action between jacket and pier. This situation corresponds to perfect bond provided by the glue layer,
- no composite action between jacket and pier. This situation corresponds to a glue layer that only provides transverse bond, so the jacket exerts only a confining action.

It should be noted that, as opposed to the former case where an infinitely stiff glue layer in both directions is considered, the latter situation corresponds to having a glue layer that is infinitely stiff in the transverse direction and infinitely flexible in the longitudinal direction. This is of course a speculative case, that has the purpose of defining a lower bound for the composite action, since the former one defines an upper bound. The real response should be in between these two bounds. Further studies are necessary to include the effect of the stiffness of the glue layer in the model. However, for practical purposes, since it is recognized that the commercially available epoxy resins provide quasi-perfect bond in both directions, the former case can actually be considered as a satisfactory representation of a real behavior.

The following assumptions were made:

- The jacket exerts its action until the maximum theoretical strength and strain,
- The compressive elastic moduli of FRP materials are equal to the tensile ones,
- The failure criteria of the jackets are based on the ultimate strain theory. In the analyses without composite action, the jackets fail when the equivalent transverse ultimate strain is reached. In the analyses with full composite action, the jackets fail when either the ultimate transverse strain or the ultimate longitudinal compressive/tensile strain is reached,
- The failure point of the pier was determined by first ply-failure of the jackets. That is, no subsequent stress redistribution among the remaining plies is considered,
- The contribution from concrete tensile strength is ignored, as well as shear stresses on the section and possible bond-slip of the rebars.

The parameters considered in this study were the jacket thickness and the fibers winding-angle. Confinement was provided by an external FRP jacket made of several plies with $\pm\theta$ fiber winding-angle. Four different jacket volumetric ratio ($\rho_j = 0, 0.016, 0.024$ and 0.032 mm) and seven winding angles ($\theta = 0, 15, 30, 45, 60$ and 90°) were analyzed. For the jacket material carbonfiber/epoxy was selected.

As regards the failure criteria, the envisaged mechanisms are in Table 4.11.

Table 4.11. Failure mechanisms.

Full composite action	Without composite action
1. Crushing of concrete (transverse tensile failure of jacket)	1. Crushing of concrete (transverse tensile failure of jacket)
2. Longitudinal tensile failure of jacket	2. Tensile failure of reinforcing steel
3. Longitudinal compressive failure of jacket	

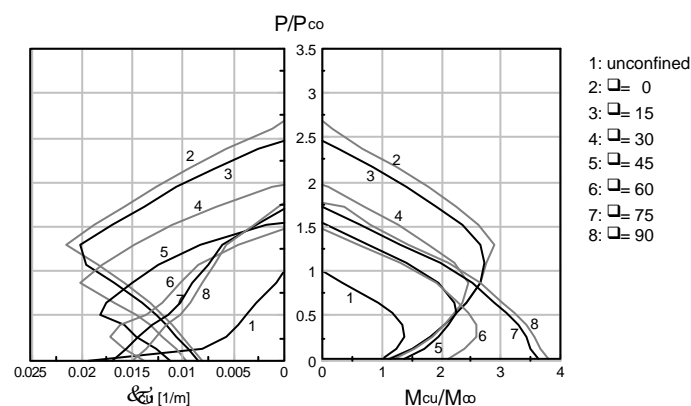


Figure 4.22 Interaction diagrams with full composite action.
Effect of winding angle θ variation for $\rho_j = 0.016$.

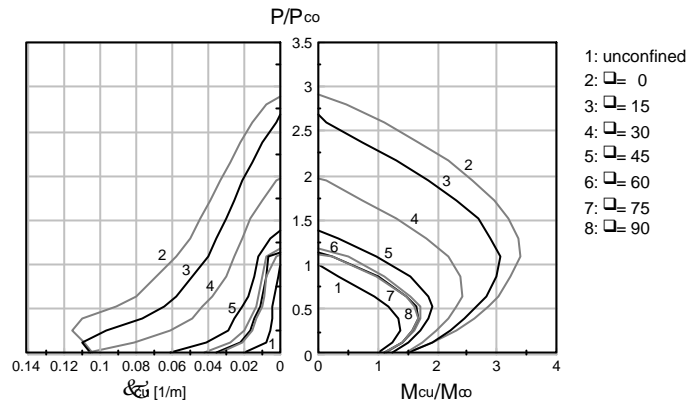


Figure 4.23. Interaction diagrams without composite action.
Effect of winding angle θ variation for $\rho_j = 0.016$.

The results are presented in terms of normalized interaction diagrams with respect to the unconfined properties: the ratio of confined to unconfined axial force (P/P_{co}) is plotted versus the ratio of confined to unconfined flexural strength (M_{cu}/M_{co}) and versus the ratio of confined to unconfined ultimate curvature (κ_{cu}/κ_{co}). The unconfined pier properties are: $P_{co} = f_{co} A_{gr} = 61,850$ kN, $M_{co} = 10,454$ kN and $\kappa_{co} = 0.0194$ 1/m.

Figure 4.22 and Figure 4.23 show the axial load/flexural strength and axial load/ultimate curvature interaction diagrams for $\rho_j = 0.016$ and various winding-angles, with and without composite action. In Figure 4.22, it is noticed that under pure bending ($P/P_{co} = 0$), an enhancement of the flexural strength is obtained for all winding angles, with a maximum of almost four times when the fiber winding angle is 90° . Also for as regards the ultimate curvature, there is an increase which is more significant for higher axial load (for example, for $P/P_{co} = 0.5$, the ultimate curvature is increased by a factor that varies from 3 to 4). On the other hand, looking at the case of pure axial load, it is observed that the sectional axial strength increases by reducing the winding angle: with $\theta = 0^\circ$ the increase is more than three times. In the cases where both the axial load and the bending moment are acting on the section, the shape of the interaction diagrams changes according to the dominant failure mechanism. In the range of low axial loads (say, $P/P_{co} < 0.75$), which is more interesting from the practical standpoint, it should be observed that for the cases with $\theta = 75^\circ, 90^\circ$, the flexural strength decreases for increasing axial load, as opposed to the other cases where the behavior is like one would expect. This is essentially due to the fact that collapse of the section occurs due to longitudinal tensile failure of the jacket, before the reinforcing bars have completely exerted their ductility. It can be concluded, therefore, that jackets under full composite action are better suited for flexural strength increase instead of ductility enhancement.

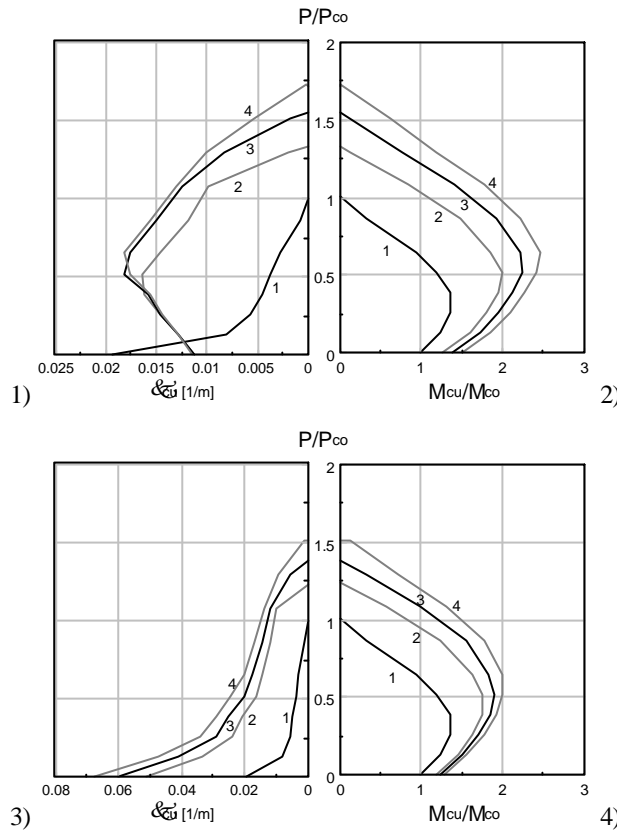


Figure 4.24. Interaction diagrams with full composite action.
Effect of $\rho_j = 0$ (1), 0.016 (2), 0.024 (3), 0.032 (4) for winding angle of 45° .

In Figure 4.23, under pure bending ($P/P_{co}=0$), there is no significant increase of flexural strength (at most 1.5 times the unconfined one), but the available ductility sensibly increases as the winding angle decreases (up to 5.5 times when $\theta=0^\circ, 15^\circ, 30^\circ$), attaining much higher values than the previous case where full composite action is considered. Note that in this case the shape of the interaction diagrams does not change with the wrapping configuration: they are simply scaled up. This reflects the fact that the failure mechanism is always due to concrete crushing, as opposed to the previous case where the jacket can also fail due to longitudinal strain. As expected, it is observed that significant improvements are obtained only for winding angles less than 45° . In this case, the conclusive remarks is opposite than that of the previous case: jackets without composite action are better suited for ductility enhancement instead of flexural strength increase. As already observed, the actual behavior of a jacketed section is in between the two cases analyzed above.

In Figure 4.24 the effect of the jacket thickness is studied for a winding-angle of 45° , with full composite action. It is seen that significant ductility increase is obtained above values of $P/P_{co}=0.2$, while for lower values, the ductility is essentially the same as that of the unconfined section. It is important to notice that

for low values of the axial load, any increase in thickness brings no significant improvement to the response.

From the analyses performed, the following conclusions can be drawn:

- The failure mechanism is the most important concern in the evaluation of flexural strength and ductility. The observed failure mechanism is strongly dependent on jacket thickness, winding angle and axial load level.
- Composite action does not significantly improve the pure axial capacity; it can even impart a decrease, due to the relative poor compressive behavior of the jackets.
- Composite action improves flexural strength for the larger ($>45^\circ$) winding-angles. The source of increase is the direct load-carrying capacity of the jacket, rather than its confining action. This further explains why larger winding-angles result in higher flexural capacity. For (very) high levels of axial load and small winding angles, flexural strength is decreased.
- Composite action strongly decreases the available ductility for smaller ($<45^\circ$) winding-angles, for the larger winding-angles and high axial load levels ($P/P_{co} > 1.0$) the decrease is less apparent or even can revert to an increase.
- As the thickness of the jacket increases, the axial and flexural capacity and the available ductility all increase, but the rate of increase depends on axial load and the presence or absence of composite action.
- The winding-angle has no significant impact on pure flexural capacity of the pier without composite action, but a large decrease in pure ductility is occurring for increasing winding-angles. With composite action, an increased winding-angle strongly increases both pure flexural strength and pure ductility.

4.3 Design criteria for upgrading through FRP wrapping

In this section, a design equation, which was the final objective of the above developments, is proposed to determine the optimal thickness of FRP jackets, for enhancing the ductility of existing reinforced concrete bridge piers, having circular cross-section. The design procedure stems from the definition of an upgrading index, given as the ratio of the target-to-available ductility at the pier base section, to be attained through FRP jacketing. The available ductility is that identified through the usual assessment procedures on the r.c. member to upgrade, while the target ductility is evaluated based on the expected actions on the bridge. The upgrading index is initially defined in general terms and is subsequently extended to the case of piers built in seismic regions. It results in a simple expression in terms of easily computable quantities, such as the ultimate strain and the peak strength of concrete, before and after upgrading. A parametric study on old-code-designed bridge piers sections, upgraded with either glass or carbon fiber jackets, is performed, based on a fiber-section model, equipped with a newly developed FRP-confined concrete model. This study shows that the index, despite its simplicity, yields excellent predictions of the ductility increase obtained through FRP wrapping, and it is therefore used to develop a design equation. Such equation allows to design the optimal thickness of

FRP jackets in terms of: the desired upgrading index, the mechanical characteristics of the selected composite material, and the quantities defining the initial state of the pier section. The design procedure has been applied to available experimental tests of a scaled bridge pier wrapped with FRP and tested to failure, and it has demonstrated to be very effective.

4.3.1 *Upgrading index of FRP-wrapped pier sections*

The final objective of the design procedure here proposed is to find an analytical correspondence between unknown design parameters (*e.g.*, jacket thickness and FRP material type) and a measure of the intervention effectiveness. In general, the upgrading of structures located in seismic areas aims at improving the performance of the resisting elements by modifying their strength and/or ductility and/or stiffness. This latter is more difficult to obtain (and in most cases it is not an objective of the intervention) when using jackets and wrappings, so the member stiffness can be assumed as constant, before and after the intervention.

In most cases, upgrading interventions aim at increasing the performance of certain critical sections along the member. For those simple cases where the pier is of the single-bent type, the intervention is usually localized at the pier base, so that its effectiveness can be measured, without loss of generality, with reference to some critical section. A *section upgrading index* I_{sec} is therefore introduced, which measures the increase from the (*available*) ultimate moment M^{ava} and curvature ductility δ_{χ}^{ava} of the “as built” section, to the (*target*) ultimate moment M^{tar} and curvature ductility δ_{χ}^{tar} , to be obtained through the upgrading, and defined as follows:

$$I_{sec} = \frac{M^{tar} \delta_{\chi}^{tar}}{M^{ava} \delta_{\chi}^{ava}} \quad (21)$$

The quantities at the denominator should be determined through a preliminary assessment procedure, while those at the numerator are consequent to the evaluation of the expected load actions. When the index is lower than 1, no upgrading is necessary. Values of the index greater than 1 imply the necessity of upgrading. This latter situation can arise either from a reduction of the denominator (damaged sections) or from an increase of the numerator (increase of the action) with respect to the original design conditions.

The index (21) can be simplified, if one considers the most common case of unidirectional fibers wrapped (sometimes automatically) at 90° with respect to the column axis. Such upgrading interventions always result in relevant increases of section ductility, while only determining limited increases in flexural strength. This also emerges from the parametric analyses that will be shown in the following section, where, for the piers examined, an average strength increase of 10% with a maximum of 20% was observed. As a consequence, for design purposes, the upgrading index (21) can be simplified as:

$$I_{sec} = \frac{\delta_{\chi}^{tar}}{\delta_{\chi}^{ava}} \quad (22)$$

This expression allows to determine the value of the upgrading index, once the available ductility has been assessed and when the target ductility, that is, the most probable required ductility, has been prognosticated. It should be recognized that:

$$I_{sec} = \frac{\delta_{\chi}^{tar}(\text{FRP jacket properties})}{\delta_{\chi}^{ava}(\text{assessed pier conditions})} \quad (23)$$

that is, the available ductility depends on both, the pier geometrical and mechanical properties, and the axial load, while the target ductility depends on the properties and the thickness of the FRP jacket to be designed. Thus, it would be expedient to express the above equation in such a way that the sought FRP jacket properties can be easily determined, once the available ductility has been assessed and a value of the upgrading index has been established. This is exactly the objective of this work, which will be pursued in the following sections.

4.3.2 Mechanical Model of the Upgrading Index

A simple mechanical model of a circular r.c. pier section is here adopted, with the aim of arriving at an expression of the upgrading index (22) in terms of basic geometrical and mechanical quantities.

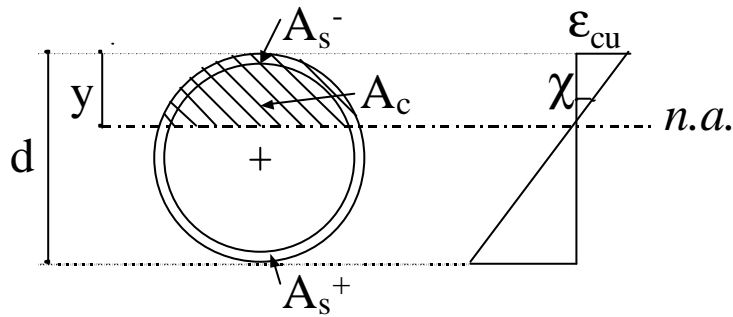


Figure 4.25. Simplified model of the section.

With reference to Figure 4.25, it is observed that the section upgrading index (22) can be expressed as:

$$I_{sec} = \frac{(\chi_u/\chi_y)^{tar}}{(\chi_u/\chi_y)^{ava}} \quad (24)$$

where the, either target or available, sectional ductility δ_{χ} is expressed as the ratio of the ultimate curvature χ_u to the yield one χ_y .

From several numerical analyses performed and presented in the following section, it has been observed that the yield curvature is not significantly altered by the presence of the FRP wrapping, therefore it can be assumed that $\chi_y^{tar} \cong \chi_y^{ava}$, and the index simplifies to:

$$I_{sec} = \frac{\chi_u^{tar}}{\chi_u^{ava}} \quad (25)$$

Using the definition of curvature, under the assumption of section planarity, the above equation can be written as:

$$I_{sec} = \frac{\epsilon_{cu}^{tar} y^{ava}}{y^{tar} \epsilon_{cu}^{ava}} \quad (26)$$

where ϵ_{cu} is the ultimate concrete strain and y is the neutral axis position, both considered in the initial (*ava*) and the final (*tar*) situation.

ϵ_{cu}^{ava} in (26) is the initially available concrete ultimate strain when only the steel hoops confinement is present, and it can be computed through a widely accepted experimentally-derived formula (Seible *et al.* 1995b):

$$\epsilon_{cu}^{ava} = 0.004 + \frac{1.4 \rho_{st} f_{sy} \epsilon_{su}}{f'_{cc}} \quad (27)$$

where $\rho_{st} = 4A_{st}/(s_{st} d_{st})$ is the volumetric ratio of steel hoops (spiral) having area A_{st} , spacing (pitch) s_{st} , and diameter d_{st} ; and f_{sy} , ϵ_{su} = steel yield strength and ultimate strain (usually 0.12), respectively. The confined concrete peak strength $f'_{cc} = f'_{co} \cdot \bar{f}'_{cc}$ is the product of the unconfined concrete strength f'_{co} and the normalized confined strength \bar{f}'_{cc} (Mander *et al.* 1988):

$$\bar{f}'_{cc} = 2.254 \sqrt{1 + 7.94 \bar{f}_l} - 2 \bar{f}_l - 1.254 \quad (28)$$

where $\bar{f}_l = f_l/f'_{co}$ = normalized confining pressure, with:

$$f_l = \frac{1}{2} k_e \rho_{st} f_{sy} \quad (29)$$

where k_e = tie-by-tie arching-effect coefficient (usually 0.8).

ϵ_{cu}^{tar} in (26) is the target concrete ultimate strain to be attained through FRP confinement, and it can be computed through a recently proposed formula (Spoelstra and Monti 1999):

$$\epsilon_{cu} = \epsilon_{co} \left(2 + 1.25 \bar{E}_c \epsilon_{ju} \sqrt{\bar{f}_l} \right) \quad (30)$$

where ε_{co} = unconfined concrete strain at peak stress (usually, $\varepsilon_{co} = 0.002$), $\bar{E}_c = E_c / f'_{co}$ = concrete normalized initial modulus, ε_{ju} = FRP jacket ultimate strain. In this case, the confining pressure f_l can be evaluated analogously to (10) as:

$$f_l = \frac{1}{2} \rho_j f_{ju} = \frac{1}{2} \rho_j E_j \varepsilon_{ju} \quad (31)$$

where $\rho_j = 4t_j/d_j$ is the volumetric confinement reinforcement ratio of an FRP jacket having thickness t_j and diameter d_j . The mechanical characteristics of the FRP jacket are: the ultimate strength f_{ju} , the elastic modulus E_j and the ultimate strain ε_{ju} . On passing, note that $k_e = 1$ for jackets.

Having determined the two strains in (26), the two remaining quantities: y^{tar} and y^{ava} need be found. To this purpose, consider Figure 4.25. The neutral axis position y can be found through equilibrium considerations, writing:

$$\alpha f'_{cc} A_c(y) + f_{sy} A_s^-(y) - f_{sy} A_s^+(y) = n A_{gr} f'_{co} \quad (32)$$

where α = equivalent stress-block coefficient, $A_c(y)$ = compressed area of concrete, $A_s^-(y)$ = area of steel under compression, $A_s^+(y)$ = area of steel under tension, n = reduced axial load, A_{gr} = gross area of concrete. Note that both steel areas have been attributed the yield strength f_{sy} : this is not strictly exact, in fact, the steel bars close to the neutral axis are still elastic; however, their contribution approximately cancels out in the equilibrium and does not affect the correctness of the formula. It is important to notice that the areas of both concrete and steel depend on y . In general, equation (32) can be written as:

$$\alpha f'_{cc} (A_{gr} \cdot F_c(\bar{y})) + f_{sy} (A_s \cdot F_s^-(\bar{y})) - f_{sy} (A_s \cdot F_s^+(\bar{y})) = n A_{gr} f'_{co} \quad (33)$$

where A_s = total steel area. The F 's are functions giving the variation of the respective areas in terms of the neutral axis position (here normalized with respect to the section diameter d : $\bar{y} = y/d$; also note that the internally confined diameter is taken approximately equal to the external diameter). Note that it must be: $F_s^+(\bar{y}) = 1 - F_s^-(\bar{y})$, therefore, calling $F_s^- \equiv F_s$, and dividing both members by $A_{gr} f'_{co}$ and rearranging, one obtains:

$$\alpha \bar{f}'_{cc} F_c(\bar{y}) + 2 \mu_s F_s(\bar{y}) = n + \mu_s \quad (34)$$

where \bar{f}'_{cc} = normalized confined concrete strength defined in (9), and $\mu_s = (A_s f_{sy}) / (A_{gr} f'_{co})$ = mechanical ratio of longitudinal reinforcement.

The exact expressions for the F functions are:

$$F_c(\bar{y}) = \frac{1}{2\pi} [2\arcsin(1-2\bar{y}) - \sin 2\arcsin(1-2\bar{y})] \quad (35)$$

$$F_s(\bar{y}) = \frac{1}{\pi} \arcsin(1-2\bar{y})$$

which clearly hamper the search for a closed-form solution of \bar{y} . Thus, in order to facilitate the determination of \bar{y} in (34), an approximation is introduced, whose consequences will be examined later. The above F functions are written as the product of a linear quantity times the corresponding error function E:

$$F_c(\bar{y}) \approx \bar{y} \cdot E_c(\bar{y}) \quad (36)$$

$$F_s(\bar{y}) \approx \bar{y} \cdot E_s(\bar{y})$$

Substituting the above functions into (34), the following *approximate* equilibrium equation is obtained:

$$\alpha \bar{f}'_{cc} \bar{y} \cdot E_c(\bar{y}) + 2 \mu_s \bar{y} \cdot E_s(\bar{y}) \approx n + \mu_s \quad (37)$$

from which the sought value \bar{y} is found as:

$$\bar{y} \approx \frac{n + \mu_s}{\alpha \bar{f}'_{cc} \cdot E_c(\bar{y}) + 2 \mu_s \cdot E_s(\bar{y})} \quad (38)$$

The final step requires substituting (38) into (26) and, by considering the initial (*ava*) and the final (*tar*) conditions, the expression for the upgrading index is obtained as:

$$I_{\text{sec}} = \frac{\varepsilon_{cu}^{\text{tar}}}{\varepsilon_{cu}^{\text{ava}}} \cdot \frac{n^{\text{ava}} + \mu_s}{n^{\text{tar}} + \mu_s} \cdot \frac{\alpha^{\text{tar}} \bar{f}'_{cc}{}^{\text{tar}} \cdot E_c^{\text{tar}}(\bar{y}) + 2 \mu_s \cdot E_s^{\text{tar}}(\bar{y})}{\alpha^{\text{ava}} \bar{f}'_{cc}{}^{\text{ava}} \cdot E_c^{\text{ava}}(\bar{y}) + 2 \mu_s \cdot E_s^{\text{ava}}(\bar{y})} \quad (39)$$

where it has been obviously considered that $\mu_s = \mu_s^{\text{ava}} \equiv \mu_s^{\text{tar}}$. Note that, in general, although the FRP-confined concrete diagram has a different shape from the steel-confined one (see, for ex., Spoelstra and Monti 1999), it was ascertained that $\alpha^{\text{ava}} \approx \alpha^{\text{tar}}$, and therefore $\alpha = \alpha^{\text{ava}} = \alpha^{\text{tar}} = 0.8$ is here assumed without loss of accuracy. Moreover, if one also considers the probable case of no increase in axial load ($n^{\text{ava}} = n^{\text{tar}}$), the index simplifies to:

$$I_{\text{sec}} = \frac{\varepsilon_{cu}^{\text{tar}}}{\varepsilon_{cu}^{\text{ava}}} \cdot \frac{\alpha \bar{f}'_{cc}{}^{\text{tar}} \cdot E_c^{\text{tar}}(\bar{y}) + 2 \mu_s \cdot E_s^{\text{tar}}(\bar{y})}{\alpha \bar{f}'_{cc}{}^{\text{ava}} \cdot E_c^{\text{ava}}(\bar{y}) + 2 \mu_s \cdot E_s^{\text{ava}}(\bar{y})} \quad (40)$$

where $\varepsilon_{cu}^{\text{tar}}$ is obtained through (30), while $\varepsilon_{cu}^{\text{ava}}$ through (27); $\bar{f}'_{cc}{}^{\text{tar}}$ is obtained through (9) with f_l from (13), while $\bar{f}'_{cc}{}^{\text{ava}}$ is obtained through (9) with f_l from (10). The treatment of the error functions E will be dealt with in the following section.

4.3.3 Considerations over the error functions E

The upgrading index in (40) embodies the approximations introduced with equations (36). It should be clear that the choice of the error functions E is a key point in the development of an explicit expression for I_{sec} : in fact, simple expressions of the E's would lead to a simpler upgrading index, but possibly to unacceptable errors, whereas more accurate expressions of the E's would possibly improve the index accuracy and reliability, but probably at the cost of a higher complexity of its expression.

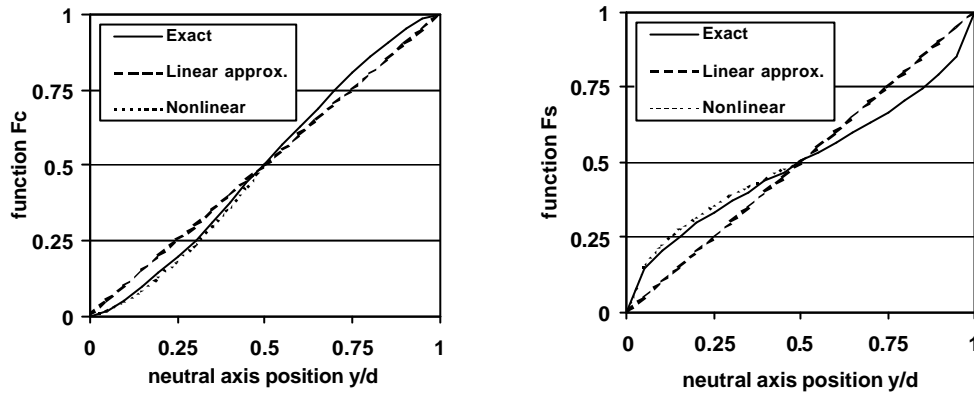


Figure 4.26. Functions F_c (left) and F_s (right) in (36) resulting from two approximation levels: linear (41) and nonlinear (42), compared with the exact expressions (35).

Two possible choices of the error functions have been considered:

$$E_{c1}(\bar{y}) = 1 \quad E_{s1}(\bar{y}) = 1 \quad (41)$$

$$E_{c2}(\bar{y}) = \sqrt{2\bar{y}} \quad E_{s2}(\bar{y}) = \frac{1}{\sqrt{2\bar{y}}} \quad (42)$$

where equations (41) imply that a linear approximation of (36) is accepted, while equations (42) imply a more refined (nonlinear) approximation. Figure 4.26 shows the F functions of (36), as resulting from the adoption of the error functions above, compared with the exact expressions of (35). Note that equations (42) are valid for $0 \leq \bar{y} \leq 0.5$, which however brackets the neutral axis position range at collapse.

Thus, the index results, for the case of linear approximation (41), in:

$$I_{secl} = \frac{\epsilon_{cu}^{tar}}{\epsilon_{cu}^{ava}} \cdot \frac{\alpha \bar{f}'_{cc}{}^{tar} + 2\mu_s}{\alpha \bar{f}'_{cc}{}^{ava} + 2\mu_s} \quad (43)$$

while for the case of nonlinear approximation (42), in:

$$I_{sec2} = \frac{\epsilon_{cu}^{tar}}{\epsilon_{cu}^{ava}} \cdot \frac{\alpha \bar{f}'_{cc}{}^{tar} \cdot \sqrt{2\bar{y}^{tar}} + 2\mu_s / \sqrt{2\bar{y}^{tar}}}{\alpha \bar{f}'_{cc}{}^{ava} \cdot \sqrt{2\bar{y}^{ava}} + 2\mu_s / \sqrt{2\bar{y}^{ava}}} \quad (44)$$

In expression (44), it has been verified that for $0.1 \leq \bar{y} \leq 0.5$ a good approximation can be obtained by simply setting:

$$\alpha \bar{f}'_{cc} \cdot \sqrt{2\bar{y}} + 2\mu_s / \sqrt{2\bar{y}} \approx \sqrt{\bar{f}'_{cc}} \quad (45)$$

as it can be seen in Figure 4.27, where as an example, the error committed in the approximation for the case $\bar{f}'_{cc} = 1.1$ is reported. The index results then in the simple expression:

$$I_{sec2} = \frac{\epsilon_{cu}^{tar}}{\epsilon_{cu}^{ava}} \cdot \frac{\sqrt{\bar{f}'_{cc}{}^{tar}}}{\sqrt{\bar{f}'_{cc}{}^{ava}}} \quad (46)$$

The effects of the approximation introduced with (45) on the upgrading index will be examined in the next section.

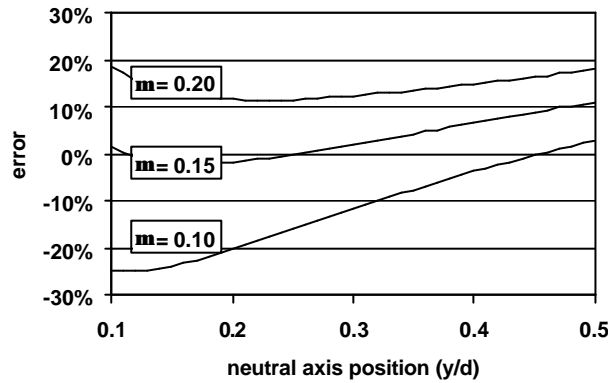


Figure 4.27. Error in the approximation of (45).

The scope of the next section is to verify the accuracy of the upgrading indices (43) and (44). To this aim, a parametric study has been carried out where the values of the upgrading index obtained through both (43) and (44) are compared to the values obtained through numerical analyses performed with a fiber-section model, presented next, which stepwise accounts for the confinement effect of FRP wrapping in the concrete core (Monti and Spoelstra 1997a, 1997b).

4.3.4 Comparison between analytical and numerical indices

The effects of the confining action of both GFRP and CFRP wrapping on the performance of bridge pier sections have been studied on a set of selected full circular sections, deemed to be representative of a class of bridge piers built in Europe in the 60's and 70's. Using the fiber model presented above, the pier sections

are first assessed (their available ductility δ_{χ}^{ava} is computed) under “as-built” conditions, then they are upgraded with different FRP jackets, and then assessed again (the obtained δ_{χ}^{tar} ductility is computed). For each pier examined, the corresponding (numerically evaluated) upgrading index is compared with the (analytically computed) upgrading indices of (43) and (44).

In the analyses, the conventional yield point is found *a posteriori*, as the intersection point between the line starting from the origin and passing through the first yield of a bar in tension, and the line with zero slope passing at 85% of the maximum moment (which coincides with the ultimate one, if no softening takes place). The conventional collapse point corresponds to the failure of the uppermost confined concrete fiber, whose ultimate strain is determined with (27) under as-built conditions and with (30) under upgraded conditions.

Table 4.12. Parameters considered in the parametric study.

Parameter	Range
“As built” section	
Diameter of section D (m)	1.60
Reduced axial load n	0.04, 0.08, 0.12
Concrete strength f'_{co} (MPa)	30, 35, 40
Steel strength f_{sy} (MPa)	300, 400, 500
Longitudinal reinforcement ratio ρ_{sl} (%)	0.50, 0.75, 1.00
Transverse reinforcement ratio ρ_{st} (%)	0.05, 0.10, 0.15
Composite materials for upgrading	
GFRP - Jacket volumetric ratio ρ_j (%)	0.25, 0.50, 0.75
GFRP - Tensile strength f_{ju} (MPa)	800, 1000, 1400
GFRP - Young's modulus E_j (GPa)	35, 45, 65
CFRP - Jacket volumetric ratio ρ_j (%)	0.25, 0.50, 0.75
CFRP - Tensile strength f_{ju} (MPa)	1200, 1500, 1700
CFRP - Young's modulus E_j (GPa)	120, 140, 150

Table 4.12 lists the parameters considered in the study, along with the considered range of variation. The adopted values and also the construction material strengths are deemed to represent those used in old construction standards in the 60's and 70's. The piers diameter is kept constant throughout the analyses, thus neglecting possible scale effects, which however are not deemed to be particularly significant for the ‘typical’ range of diameters (1.0 to 3.0 m) of bridge piers. This amounts to

assuming that the confining effect only depends on the jacket volumetric ratio ρ_j . Here, unidirectional fibers orthogonal to the pier axis have been considered.

The results obtained in the parametric studies are presented in Figure 4.28, where the indices numerically obtained from the fiber-section model are first compared to the indices analytically obtained with equation (43), for both upgrading cases with GFRP and CFRP jackets. Considering that the solid line represents the perfect coincidence between the analytical and the numerical index, it is seen that most of the dots representing the numerical outcomes lay very close to it, thus corroborating the correctness of the formulation developed for the analytical index.

However, it is noticed that for high upgrading values, say, in excess of 4, the analytical index I_{sec1} tends to become under-conservative and to overestimate the effectiveness of the upgrading. This can be imputed to the approximation introduced with the error function (41): as shown in Figure 4.26, the error is maximum when $0.1 \leq \bar{y} \leq 0.2$, that is, where the neutral axis is more likely located at high ductility levels, which occur for high upgrading values. On the other hand, for values of the index I_{sec1} comprised between 2 and 4, the neutral axis is located in the range where the approximation errors are lower, and the index, even though obtained with a crude linearization, predicts the upgrading with sufficient accuracy.

The results obtained with the index I_{sec2} in (46) are presented in Figure 4.29, where it can be seen that its performance is extremely improved with respect to the previous index, notwithstanding the approximation introduced with (45). Thus, it can be concluded that the upgrading index (46) can be reliably used to optimally design FRP jackets, for both light and heavy upgrading interventions on r.c. circular sections. It is interesting to note that higher upgrade levels are attained with GFRP jackets, rather than with CFRP jackets, thanks to the higher flexibility of GFRP that allows concrete to reach higher ultimate strains (see also Spoelstra and Monti 1999).

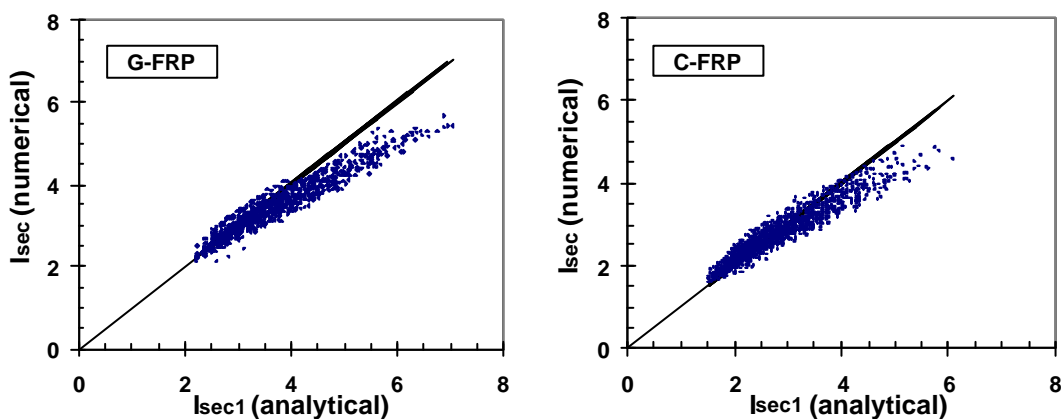


Figure 4.28. Results of the parametric study. Comparison between the indices obtained numerically from the fiber-section model and the index I_{sec1} of equation (43).

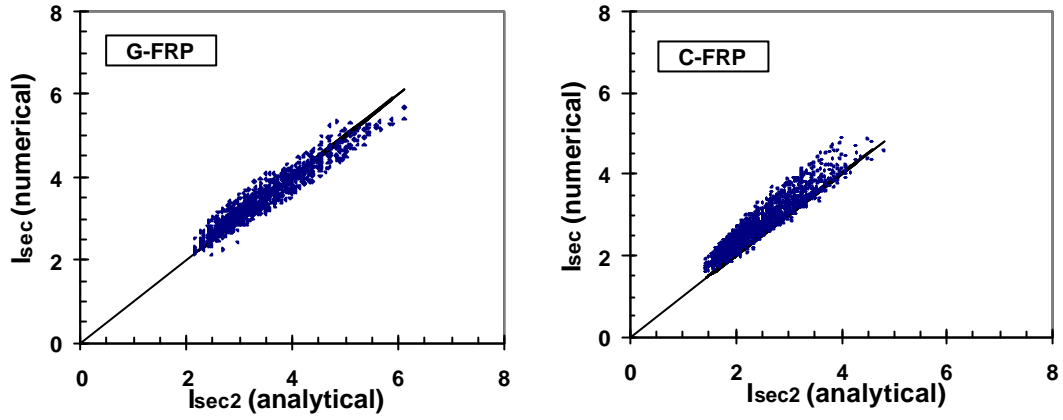


Figure 4.29. Results of the parametric study. Comparison between the indices obtained numerically from the fiber-section model and the index I_{sec2} of equation (46).

4.3.5 Use of the upgrading index for design of FRP jackets

With equation (46), the upgrading index is now cast as initially intended with equation (23), that is, it incorporates *target* (TAR) quantities that can be expressed as the product of *available* (AVA) quantities, times the desired upgrading index (I), as follows:

$$\epsilon_{cu}^{tar} \sqrt{\bar{f}_{cc}^{tar}} = I_{sec2} \cdot \left(\epsilon_{cu}^{ava} \sqrt{\bar{f}_{cc}^{ava}} \right) \longrightarrow \text{TAR} = I \cdot \text{AVA} \quad (47)$$

The unknown quantity TAR is a function, through ϵ_{cu}^{tar} and \bar{f}_{cc}^{tar} , of the normalized confining pressure $\bar{f}_l = \frac{1}{2} \rho_j \bar{f}_{ju}$, of the jacket ultimate strain ϵ_{ju} , and of the concrete normalized initial modulus \bar{E}_c . Actually, the dependence on this latter has been observed to be very weak, so that:

$$\text{TAR}(\rho_j, \bar{f}_{ju}, \epsilon_{ju}) = I \cdot \text{AVA} \quad (48)$$

where the terms in parenthesis represent the sought quantities of the design procedure, in the sense that, once the jacket material (*i.e.*, \bar{f}_{ju} and ϵ_{ju}) has been selected, one can determine the quantity ρ_j . Unfortunately, the complexity of the function TAR prevents to explicitly express these quantities in terms of the known quantity $I \cdot \text{AVA}$. Therefore, a more treatable expression for $\text{TAR}(\rho_j, \bar{f}_{ju}, \epsilon_{ju})$ has been sought through a multivariate regression analysis, whose results are condensed in Figure 4.30, where the solid lines represent the function:

$$\text{TAR}(\rho_j, \bar{f}_{ju}, \epsilon_{ju}) = \left(2.5 \bar{f}_l \epsilon_{ju}^{\frac{3}{2}} \right)^{\frac{1}{2}} \quad (49)$$

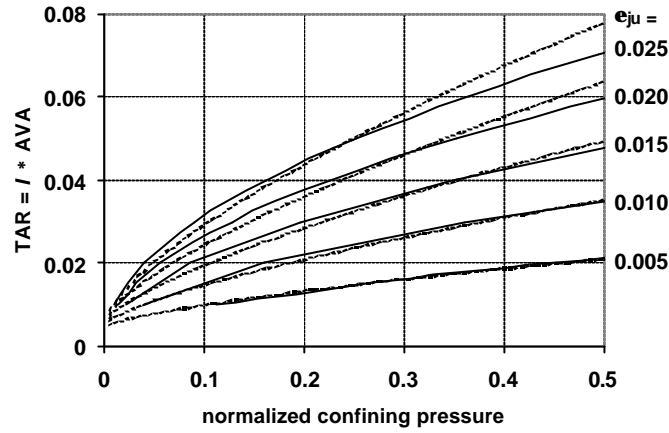


Figure 4.30. Function TAR: exact (dashed lines) vs. regression (solid lines).

Thus, equation (48) can be now expressed as:

$$\left(2.5 \bar{f}_l \varepsilon_{ju}^{\frac{3}{2}}\right)^{\frac{1}{2}} = \left(1.25 \rho_j \bar{f}_{ju} \varepsilon_{ju}^{\frac{3}{2}}\right)^{\frac{1}{2}} = I \cdot \varepsilon_{cu}^{ava} \sqrt{\bar{f}'_{cc}{}^{ava}} \quad (50)$$

from which the expression that defines the jacket volumetric ratio as function of known quantities (I , $\bar{f}'_{cc}{}^{ava}$ and ε_{cu}^{ava}) and selected quantities (\bar{f}_{ju} and ε_{ju}), is finally found:

$$\rho_j = 0.8 I^2 \cdot \frac{\bar{f}'_{cc}{}^{ava}}{\bar{f}_{ju}} \cdot \frac{\varepsilon_{cu}^{ava^2}}{\sqrt{\varepsilon_{ju}^3}} \quad (51)$$

where $\bar{f}'_{cc}{}^{ava}$ is obtained through (9) with f_l from (10) and ε_{cu}^{ava} is obtained from (27).

It should be noticed that the design equation (51) is best suited for cases having TAR larger than 0.01, because of the steep gradient of the function below that point (as seen from the concentration of lines in Figure 4.30). Note also that, for FRP jackets having large ultimate strain ε_{ju} (say, larger than 0.02), the design equation tends to underestimate the jacket effectiveness for values of the function TAR larger than 0.05. It should however be remarked that both ranges of values are rather unlikely to occur.

The design procedure for designing an FRP jacket can be summarized as follows:

1. Assess (through survey) the quantities: f'_{co} , n , μ_s and μ_{st} ,
2. Compute $\bar{f}'_{cc}{}^{ava}$ from (9) with f_l from (10), and ε_{cu}^{ava} from (27),

3. Assess the available curvature ductility δ_{χ}^{ava} at the pier base section, through a section model, using f'_{co} , n , μ_s and μ_{st} ,
4. Evaluate the target one δ_{χ}^{tar} , based on expected loads (for the case of seismic action, see next section),
5. Compute the upgrading index $I = I_{sec} = \delta_{\chi}^{tar} / \delta_{\chi}^{ava}$, verify that $I \cdot AVA > 0.01$,
6. Select the material for the FRP jacketing (\bar{f}_{ju} and ε_{ju}),
7. Determine the FRP jacket thickness t_j from (51) and $t_j = \rho_j d_j / 4$.

4.3.6 Design Example

The design procedure outlined in the previous paragraph is here applied to the r.c. circular bridge pier by Seible *et al.* (1995c), presented previously, and then the value found for the jacket thickness is compared to the actual value actually adopted in the test. The test by Saadatmanesh *et al.* (1997) was discarded because the computed value of $I \cdot AVA = 0.011$ was considered too close to the lower limit of 0.01 under which the design equation is considered to fail.

Pier by Seible *et al.* (1995c):

1. $f'_{co} = 44.3$ MPa, $n = 0.046$, $\mu_s = 0.025 \cdot 293/44.3 = 0.165$ and $\mu_{st} = 0.003 \cdot 403/44.3 = 0.027$ (used in the test),
2. $\bar{f}'_{cc}{}^{ava} = 1.074$ from (9) with $f_l = 0.5 \cdot 0.8 \cdot 0.003 \cdot 403 = 0.48$ MPa, and $\varepsilon_{cu}^{ava} = 0.008$ from (27).
3. $\delta_{\chi}^{ava} = 8.1$ at the pier base section (computed with (54) from the experimental displacement ductility δ_d^{ava} in Table 4.10, with $l_p = 0.3$ m from (20)),
4. $\delta_{\chi}^{tar} = 38.8$ (computed from δ_d^{tar} as above),
5. $I = I_{sec} = \delta_{\chi}^{tar} / \delta_{\chi}^{ava} = 4.8$, $I \cdot AVA = 0.04 > 0.01$,
6. $\bar{f}_{ju} = 793/44.3 = 17.9$ and $\varepsilon_{ju} = 0.023$ (used in the test),
7. $\rho_j = 0.022$ and $t_j = 0.25 \cdot 608 \cdot 0.022 = 3.3$ mm.

Note the acceptable difference with respect to the values actually used in the test: $\rho_j = 0.0247$ and $t_j = 3.81$ mm.

4.3.7 Ductility upgrading of piers in seismic regions

When designing upgrading interventions on structures in seismic areas, one deals with spectral ordinates that measure the seismic action felt by the structure (usually, in terms of forces). In a ductility-based design, it is known that the spectral ordinates used for evaluating the forces acting on a structure are related to the amount of available ductility. In this view, it is all too natural to define a *pier*

upgrading index I_{pier} , analogous to that already defined in terms of ductility, and to relate it to the spectral ordinates corresponding to different ductility values.

In order to do this, let us consider an elastic-plastic oscillator. The non-collapse requirement is expressed as:

$$\delta_d^{\text{tar}} = \frac{m R(T) a_g}{F_y} \leq \delta_d^{\text{ava}} \quad (52)$$

The above formula states that a SDOF system having mass m , elastic period T , yield force F_y , under a response acceleration $R(T)a_g$ (with $R(T)$ = response spectrum and a_g = peak ground acceleration) is required a *target* displacement ductility δ_d^{tar} , and it survives if this is not greater than the *available* ductility δ_d^{ava} .

The above inequality can be also expressed in terms of the pier upgrading index I_{pier} as:

$$I_{\text{pier}} = \frac{\delta_d^{\text{tar}}}{\delta_d^{\text{ava}}} = \frac{m R(T) a_g}{F_y^{\text{ava}} \delta_d^{\text{ava}}} \quad (53)$$

For well-designed or sound structures, the above equation yields a results lower than 1, then no upgrading is necessary. For insufficiently-designed or damaged structures, the above equation yields an upgrading index I_{pier} greater than 1. This might occur, in practical cases, if: a) the mass m on top of the pier increases (*e.g.*, enlargement of the deck to accommodate more lanes, or replacement of traffic barriers with heavier ones); b) the response spectrum (amplification factor) $R(T)$ ordinate increases (*e.g.*, change of the design spectrum in the seismic code); c) the peak ground acceleration a_g increases (*e.g.*, change in the conventional seismic classification); d) the pier strength F_y^{ava} decreases because of damage; e) the available ductility δ_d^{ava} decreases because of damage. This two latter values can be found through usual assessment procedures.

From the element displacement ductility demand δ_d^{tar} , the section curvature ductility demand δ_χ^{tar} should be recovered. For ex., for the simplest case of single-bent pier, from (19) one gets:

$$\delta_\chi = 1 + \frac{\delta_d - 1}{3 \frac{l_p}{L} \left(1 - 0.5 \frac{l_p}{L} \right)} \quad (54)$$

Thus, the value of the section upgrading index I_{sec} which satisfies the *target* condition can be found:

$$I_{\text{pier}} = \frac{\delta_d^{\text{tar}}}{\delta_d^{\text{ava}}} \xrightarrow{\text{use equation(38)}} \frac{\delta_\chi^{\text{tar}}}{\delta_\chi^{\text{ava}}} = I_{\text{sec}} \quad (55)$$

Given the index value as a measure of upgrading requirement of the section, is then possible to design the upgrading jacket, through the procedure outlined in the previous section.

4.4 Conclusions

The use of fiber reinforced polymers (FRP) materials is gaining widespread acceptance in the engineering community, even though in Europe few applications have been developed, also due to the absence of pertinent regulations in the building codes. This is mainly related to the fact that necessary studies are currently under way and aim at clarifying the properties of these innovative materials used in conjunction with reinforced concrete structures.

One of the aspects that deserves a deeper insight is the ductility enhancement that is obtainable on bridge piers by wrapping them with FRP sheetings. This is exactly the goal that has been pursued in the studies presented above: the development of new, simple and rational design rules for designing the optimal thickness of FRP jackets in plastic hinge regions of existing reinforced concrete bridge piers, having circular cross-section. The procedure is deemed for the design of interventions in seismic regions, but it is initially cast in a general framework and subsequently specified for the seismic case. To this purpose, an upgrading index has been defined, which relates the available ductility at the pier base section to the desired level of ductility to attain through FRP jacketing. The available ductility is identified through the usual assessment procedures, while the target ductility is evaluated based on the expected actions on the bridge. It is clear that a ductility upgrade is a task essentially pursued in cases of seismic strengthening or retrofitting, nonetheless the procedure is developed for general purposes and the application to the seismic case is presented as an extension. Once the index has been defined, an expression suitable for design was sought, which could express ductility as function of easily computable quantities.

The ability of the proposed index to represent the actual ductility increase due to upgrading with FRP jackets was tested through a parametric study on bridge piers sections, deemed to represent the result of an obsolete design procedure, which are then upgraded with either glass or carbon fiber jackets.

In order to run the numerical analyses to assess the accuracy of the design equation, a uniaxial concrete model has been developed (see paragraph 4.1), which explicitly accounts for the continuous interaction with the confining device. The model can be used for concrete confined with either steel or FRP and it is meant to be included in fiber-type finite element models for the analysis of FRP-strengthened reinforced concrete structures.

This model relies on an iterative procedure, through which the stress-strain curve is obtained as one that crosses a family of stress-strain curves at constant confinement pressure, where at each point the confinement pressure is equal to that

induced by the FRP jacket subjected to the corresponding lateral expansion. In order to evaluate the lateral strain at a given level of axial strain, a damage model proposed by Pantazopoulou and Mills (1995) has been adapted to the case of varying confinement pressure. This model is strongly dependent on the value attributed to the coefficient β , of which a new equation for its determination has been proposed.

For FRP-confined concrete, the resulting stress-strain curve show a gradually increasing behavior, until the jacket fails. The simulated compressive response of normal strength concrete confined with FRP has been compared to available tests on wrapped cylinders, showing excellent agreement both in terms of stress-strain behavior and ultimate state. Also, the lateral strain, volume strain, and dilation rate curves are satisfactorily modeled.

Through the developed model, predictive equations have been derived to determine the ultimate compressive strength and strain of FRP-confined concrete, that are useful in the analysis of the response of r.c. sections strengthened with FRP wrappings. In fact, the proposed confinement model proved to be very effective in moment-curvature analyses through fiber-section to predict the increase in strength and ductility of concrete confined with fiber-reinforced plastics, in a more realistic manner than the commonly used confinement models (see paragraph 4.2).

Going back to the design equation developed in paragraph 4.3, such fiber section model was used in the analyses. The numerical indices obtained with the parametrized fiber section models were then compared with two different analytical indices, each one corresponding to a different approximation introduced in its formulation. One index has been derived by linearizing the law of variation of the compressed areas of concrete and steel and the steel tensile area, while the other uses nonlinear approximations. It has been shown that both analytical indices yields excellent predictions of the ductility increase obtained through FRP wrapping, but the second index should be preferred, both, for its better accuracy even at higher index values, and because of its simplicity, since it requires the knowledge of only the ultimate strain and the peak strength of concrete. A last step was to split the index into known (available, from assessment) and unknown (target, to be designed) quantities and define these latter in terms of the mechanical and geometrical characteristics of the jacket to be designed.

Eventually, a design equation is obtained that allows to determine the thickness of the FRP jacket in terms of: the upgrading index, which is the objective of the design, the selected mechanical characteristics of the jacket, and the quantities defining the initial state of the section. An example application of the design procedure to a scaled bridge pier, wrapped with FRP and tested to failure, has demonstrated the accuracy of this equation for designing FRP jackets for the upgrade of circular r.c. sections.

4.5 References

Chai, Y.H., Priestley, M.J.N. and Seible, F. (1991). Seismic retrofit of circular bridge columns for enhanced flexural performance, *ACI Structural Journal*, Vol. 88, September-October, 572-584.

- Chang, G.A. and Mander, J.B. (1994). Seismic energy based fatigue damage analysis of bridge columns: Part 1 - Evaluation of seismic capacity, *Report No. NCEER-94-0006*, National Center for Earthquake Engineering Research, State University of New York at Buffalo, New York, USA.
- Fardis, M.N. and Khalili, H. (1982). Concrete encased in fiberglass reinforced plastic, *Journal of the American Concrete Institute*, 78(6), 440-446.
- Harmon, T., Slattery, K. and Ramakrishnan, S. (1995). The effect of confinement stiffness on confined concrete, Non-Metallic (FRP) Reinforcement for Concrete Structures, *Proc. of the 2nd International RILEM Symposium*, Ghent, Belgium, August, 585-600.
- Hoshikuma, J., and Unjoh, S. (1997). Seismic retrofit of existing reinforced concrete columns by steel jacketing. *Proceedings of the Second Italy-Japan Workshop on Seismic Design of Bridges*, 27-28 February, Roma, Italy.
- Howie, I. and Karbhari, V.M. (1995). Effect of tow sheet composite wrap architecture on strengthening of concrete due to confinement: I – Experimental studies, *Journal of Reinforced Plastic and Composites*, 14(9), 1008-1030.
- Imran, I. and Pantazopoulou, S.J. (1996). Experimental study of plain concrete under triaxial stress, *ACI Materials Journal*, Vol. 93, November-December, (589-601).
- JSCE (1995). State-of-the-Art-Report on Continuous Fibre Reinforcing Materials. *Concrete Engineering Series 3*, Japan Society of Civil Engineering, Japan.
- Karbhari, V.M. and Gao, Y. (1997). Composite jacketed concrete under uniaxial compression Verification of simple design equations, *J. of Composites in Structures*, ASCE, to appear.
- Kawashima, K., Hosotani, M. and Hoshikuma, J. (1997). A model for confinement effect for concrete cylinders confined by carbon fiber sheets, *NCEER-INCEDE Workshop on Earthquake Engineering Frontiers of Transportation Facilities*, March, NCEER SUNY, Buffalo, USA.
- Kim, D.H. (1995). **Composite structures for civil and architectural engineering**, E&FN Spon Eds., New York, USA.
- Mander, J.B., Priestley, M.J.N. and Park, R. (1988a). Theoretical stress-strain model for confined concrete, *Journal of Structural Engineering*, ASCE, Vol. 114(8), 1804-1826.
- Mander, J.B., Priestley, M.J.N. and Park, R. (1988b). Observed stress-strain behavior of confined concrete, *Journal of Structural Engineering*, ASCE, Vol. 114(8), 1827-1849.
- Matthys, S., Taerwe, L., and Monti G. (1999). Confinement of concrete columns with fibre reinforced polymers. *Fib Symposium*, Praga 1999.
- Mier, J.G.M. van (1984). Strain-softening of concrete under multiaxial loading conditions, *B.S. Thesis*, Eindhoven University, The Netherlands.
- Mirmiran, A. and Shahawy, M., (1997). Behavior of concrete columns confined by fiber composites, *Journal of Structural Engineering*, ASCE, Vol. 123(5), May, 583-590.
- Mirmiran, A., Kargahi, M., Samaan, M. and Shahawy, M. (1996). Composite FRP-concrete column with bi-directional external reinforcement, *Proc. 1st International Conference on Composites in Infrastructure*, Tucson, Arizona, USA, 888-902.
- Monti, G. and Spoelstra, M.R. (1997a). Analysis of RC bridge piers externally reinforced with fiber-reinforced plastics. *Proc. 2nd Italy-Japan Workshop on Seismic Design and Retrofit of Bridges*, Rome, Italy, February.

- Monti, G. and Spoelstra, M.R. (1997b). Fiber-section analysis of RC bridge piers retrofitted with FRP jackets. *ASCE Structures Congress*, Portland, Oregon, USA, April.
- Monti, G., Nisticò, N. and Santini S. (2001). Design of FRP jackets for upgrade of circular bridge piers. *Journal of Composite Materials in Construction*, ASCE, Vol. 5(2), June.
- Monti, G., Nuti, C. and Santini, S. (1996). CYRUS: Cyclic Response of Upgraded Sections. *Report DSSAR 1/96 Materiali, Dipartimento di Scienze Storia dell'Architettura e Restauro*, Università degli Studi G. D'Annunzio, Chieti, Italy.
- Nanni, A. and Bradford, N.M. (1995). FRP jacketed concrete under uniaxial compression, *Construction and Building Materials*, 9(2), 115-124.
- Newman, K. and Newman, J.B., (1971). Failure theories and design criteria for plain concrete, *Proceedings, International Civil Engineering Materials Conference on Structures, Solid Mechanics and Engineering Design*, Wiley Interscience, New York, USA, 936-995.
- Pantazopoulou, S.J. (1995). Role of expansion on mechanical behavior of concrete, *Journal of Structural Engineering*, ASCE, Vol. 121(12), 1795-1805.
- Pantazopoulou, S.J. and Mills, R.H. (1995). Microstructural Aspects of the mechanical response of plain concrete, *ACI Materials Journal*, Vol. 92, November-December, 605-616.
- Picher, F., Rochette, P. and Labossière, P. (1996). Confinement of concrete cylinders with CFRP, *Proc. First International Conference on Composite Infrastructures*, Tucson, Arizona, USA, 829-841.
- Popovics, S. (1973). Numerical approach to the complete stress-strain relation for concrete, *Cement and Concrete Res.*, Vol. 3(5), 583-599.
- Priestley, M.J.N. and Seible, F. (1992). Design guidelines for assessment, retrofit and repair of bridges for seismic performance, *Report No. SSRP-92/01*, Department of Applied Mechanics and Engineering Sciences, University of California, San Diego, USA.
- Priestley, M.J.N., Seible, F. and Fyfe, E. (1992). Column seismic retrofit using fiberglass/epoxy jackets, *Proc. First International Conference on Advanced Composite Materials in Bridges and Structures*, Sherbrooke, Canada, 287-298.
- Priestley, M.J.N., Seible, F., and Calvi, M. (1996). **Seismic design and retrofit of bridges**. *John Wiley & Sons*, New York.
- Saadatmanesh, H., Ehsani, M. R., and Jin, L. (1997). Seismic strengthening of circular bridge piers with fiber composites. *ACI Structural Journal*, Vol. 93, N. 6, 639-647.
- Saadatmanesh, H., Ehsani, M.R. and Li, M.W. (1994). Strength and ductility of concrete columns externally reinforced with fiber composite straps, *ACI Structural Journal*, Vol. 91, July-August, 434-447.
- Saatcioglu, M. and Razvi, S.R., (1992). Strength and ductility of confined concrete, *Journal of Structural Engineering*, ASCE, Vol.118(6), June, 1590-1607.
- Seible, F., Hegemier, G. A., Priestley, M. J. N. and Innamorato, D. (1995a). Developments in bridge column jacketing using advanced composites. *Proc. National Seismic Conference on Bridges and Highways*, San Diego, CA, USA.
- Seible, F., Burgueño, R., Abdallah, M.G. and Nuismer, R. (1995). Advanced composite carbon shell systems for bridge columns under seismic loads, *Progress in research and*

practice, Proc. National Seismic Conference on Bridges and Highways, San Diego, CA, USA.

- Seible, F., Hegemier, G. A., Priestley, M. J. N. and Innamorato, D. (1995c). Fiberglass shell jacket retrofit test of a circular shear column with 2.5% reinforcement. *Advanced Composites Technology Transfer Report, ACTT-95/13*, San Diego, CA, USA.
- Seible, F., Priestley, M.J.N. and Innamorato, D. (1995d). Earthquake retrofit of bridge columns with continuous fiber jackets, Volume II, Design guidelines, Advanced composite technology transfer consortium, *Report No. ACTT-95/08*, University of California, San Diego, USA.
- Spacone, E., Filippou, F.C., and Taucer, F.F. (1996). Fiber Beam-Column Model for Nonlinear Analysis of R/C Frames. Part I: Formulation. Part II: Applications. *Earthquake Engineering and Structural Dynamics*, **25**(7), 711-742.
- Spoelstra, M. R. and Monti, G. (1999). FRP-confined concrete model. *Journal of Composite Materials in Construction*, ASCE, 3(3), 143-150.
- Spoelstra, M.R. (1997). Flexural retrofitting of full circular concrete bridge columns with fiber-reinforced plastic jackets for enhancement of seismic performance, *M.Sc. Thesis*, Delft University of Technology, The Netherlands, August.
- Xiao, Y., Martin, G. R., Yin, Z. and Ma, R. (1995). Retrofit design of existing reinforced concrete bridge columns using prefabricated composite jacketing. *Proc. National Seismic Conference on Bridges and Highways; December 10-13, San Diego, CA, USA.*